Physics and Chemistry of the Te and HgTe-based Ternary Melts

Ching-Hua Su

Materials and Processing Laboratory, EM31 NASA/Marshall Space Flight Center, Huntsville, Alabama 35812 USA.

E-mail address: ching.h.su@nasa.gov

Abstract

Historically, the theoretical treatment of the liquid phases has always been more difficult and complicated than that for solid and gas phases. A liquid has no lattice structure as crystalline solids and the atoms/molecules in the liquid can migrate through it relatively rapidly. On the other hand, it is also interacting with many other atoms/molecules so that the simplifications of the kinetic theory of gases cannot be employed. For more complicated liquids, such as the liquids of high ionicity and those containing hydrogen bonds and electric dipoles, the understanding is far from complete. At the same time, accurate information on the physics and chemistry of semiconductor melts is needed for the quantitative descriptions of the process of crystal growth from melt. The pre-crystallization phenomena in the liquid phase are critical because the properties of the grown crystals depend on the state and structure of the melt as well as the thermal history of the melt during solidification process. However, the data on the liquid phase, such as thermophysical properties of semiconductor melts are scarce, especially for the HgTe-based II-VI ternary compound semiconductors because of their high vapor pressure and extreme toxicity. Analysis of the thermophysical properties of the melt can provide information about structural transitions of the melt during the solidification process. From a broader point of view, the structure of liquids is much more complicated than the crystalline solids, especially the relaxation behavior through different thermal histories. The theory of hetero-phase fluctuations of liquids is applicable to any many-body systems including condensed-matter physics, field theory, physics of nuclear-matter, cosmology, biology and even sociology.

This book summarizes the physics and chemistry from the experimental measurements and theoretical analyses of phase diagram, thermodynamic properties, density, thermal conductivity, viscosity, and electrical conductivity on the binary, pseudo-binary and ternary melts of the most advanced IR-detector material systems of HgCdTe and HgZnTe as well as the analyses of these results. The main objectives of this study are:

(1) to provide the phase diagrams and thermodynamic properties of Hg-Cd-Te and Hg-Zn-Te systems through quantitatively fitting the experimental data by assuming an associated solution model for the liquid phase,

(2) to experimentally measure the thermophysical properties of the Hg-Cd-Te and Hg-Zn-Te melts, including density, viscosity, electrical conductivity and thermal conductivity as functions of temperature and composition and

(3) to enhance the fundamental knowledge of hetero-phase fluctuations and relaxation phenomena in the melts and extend our understanding of the solidification process in order to interpret the experimental results of crystal growth so as to improve the melt growth processes of the compound semiconductor.

The physics and chemistry of Te and HgTe-based ternary melts were explored through the studies of the structural transformation during melting, the supercooling during solidification, the relaxation phenomena after rapid cooling of the melts and the metal-semiconductor transition in the melts through the analyses of electrical conductivity and Lorenz number. An in-depth study on the thermophysical properties and their time-dependent structural dynamic processes taking place in the vicinity of the solid-liquid phase transition of the narrow homogeneity range HgTe-based ternary semiconductors as well as the analysis of the homogenization process in the melt will also be presented.

Table of Contents

Chapter 1
Introduction

Abstract: The essences of material processing consist of (1) selecting material systems with certain compositions of chemical elements and (2) designing and processing material to achieve the desired properties for specific applications. There are various processing methods, such as synthesis and homogenization, solidification from melt, solidification by vapor transport and condensation, sintering by hot pressing, additive manufacture, etc., which all involves the heating, soaking and cooling history of the process. The processing and production of high-quality single crystals of compound semiconductors are needed for various electro-optical applications. At present, the majority of the semiconducting crystals are grown from the melt. Consequently, the pre-crystallization thermophysical properties, including thermal and electrical conductivity, viscosity and density, and structural phenomena of the liquid phase are critical because the properties of the grown crystals depend on the state and structure of the pre-growth melt as well as the thermal history of the solidification process. On the other hand, thermophysical properties of the melts are also required for accurate simulations of numerical models on the process. However, because of restrictions, such as high vapor pressure and extreme toxicity, imposed by most of the II-VI melts at elevated temperatures, especially the Hg-based systems, the samples are required to be sealed inside closed ampoules. Therefore, the thermophysical property database on the majority of the technologically important II-VI melts are scarce and sometimes inaccurate due to the measuring difficulties, the complexity in operation and the performing limitations of existing techniques. At the same time, the measured viscosity and electrical conductivity of HgZnTe and HgCdTe pseudo-binary melts showing a slow relaxation phenomenon at temperatures near the liquidus point was reproducibly observed. In this book, relaxation phenomenon is defined as the lagging or delayed response of certain properties after a temperature change. These relaxation phenomena can be attributed to hetero-phase fluctuations with the formation of molecular complexes, or nuclei, of competing thermodynamic phases inside a host phase. The main objectives of this study are: (1) to perform accurate measurements of various thermal and physical properties as functions of temperature and composition of the HgTe-based melts (2) to extend our understanding of the physics and chemistry of these melts in order to interpret and improve the quality of crystal growth and (3) to enhance the fundamental knowledge of hetero-phase fluctuations phenomena in the melts so as to improve the melt growth processes of other similar semiconductor systems.

Keywords: Thermophysical properties; Thermal conductivity; Electrical conductivity; Viscosity; Density; Relaxation; Tellurium (Te); Mercury-cadmium-tellurium (Hg-Cd-Te) system; Mercury-zinc-tellurium (Hg-Zn-Te) system

1.1 Essences of Material Processing

The objective of material processing is to produce material for certain specific applications. The essences of the process consist of (1) selecting material systems with specific composition of chemical elements and (2) designing and processing material to achieve the desired properties for these applications. There are various processing methods to be selected from: synthesis and homogenization, solidification from melt, solidification by vapor transport and condensation, sintering by hot pressing, additive manufacture, heat treatments, etc. After

selecting the material system and the applied method, to produce the material with specific properties the material needs to be processed under a combination of imposed controlled environments as exemplifying below:

1. Thermal history (heating, soaking, cooling; rate and duration for each stage)
2. External pressure
3. External containment
4. Vacuum/inert gas/O_2/H_2 environment
5. Electric field (e.g., containerless levitation)
6. Magnetic field (e.g., fluid flow adjustment in electric conductive materials, Eddy current to modify electrical/thermal conductivity)
7. Mechanical force (stirring, rocking, shaking, tapping; frequency and duration)
8. Solidification (nucleation control)
9. Controlled thermodynamic conditions (e.g., apply over-pressures to control chemical potential)
10. Low gravity (in orbiting spacecrafts to reduced gravity effects)
11. High artificial gravity (centrifuge)

    and many other environments.

When applying these environments to achieve the desired effects during the processing, the thermophysical properties of the material system, as functions of temperature and composition, are required to provide the critical information for the designing and construction of the optimal processing conditions. The basic thermophysical properties include density, heat capacity, heat of fusion, thermal conductivity, emissivity, surface tension, electrical conductivity and viscosity, etc.

1.2 HgTe-based Ternary Systems

High quality single crystals of compound semiconductors are needed for various electro-optical applications. At present, the majority of the semiconducting crystals are grown from the melt. Consequently, the pre-crystallization phenomena in the liquid phase are critical because the state and structure of the melt affects the structure and properties of the crystals formed from it. A fundamental understanding of molecular structural dynamics in melts will be helpful in understanding the relations between the interfacial flows and molecular attachment mechanisms, including those generating lattice defects. If the relationship between the processing conditions of the melt and the microstructural development of the solid is well understand then a first-principles design of materials with the desired properties can be greatly enhanced. Therefore, an in-depth study on the time-dependent structural processes taking place in the vicinity of the solid-liquid phase transition as well as the *in-situ* structural analysis of the alloy homogenization process in the melt is needed to understand and to improve the crystal growth processes.

On the other hand, thermophysical properties of the melts are also required for any meaningful investigation of the crystal growth processes, in particular for the accurate simulations of numerical models. Thermal and electrical conductivity, viscosity and density are the basic thermophysical properties of semiconductor melts. The experimental values of these properties as functions of temperature and composition are required for virtually all melt systems

in the materials processing as well as in the field of fundamental fluid physics. However, because of restrictions, such as toxicity, high vapor pressure and contamination, imposed by the II-VI melts at elevated temperatures, the samples are required to be sealed inside closed ampoules. Hence, the thermophysical data on an overwhelming majority of the technologically important II-VI melts are scarce and inaccurate due to the difficulties, the complexity in operation and the performance limitations of existing techniques. The ability to accurately measure these properties of semiconductor melts as functions of temperature and composition would significantly increase the quality of the research and would make numerical modeling work more meaningful.

The studies in this book will be focused on HgTe-based ternary systems, including Hg-Cd-Te and Hg-Zn-Te, which is the ternary system consisting of the binary systems of Hg-Te and Cd-Te and Hg-Te and Zn-Te, respectively. The II-VI binary compounds of HgTe, CdTe and ZnTe are the congruently melting stoichiometric solids with zinc blende structure, i.e., two interpenetrating face center cubic lattice with Group II occupying one sub-lattice and Group VI occupying the other. Each two compounds form complete ternary solid solutions, also known as pseudo-binaries, $Hg_{1-x}Cd_xTe$, $Hg_{1-x}Zn_xTe$ and $Cd_{1-x}Zn_xTe$ with x, the amount of Hg, or Cd, replacing by Cd or Zn atom, ranging from 0 to 1.0. The direct energy bandgap of the solid solution varies with x, from the semi-metal HgTe to the large bandgap semiconductors of CdTe/ ZnTe as shown in Figure 1.1. At a fixed temperature, the light valence band of HgTe, Γ_6, goes up with increasing x, flips up to become a conduction band at the crossover of a specific x and becomes a semiconductor. Then the energy bandgap, $\Gamma_6 - \Gamma_8$, keeps on increasing almost linearly with x until it reaches the end members of CdTe/ZnTe.

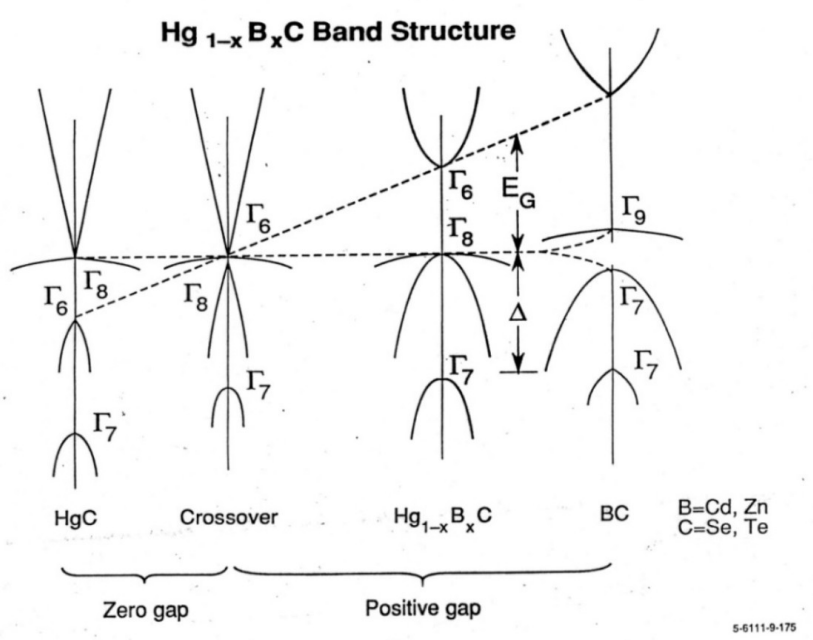

Fig. 1.1 The energy band structure of Hg-based II-VI ternary compound semiconductors, $Hg_{1-x}B_xC$, where B represents Cd or Zn, and C represents Se or Te.

The versatility of the tunable bandgap makes the HgCdTe and HgZnTe compounds two of the most advanced IR detectors which can cover the atmospheric windows of long-wavelength

IR (LWIR) of 8 – 12μm and short wavelength IR (SWIR) of 3 – 5μm. The energy bandgap, E_g, for $Hg_{1-x}Cd_xTe$, has been fitted well with experimental data [1] as functions of x and T (in K) as:

$$E_g\,(\text{eV}) = -0.302 + 1.93x - 0.81x^2 + 0.832x^3 + 5.35 \times 10^{-4}\,(1 - 2x)T \qquad (1.1)$$

For $Hg_{1-x}Zn_xTe$, the similar best-fit expression is given by [2]:

$$E_g\,(\text{eV}) = -0.3 + 0.0324x^{1/2} + 2.731x - 0.629x^2 + 0.533x^3 + 5.3 \times 10^{-4}T(1 - 0.76x^{1/2} - 1.29x) \qquad (1.2)$$

The values of E_g at 77K calculated from these expressions are plotted in Figure 1.2 as functions of x for $Hg_{1-x}Cd_xTe$ and $Hg_{1-x}Zn_xTe$. The wavelengths corresponding to the values of E_g are given by the right labels and the ranges of 3 – 5 and 8 – 12μm are illustrated as a blue and red band, respectively. The bands show that the optimal composition for LWIR is 0.215 to 0.245 for HgCdTe and 0.14 to 0.16 for HgZnTe, respectively, whereas the composition for SWIR is 0.315 to 0.415 for HgCdTe and 0.20 to 0.27 for HgZnTe. Hence, most of the data presented here are for materials of $Hg_{1-x}Cd_xTe$ and $Hg_{1-x}Zn_xTe$ with x less than 0.3.

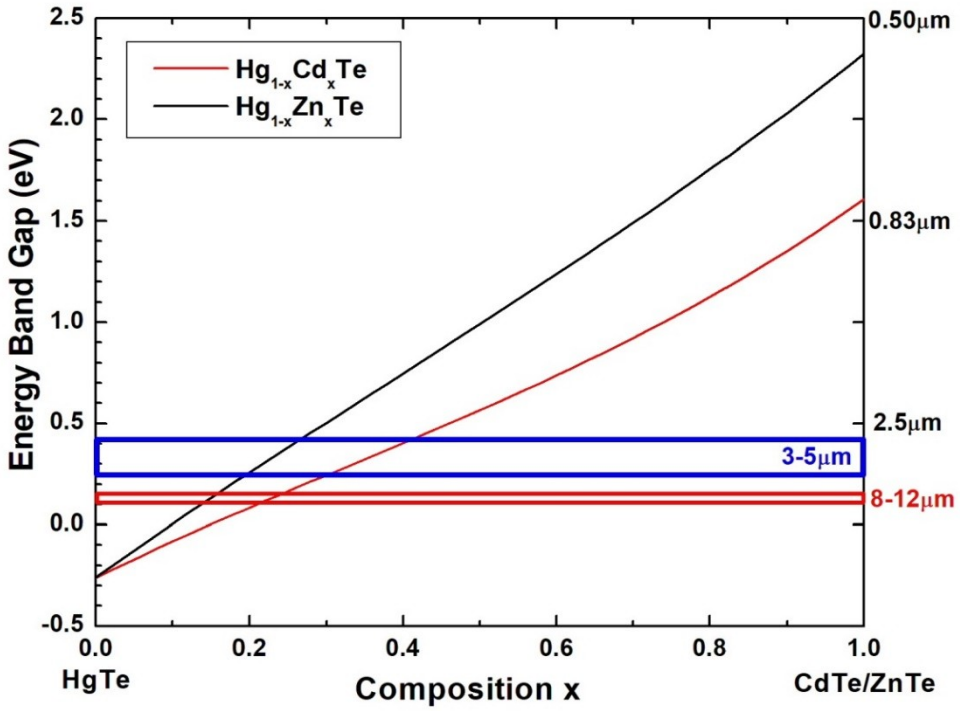

Fig. 1.2 Energy bandgap as functions of x for $Hg_{1-x}Cd_xTe$ and $Hg_{1-x}Zn_xTe$ at 77K. The right labels give the wavelengths corresponding to the values of E_g and the ranges of 3 – 5 and 8 – 12 μm are illustrated as a blue and red band, respectively.

1.3 Thermophysical Properties

Because of restrictions, such as toxicity, high vapor pressure and contamination, imposed by the HgTe-based systems, the samples are required to be sealed inside closed ampoules. There existed only limited amounts of data [3-9] on the thermodynamic and thermophysical properties of the HgTe-based molten semiconductors. These data will also be critical in the research of fundamental fluid physics. From a broader point of view, the structure of liquids is much more complicated than the crystalline solids, especially the relaxation behavior through different thermal histories. The theory of hetero-phase fluctuations of liquids is applicable to any many-body systems including condensed-matter physics, field theory, physics of nuclear-matter, cosmology, biology and even sociology. For instance, many anomalous events in the life of various societies can be understood as hetero-phase fluctuations occurring around the sociological phase transitions, either discontinuous (revolutionary) or continuous (evolutionary).

At the same time, in the cases of unseeded melt growth of II-VI compounds, namely, CdTe, CdZnTe and ZnSe, there were a large number of experimental facts showing the correlation between melt state and crystal quality [10-21]. It is believed that the crystalline quality can be improved, i.e., reduced number of large angle grains and twins, if the melt was markedly superheated (about 20^{o}C higher than the melting point for CdTe) or long-time held before growth. The viscosity of HgZnTe pseudo-binary melt was measured using an oscillating-cup viscometer [22]. An unexpected time drift of the measured viscosity, which shows a slow relaxation phenomenon at temperatures near the liquidus point, was reproducibly observed. Figure 1.3 displays two sets of data obtained by cooling the $Hg_{0.84}Zn_{0.16}Te$ melt rapidly from 850^{o}C to be stabilized at temperatures of 810^{o}C and 790^{o}C, which is just above the liquidus temperature. While it took one day to reach equilibration at 810^{o}C, five days were required at 790^{o}C as the value went up by almost a factor of two. A similar relaxation phenomenon was also observed in the measured density of the same liquid [23].

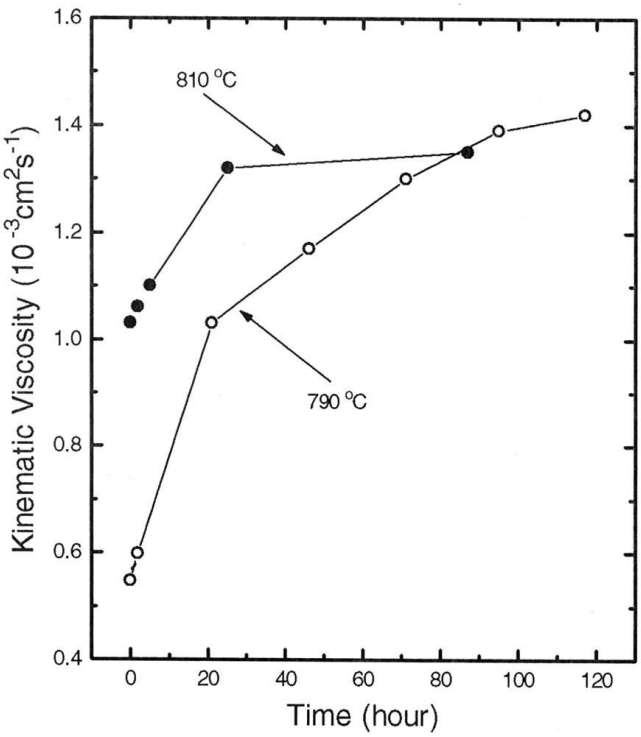

Figure 1.3 Time variation of the measured viscosity after cooling the $Hg_{0.84}Zn_{0.16}Te$ melt rapidly from 850°C to the prescribed temperatures, 810 and 790°C (taken from Figure 4 in Ref.[22])

Similar phenomena [24] were observed in the time dependence of the measured electrical conductivity and viscosity of the $Hg_{0.8}Cd_{0.2}Te$ melt after the temperature was lowered from 857°C to 800°C, which took the furnace approximately 20 min. The measured viscosity of the $Hg_{0.8}Cd_{0.2}Te$ melt as functions of time, given in Figure 1.4, showed that the viscosity increased initially as a function of time after the cooling. Then, at approximately 2 hrs, it went through a maximum of $5.0\times10^{-7}m^2/s$ and started to decline for approximately 50 hrs to reach its equilibrium value of $3.75\times10^{-7}m^2/s$.

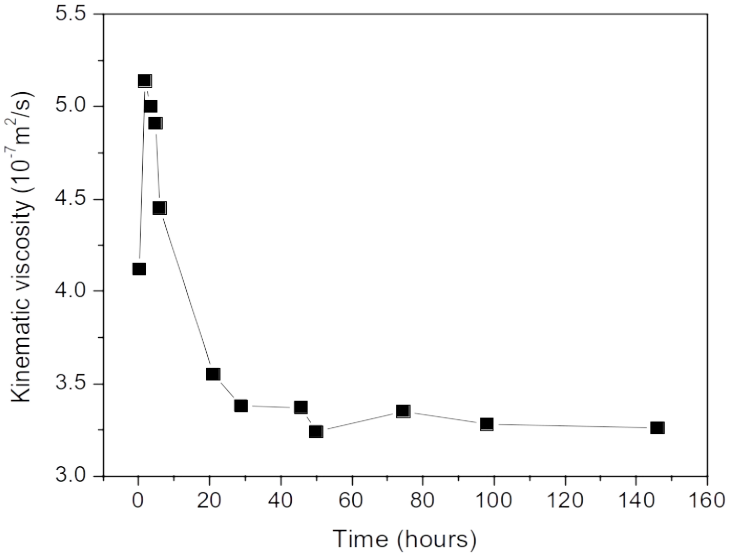

Figure 1.4 Time variation of the kinematic viscosity of the $Hg_{0.8}Cd_{0.2}Te$ melt after cooling from 857ºC to 800ºC (taken from Figure 81 of Ref.[24]).

The relaxation phenomena were even observed on an element of II-VI compounds. The measured thermal diffusivity and viscosity of Te melt are displayed in Figure 1.5 as functions of time after the melt was quenched from 900 to 560ºC. While it took 1 hr, after the sample reaching the temperature of 560ºC, for the measured thermal diffusivity to reach the steady state value, about 6 hrs was needed for the measured values of viscosity [25]. Using a simple kinetic scheme for polymerization of tellurium atoms which assuming the rate of reaction for attaching and detaching one Te atom is the same for each step of polymerization, the change of Te viscosity as a function of time was calculated and agrees well with the experimental data [25].

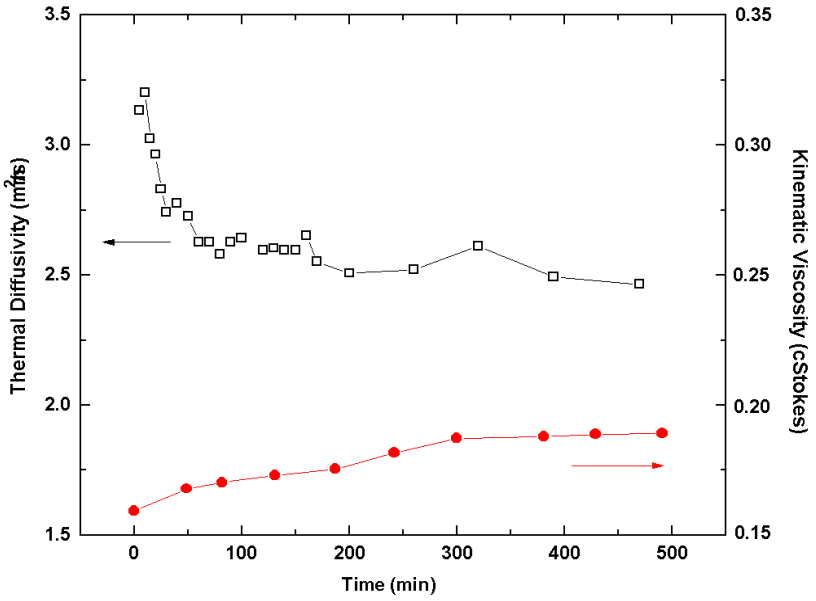

Figure 1.5 Measured thermal diffusivity and viscosity of Te melt as functions of time after the melt was quenched from 900 to 560ºC (take from Ref.[25]).

In a broad sense, these relaxation phenomena can be attributed to hetero-phase fluctuations with the formation of molecular complexes, or nuclei, of competing thermodynamic phases inside a host phase. Systems with hetero-phase fluctuations are in quasi-equilibrium, or local equilibrium. On the other hand, homo-phase fluctuations existing in equilibrium systems and need to be described by methods of equilibrium thermodynamics or statistical mechanics. Phonons in crystals, magnons in magnets or polaritons in ferroelectrics are a few examples of common homo-phase fluctuations.

The II-VI elements are known to form associated species, such as CdTe and ZnTe, in the liquid phase [26] and the level of the association decreases as temperature increases. It is speculated that during melt growth with low superheating the associated complexes remain associated even after long relaxation time. This resulted in the multi-grain crystal growth because the spontaneous single nucleation was retarded. It has been established that grain boundaries can cause severe electron trapping and thereby substantially degrade the spectroscopic performance of the device [27]. Seeded growth can help reduce the number of grains in the grown boule but it also causes complication during pre-growth heating in that it is difficult to adjust the initial temperature profile of the melt adjacent to the seed such that a desired melt-back solid-liquid interface can be established prior to the commencing of growth.

Historically, the theoretical treatment of the liquid phases has always been more difficult than that for solid and gas phases. A liquid has no lattice structure, and a molecule can migrate through it relatively rapidly. On the other hand, it is also interacting with many other molecules so that the simplifications of the kinetic theory of gases are not available either. Even so, after

decades of investigation the behavior of a “simple” liquid is reasonably well understood, except in the neighborhoods of the triple and the critical points [28]. For more complicated liquids, such as the liquids of high ionicity and those containing hydrogen bonds and electric dipoles, the understanding is far from complete. Therefore, an in-depth study on the thermophysical properties and their time-dependent structural dynamic processes taking place in the vicinity of the solid-liquid phase transition of the narrow homogeneity range HgTe-based semiconductors as well as the structural analysis of the homogenization process in the melt is needed to understand and to improve the crystal growth processes. The main objectives of this reseach are: (1) to perform accurate measurements of various thermal and physical properties as functions of temperature and composition of the HgTe-based melts (2) to extend our understanding of the physics and chemistry of these melts in order to interpret and improve the experimental results of crystal growth and (3) to enhance the fundamental knowledge of hetero-phase fluctuations phenomena in the melts so as to improve the melt growth processes of other similar semiconductor systems.

After this chapter of Introduction, Chapter 2 will present a thorough literatual review on the topics of phase transition, hetero-phase fluctuation and transformation as well as the relaxation phenomena on thermophysical properties of the melts with congruently melted compound semiconducting solids. Chapter 3 will present a thermodynmic analysis where experimental data of phase diagram and thermodynic properties of Hg-Cd-Te and Hg-Zn-Te systems were fit by assuming the liquid phase by an associated solution model and the interaction parameters of the models were determined from the best-fit scenario. Then, the thermodynamic properties of the melt in the systems, such as heat of mixing, heat capacity and composition fluctuation factor, can be generated as functions of temperature and composition. The detailed setup of the measurements and discussions of the results on variou thermophysical properties will be given in Chapters 4 – 6. First, the density as functions of temperature for the melts of Te, HgTe, $Hg_{0.9}Cd_{0.1}Te$, $Hg_{0.8}Cd_{0.2}Te$, $Hg_{0.9}Zn_{0.1}Te$ and $Hg_{0.84}Zn_{0.16}Te$ measured by the pycnometry will be given in Chapter 4. Chapter 5 will present the measurements and results of viscosity and electrical conductivity as functions of temperature as well as their relaxation phenomena by an oscillating-cup viscometer as well as by a transient torque viscometer on the melts of Te, HgTe, $Hg_{0.9}Cd_{0.1}Te$, $Hg_{0.8}Cd_{0.2}Te$ and $Hg_{0.84}Zn_{0.16}Te$ melt. In Chapter 6, thermal conductity were determined on $Hg_{1-x}Cd_xTe$ solids and melts (x = 0, 0.05, 0.10, 0.20 and 0.3), $Hg_{1-x}Zn_xTe$ solids and melts (x = 0.10, 0.16, and 0.30) from three thermophysical properties: (1) thermal diffusivity measured by laser flash method (2) density determined in Chapter 4 and (3) heat capacity derived from the best-fit parameters in the associated solution model given in Chapter 3. Chapter 7 will summarized the physics and chemistry of the $Hg_{1-x}Cd_xTe$ and $Hg_{1-x}Zn_xTe$ systems and the metal-semiconductor transition in the melts with discussions on the implications of the experimental Lorenz number and the effects of supercooling during crystal growth from the melt.

Lastly, it would be helpful to clarify the difference between the usages of *melt* and *liquid*, at least in the language of this book. For physists and material scientists in general, *melt* is usually used to described the liquid phase within a small temperature range just above its melting point whereas *liquid* can cover whole range of the liquid phase up to its triple and the critical points. In this book, the studies on the HgTe-based melts will mostly cover the temperature range

from the melting point, or the liquidus, to about 200°C above except for the low melting Te melt where the range would be 650°C above its melting temperature of 450°C.

References

[1] G. L. Hansen, J. L. Schmidt, and T. N. Casselman, J. Appl. Phys. 53 (1982) 7099.
[2] B. Toulouse, R. Granger, S. Rolland and R. Triboulet, J. Physique 48 (1987) 247.
[3] V. M. Glazov, S. N. Chizhevskaya, and N. N. Glagoleva, *Liquid Semiconductors* (Plenum, New York, 1969).
[4] A. R. Regel, I. A. Smirnov, and E. V. Shadrichev, Phys. Status Solidi 5 (1971) 13.
[5] B. J. Keene, Surf. Interface Anal. 10 (1987) 367.
[6] S. Nakamura and T. Hibiya, Int. J. Thermophys. 13 (1992) 1061.
[7] L. R. Holland and R. E. Taylor, J. Vac. Sci. Technol. A1 (1983) 1615.
[8] D. Chandra and L. R. Holland, J. Vac. Sci. Technol. A1 (1983) 1620.
[9] H. Maleki and L R. Holland, J. Appl. Phys. 76 (1994) 4022.
[10] P. Rudolph and M. Muhlberg, Mater. Sci. Eng. B16 (1993) 8.
[11] P. Rudolph, Prog. Crystal Growth Charact. 29 (1995) 275.
[12] P. Rudolph, N. Schafer and T. Fukuda, Mater. Sci. Eng. R15 (1995) 85.
[13] M. Muhlberg, P. Rudolph, M. Laasch, and E. Treser, J. Crystal Growth 128 (1993) 571.
[14] B. W. Choi and H. N. G. Wadley, J. Crystal Growth 208 (2000) 219.
[15] I. Kikuma and M. Furukoshi, J. Crystal Growth 44 (1978) 467.
[16] I. Kikuma and M. Furukoshi, J. Crystal Growth 71 (1985)136.
[17] Y.-C. Lu, J.-J. Shiau, R. S. Feigelson an R. K. Route, J. Crystal Growth 102 (1990) 807.
[18] M. P. Kulakow, V. D. Kulakovskii and A. V. Fadeev, Inorg. Mater. 12 (1976) 1867.
[19] L. Shcherbak, P. Feichoul and O. Panchouk, J. Crystal Growth 161 (1996) 16.
[20] L. Shcherbak, J. Crystal Growth 197 (1999) 397.
[21] J.-P Gaspard, J.-Y. Raty, R. Ceolin and R. Bellissent, J. Non-Cryst. Solids 205-207 (1996) 75.
[22] K. Mazuruk, Ching-Hua Su, Yi-Gao Sha and S. L. Lehoczky, J. Appl. Phys. 79 (1996) 9080.
[23] Ching-Hua Su, Yi-Gao Sha, K. Mazuruk and S. L. Lehoczky, J. Appl. Phys. 80 (1996) 137.
[24] C. Li, Ph.D. dissertation "*Thermophysical properties of Te, HgTe and $Hg_{1-X}Cd_XTe$ melts*" University of Alabama at Birmingham, United States (2003).
[25] C. Li, Ching-Hua Su, R.N. Scripa, B. Lin, H. Ban, and S. L. Lehoczky, "Observed Relaxation Phenomena in the Viscosity of Liquid Tellurium", presented at the Fourteenth American Conference on Crystal Growth and Epitaxy (ACCGE-14), Seattle, Washington August 5-9, 2002.
[26] R. F. Brebrick, Ching-Hua Su, and Pok-Kai Liao, in *Semiconductors and Semimetals,* Vol. 19, Chap. 3, edited by R. K. Willardson and A. C. Beer, Academic, New York (1983).
[27] P. N. Luke, Mark Amman and J. S. Lee, IEEE Trans. Nucl. Sci. 51 (2003) 3295.
[28] H. N. V. Temperley, edited by J. S. Rowlinson and G. S. Rushbrooke, *Physics of Simple Liquids,* Wiley, New York (1968).

Chapter 2
Review on Hetero-phase Structural Fluctuation in Semiconductor Melts

Abstract: Phase transitions in various systems are often accompanied by pre-transitional or precursor phenomena, when drastic changes of system properties occur, sometimes displaying different anomalies in the behavior of observable quantities. The origin of these phenomena is the formation of molecular complexes, or nuclei, of competing thermodynamic phases inside a host phase. These nuclei are called the hetero-phase fluctuations. As opposed to homo-phase fluctuations which are equilibrium ones and can be described by equilibrium thermodynamics or statistical mechanics, systems with hetero-phase fluctuations are in quasi-equilibrium, or local equilibrium. Those phase transitions in which one or more first derivatives of the relevant thermodynamic potentials exhibit discontinuities as a function of their variables may be called first-order, or discontinuous, transitions. Transitions in which the first derivatives of the thermodynamic potentials remain continuous while only higher-order derivatives are divergent or change discontinuously at the transition points, may be termed continuous transitions. In a normal scientific sense, a transition should exist over a region, not at one point and the hetero-phase fluctuation around a phase-transition point can be considered as a phenomenon that smears a transition into a region. A great number of experiments describing the hetero-phase states during the nucleation process from a metastable phase has been reported in various phase transitions which included crystal-liquid, liquid-vapor, glass-liquid, martensitic, superconducting, ferroelectric and magnetic transitions. There were also experimental studies of the semiconductor-metal transition as a kind of structural phase transition on Se-Te solutions, liquid Ga_2Te_3, In_2Te_3 and Al_2Te_3 as well as on the $Hg_{1-x}Cd_xTe$ melts by the measurements on isothermal compressibility, volume expansion coefficient, Knight shift, magnetic susceptibility, electrical conductivity, Hall coefficient and mobility, thermoelectric power, relaxation rate and structure factor. The results have confirmed the inhomogeneous hetero-phase description that the liquids consist of two well-defined domains, which have the same overall composition but different structures and transport properties. Investigations of the thermophysical properties on various semiconducting compound melts, such as the electrical conductivity, magnetic susceptibility, viscosity, density, etc., have been conducted to understand and to develop the fundamentals of the growth processes. Some interesting experimental results have been observed for those systems with narrow homogeneity ranges solid phase such as the Zn-Te, Cd-Te, Mg-Bi, Tl-Te, In-Te and Ga-Te systems. In other cases of unseeded melt growth of II-VI compounds, namely, CdTe, CdZnTe and ZnSe, there were a large number of experimental facts showing the correlation between melt state and crystal quality. It is believed that the crystalline quality can be improved if the melt was markedly superheated or long-time soaking before growth. It was suggested that the structure of the molten state is determined by the thermal history of how the solid sample was solidified. These results suggest that the liquid state and structure of these narrow homogeneity range II-VI semiconductors need an in-depth examination to enhance the fundamental knowledge of heterophase fluctuations phenomena in the melts so as to improve the melt growth processes of these semiconductors.

Keywords: Phase transition; Hetero-phase fluctuation; Homo-phase fluctuation; Relaxation; Quasi-equilibrium

2.1 Introduction

During the viscosity measurements of HgZnTe pseudo-binary melt using an oscillating-cup viscometer [1] at NASA/Marshall Space Flight Center, an unexpected time drift of the measured viscosity, which shows a slow relaxation phenomenon at temperatures near the liquidus point, was reproducibly observed. The phenomenon of relaxation is defined as the lagging or delayed change of certain properties in response to a temperature change. Figure 2.1 displays two sets of data obtained by cooling the $Hg_{0.84}Zn_{0.16}Te$ melt from 850°C and stabilizing at temperatures of 810°C as well as 790°C, which is just above the liquidus temperature. While it took one day for the measured data to reach equilibration at 810°C, five days were required at 790°C. A similar relaxation phenomenon was also observed in the measured density of the same liquid [2]. Furthermore, in the density measurements of the HgCdTe melts, a negative thermal expansion was reported [3]. The liquid density increases from the liquidus point to a maximum value at a temperature approximately 70°C above the liquidus, where normal thermal expansion progressively resumes.

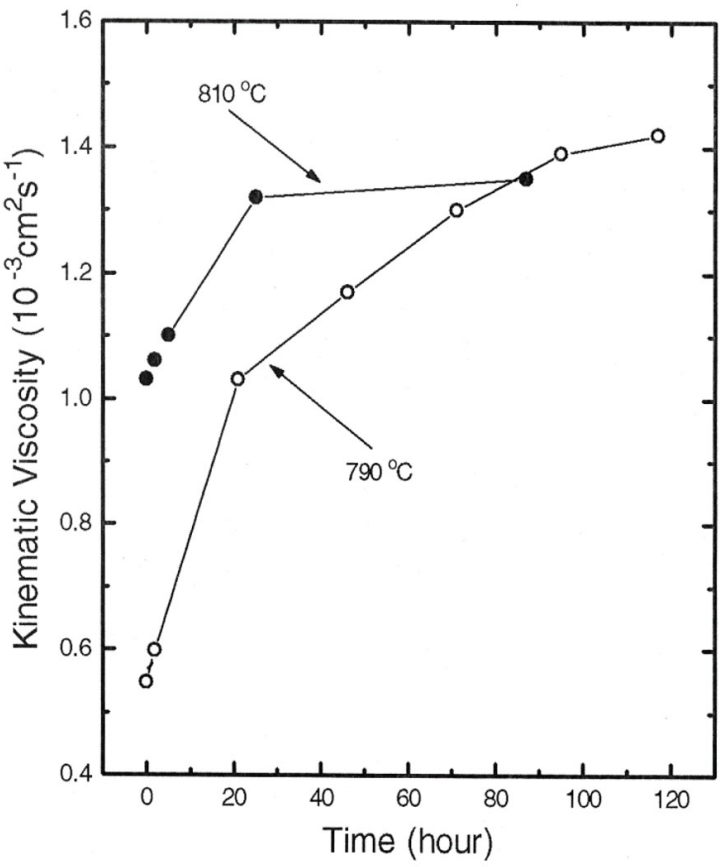

Figure 2.1 Time variation of the measured viscosity after cooling from 850°C to the prescribed temperatures of 810 and 790°C (taken from Figure 4 of Ref.[1]).

Possible mechanisms for the observed relaxation phenomena during temperature cycling in the HgZnTe melts and for the anomalous thermal expansion observed in the HgCdTe melts could be attributed to either macroscopic or microscopic inhomogeneities. Macroscopic inhomogeneities can be present, for instance, due to insufficient mixing during sample preparation. In fact, any local departure from stoichiometry will significantly change the thermophysical properties of the melts. An inhomogeneity can also arise from the evaporation/condensation of mercury into/from a free volume in the ampoule. This could create a thin mercury boundary layer around the sample, thus modifying the wetting condition of the melt to the ampoule wall and changing the surface tension of the top free surface of the melt. It is, however, unlikely that the different effect would be present only in the small temperature range of 790 to 810^{o}C and not being observed at higher temperatures. Finally, bubble formation in the melt may cause significant effects. Although direct visual observation of the melt during the density measurement [2] did not show any visible ones, the existence of small bubbles was still possible.

The nature of the relaxation effect more likely can be attributed to microscopic inhomogeneities. Density and composition fluctuations in the melts near the liquidus point can be significantly different from those at higher temperature. For instance, hetero-phase fluctuations in the form of subcritical clusters of the second phase can be present [4]. For the ionic binary and ternary systems, as compared to single-element melts, hetero-fluctuations would be more likely to occur. Any changes in the temperature will induce a redistribution in the cluster size and composition. This is a diffusion-controlled process of heat and mass transfer, which may be similar to the Ostwald ripening phenomenon and can be rather slow. From a much broader point of view, the theory of hetero-phase fluctuations is applicable to any many-body systems including condensed-matter physics, field theory, physics of nuclear-matter, cosmology, biology and even sociology.

2.2 Review of relevant research

2.2.1 Theoretical Investigations

2.2.1.1 Hetero-phase structural fluctuations. Phase transitions in various systems are often accompanied by the so-called pre-transitional, or precursor phenomena, when drastic changes of system properties occur, sometimes displaying different anomalies in the behavior of observable quantities [4]. The origin of these phenomena is the formation of molecular complexes, or nuclei, of competing thermodynamic phases inside a host phase. Frenkel [4] called this phenomenon “the hetero-phase fluctuations”. Systems with hetero-phase fluctuations are in quasi-equilibrium. The nature of hetero-phase fluctuations is different from that of homo-phase fluctuations existing in equilibrium systems. Phonons in crystals, magnons in magnets or polaritons in ferroelectrics are just a few examples of common, homo-phase fluctuations. These fluctuations, or elementary excitations, exist in the frame of the same thermodynamic phase, never surpassing the limits of the corresponding aggregate state. Each elementary excitation is expressible by a sole wave function; consequently, it corresponds to a quantum-mechanical, or fundamental/microscopic state. Homo-phase fluctuations are equilibrium ones and can be described by methods of equilibrium thermodynamics or statistical mechanics. On the other hand, a hetero-phase

fluctuation represents a thermodynamic, microscopic state including an infinite set of wave functions. A system with hetero-phase fluctuations is in quasi-equilibrium, or local equilibrium.

There are three possible mechanisms responsible for hetero-phase fluctuations: intrinsic, extrinsic and intermediate. The typical case for intrinsic mechanisms is caused by energy fluctuations inside a system where thermal fluctuations increase, leading to a coherent state macroscopically different from that of the host system. This is essentially a process of hetero-phase nucleation which is a type of local-equilibrium self-organization and can be described by local-equilibrium thermodynamics [5]. The extrinsic mechanism interprets the appearance of hetero-phase fluctuations as the fact that all systems are actually nonequilibrium because of their unavoidable interaction with their surroundings [6]. The intermediate mechanism assumes that it is sufficient for a system to have been subjected to the action of external forces at least once for the onset of hetero-phase fluctuations which, being the characteristics for the system, can exist forever without any additional action of external sources. Quite often only an initial nonequilibrium is sufficient to lead to the appearance of oscillatory solutions with a long lifetime [5].

After a hetero-phase fluctuation is formed, there are two possible ways in which a hetero-phase fluctuation can decay, fast and slow. The former is specific for those hetero-phase fluctuations that have coherent structures such as those occurring in nonequilibrium radiating systems in which a self-organization of coherent structures can rise [7]. The nonequilibrium state of such a system can decay through the usual spontaneous emission. The more common mechanism for hetero-phase fluctuations to decay is the slow way, and it usually involves the diffusion processes of heat and mass transfer.

2.2.1.2 Phase transition. Fisher [8] suggested that there could be two kinds of phase transitions, i.e., discontinuous, or first-order, and continuous. Those transitions in which one or more first derivatives of the relevant thermodynamic potentials exhibit discontinuities as a function of their variables may be called first-order, or discontinuous, transitions. Transitions in which the first derivatives of the thermodynamic potentials remain continuous while only higher-order derivatives are divergent or change discontinuously at the transition points, may be termed continuous transitions. However, Frenkel [9] stated that there is no such drastic difference between first-order and second-order transitions. The second-order phase transitions can be considered as first-order ones occurring not at a point but in a finite interval and vice versa, i.e., first-order transitions can be treated as second-order ones for which the transition interval becomes increasingly narrow. In a general scientific sense, a transition should exist over a region, not at one point. The hetero-phase fluctuation around a phase-transition point can be considered as a phenomenon that smears a transition into a region. Theoretically, the statistical theory on hetero-phase fluctuations has been developed and applied to various phase transitions, e.g., melting and crystallization [10-13], magnetic transitions [14-16], and ferroelectric transitions [17-18]. In the statistical analyses of melting and crystallization [10-13], the order parameter for the local density of particles, $n(\mathbf{r})$, was set differently for the crystalline and the liquid phases. The liquid phase should have a uniform local density along the radial distance $\mathbf{r}$, i.e., $n_2(\mathbf{r}) = n_2(\mathbf{0})$, whereas the periodicity of the particle density with respect to the crystalline lattice vector, $\mathbf{a}$, should be imposed on the local particle density of the crystalline phase, i.e., $n_1(\mathbf{r}) = n_1(\mathbf{r} + \mathbf{a})$. The calculated probability, w, of a crystalline and a liquid phase are plotted

schematically in Figure 2.2(a) and (b), respectively, as a function of the dimensionless temperature $\theta = T/\varepsilon$, where ε is the energy constant of the assumed Lennard-Jones potential between the particles. As shown in Figure 2.2(a), at temperature zero the solid is an ideal crystal, w_1 (0) = 1. When the temperature increases, w_1 changes along the line AB slowly decreasing from unity and then, w_1 jumps from B to E at the melting point θ_M, after which it follows the curve EF. The curve BC describes a metastable overheated crystal. On the other hand, as temperature decreases, w_1 changes along the line FE then jumps from E to B when crystallization occurs and w_1 continues to increase along the curve BA. The curve ED corresponds to solid-like clusters in a metastable supercooled liquid. The temperatures, θ_1 and θ_2, are spinodal points representing the boundaries of absolute stability of a supercooled liquid and an overheated crystal, respectively. Figure 2.2(b) plots the calculated probability of liquid phase, w_2, derived from $w_1 + w_2 = 1$. It can be seen that, at temperatures just above zero, the probability of a crystalline phase has deviated, maybe very slightly, from 1. At the same time, the probability of a liquid phase, even at very high temperature, is slightly less than 1.

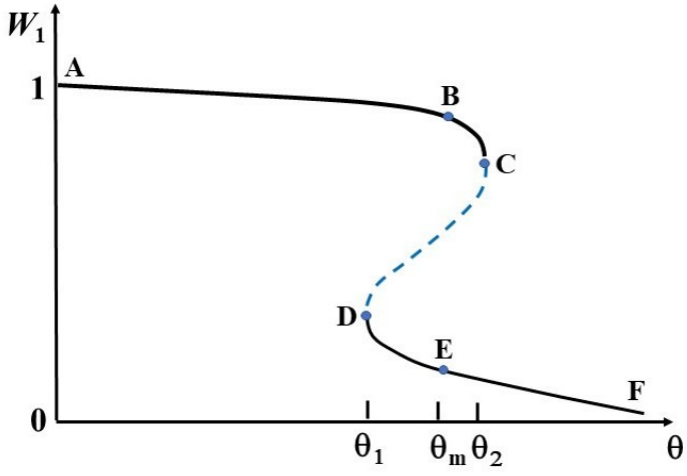

(a)

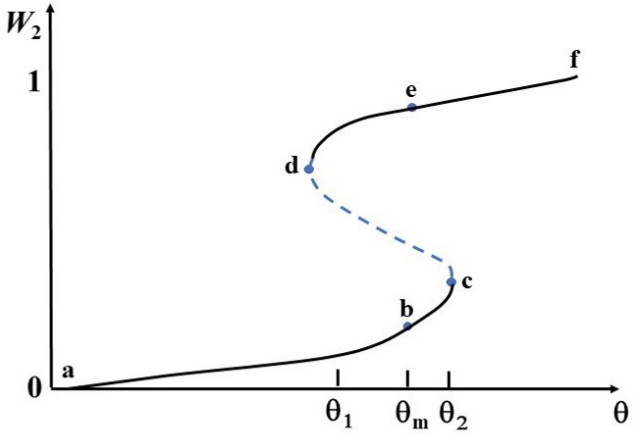

(b)

Figure 2.2 The calculated probability, w, for (a) a crystalline phase and (b) a liquid phase vs. dimensionless temperature, θ.

Historically, the theoretical treatment of the liquid phases has always been more difficult than that for solid and gas phases. A liquid has no lattice structure, and a molecule can migrate through it relatively rapidly. On the other hand, it is always interacting with a great many other molecules so that the simplifications of the kinetic theory of gases are not available either. Even so, after decades of investigation the behavior of a "simple" liquid is reasonably well understood, except in the neighborhoods of the triple and the critical points [19]. For more complicated liquids, such as the liquids of high ionicity and those containing hydrogen bonds and electric dipoles, the understanding is far from complete.

2.2.2 Experimental investigations

A great number of experiments describing the hetero-phase states during the nucleation process from a metastable phase has been discussed [20-24]. The hetero-phase fluctuations were observed experimentally in various phase transitions which included crystal-liquid, liquid-vapor, glass-liquid, martensitic, superconducting, ferroelectric and magnetic transitions. In the field of crystal-liquid transition, Brody [25] was presumably the first to perform some phenomenological calculations for the specific heat of solids close to melting and showed that there existed an additional specific heat due to the fluctuations of the liquid phase. With this additional specific heat, he managed to explain experimentally observed anomalies near the melting points of various substances. Using the same approach, Bartenev [26-29] presented an explanation of temperature anomalies in specific heat, thermal expansion and shear moduli for a number of materials. Ubbelohde [30] analyzed a huge number of experiments discussing the role of hetero-phase fluctuations in pre-melting and pre-crystallization phenomena. The experiments showed that in many crystals below the melting point, a small degree of dissociation was observed when defects grouped together in domains, thus forming liquid-like droplets. In liquids above the melting point, quasi-crystalline clusters were also observed. A number of experiments displaying an abnormal behavior during freezing and melting were analyzed by Bilgram [31], who interpreted the anomalies of thermal properties in terms of intermediate states around the melting point. The width of the intermediate region, or the hetero-phase states, varies from several percent up to 40 % of the absolute melting temperature [30,32] for different materials. Molecular dynamics as well as Monte Carlo methods have been used for treating the solid-liquid phase transition. These computer simulation methods [33-36] have explicitly shown the coexistence of two kinds of configurations in a wide temperature range with the solid phase containing fluctuated disordered droplets in the solid phase and crystalline clusters in the liquid phase. The scattering experiments [37] showed that liquids above the crystallization temperature contain quasi-crystalline clusters. The number of molecules in each cluster is about 100 to 1000 [38]. The existence of these clusters including 10 to 1000 molecules was also confirmed by further X-ray analysis [39]. The experimental results on structural phase transitions in simple liquids, liquid mixtures and liquid crystals have been reviewed by Anisimov [40]. He showed that a quasi-crystalline structure in many liquids exists in a temperature interval above the melting temperature. The quasi-crystalline clusters contain about 1000 molecules each. When the temperature is at the edge of the hetero-phase region where structural clusters and liquid-like parts begin to coexist, there is a jump in the specific heat. The specific-heat measurements, X-ray and neutron diffraction data, as well as molecular dynamics computer simulations are entirely consistent with the existence of an inherent structure of liquids close to the crystallization point [41-42].

Among all fluids, simple liquids such as water have attracted high interest [40,43-50]. Examining the known experimental findings on the properties of water, including data on light and neutron scattering, density behavior, thermal expansion, isothermal compressibility, sound and ultrasound velocities, shear viscosity and specific heat, it is possible to formulate the followings [51-53]. Water may be regarded as a hetero-phase mixture of two or more different structures; each has a well-defined bonding pattern and exists as clusters of similarly bonded molecules. The clusters are not permanent entities but are continuously formed and dissociated under the influence of thermal fluctuations. The hetero-phase clusters have size ranges from 10 to 100 molecules and configurations on time scales in the range of 10^{-10} to 10^{-12} sec. Using the hetero-phase picture, almost all the anomalies in water, such as the density maximum at 4°C, were naturally explained [51-53]. The molecular dynamics calculation confirmed the existence of large local energy fluctuations in water, yielding the formation of inherent structures with clusters involving a collection of 10 to 1000 molecules with lifetime of 10^{-11} to 10^{-12} sec [54-55].

A limited number of investigations have been performed on more complicated systems. In the metallic and semiconducting liquids containing free electrons, structural transformation can result in a semiconductor-metal transition. This double phase transition often proceeds in a gradual manner with the existence of hetero-phase states in a large region of temperatures and densities. Cohen and Jorter [56-59] explored such continuous semiconductor-metal transitions in liquid Te, liquid Hg, liquid binary mixtures of In_2Te_3, Ga_2Te_3, Te_2Tl, Mg_xBi_{1-x}, Te_xSe_{1-x} and metal-ammonia solutions of Li-NH_3 and Na-NH_3. They analyzed the measured electrical conductivity, paramagnetic susceptibility, chemical potential and the Knight shift as well as the small-angle X-ray and neutron scattering data. The overall analysis reached the following physical interpretation: there exists a wide region of an inhomogeneous state between the semiconductor and metal phases with strong local density fluctuations yielding the formation of clusters with different densities and conductivities. The temperature range of the hetero-phase region, in relative units, is about 60%, and the density width about 20%. The clusters are randomly distributed in the melt with radii in the order of 10 to 1000 molecules. The density fluctuations, causing significant local modifications of the electronic structure and transport properties, generate two types of clusters: semiconductor and metal.

An accurate experimental study of the semiconductor-metal transition as a kind of structural phase transition has been done by Tsuchiya et al. [60-63] on Se-Te solutions, liquid Ga_2Te_3, In_2Te_3 and Al_2Te_3 as well as on $Hg_{1-x}Cd_xTe$ melts [64,65]. The isothermal compressibility, volume expansion coefficient, Knight shift, magnetic susceptibility, electrical conductivity, Hall coefficient and mobility, thermoelectric power, relaxation rate and structure factor were measured. The results have confirmed the inhomogeneous hetero-phase description that the liquids consist of two well-defined domains, which have the same overall composition but different structures and transport properties. The proportion of domains having the characters of solid and semiconductor gradually decreases with increasing temperature and pressure while that of liquid-like metallic domains increases. Investigations of the thermophysical properties on various semiconducting compound melts [3, 64-69], such as the electrical conductivity, magnetic susceptibility, viscosity, density, etc., have been conducted to understand and to develop the fundamentals of the growth processes. Some interesting experimental results have been observed for those systems with narrow homogeneity ranges in the solid phase: (1) sharp minima and

maxima were observed for, respectively, the electrical conductivity and viscosity isotherms in the Zn-Te and Cd-Te systems when the composition of the melts approaches that of the solid compounds, i.e. 50% Te [66], (2) sharp maximum for the resistivity and Hall coefficient in the Mg-Bi and Tl-Te systems, respectively, were also observed near the compound compositions of Mg_3Bi_2 and Tl_2Te [70] and (3) the measured specific heat isotherms of In-Te [71] and Ga-Te [72] liquids showed that the specific heats around the compositions In_2Te_3 and Ga_2Te_3 are anomalously high at temperatures just above the respective liquidus temperatures and tend to become small as the temperature increases.

Theoretically, the data on the Mg-Bi and Tl-Te melts were explained quantitatively in terms of the formation of chemical complexes in the liquid phase [70]. From the thermodynamic formulation, the composition structure factors and their long wavelength limit in multicomponent fluid mixtures were derived [73]. The In-Te and Ga-Te data above were satisfactorily explained in terms of the partial dissociation of the compound complex in the liquid phase with increasing temperature [71,72]. A thermodynamic model assuming the existence of associated II-VI species in the liquid phase has also been developed [74], and various thermodynamic properties in the In-Ga-Sb, Hg-Cd-Te [74] and Hg-Cd-Zn-Te [75] systems calculated by the model agree quantitatively with the experimental results. The calculation indicated that the mole fraction of the associated species, HgTe and CdTe, in the melt at the melting point is generally quite high; 0.42 and 0.93, respectively, for the Hg-Te and Cd-Te binary systems [74]. Supercooling in the II-VI melt was observed regularly. In the cooling cycle of the differential thermal analysis (DTA), 20°C of supercooling was observed for HgCdTe melts [76]. The cooling curve for the DTA measurement on CdTe melt showed a supercooling of 50°C [77].

Consequently, the phenomena of hetero-phase fluctuation and its relaxation behavior have many effects on the process of crystal growth from melt. During the unseeded growth of $Hg_{1-x}Zn_xTe$, $x = 0.16$, crystals by directional solidification, the axial compositional profiles of the grown crystals always exhibited a supercooled region at the first-freeze tip [78]. This supercooled length depended on the furnace translation rate, and it could be as much as 4cm in a 10cm long crystal. From the thermal gradient at the growing interface the degree of supercooling for the HgZnTe melts was estimated to be 50° to 70°C. The mole fraction of ZnTe, x, in the supercooled region was typically about 0.5 as compared to the nominal starting composition of 0.16 to 0.22. The transport mechanisms in the melt during the nucleation stage of the liquid-solid phase transition are not well understood. It seems to be unlikely that a 4cm long $Hg_{0.50}Zn_{0.50}Te$ solid can be formed from a 10cm long $Hg_{0.78}Zn_{0.22}Te$ melt during the short spontaneous nucleation process through diffusive or even convective mechanisms unless the hetero-phase fluctuations of a high ZnTe-content solid-like phase were already overwhelming in this highly supercooled liquid.

To promote nucleation under the condition of small supercooling, a method was employed to induce nucleation by mechanical perturbation at a critical time during melt growth [77,79]. The technique was applied to the bulk crystal growth process of $Cd_{1-x}Zn_xTe$ ingots. The comparison between the crystalline quality of the crystals grown with and without the mechanically induced nucleation shows that the yield of single crystalline can been vastly improved with the application of the technique. The effect of this acoustic vibration has been examined theoretically [80] on the possibility that acoustic pressure can affect the rate of

nucleation. By assuming a nucleus having spherical shape, Young-Laplace equation has been adopted to relate the pressure inside the nucleus to the ambient pressure. It was found that the proximate effect of acoustic pressure is to reduce both the size of the critical nucleus as well as the work required to form it from monomers. As the work serves as the activation energy, the ultimate effect of acoustic pressure is to increase the rate of nucleation. It is interesting that, when assuming that the atomic structure of the nucleus is the same as that of an ordinary solid, the compressibility is too small for acoustic vibration effects to be noticeable. However, if it is assumed that the structure is similar to that of a loosely bound colloidal particle, then the effects of acoustic vibration become potentially observable.

In other cases of unseeded melt growth of II-VI compounds, namely, CdTe, CdZnTe and ZnSe, there were a large number of experimental facts showing the correlation between melt state and crystal quality [81-92]. It is believed that the crystalline quality can be improved, i.e., with reduced number of large angle grains and twins, if the melt was markedly superheated (about 20^{o}C higher than the melting point in the case of CdTe) or long-time soaking before growth. The II-VI elements are known to form associated species, such as CdTe and ZnTe, in the liquid phase [74] and the level of the association decreases as temperature increases. It is speculated that after high superheating the associated complex dissociate, and the multiple nucleation is retarded. Similar behavior has been reported on DTA near the melting point of CdTe [93] that some additional endothermic peaks above the melting point were observed. It was suggested that the structure of the molten state is determined by the thermal history of how the solid sample was solidified and the fragments/clusters of the crystal lattice retain in the melt in a certain temperature range.

All these results, theoretical or experimental, suggest that the liquid state and structure of these narrow homogeneity range II-VI semiconductors need an in-depth examination to enhance the fundamental knowledge of hetero-phase fluctuations phenomena in the melts so as to improve the melt growth processes of these semiconductors.

References

[1] K. Mazuruk, Ching-Hua Su, Yi-Gao Sha and S. L. Lehoczky, J. Appl. Phys. 79 (1996) 9080.
[2] Ching-Hua Su, Yi-Gao Sha, K. Mazuruk and S. L. Lehoczky, J. Appl. Phys. 80 (1996) 137.
[3] D. Chandra and L. R. Holland, J. Vac. Sci. Technol A1 (1983) 1620.
[4] J. Frenkel, J. Chem. Phys. 7 (1939) 538.
[5] G. Nicolis and I. Prigogine, *Self-Organization in Nonequilibrium Systems,* Wiley, New York (1977).
[6] J. E. Mayer and M. G. Mayer, *Statistical Mechanics*, Wiley, New York (1977).
[7] *Resonance Fluorescence, Optical Bistability and Superfluorescence*, edited by R. Bonifacio, Springer, Berlin (1982).
[8] M. E. Fisher, Rep. Prog. Phys. 30 (1967) 615.
[9] J. I. Frenkel, *Statistical Physics*, Akademiya Nauk, Moscow (1948).
[10] V. I. Yukalov, Math. Phys. 26 (1976) 274.
[11] V. I. Yukalov, Physica A 89 (1977) 363.
[12] V. I. Yukalov, Phys. Lett. A 81 (1981) 433.

[13] V. I. Yukalov, Phys. Rev. B 32 (1985) 436.
[14] V. I. Yukalov, Physica A 144 (1987) 369.
[15] V. I. Yukalov, Phys. Lett. A 85 (1981) 68.
[16] V. I. Yukalov, Physica A 155 (1989) 519.
[17] V. I. Yukalov, Ferroelectrics 82 (1988) 11.
[18] E. K. Bashkirov and V. I. Yukalov, in: *Problems of Classical and Quantum Physics*, edited b y Y. I. Granovsky, Samara University, Samara (1983) p.99.
[19] H. N. V. Temperley, J. S. Rowlinson and G. S. Rushbrooke eds. *Physics of Simple Liquids*, Wiley, New York (1968).
[20] J. S. Langer, Ann. Phys. 54 (1969) 258.
[21] K. Binder and D. Stauffer, Adv. Phys. 25 (1976) 343.
[22] F. F. Abraham, *Homogeneous Nucleation Theory*,Academic Press, New York 1974).
[23] V. P. Skripov and V. P. Koverda, *Spontaneous Crystallization of Supercooled Liquids*, Nauka, Moscow (1984).
[24] D. Curran, L. Seaman and D. Shockey, Phys. Rep. 147 (1987) 253.
[25] V. E. Brody, Phys. Z. 23 (1922) 197.
[26] G. M. Bartenev, Z. Fiz. Khim. 22 (1948) 587.
[27] G. M. Bartenev, Z. Fiz. Khim. 23 (1949) 1075.
[28] G. M. Bartenev, Z. Fiz. Khim. 24 (1950) 1016.
[29] G. M. Bartenev, Z. Fiz. Khim. 24 (1950) 1437.
[30] A. R. Ubbelohde, *The Molten State of Matter*, Wiley, New York (1978).
[31] J. H. Bilgram, Phys. Rep. 153 (1987) 1.
[32] W. Hayes, Contemp. Phys. 27 (1986) 519.
[33] H. N. Temperley, J. S. Rowlinson and G. S. Rushbrook, eds. *Physics of Simple Liquids*, North Holland, Amsterdam (1968).
[34] J. Barker and D. Henderson, Rev. Mod. Phys. 48 (1976) 587.
[35] F. F. Abraham, Phys. Rep. 80 (1981) 339.
[36] J. M. Ziman, *Models of Disorder*, Cambridge University, Cambridge (1979).
[37] I. Z. Fisher, *Statistical Theory of Liquids*, Fizmatgiz, Moscow (1961).
[38] N. F. Otpushchennikov, Sov. Phys. – Crystallogr. 7 (1962) 237.
[39] N. K. Ailawadi, Phys. Rep. 57 (1980) 241.
[40] M. A. Anisimov, *Critical Phenomena in Liquids and Liquid Crystals*, Nauka, Moscow (1987).
[41] Y. Tsuchiya, J. Phys. C 20 (1987) 1209.
[42] J. Hafner, J. Phys. F 18 (1988) 153.
[43] J. D. Bernal and R. H. Fowler, J. Chem. Phys. 1 (1933) 515.
[44] A. C. Zettlemoyer, ed. *Nucleation*, Dekker, New York (1969).
[45] N. Dass and N. Gilra, J. Phys. Soc. Jpn. 21 (1966) 2039.
[46] N. Gilra, J. Phys. Soc. Jpn. 23 (1967) 1431
[47] N. K. Gilra, Phys. Lett. A 28 (1968) 51.
[48] N. K. Gilra and N. Dass, J. Phys. Soc. Jpn. 24 (1968) 910.
[49] D. H. Rasmussen and A. P. Mackenzie, J. Chem. Phys. 59 (1973) 5003.
[50] G. Maisano, P. Migliardo, F. Aliotta, C. Vasi, F. Wanderlingh and G. D'Arrigo, Phys. Rev. Lett. 52 (1984) 1025.
[51] N. H. Fletcher, *The Chemical Physics of Ice*, Cambridge University Press, Cambridge, (1970).

[52] E. Trinh and R. Apfel, J. Chem. Phys. 69 (1978) 4245.
[53] G. D'Arrigo, Nuovo Cimento 61B (1981) 123.
[54] H. Tanaka and I. Ohmine, J. Chem. Phys. 87 (1987) 6128.
[55] I. Ohmine, H. Tanaka and P. Wolynes, J. Chem. Phys. 89 (1988) 5852.
[56] M. Cohen and J. Jorter, Phys. Rev. Lett. 30 (1973) 699.
[57] M. Cohen and J. Jorter Phys. Rev. A 10 (1974) 978.
[58] M. Cohen and J. Jorter, Phys. Rev. B 13 (1976) 5255.
[59] J. Jorter and M. Cohen, Phys. Rev. B13 (1976) 1548.
[60] Y. Tsuchiya, S. Takeda, S. Tamaki, Y. Waseda and E. Seymour, J. Phys. C 15 (1982) 2561.
[61] Y. Tsuchiya and E. Seymour, J. Phys. C 15 (1982) L687.
[62] Y. Tsuchiya, S. Takeda, S. Tamaki and E. Seymour, J. Phys. C 15 (1982) 6497.
[63] Y. Tsuchiya, J. Phys. C 20 (1987) 1209.
[64] D. Chandra, Phys. Rev. B31 (1985) 7706.
[65] Ching-Hua Su, submitted to J. Appl. Phys.
[66] V. M. Glazov, S. N. Chizhevskaya and N. N. Glagoleva, *Liquid Semiconductors*, Plenum Press, New York (1969).
[67] L. R. Holland and R. E. Taylor, J. Vacuum Sci. Tech. A1 (1983) 1615.
[68] Ching-Hua Su, J. Crystal Growth 78 (1986) 51.
[69] K. Mazuruk, Ching-Hua Su, S. L. Lehoczky and F. Rosenberger, J. Appl. Phys. 77 (1995) 5098.
[70] V. K. Ratti and A. B. Bhatia, J. Phys. F 5 (1975) 893.
[71] S. Takeda, H. Okazaki and S. Tamaki, J. Phys. C 15 (1982) 5203.
[72] S. Takeda, S. Tamaki, A. Takano and H. Okazaki, J. Phys. C 16 (1983) 467.
[73] A. B. Bhatia and V. K. Ratti, Phys. Chem. Liq. 6 (1977) 201.
[74] R. F. Brebrick, Ching-Hua Su, and Pok-Kai Liao, in *Semiconductors and Semimetals,* Vol. 19, Chap. 3, edited by R. K. Willardson and A. C. Beer, Academic, New York (1983).
[75] T.-C. Yu and R. F. Brebrick, J. Phase Equilibria, 13, 476 (1992).
[76] F. R. Szofran and S. L. Lehoczky, J. Electron. Mater. 10 (1981) 1131.
[77] Ching-Hua Su, J. Crystal Growth 410 (2015) 35.
[78] Ching-Hua Su, U. S. Patent # 8,535,440, September 2013.
[79] Ching-Hua Su, S. L. Lehoczky and F. R. Szofran, J. Crystal growth 86 (1988) 87.
[80] James K. Baird and Ching-Hua Su, J. Crystal Growth 487 (2018) 65.
[81] P. Rudolph and M. Muhlberg, Mater. Sci. Eng. B16 (1993) 8.
[82] P. Rudolph, Prog. Crystal Growth Charact. 29 (1995) 275.
[83] P. Rudolph, N. Schafer and T. Fukuda, Mater. Sci. Eng. R15 (1995) 85.
[84] M. Muhlberg, P. Rudolph, M. Laasch, and E. Treser, J. Crystal Growth 128 (1993) 571.
[85] B. W. Choi and H. N. G. Wadley, J. Crystal Growth 208 (2000) 219.
[86] I. Kikuma and M. Furukoshi, J. Crystal Growth 44 (1978) 467.
[87] I. Kikuma and M. Furukoshi, J. Crystal Growth 71 (1985)136.
[88] Y.-C. Lu, J.-J. Shiau, R. S. Feigelson an R. K. Route, J. Crystal Growth 102 (1990) 807.
[89] M. P. Kulakow, V. D. Kulakovskii and A. V. Fadeev, Inorg. Mater. 12 (1976) 1867.
[90] L. Shcherbak, P. Feichoul and O. Panchouk, J. Crystal Growth 161 (1996) 16.
[91] L. Shcherbak, J. Crystal Growth 197 (1999) 397.
[92] J.-P Gaspard, J.-Y. Raty, R. Ceolin and R. Bellissent, J. Non-Cryst. Solids 205-207 (1996) 75.
[93] V. M. Glazov and L. M. Pavlova, S. V. Stankus, J. Chim. Phys. 94 (1997) 1816.

Chapter 3
Phase Diagrams and Associated Solution Model for the Liquid Phase of HgTe-based Ternary Systems

Abstract: In the associated solution treatment of a three-element system such as the Hg-Cd-Te (or Hg-Zn-Te) system, the liquid is assumed to consist of five species: Hg, Cd and Te atomic species and HgTe and CdTe (or ZnTe) molecular species. The various thermodynamic quantities will be derived from the model in terms of the mole fractions of these species. Having chosen the species in the liquid phase, the thermodynamic characterization of the liquid will be completed by assuming an expression for the excess Gibbs energy of mixing, ΔG_M^x, of forming the solution from the liquid elements with interaction parameters between various species. To optimize the values of these parameters and to delineate the phase diagram of the ternary system, such as liquidus temperatures, a thermodynamic description for the solid solution $(A_{1-u}B_u)_{2-y}C_y$ is also required and the experimental information from partial pressure measurements on the solid solution is consistent with a simple quasi-regular solution. The procedure of fitting the phase diagram and thermodynamic properties starts with selecting values from the experimental data on the constant pressure heat capacity for the elements and the binary compounds as well as the vapor pressures of the elements. Then, values for the standard enthalpy and entropy of formation at 298K (25^{o}C), the melting point, and the enthalpy of fusion are chosen for each compound. Before the fitting, certain thermodynamic constraints and auxiliary conditions were imposed to reduce the number of interaction parameters and to provide thermodynamic consistence of the model. With such constraints applied, the remaining liquid model parameters for each binary telluride system are fixed by obtaining the closest fit possible to the liquidus line and the partial pressures along some portion of the three-phase curve of the compound. The remaining parameters of the liquid phase model for each ternary system are fixed by obtaining an optimal fit to the experimental pseudo-binary liquidus and solidus. The calculated values for any remaining data, such as ternary liquidus points or partial pressures along the solid solution three-phase curves, are obtained and a measure of fit calculated. Then, all the thermodynamic properties of the melt in the systems, such as heat of mixing, heat capacity and composition fluctuation factor, can be generated as functions of temperature and composition either for the comparison with other existing data or to extrapolate the knowledge where no experiments have been performed. The liquid model and the procedure described above have also been practiced on the In-Ga-Sb systems with satisfactory results. Using the same approach, the recent analysis on the Hg-Cd-Zn-Te quaternary systems is more exact in a thermodynamic sense than the previous one although both obtained quite similar fits for the Hg-Cd-Te system. The results on the ternary systems of Hg-Cd-Te and Hg-Zn-Te will be presented here.

Keywords: Associated solution model; Quasi-regular solution model; Three phase curve; Mercury-cadmium-tellurium (Hg-Cd-Te) system; Mercury-zinc-tellurium (Hg-Zn-Te) system

3.1 Introduction

As pointed out in Chapter 1, the theoretical treatment of the liquid phases has always been more difficult and complicated than that for solid and gas phases. Many thermodynamic models have been used for the calculations of phase diagram and thermophysical properties. The basic approach starts with defining the excess Gibbs free energy of mixing, ΔG^x_M. For the liquid of two components, A and B (with atomic fraction x of B), the isothermal process of mixing:

(1-x)A (pure elemental liquid) + xB (pure elemental liquid) $\rightarrow$ $A_{1-x}B_x$(liquid solution)

the Gibbs free energy of mixing is commonly adopted the following form:

$$\Delta G_M^x = Wx(1-x)\left[1+a\left(x-\frac{1}{2}\right)\right]-VTx(1-x)\left[1+b\left(x-\frac{1}{2}\right)\right] \qquad (3.1)$$

where W, a, V and b are adjustable interaction parameters independent of temperature T and composition x. The excess Gibbs energy of mixing only include the excess entropy of mixing without the ideal mixing, i.e., $R[(x\ln x + (1-x)\ln(1-x)]$, where R is gas constant. Comparing with the standard form of Gibbs free energy given in Eq.(3.2), the first term in Eq.(3.1) is the enthalpy of mixing, ΔH_M, and the second term is the negative of excess entropy of mixing, ΔS^x_M.

$$\Delta G_M^x = \Delta H_M - T\Delta S_M^x \qquad (3.2)$$

When the four interaction parameters, W, a, V and b in Eq.(3.1) are zero, the liquid is an ideal solution with only entropy of ideal mixing and zero ΔH_M and ΔS^x_M. In the case of $a = b = 0$ [1], the model has been called the quasi-regular model. With all the four interaction parameters in Eq.(3.1) un-zero [2], the model has become the full sub-regular solution model.

For an increasing number of liquids, it has been found that, at a fixed temperature, the composition dependence of one or more properties shows a pronounced change near a composition where a solid is formed at lower temperatures [3]. On the transport property measurements in the melts, Glazov et al. [4] found that, in many binary systems, the measured isothermal electrical conductivity shows a minimum and the viscosity has a maximum at the compositions of the solid compounds, such as AlSb, GaSb and InSb of the III-V group, GaTe, Ga_2Te_3, InTe and In_2Te_3 from the III-VI group, GeTe, SnTe and PbTe of the IV-VI group and CdTe and ZnTe of the II-VI group. Figure 3.1 shows the results of the Cd-Te and Zn-Te systems where the minima and maxima occur at 50% Te composition. The nature of these isotherms indicates a strong chemical interaction between Cd (or Zn) and Te in the liquid state and the retention of the properties of CdTe (or ZnTe) solid compound above the melting point. At the same time, the simple solution models (i.e. ideal solution, quasi-regular solution and sub-regular solution models), the quasi-chemical model [5] and the so-called regular associated solution (RAS) model [6,7] were found to be inadequate for the simple Hg-Te binary system as they gave a liquidus line that is symmetric about 50 atomic % of Te. This has led to the development of associated solution model for the liquid phase.

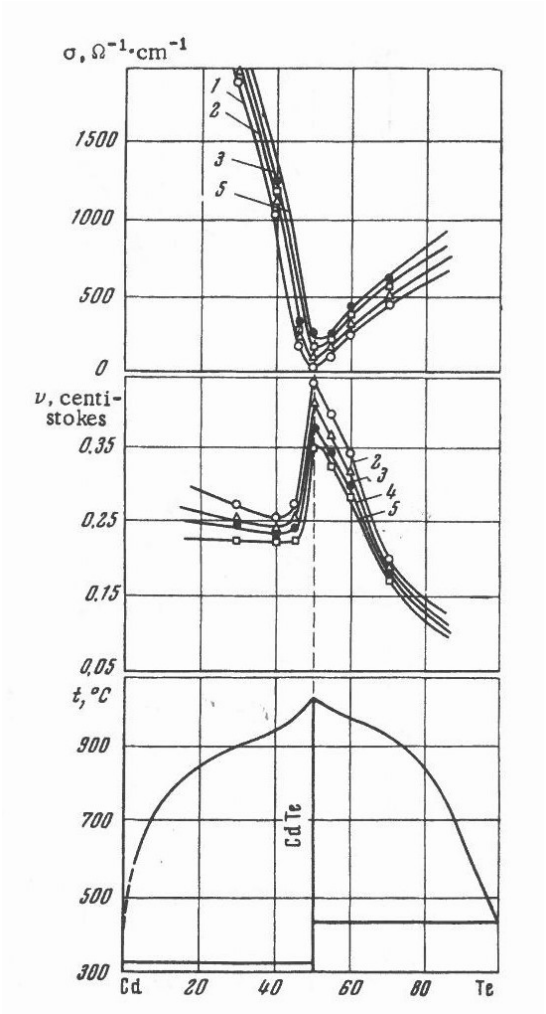

(a)

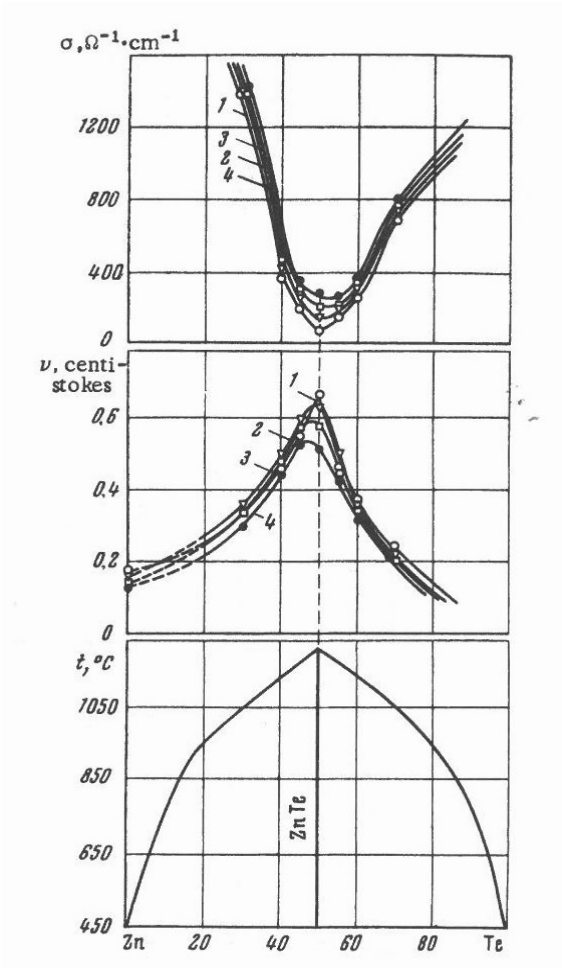

(b)

Figure 3.1Viscosity and electrical conductivity isotherms and phase diagrams. (a) CdTe; curve 1: 1050ºC, 2: 1100ºC, 3:1150ºC, 4: 1200ºC and 5: 1250ºC. (b) ZnTe; 1: 1280ºC, 2: 1300ºC, 3: 1350ºC and 4: 1480ºC (taken from Figures 121 and 122 of Ref.[4]).

The solid crystalline of HgTe has zinc-blende structure with two inter-penetrating face-center-cubic (FCC) sublattices occupied by Hg and Te atoms, respectively. When a fraction, x, of the Hg atoms is substituted by Cd (or Zn), the solid solution of $Hg_{1-x}Cd_xTe$ (or $Hg_{1-x}Zn_xTe$) is formed. The phase diagram of the HgTe-based ternary systems, Hg-Cd-Te and Hg-Zn-Te, shows a prominent feature of a complete range of solid solutions from the binary compounds with narrow homogeneity ranges, i.e., HgTe and CdTe in the first system and HgTe and ZnTe in the second. One important thermodynamic characteristic for the narrow homogeneity range compounds is that the Gibbs free energy of formation for the compound is, within experimental error, independent of the deviation from stoichiometry and is a function of temperature only [8]. In setting up equations during thermodynamic modeling, this stoichiometric invariant has provided a helpful simplification that the line compound of elements A and B can be treated like a component, $A_{0.50}B_{0.50}$, with its chemical potential a function of temperature only. To fully

characterize the system, it is a common practice to divide the analysis into two independent parts. In the first part, a thermodynamic model for the liquid phase and a thermodynamic characterization of the solid phase are needed so that the adjustable interaction parameters can be optimized for a quantitatively good fit to various experimental data of phase diagram and thermodynamic properties. Both the liquid surface and the solid will be delineated with the corresponding tie-lines connecting the compositions of liquid and solid solution in equilibrium at fixed temperatures along with the corresponding thermodynamic properties. The second part of the study requires the defect chemistry analysis as the first part analysis of the liquid phase does not provide any information on the thermodynamic behavior of the solid solution with compositions interior to its stable compositional range. The latter would require specifications for the composition dependence of the chemical potentials of all components in the solid-solution phase and would involve the defect chemistry of the solid solution. Following a statistical thermodynamic derivation and energy band structure analysis, the equilibrium equations for various defect models have been established for several compositions of $Hg_{1-x}Cd_xTe$ [9] and CdTe [10]. With a specific defect model, the interaction parameters for the excess Gibbs energies to create the neutral atomic point defects will be determined from a best fit of the theoretical equilibrium equations to the experimental composition-temperature-partial pressure (X-T-P) data. Using these parameters the analysis will generate the complete X-T-P phase diagram of the solid phase. Since this book will focus on the physics and chemistry of the melts, only the first part of the analysis, i.e., the liquid-solid equilibrium, will be presented here.

3.2 Associated Solution Model for Liquid phase

3.2.1 Solution thermodynamics

The binary system of A-C, such as Hg-Te, Cd-Te and Zn-Te, forms only one intermetallic compound which is a congruently melting solid AC(s) with 1:1 atomic ratio. The ternary systems of Hg-Cd-Te and Hg-Zn-Te can be described, respectively, as binary systems of HgTe-CdTe and HgTe-ZnTe which form solid solution over the entire composition, the so-called pseudo-binary. In the associated solution model for a binary system, such as Hg-Te as an example, the liquid is assumed to consist of species of Hg and Te elements and HgTe molecule. The mole fraction of each species is determined by the atomic fraction of each element, i.e., Hg and Te, and the equilibrium constants for the association/dissociation reactions of:
$Hg(l)+Te(l) \leftrightarrow HgTe(l)$.

In the associated solution treatment of a three-element system such as the Hg-Cd-Te system, the liquid is assumed to consist of five species: Hg, Cd and Te atomic species and HgTe and CdTe molecular species. The various thermodynamic quantities will be derived from the model in terms of the mole fractions of these species. However, the experimental results are given in terms of the atomic fractions of the chemical elements comprising the system, i.e., Hg, Cd and Te. Before assuming any specific forms for the Gibbs energy of mixing for the liquid, general relations between these two sets of quantities need to be obtained to establish the standard conversion to correlate the theoretical and experimental results. Given the Hg-Cd-Te (or Hg-Zn-Te) system by the symbol of A-B-C, the component A, B and C is represented by component 1, 2 and 3, respectively, and the species A, B, C, AC and BC is represented by

species 1, 2, 3, 4 and 5, respectively. If N_i is the number of gram-atoms of component i and n_j is the number of moles of species j, then the conservation of mass for each atom type requires:

$$N_1 = n_1 + n_4 \tag{3.3}$$

$$N_2 = n_2 + n_5 \tag{3.4}$$

$$N_3 = n_3 + n_4 + n_5 \tag{3.5}$$

Defining the atom fractions of components as x_i and the mole fractions of species as y_i, the mole fractions of the uncombined species, $i = 1, 2, 3$, are:

$$y_i = x_i\left(1 + y_4 + y_5\right) + \left[\delta(i,2) - 1\right] y_4 + \left[\delta(i,1) - 1\right] y_5$$
$$\delta(i,j) = \begin{cases} 1 \; if \; i = j \\ 0 \; if \; i \neq j \end{cases} \tag{3.6}$$

By adding Eqs.(3.3) – (3.5), with the same amount of mass of each element, the ratio of the number of gram-atoms of component to the number of moles of species is $1 + y_4 + y_5$. Therefore, the Gibbs energy of mixing, ΔG_M, from the components and from the species can be related:

$$\Delta G_M\left(gram - atom\, component\right) = \left(1 + y_4 + y_5\right)^{-1} \Delta G_M\left(mole\, species\right) \tag{3.7}$$

The next step is to convert the experimental data into the environment of theoretical modeling, i.e., to obtain the mole fractions of each species, y_i, when the atomic fractions of each component, x_i, and the temperature T are given. The association/dissociation reactions between the atomic species and the molecular species are:

$$A(l) + C(l) \leftrightarrow AC(l) \wedge B(l) + C(l) \leftrightarrow BC(l) \tag{3.8}$$

and under equilibrium condition, the relative chemical potentials for the reactions give:

$$\acute{\mu}_4 = \acute{\mu}_1 + \acute{\mu}_3 \wedge \acute{\mu}_5 = \acute{\mu}_2 + \acute{\mu}_3 \tag{3.9}$$

The chemical potential $\acute{\mu}_i$ is relative to the component i, or the uncombined species i. The specific relative chemical potential for species p, $p = 1, \ldots, 5$, can be expressed by the generalized expression for the chemical potential:

$$\acute{\mu}_p = RTln\left(\gamma_p\, y_p\right) - \delta(p,4)\,\Delta G_4^o - \delta(p,5)\,\Delta G_5^o \tag{3.10}$$

where R is the gas constant, T is temperature in K, γ_p is the activity coefficient of species p and ΔG_4^o and ΔG_5^o are the standard Gibbs energy of dissociation for species 4, or AC, and species 5, or BC, respectively. As a term of Gibbs energy, they have the usual form of $\Delta G_D^o = \Delta H_D - T\,\Delta S_D$. The specific form of the liquid model will be given in next section and the activity coefficient

for each species can be calculated from the best-fit interaction parameters together with the best-fit values of ΔH_D and ΔS_D for ΔG_4^o and ΔG_5^o. After substituting Eq.(3.10) into Eq.(3.9) and rearranging them, the equations become:

$$\frac{y_1 y_3}{y_4} = \left(\frac{\gamma_4}{\gamma_1 \gamma_3} \right) \exp \text{¿)} \tag{3.11}$$

$$\frac{y_2 y_3}{y_5} = \left(\frac{\gamma_5}{\gamma_2 \gamma_3} \right) \exp \left(\frac{-\Delta G_5^o}{RT} \right) \tag{3.12}$$

After substituting Eq.(3.6) for y_i, i = 1, 2, 3 into Eqs.(3.11) and (3.12), these equations become two simultaneous equations for y_4 and y_5 which can be solved numerically. Once the values of y_4 and y_5 are known, y_1, y_2 and y_3 and all of the thermodynamic quantities can be calculated.

3.2.2 Associated solution model. Having chosen the species in the liquid phase, the thermodynamic characterization will be completed by assuming an equation for the excess Gibbs energy of mixing, ΔG_M^x, of forming the solution from the liquid elements:

$$\Delta G_M^x = \sum_{j=1}^{5} \sum_{i=1}^{5} (\alpha_{ij} + \beta_{ij} y_j \text{¿¿}) y_i y_j + \sum_{i=1}^{5} \sum_{j>i}^{5} \sum_{k>j}^{5} \gamma_{ijk} y_i y_j y_k - y_4 \Delta G_4^o - y_5 \Delta G_5^o \text{¿¿} \tag{3.13}$$

On the composition-independent interaction parameters, the parameters α_{ij} are set to be equal to α_{ji} because they represent the same interaction between the two species i and j. The interaction parameter between two identical species, α_{jj} is set to be zero as they provide zero contribution to the mixing. Also, the interaction parameters, β_{ij}, between the three species of y_i, y_j and y_j is set to be equal – β_{ji}, the interaction parameter between y_i, y_i and y_j. In the special case that all of the β_{ij} and γ_{ijk} are zero, the species interact as quasi-regular solution. During the analyses of the Hg-Cd-Te and Hg-Zn-Te systems, it was possible to obtain good fits without using the ternary parameters γ_{ijk} and, therefore, they were set to be zero. Once the Gibbs energy of mixing is set, the relative excess chemical potential of species j can be derived from

$$\acute{\mu}_j^x \text{¿} \left(\frac{\partial \Delta G_M^x}{\partial y_j} \right)_{T,P,y_{i \neq j}} \tag{3.14}$$

which is simply related to the relative chemical potential by:

$$\acute{\mu}_j = \acute{\mu}_j^x + RT \ln y_j \tag{3.15}$$

Using Eq.(3.13) for ΔG_M^x with $\gamma_{ijk} = 0$, Eq.(3.14) can be express as:

$$\acute{\mu}_p^x = 2\sum_{i=1}^{5}[\alpha_{ip}¿ + (\frac{y_i}{2} - y_p)\beta_{pi}]y_i - \sum_{i=1}^{5}\sum_{j=1}^{5}(\alpha_{ij}¿¿ + 2\beta_{ij}y_j)y_i y_j ¿¿¿$$

$$-\delta(p,4)\Delta G_4^o - \delta(p,5)\Delta G_5^o \qquad (3.16)$$

After defining the species of the solution, the Gibbs energy of dissociation for the molecular species and the Gibbs energy of mixing from these species, the chemical potential of each species can be derived, and the thermodynamic description of the liquid phase is complete.

3.3 Liquidus equations and optimization of interaction parameters

Although this book is focusing on the melt, or the liquid phase of the HgTe-based ternary systems, the most reliable and available experimental data to optimize the interaction parameters in the liquid were the experimental measurements of liquidus points. To delineate the phase diagram of the ternary system, such as liquidus temperatures, a thermodynamic description for the solid solution $(A_{1-u}B_u)_{2-y}C_y$ is needed. It has been shown theoretically [11] and experimentally for $(Hg_{1-u}Cd_u)_{2-y}Te_y$ [12,13] that, within the small range of homogeneity, the sum of the chemical potentials of A and C and that of B and C in the solid are independent of the small deviation of stoichiometry when y is confined to a value near unity:

$$\mu_A^s + \mu_C^s = \mu_{AC}^s(T,u) \qquad (3.17)$$

$$\mu_B^s + \mu_C^s = \mu_{BC}^s(T,u) \qquad (3.18)$$

Thus AC and BC can be treated as thermodynamic components of the solid solution, with their chemical potentials as functions of T and u only, and formally expressed in terms of activity coefficient Γ_{ij} as:

$$\mu_{AC}^s = RTln[(1-u)\neg\ \mathrm{AC}] + \mu_{AC}^{o,s} \qquad (3.19)$$

$$\mu_{BC}^s = RTln[u\neg\ \mathrm{BC}] + \mu_{BC}^{o,s} \qquad (3.20)$$

For the binary compound AC, u = 0, $\Gamma_{AC} = 1$ and the chemical potential μ_{AC}^s corresponds to that of the binary solid AC(s), $\mu_{AC}^{o,s}$. The same is true for the other end member BC.

When the liquid and solid-solution phases coexist in equilibrium, the chemical potential of each component must be the same in the liquid and solid phases. Therefore, the sum of the chemical potentials of A and C as well as that for B and C must be the same in both phases:

$$\mu_A^l + \mu_C^l = \acute{\mu}_A^l + \acute{\mu}_C^l + \mu_A^{o,l} + \mu_C^{o,l} = \mu_{AC}^s \qquad (3.21)$$

$$\mu_B^l + \mu_C^l = \acute{\mu}_B^l + \acute{\mu}_C^l + \mu_B^{o,l} + \mu_C^{o,l} = \mu_{BC}^s \qquad (3.22)$$

where $\mu_A^{o,l}$, $\mu_B^{o,l}$ and $\mu_C^{o,l}$ are the chemical potentials of the pure liquid element, A, B and C, respectively. As discussed earlier, this is where the analysis is being divided into two independent parts as the addition of the chemical potentials results in two equations in place of the original three equations for each of the elements.

It is recognized from Eq.(3.19) to Eq.(3.22), that the Gibbs energy of formation for the binary compound are the differences in chemical potentials of the compound and the elements forming the compound:

$$\Delta G_f^o[AC(s)] = \mu_{AC}^{o,s} - \mu_A^{o,l} - \mu_C^{o,l} \tag{3.23}$$

$$\Delta G_f^o[BC(s)] = \mu_{BC}^{o,s} - \mu_B^{o,l} - \mu_C^{o,l} \tag{3.24}$$

By substituting Eqs.(3.23), (3.24), (3.19) and (3.20) into Eqs.(3.21) and (3.22), the liquidus equations become:

$$\acute{\mu}_A^l + \acute{\mu}_C^l = RTln[(1-u)^{\neg}\ \mathrm{AC}] + \Delta G_f^o[AC(s)] \tag{3.25}$$

$$\acute{\mu}_B^l + \acute{\mu}_C^l = RTln[u^{\neg}\ \mathrm{BC}] + \Delta G_f^o[BC(s)] \tag{3.26}$$

Comparing with other different but equivalent forms for the liquidus equations [14], Eqs.(3.25) and (3.26) are more precise and convenient.

With the thermodynamic model specified for the liquid phase given in 3.2.2, the characteristics of the solid solution are also needed to solve the liquidus equations (3.25) and (3.26). The experimental information on the Hg-Cd-Te solid solution from partial pressure measurements [12,13,15] is consistent with a simple quasi-regular solution:

$$RTln[^{\neg}\ \mathrm{AC}] = (W_S - V_S T)u^2 \tag{3.27}$$

$$RTln[^{\neg}\ \mathrm{BC}] = (W_S - V_S T)(1-u)^2 \tag{3.28}$$

where W_S and V_S are composition- and temperature-independent interaction parameters.

With the large number of interaction parameters to be optimized, several imposed thermodynamic constraints and auxiliary condition have been applied to reduce the number of variable parameters prior to fitting the experimental data. The experimental values of melting temperatures for AC and BC compounds are treated as special and reliable and, therefore, it was required that the calculated melting points always match the experimental values. There are also auxiliary thermodynamically-consistent conditions that follow immediately from the zero change of Gibbs energy during the congruent melting of AC(s) and BC(s) compounds. With the regular form for $G_f^o(AC(s)) = \Delta H_f^o - T\Delta S_f^o$, the constraints are shown below for AC(s):

$$\Delta H_f^o(AC(s), T_{AC}) + \Delta H_{AC}^m = 2\Delta H_M(x_A = x_c = \frac{1}{2} at\ T_{AC}) \quad (3.29)$$

$$\Delta S_f^o(AC(s), T_{AC}) + \Delta H_{AC}^m / T_{AC} = 2\Delta S_M(x_A = x_c = \frac{1}{2} at\ T_{AC}) \quad (3.30)$$

where ΔH_f^o and ΔS_f^o are the enthalpy and entropy of formation per mole of AC(s) from pure liquid A and C at the melting temperature of AC(s), T_{AC}. The quantity ΔH_{AC}^m is the enthalpy of fusion of AC(s) and ΔH_M and ΔS_M are, respectively, the enthalpy and entropy of mixing per mole of the liquid $A_{0.50}C_{0.50}$ at T_{AC}. In these two equations, the left-hand side can be viewed as two-steps process of (1) forming of AC(s) from the pure elemental liquids and (2) melting of the AC solid at T_{AC} . This two-step process is equivalent to the right-hand side of mixing the pure liquids to form the stoichiometric liquid at T_{AC}. The same conditions can also be imposed on the compound BC during congruent melting. The employment of the constraints of the calculated melting points, T_{AC} and T_{AC}, matching the experimental values together with these auxiliary conditions not only reduces the number of interaction variables but also provides thermodynamic consistency.

Usually, the optimization of parameters started with the collection of all the reliable experimental data for each element, the binary and the ternary systems. These include the melting points, liquidus temperatures, eutectic temperature, heat capacity, enthalpy and entropy of melting and enthalpy and entropy of formation for the compounds, partial pressures of each element as functions of composition and temperature, etc… Then, the values of the interaction parameters for each binary system were varied to obtain a best fit by minimizing the quantitative measure of the fit σ which is defines as:

$$\sigma^2 = ¿ \quad (3.31)$$

where σ_T and σ_i are, respectively, the standard deviation of the fit to the liquidus temperature and partial pressures of species *i*, where *i* = Hg, Cd, Zn, or Te_2. The numbers W_T and W_i are the weighing factors for the fit to liquidus and partial pressure, respectively. The two standard deviations are defined as:

$$\sigma_T^2 = \sum_{j=1}^{M} (T_{j,cal} ¿ - T_{j,obs})^2 / M ¿ \quad (3.32)$$

$$\sigma_i^2 = \sum_{j=1}^{N} \left(\frac{P_{j,cal} - P_{j,obs}}{P_{j,obs}}\right)^2 / N \quad (3.33)$$

where the subscripts *j,cal* and *j,obs* stand for the calculated and the experimentally observed values, respectively. The standard deviation for the thermodynamic properties, such as partial pressures, the percentage difference between calculated and observed values were adopted as shown in Eq.(3.33).

After the establishment of the optimal parameters for the binaries, the interaction parameters of the ternary system were optimized by varying them together with the established parameters of the three binary systems to fit the experimental data of the ternary phase diagram. Once the set of optimal interaction parameters were established for the ternary system, all of the information on phase diagram, such as liquidus lines and surfaces, tie-lines, liquidus isotherms, solid iso-concentration lines, partial pressures of elements as functions of composition and temperature and concentration fluctuation factor, can be generated either for the comparison with other existing data or to extrapolate the knowledge where no experiments have been performed.

3.4 Phase diagram and thermodynamic properties

The procedure of fitting the phase diagram and thermodynamic properties starts with selecting values from the experimental data on the constant pressure heat capacity for the elements and the binary compounds as well as the vapor pressures of the elements. Then, values for the standard enthalpy and entropy of formation at 298K, the melting point, and the enthalpy of fusion are selected for each compound. Before the fitting, the constraints and auxiliary conditions described in last section were imposed to reduce the number of interaction parameters and to provide thermodynamic consistence of the model. With such constraints applied, the current approach was chosen to fix the remaining liquid model parameters for each binary telluride system by obtaining the closest fit possible to the liquidus line and the partial pressures along some portion of the three-phase curve of the compound. The remaining parameters of the liquid phase model for each ternary system are fixed by obtaining an optimum fit to the experimental pseudo-binary liquidus and solidus. Then the calculated values for any remaining data, such as ternary liquidus points or partial pressures along the solid solution three-phase curves, are obtained and a measure of fit calculated. The liquid model and procedure described above have been practiced on the Hg-Cd-Te and In-Ga-Sb systems with satisfactory results [16]. Using the same approach, the recent analysis on the Hg-Cd-Zn-Te quaternary systems [17] is more exact in the thermodynamic sense than the previous one [16] although both fits obtained for the Hg-Cd-Te system are quite similar. The results on the ternary systems of Hg-Cd-Te and Hg-Zn-Te from Ref.[17] will be presented here.

3.4.1 Hg-Cd-Te systems. The results of Hg-Cd-Te system will be presented below starting from the binary systems of Hg-Cd, Hg-Te and Cd-Te to the ternary of Hg-Cd-Te.

3.4.1.1 Hg-Cd binary. Since the highest liquidus temperature in this system is the melting point of Cd at 321^{o}C, no attempt was made to fit the phase diagram. The selected values by Hultgren et al. [18] are well fit by taking the parameter $\alpha_{12} = -5247$J/mole and with other parameters set to be zero.

3.4.1.2 Hg-Te binary. For the two binary systems of Hg-Te and Cd-Te, the interaction parameters were varied to find an optimal fit to the liquidus lines and the partial pressures along their three-phase curves. All of the interaction parameters β_{ij} were needed to obtain satisfactory fits. The calculated phase diagrams of Hg-Te and Cd-Te binary systems are given in Figure 2.2. It shows the liquidus curves of Hg-Te (lower) and Cd-Te (upper) and the two solid compounds as lines with the melting temperature of 670^{o}C and 1092^{o}C, respectively. The calculated values

show as solid curves which compare to the experimental points, shown as symbols, from various reports. The fit to the liquidus, as defined in Eq.(3.32) to the Hg-Te system is 4.2ºC.

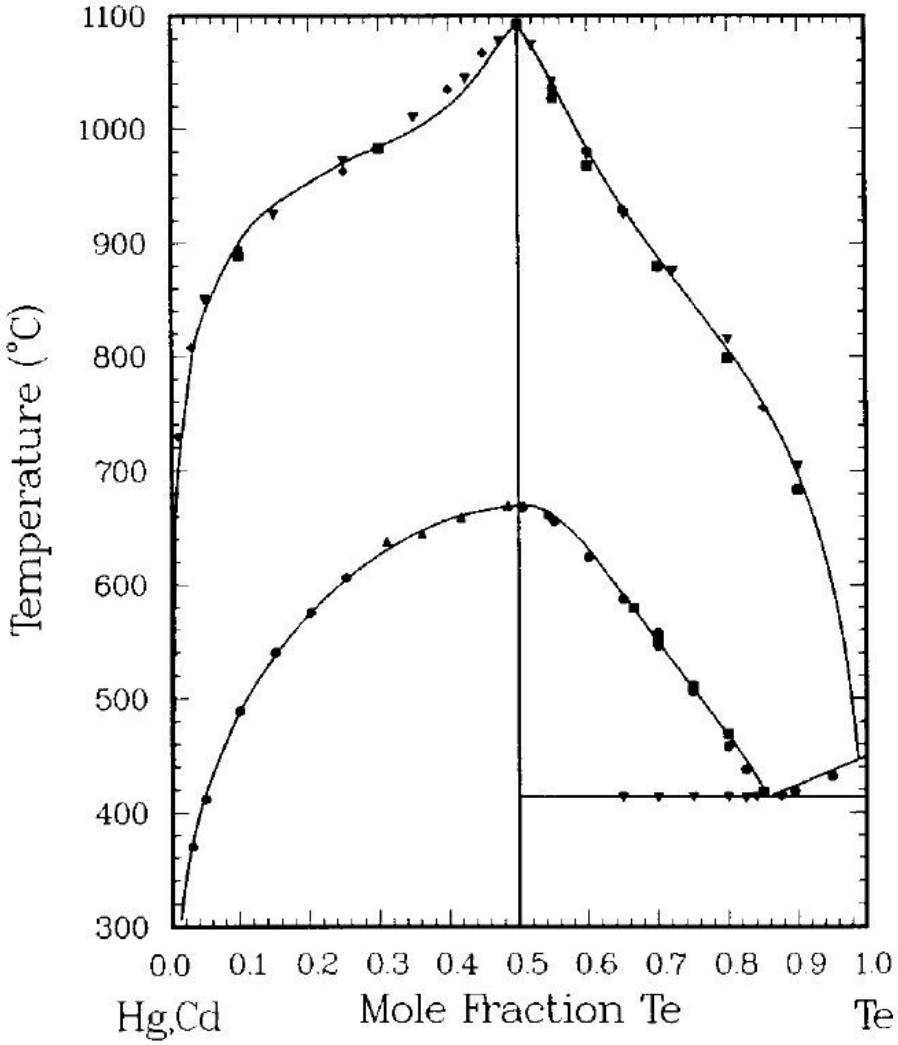

Figure 3.2 Liquidus lines for HgTe (lower) and CdTe (upper). For HgTe, the circles and inverted triangles are from Strauss [19], triangles from Brebrick and Strauss [20] and squares from Harman [21]. For CdTe, diamonds are from Kulwicki [22], circles from Brebrick [23], squares are from Steininger et al. [24] and triangles from Lorenz [25]. In all figures, solid curves are the calculated results (taken from Figure 1of Ref.[17]).

Figure 3.3 and 3.4 shows the calculated partial pressures of Hg, P_{Hg}, and Te_2, P_{Te2}, respectively. The fit along the three-phase curve is 4.9% for P_{Hg} and 6.7% for P_{Te2} whereas the fit to the partial pressure over the melts is 7.3% for P_{Hg} and 6.2% for P_{Te2}.

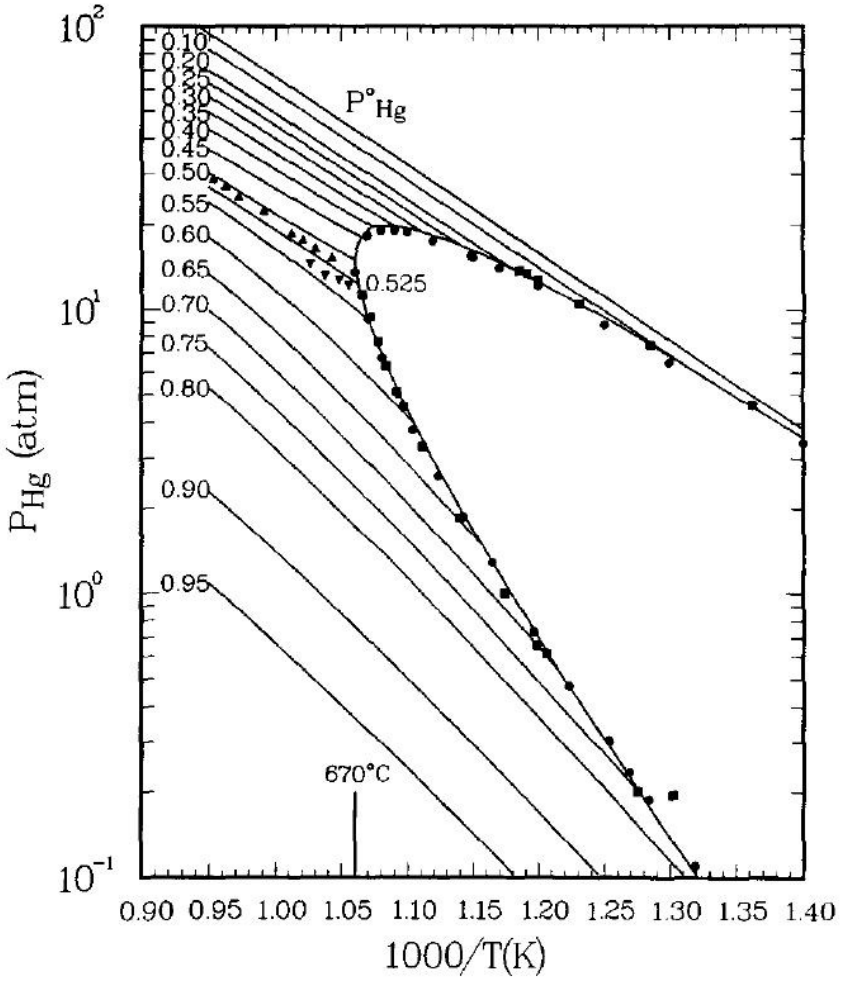

Figure 3.3 Partial pressure of Hg along the three-phase curve for HgTe(s), with a melting temperature of 670°C, and over the liquids of various composition as indicated by short segments. The labeled numbers are for different Te atom fractions in the melts. Triangles and inverted triangles are for liquids with x_{Te}= 0.5, 0.525, respectively. These points along with circles are from Ref.[24,26] and squares are from [27]. Vapor pressure of pure Hg(1) is the line labeled P^o_{Hg} (taken from Figure 2 of Ref.[17]).

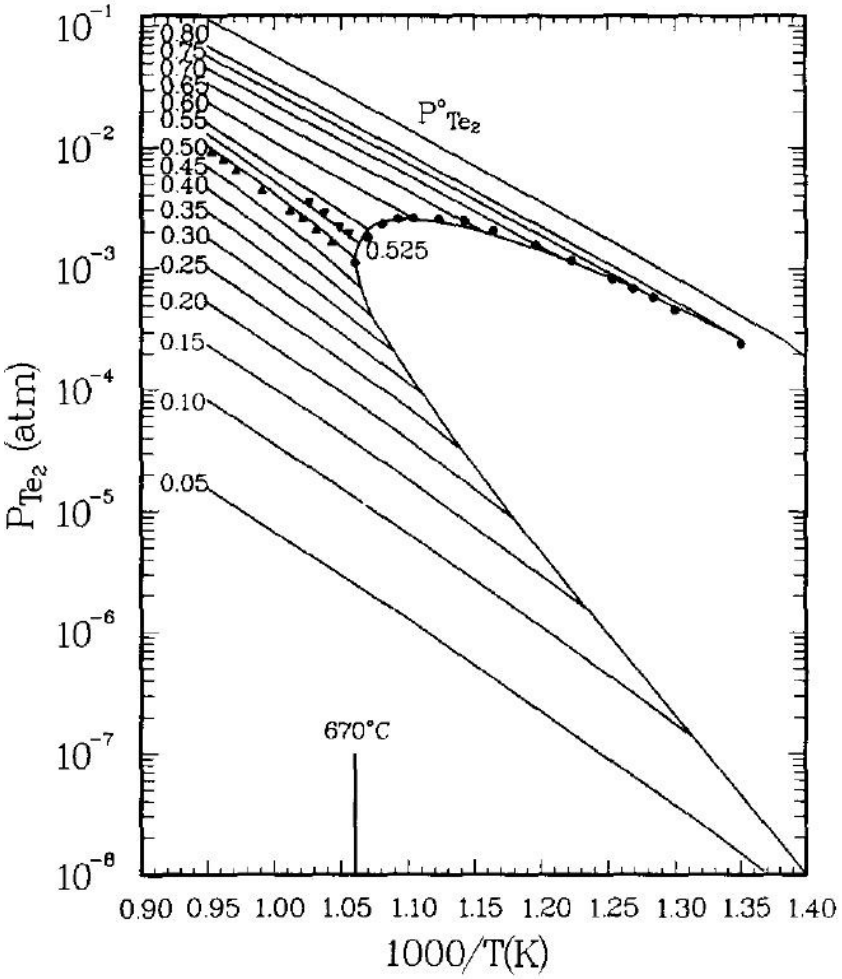

Figure 3.4 Partial pressure of Te_2 along the three-phase curve for HgTe(s) and over the liquids of various composition. Same credit sources and symbols as in Figure 3.3. Vapor pressure of Te(l) is the line labeled P_{Te2} (taken from Figure 3 of Ref.[17]).

3.4.1.3 Cd-Te binary. The selected liquidus points of Cd-Te in Figure 3.2 are fit to 9.3°C and the fits to the partial pressures of Te_2 and Cd along the three-phase loop, and P_{Te2} over the melts are 4.9 and 24.3, and 9.3% respectively. The calculated partial pressures curves and experimental points are given in Figure 3.5 and 3.6. Again, the short segments adjacent to the three-phase loop are the partial pressures of Te_2 and Cd generated from the best fit parameters for various melts with compositions in atomic fraction of Te given alongside the segments. Except for a slightly poorer fit to P_{Cd} along the three-phase curve, the overall fits to the other experimental data are better than in those in Ref.[16].

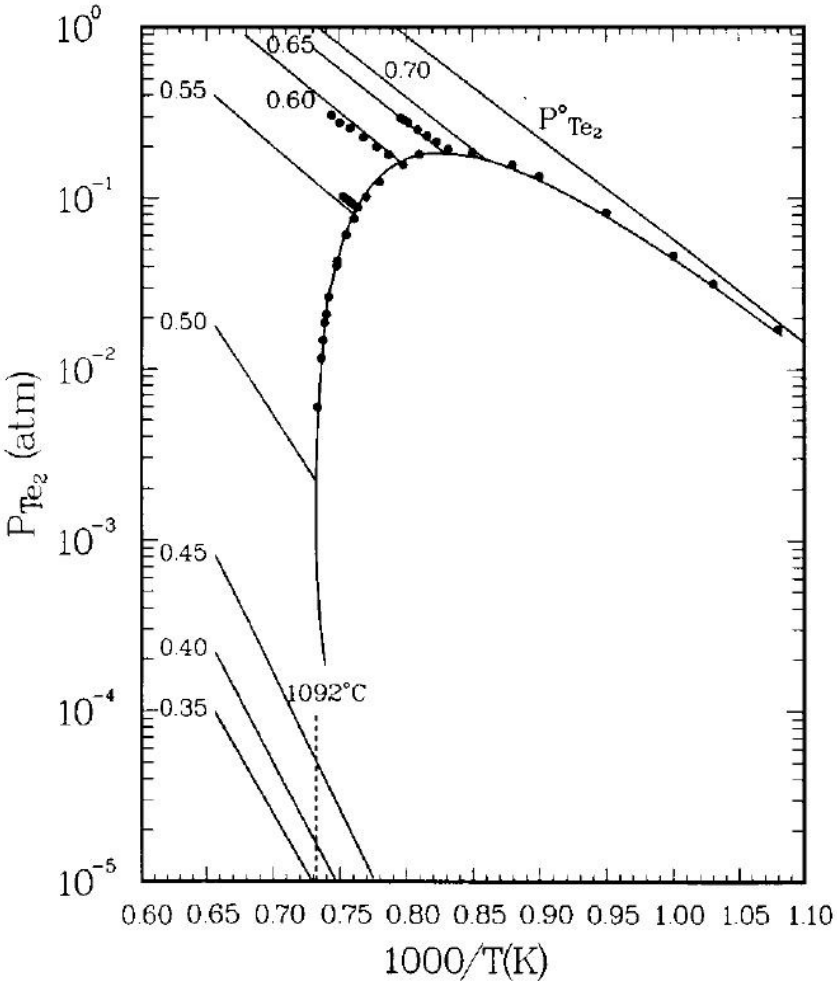

Figure 3.5 Partial pressure of Te_2 along the three-phase loop of CdTe(s), with a melting temperature of 1092°C, and over the various melts. The experimental points are from Brebrick [23]. Uppermost line labeled P°_{Te2} is the vapor pressure of Te(l). Short line segments are for liquids with labeled atomic fraction of Te (taken from Figure 4 of Ref.[17]).

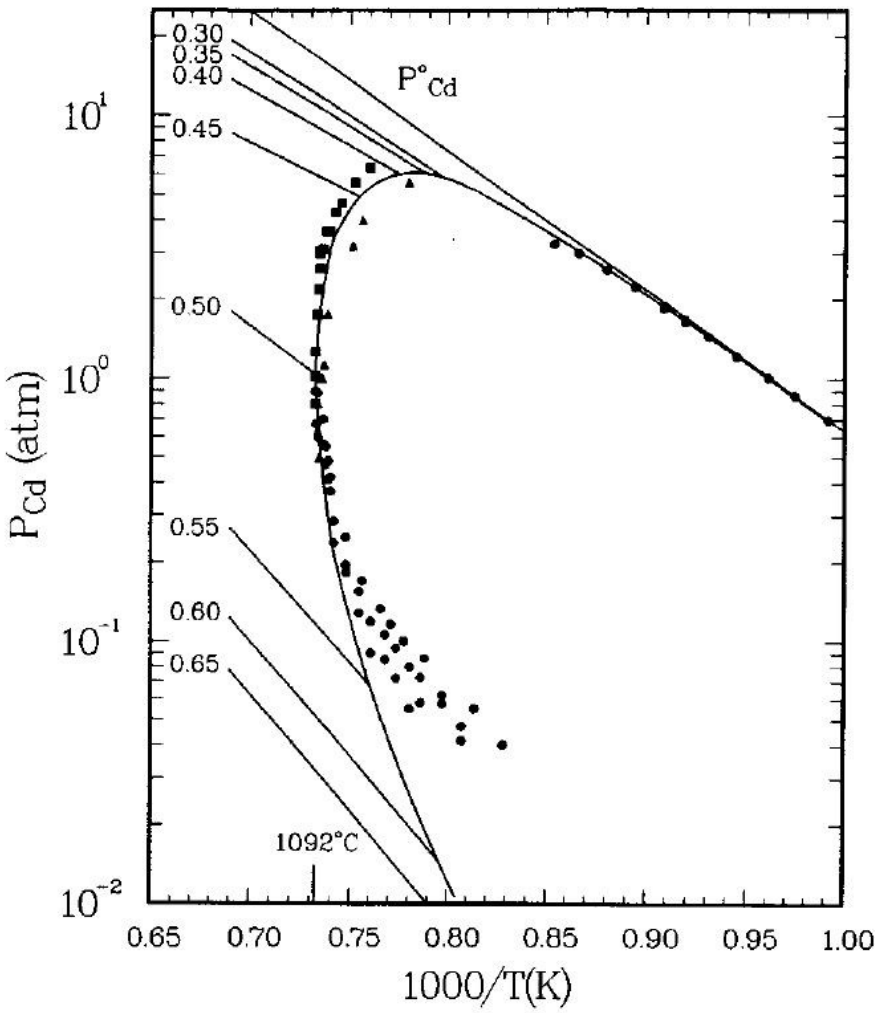

Figure 3.6 Partial pressure of Cd along the three-phase loop of CdTe(s) and over the different melts. Circles from Brebrick [23] Squares are from Lorenz [25] and triangles from de Nobel [28]. Vapor pressure of Cd(l) is line labeled P^{o}_{Cd} (taken from Figure 5 of Ref.[17]).

3.4.1.4 Hg-Cd-Te ternary. The interaction parameters for the ternary liquid and for the solid solution, W_S and V_S, were established by fitting to the selected 7 solidus and 7 liquidus points in the HgTe-CdTe pseudobinary and 23 Te-rich liquidus points determined by visual observation [21]. The calculated phase diagram along the HgTe-CdTe pseudo-binary section is shown in Figure 3.7, where the fits of the calculated solidus and liquidus points as functions of compositions x, the mole fraction of CdTe in $Hg_{1-x}Cd_xTe$, are 7.0 and 5.1°C, respectively, by varying the ternary interaction parameters. The remaining liquid phase interaction parameters to characterize the Hg-Cd-Te ternary system were determined by seeking an optimum fit to 47 liquidus and 21 solidus experimental points. An excellent fit is obtained without the use of liquid phase interaction parameters between Cd-HgTe (species 2-4). The values for the solid solution parameters, listed in Table 3.1, imply a critical temperature of 464K for the spinodal

decomposition of the solid solution which is in good agreement with 456.5K at $x_{CdTe} = 0.535$ reported by Vasil'ev *et al.* [29] by e.m.f. measurements.

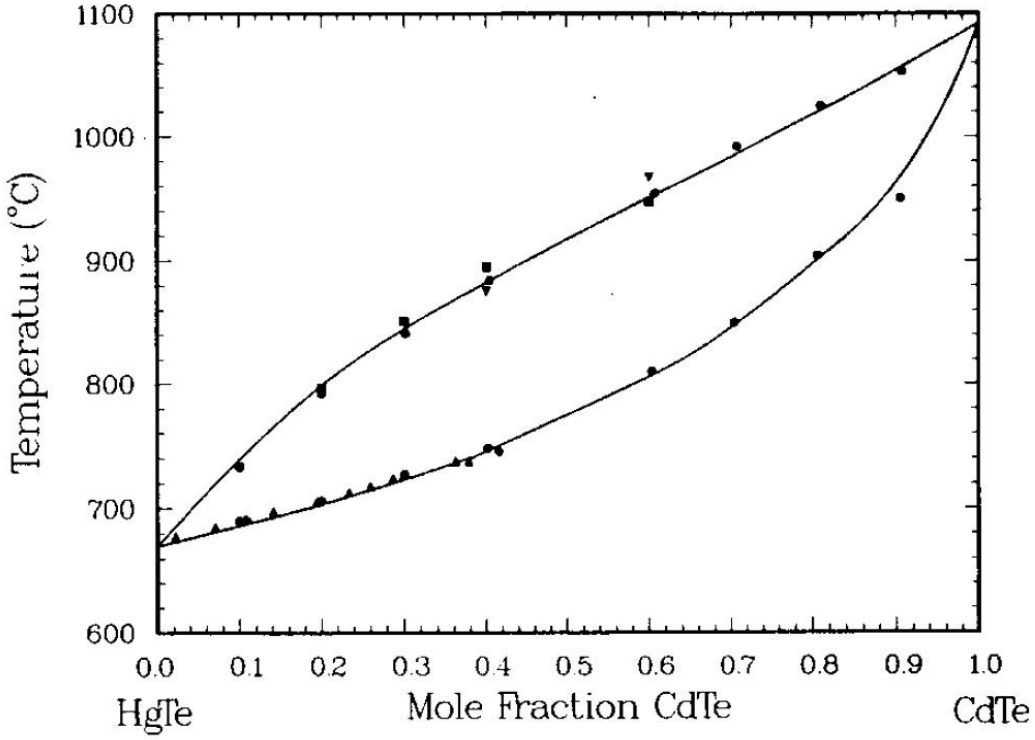

Figure 3.7 Liquidus and solidus lines in the HgTe-CdTe pseudo-binary section. Inverted triangles from Blair [30], circles are from Lehoczky and Szofran [31], squares from Steininger [32], triangles from Harman [33] and diamonds from Tung et al. [34] (taken from Figure 9 of Ref. [17]).

The partial pressures of Hg over the pseudobinary melts are calculated for different mole percent of CdTe for comparison with Steininger's data [32] measured by a high-pressure reflux technique. The results shown in Figure 3.8 are in good agreement with Steininger's statement that the activity of Hg is constant and independent of CdTe content. From the thermodynamic point of view, this kind of observation is not expected. The much stronger association of CdTe species relative to that of HgTe species in the pseudo-binary melts leads to a liquid phase in which the major species are uncombined Hg and Te and associated CdTe. The range of the measured P_{Hg}, 20 to 80atm from 740°C to 950°C, confirms the expected difficulty in the thermophysical property measurement on this system. Figures 3.9, 3.10 and 3.11 show the partial pressures of Hg, Te_2, and Cd along the three-phase curves for various solid solutions, $Hg_{l-x}Cd_xTe(s)$.

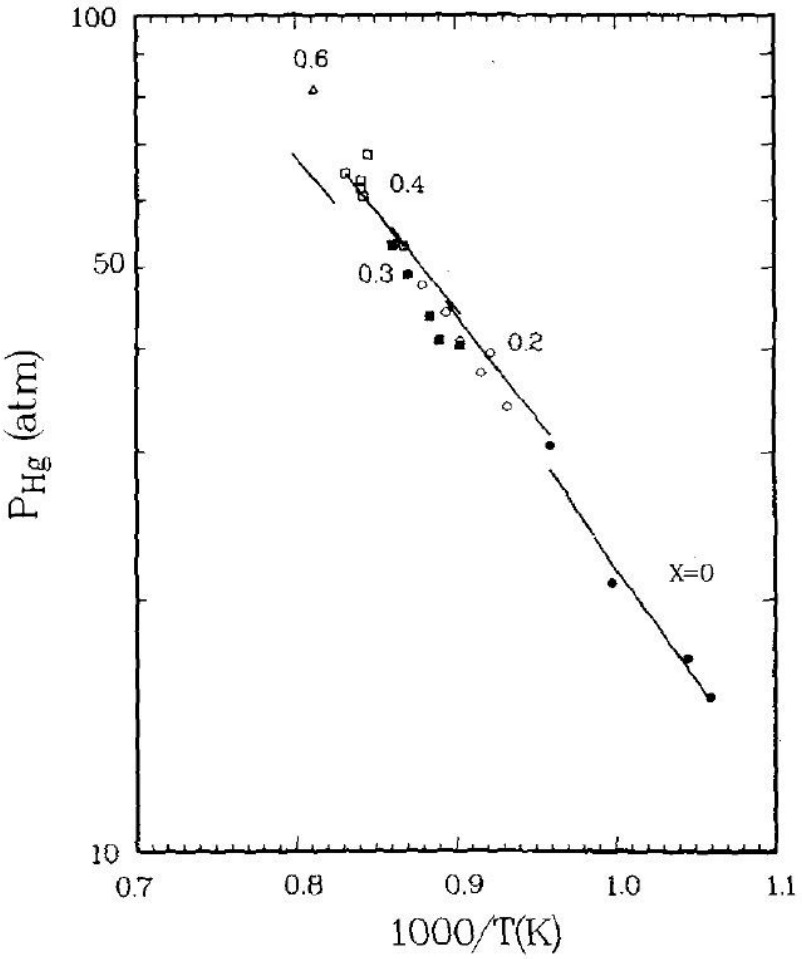

Figure 3.8 Partial pressure of Hg for various pseudo-binary melts with labeled x, the mole fraction of CdTe in $Hg_{1-x}Cd_xTe$. Experimental points of HgTe (x = 0.0) are from Su et al. [26]. Others experimental points are from Ref.[32] (taken from Figure 14 of Ref.[17]).

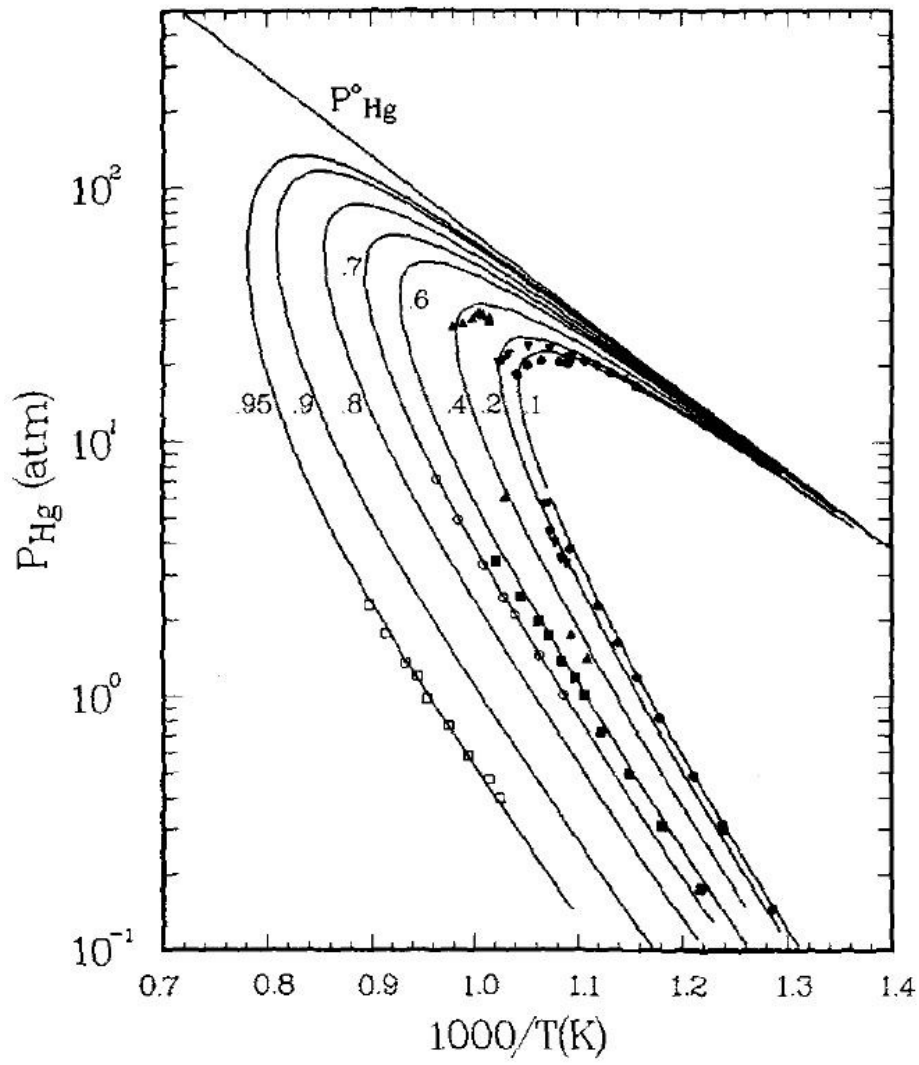

Figure 3.9 Partial pressure of Hg along the three-phase curves for various solid solutions. The number adjacent to the curve indicates the values of x in $Hg_{1-x}Cd_xTe$. Experimental points are from Schwartz et al [13], Tung et al. [34] and Su et al. [26] (taken from Figure 15 of Ref.[17]).

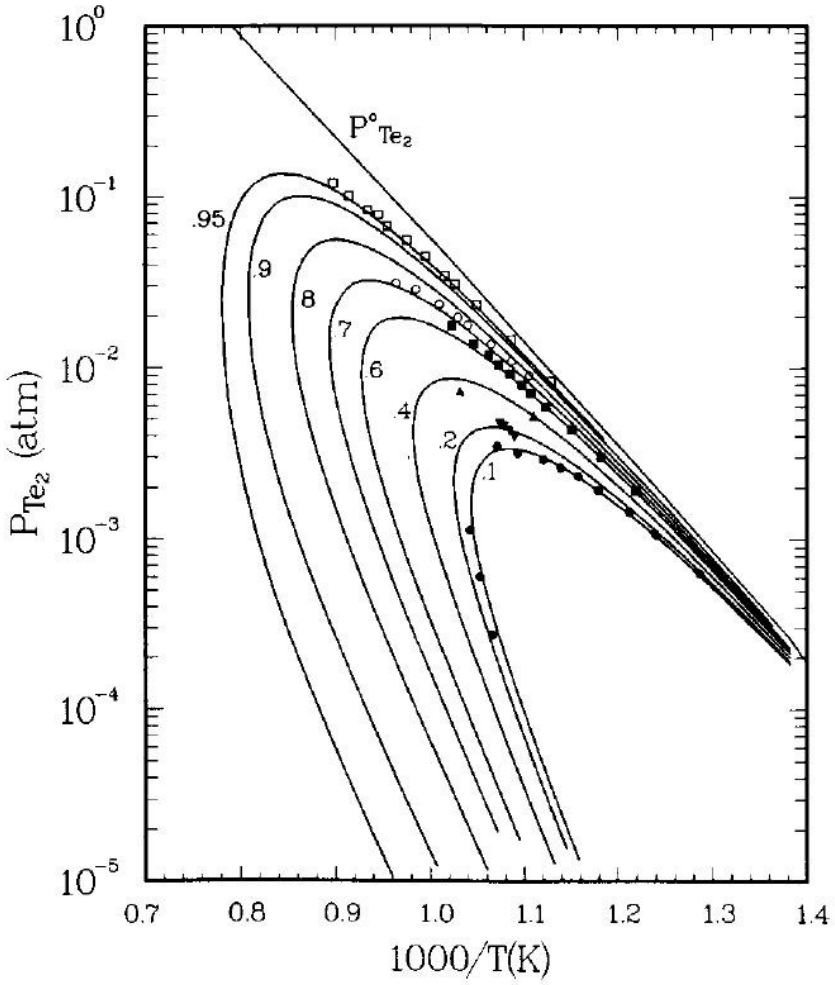

Figure 3.10 Partial pressure of Te_2 along the three-phase curves for various solid solutions of $Hg_{1-x}Cd_xTe$(s). Same credit source as Figure 3.9 (taken from Figure 16 of Ref.[17]).

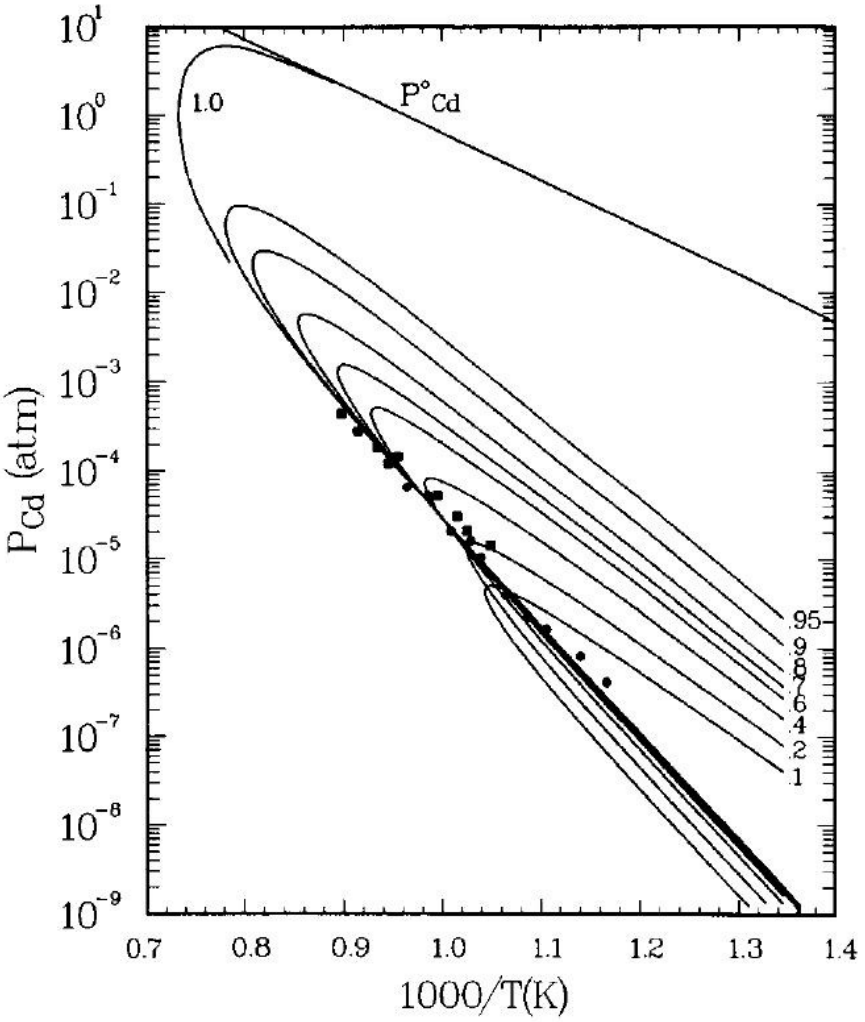

Figure 3.11 Partial pressure of Cd along the three-phase curves for various solid solutions of $Hg_{1-x}Cd_xTe$(s). The experimental points are from Su et al., [35], circles are for x = 0.7, squares for x = 0.95 (taken from Figure 17 of Ref.[17]).

There are also experimental liquidus data outside the pseudo-binary section of the phase diagram. Figure 3.12 shows the Te-rich liquidus isopleths with the experimental points determined by visual observation by Harman [21] and by DTA by Lawley [36]. The labeled number adjacent to each curve in figure is the number z in formula $(Hg_{1-z}Cd_z)_{1-y}Te_y$ for the composition of the liquid phase. The calculated curves agree very well with both sets of data, giving a fit of 3.1°C to the 23 data points by Harman [21]. The calculated Hg-Cd rich isopleths and the experimental points of Szofran and Lehoczky [31] are indicated by different symbols in Figure 3.13. Except for a single point on the very left-hand side that is 11.8°C higher than the calculated value, the remaining 13 points are fit to within a standard deviation of 6.5°C. The fit to all 47 liquidus points is 5.3°C. Generally speaking, the liquid surface of the Hg-Cd-Te ternary subsystem is reproduced very well with the model parameters obtained.

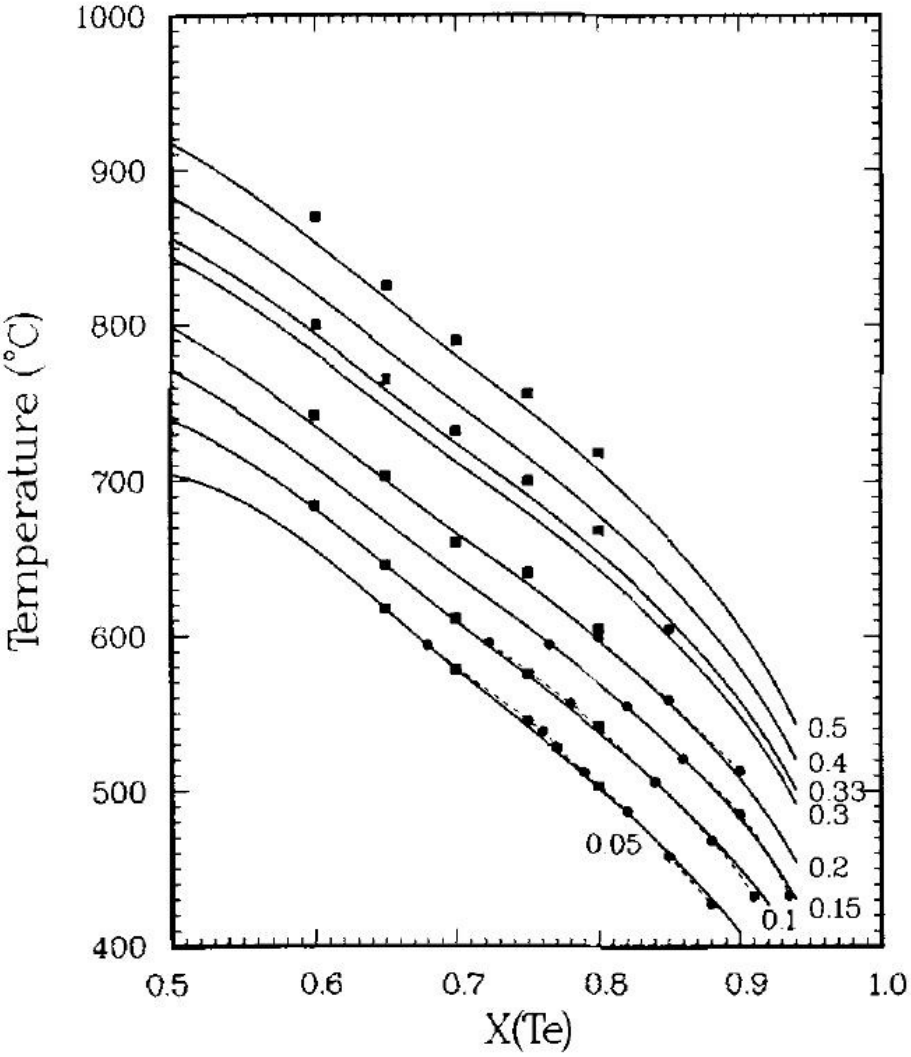

Figure 3.12 Te-rich liquidus of the Hg-Cd-Te phase diagram shown by plotting temperature versus atomic fraction of Te for different labeled values of the atomic fraction ratio of the liquid, $Z = x_{Cd}/(x_{Hg} + x_{Cd})$. Circles are from Ref.[21], squares from Lawley [36]. The abscissa is the atom fraction of Te in the liquid phase (taken from Figure 10 of Ref.[17]).

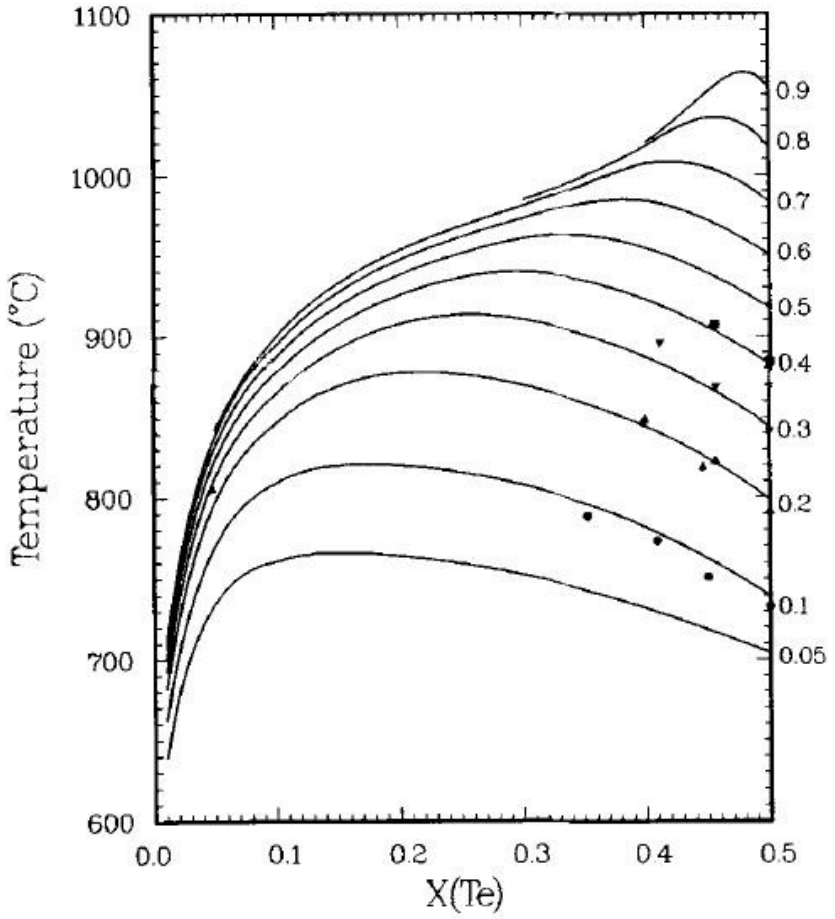

Figure 3.13 The calculated Hg-Cd rich isopleths of $(Hg_{1-z}Cd_z)_{1-y}Te_y$ and the experimental points of Szofran and Lehoczky [37] (taken from Figure 10 of Ref.[17]).

3.4.2 Hg-Zn-Te systems

3.4.2.1 Hg-Zn binary. Similar to the Hg-Cd binary, no liquid phase associated species are assumed in this system. As the 419.5°C melting point of Zn is the highest temperature of all, no attempt is made to fit the phase diagram at lower temperatures, but the thermodynamic properties of the melts are fit. The liquid phase is assumed to form a quasi-regular solution, the enthalpies of mixing and excess entropies of mixing selected by Hultgren et al. [18] are fitted well by taking $\alpha_{12} = 736.4 + 1.824T$.

3.4.2.2 Zn-Te binary. The selected data for the fitting are liquidus points from Kulwicki [22], Reynolds et al. [38] and Steininger et a1. [24] together with the partial pressure of Te_2 along the Te-rich leg of the three-phase curve [39]. No satisfactory fit was obtained without a miscibility gap with all of the available binary liquid parameters were used to fit this system. The gap, in common with the previous calculations by Jordan [40] and Sharma *et al.* [41] appears on the Zn-rich side of the liquidus line and, from the calculations, it is located between 19.0 and 39.1 atomic % Te with a monotectic at 1233.5°C. The selected liquidus points are shown in

Figure 3.14 and are fit to a standard deviation of 19.3°C. The partial pressures of Te_2 are shown in Figure 3.15.

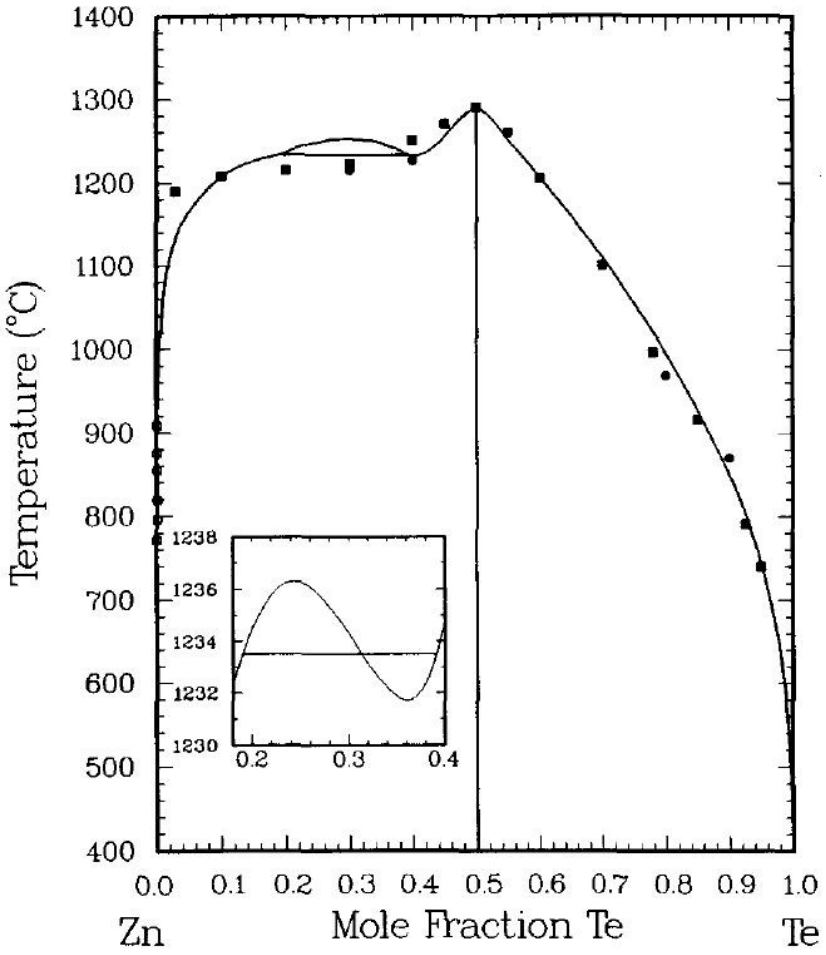

Figure 3.14 ZnTe binary phase diagram. Squares are from Kulwicki [22], circles are from Steininger et al. [24] and open circles with cross are from Reynolds et al. [38]. The subplot shows the liquidus calculated near the miscibility gap. The horizontal line is the equilibrium Monotectic (taken from Figure 6 of Ref.[17]).

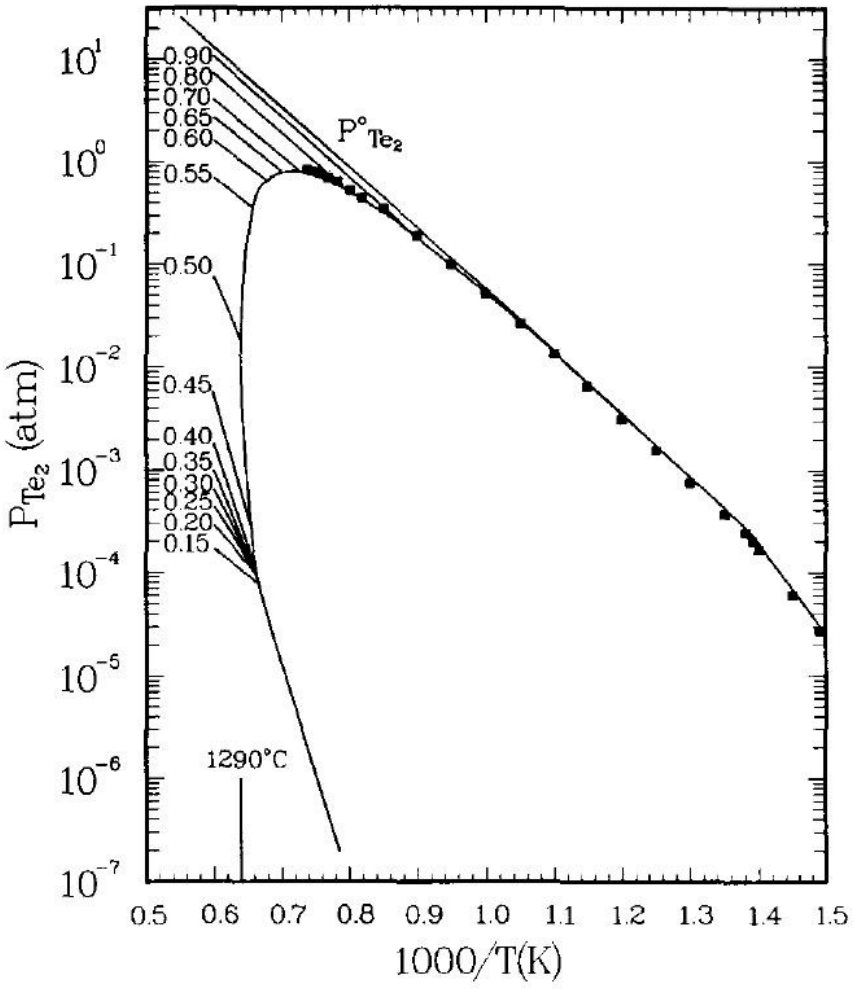

Figure 3.15 Partial pressure of Te_2 along the three-phase curve of ZnTe(s) and over the melts of various compositions. Squares are experimental points from Brebrick [39] (taken from Figure 7 of Ref.[17]).

3.4.2.3 Hg-Zn-Te ternary. Using the parameters determined earlier from the Hg-Te, Hg-Zn and Zn-Te binaries, the ternary parameters were obtained by fitting the experimental liquidus and solidus points of the HgTe-ZnTe pseudobinary. Several sets of parameters giving similar fits were found and the one set that gives the best fit to the experimental P_{Hg} was selected. The calculated liquidus and solidus curves and experimental points are shown in Figure 3.16. The calculated partial pressures of Hg along the three-phase loop for different solid solutions are shown in Figures 3.17. The open and solid symbols with the same shape represent the points from the same sample composition except that, for the open symbols, the compositions of the condensed phases deviate from the nominal values by more than 0.01 in either the mole fraction of ZnTe or that of Te due to the loss of Hg to the vapor phase. On the Te-saturated (lower) legs of the three-phase curves, the calculated Hg pressures are 10 to 20% too high for the 10 and 20

mole % ZnTe solid solutions. A critical temperature of 229.3K at $x_{ZnTe} = 0.5$ is obtained for the solid solution miscibility gap.

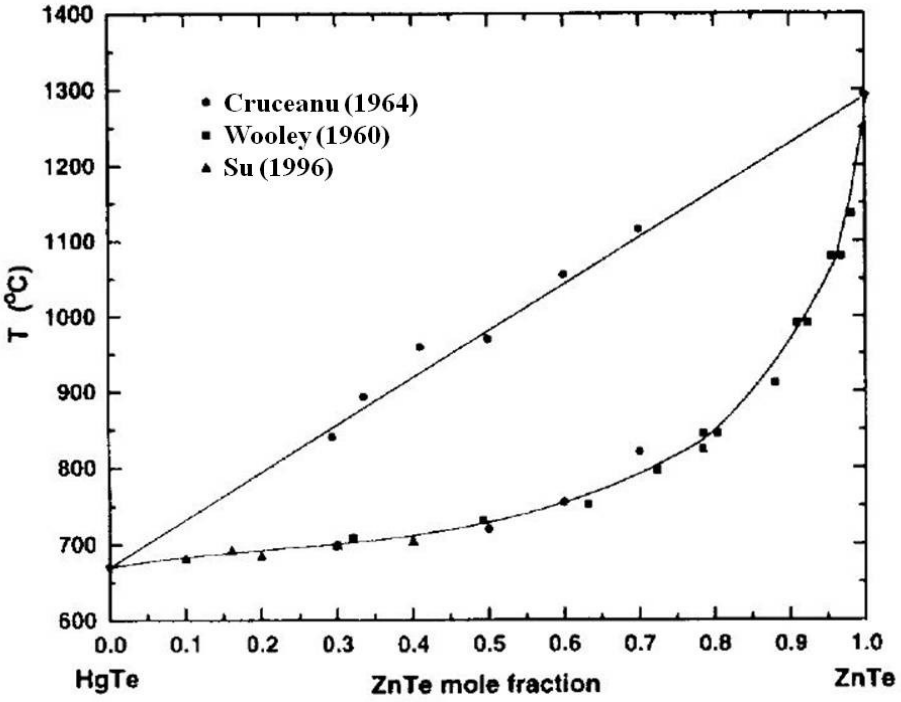

Figure 3.16 Liquidus and solidus lines in the HgTe-ZnTe pseudobinary section. Experimental data are from Woolley and Ray [42], Cruceanu et a1. [43] and Su et al. [35] (taken from Figure 2 of Ref.[35]).

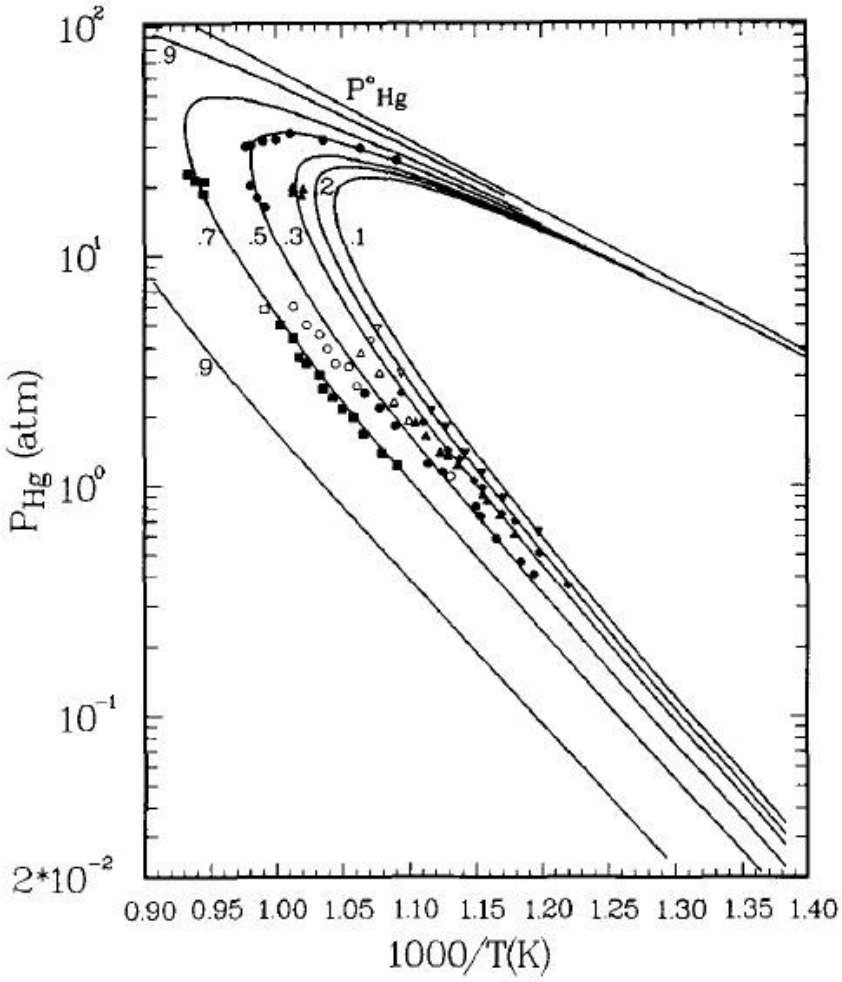

Figure 3.17 Partial pressure of P_{Hg} along the three-phase curves for various solid solutions of $Hg_{1-x}Zn_xTe$(s). The experimental points are from Chen et al. [44]. The open and solid symbols with the same shape represent the points from the same sample. The inverted triangles are for x = 0.1, diamonds for x = 0.2, triangles for x = 0.3, circles for x = 0.5, and squares for x = 0.7 (taken from Figure 21 of Ref.[17]).

In summary, using an associated solution model and a single set of interaction parameters, quantitatively good fits to extensive phase diagram and thermodynamic data in the Hg-Cd-Te and Hg-Zn-Te system have been obtained. The experimental data for these fits are comprehensive and accurate and the results can be used to smooth and extrapolate the experimental data. They are also very useful in generating thermodynamic properties of the liquid phase, such as heat capacity [35], enthalpy and entropy of mixing of the liquid [35] which no experimental measurements have been performed because of the high pressure and the toxicity of the sample. The detailed calculation will be given in Chapter 6 where the heat capacity is needed for the determination of thermal conductivity of the liquid. More detailed description of the model can be found in Ref.[16,17]. Finally, the interaction parameters for these fits, taken from Ref.[17], are tabulated in Tables 3.1 and 3.2 although small adjustments for these values have been reported by using more favorable values for the heat capacity and Gibbs energy

of formation on CdTe(s) [45]. The other experimental data used for the numerical optimization and calculation, such as melting points, enthalpy and entropy of fusion and formation for the binary compounds, vapor pressures of the pure elements as functions of temperature, heat capacity of the elements as function of temperature, etc…, can be found in Ref.[17].

Table 3.1 Interaction parameters for the Hg-Cd-Te system. The unit for all the parameters is in calories except ΔS_4^o and ΔS_5^o is in cal/K.

Hg – Cd	$\alpha_{12} = -5247$	$\beta_{12} = 0$		
Hg – Te	$\alpha_{13} = -1423 - 2.489T$ $\beta_{13} = 3943$	$\alpha_{14} = 8018 - 1.328T$ $\beta_{14} = 0$	$\alpha_{34} = 1743 + 0.4585T$ $\beta_{34} = -1317$	$\Delta H_4^o = 42230$ $\Delta S_4^o = 26.877$
Cd – Te	$\alpha_{23} = 18704 - 9.592T$ $\beta_{23} = -12943 + 1.57T$	$\alpha_{25} = 23677 - 13.07T$ $\beta_{25} = -2387 + 0.290T$	$\alpha_{35} = -3612 + 4.495T$ $\beta_{35} = 10.457 - 2.776T$	$\Delta H_5^o = 69288$ $\Delta S_5^o = -0.774$
Ternary	$\alpha_{15} = 26264 - 17.453T$ $\beta_{15} = 0$	$\alpha_{24} = 0$ $\beta_{24} = 0$	$\alpha_{45} = -9857 + 5.485T$ $\beta_{45} = 0$	
Solid solution	$W_s - V_S T = 13122 - 11.654T$			
Liquid species Number	Hg Cd Te HgTe CdTe 1 2 3 4 5			

Table 3.2 Interaction parameters for the Hg-Zn-Te system. The unit for all the parameters is in calories except ΔS_4^o and ΔS_5^o is in cal/K (note: the values on the column of Hg – Te are the same as in Table 3.1).

Hg – Zn	$\alpha_{12} = 736 + 1.824T$	$\beta_{12} = 0$		
Hg – Te	$\alpha_{13} = -1423 - 2.489T$ $\beta_{13} = 3943$	$\alpha_{14} = 8018 - 1.328T$ $\beta_{14} = 0$	$\alpha_{34} = 1743 + 0.4585T$ $\beta_{34} = -1317$	$\Delta H_4^o =$ 42230 $\Delta S_4^o =$ 26.877
Zn – Te	$\alpha_{23} = 95163 - 66.798$ $\beta_{23} = -13581 + 1.707T$	$\alpha_{25} = 7022 + 0.0073T$ $\beta_{25} = 0$	$\alpha_{35} = -3612 + 4.495T$ $\beta_{35} = 10.457 - 2.776T$	$\Delta H_5^o =$ 88499 $\Delta S_5^o = 13.611$
Ternary	$\alpha_{15} = 26264 - 17.453T$ $\beta_{15} = 0$	$\alpha_{24} = 9836 - 35.645T$ $\beta_{24} = 0$	$\alpha_{45} = 2749 - 12.168T$ $\beta_{45} = 0$	
Solid solution	$W_s - V_S T = 3050 + 3.325T$			
Liquid species Number	Hg Zn Te HgTe ZnTe 1 2 3 4 5			

References

[1] M. B. Panish and M. Ilegems, Prog. Solid State Chem. 7 (1972) 39.
[2] R. F. Brebrick, Metall. Trans. A 8A (1977) 403.
[3] M. Cutler, *Liquid Semiconductors*, Academic Press, New York (1977).
[4] V. M. Glazov, S. N. Chizhevskaya and N. N. Glagoleva, *Liquid Semiconductors*, Plenum, New York (1969).
[5] E. A. Guggenheim, *Mixtures*, Oxford Univ. Press, London and New York (1952).
[6] A. S. Jordan, Metall. Trans. 1 (1970) 139.
[7] A. S. Jordan, in: *Calculation of Phase Diagrams and Thermochemistry of Alloys Phases*, Edited by Y. A. Chang and J. F. Smith, AIME, Warrendale, PA, (1979) p. 100.
[8] R. F. Brebrick, *Progress in Solid State Chemistry*, vol.13, Ch. 5, edited by H. Reiss, Pergamon Press, Oxford (1967).
[9] Ching-Hua Su, Pok-Kai Liao, and R. F. Brebrick, J. Electron. Mater. 12 (1983) 771.
[10] R. F. Brebrick and R. Fang, J. Phys. Chem. Solids 57 (1996) 451.
[11] R. F. Brebrick, J. Phys. Chem. Solids 40 (1979) 177.
[12] T. Tung, L. Golonka and R. F. Brebrick, J. Electrochem. Soc. 128 (1981) 451.
[13] J. P. Schwartz, T. Tung and R. F. Brebrick, J. Electrochem. Soc. 128 (1981) 438.
[14] R. F. Brebrick, Tse Tung, Ching-Hua Su, and Pok-Kai Liao, J. Electrochem. Soc. 128 (1981) 1595.
[15] T. Tung, L. Golonka and R. F. Brebrick, J. Electrochem. Soc. 128 (1981) 1601.
[16] R. F. Brebrick, Ching-Hua Su, and Pok-Kai Liao, in *Semiconductors and Semimetals,* Vol. 19, Chap. 3, edited by R. K. Willardson and A. C. Beer, Academic, New York (1983).
[17] T.-C. Yu and R. F. Brebrick, J. Phase Equilib. 13 (1992) 476.
[18] R. Hultgren, P. Desai, D. Hawkins, M. Gleiser and K. K. Kelly "*Selected Values of the Thermodynamic Properties of Binary Alloys*", Am. Soc. Metals, Metals Park, Ohio (1973).
[19] A. J. Strauss, private communication of tabulated liquidus points, presented in graphical form in Ref.[33].
[20] R. F. Brebrick and A. J. Strauss, J. Phys. Chem. Solids 26 (1965) 989.
[21] T. C. Harman, J. Electon. Mater. 9 (1980) 945.
[22] B. M. Kulwicki, Ph.D. dissertation, University of Michigan, Ann Arbor, Michigan (1963).
[23] R. F. Brebrick, J. Electrochem. Soc. 118 (1971) 2014.
[24] J. Steininger, A. J. Strauss and R. F. Brebrick, J. Electrochem. Soc. 117 (1970) 1305.
[25] M. R. Lorenz, J. Phys. Chem. Solids 23 (1962) 939.
[26] Ching-Hua Su, Pok-Kai Liao, T. Tung, and R. F Brebrick, High Temp. Sci. 14 (1981) 181.
[27] T. D. Levitskaya, A. V. Vanuykov, A. N. Krestmikov and V. P. Bystrov, Izv. Akad. Nauk. SSSR, Neorg. Mater. 6 (1970) 559.
[28] D. de Nobel, Philips Res. Rept. 14 (1959) 361.
[29] V. P. Vasil'ev, M. N. Mamontov, and M. A. Bykov, Vestn. Mosk. Univ., Khim*., Set 2,* 31 (1990) 211.
[30] J. Blair and P. Newnham, *Metallurgy of Elemental and Compound Semiconductor,* edited by P. O. Grubel, Wiley 0nterscience, New York (1961).

[31] F. R. Szofran and S.L Lehoczky, J. Electron. Mater. 10 (1981) 1131.
[32] J. Steininger, J. Electron. Mater. 5 (1976) 299.
[33] T. C. Harman, in *Physics and Chemistry of II-VI Compound,* edited by M. Aven and J. S. Prener, North-Holland Publ., Amsterdam, (1967) p.769.
[34] T. Tung, Ching-Hua Su, Pok-Kai Liao, and R. F Brebrick, J. Vac. Sci. Technol. 21 (1982) 117.
[35] Ching-Hua Su, Pok-Kai Liao, and R. F. Brebrick, J. Electrochem. Soc.,132 (1985) 942.
[36] K. L. Lawley, Texas Instruments Technical Report, 10 Feb. 1980, Contract MDA903-79-C-1099
[37] F. R. Szofran and S. L. Lehoczky, J. Electron. Mater, 12 (1983) 713.
[38] R. A. Reynolds, D. G. Stroud and D. A. Stevenson, J. Electrochem.Soc. 114 (1967) 1281.
[39] R. F. Brebrick, J. Electrochem. Soc. 116 (1969) 1274.
[40] A. S. Jordan, Metall. Trans. 1 (1970) 239.
[41] R. C. Sharma and Y. A. Chang, Bull. Alloy Phase Diagrams 8 (1987) 14.
[42] C. Wooley and B. Ray, J. Phys. Chem. Solids 13 (1960) 151.
[43] E. Cruceanu, D. Niculescu, N. Nistor, and A. Aldea, Rev. Roum Phys, 9 (1964) 499.
[44] K.-T. Chen, Y.-G. Sha, and R.F. Brebdck J. Vac. Sci. Technol. A 8 (1990) 1086.
[45] T.-C. Yu and R. F. Brebrick, J. Phase Equilib. 14 (1993) 271.

Chapter 4
Density Measurements and Results

Abstract The density of Te, HgTe, $Hg_{0.9}Cd_{0.1}Te$, $Hg_{0.8}Cd_{0.2}Te$, $Hg_{0.9}Zn_{0.1}Te$ and $Hg_{0.84}Zn_{0.16}Te$ melts were measured by a method similar to the pycnometric technique which measures the volume of a melt, with known mass, in a sealed fused silica ampoule positioning coaxially inside a transparent furnace. The volume was determined from the height of the meniscus, by in-situ visual observation, and the calibration of volume vs. height for the ampoule which was performed by measuring the mass of water at different heights before the sample was loaded. The density measurements covered the temperature ranging from the corresponding melting points or liquidus temperatures to about 1130K. The Te liquid showed the normal thermal expansion, i.e., its density decreases as temperature increases except at temperatures just above the melting point where it went through a maximum. Similar to the behavior of the Te melt, the density of HgTe, $Hg_{0.9}Cd_{0.1}Te$ melts also went through a maximum as a function of temperature. It has been reported by other measurements, such as neutron scattering and nuclear magnetic resonance, that the melt consists of a mixture of two domains – one low coordination number and the other high coordination number structure which corresponding to low- and high-density melt, respectively. At temperature just above the melting point, the melt structure started to evolve with the low coordination number domain changing into high coordination number one which resulted in an increase in melt density. As temperature increasing to the density maximum, most of the structural changes has been completed and the normal thermal expansion took over and the density started to decrease as the temperature keeps on increasing. The measurements on the melts of $Hg_{0.8}Cd_{0.2}Te$, $Hg_{0.9}Zn_{0.1}Te$ and $Hg_{0.84}Zn_{0.16}Te$ did not show a maximum as functions of temperature probably because the liquidus of these melts are higher than the temperature where the density maximum occurred.
Relaxation

Keywords: Density; II-VI compound semiconductors; Pycnometry; Tellurium (Te); Mercury-cadmium-tellurium (Hg-Cd-Te) system; Mercury-zinc-tellurium (Hg-Zn-Te) system

4.1 Density Measurements by Pycnometry

The density of the HgTe-based semiconductor melts has been measured mainly by two different methods: the gamma ray radiation attenuation method [1-3] and a method similar to the pycnometric technique [4-6]. During the former measurement, after the incident gamma ray beam interacts with the molten sample in a sealed crucible, the attenuated beam intensity is recorded by a radiation counter. The density of the melts can be derived using the absorption equation with the measured intensities of the incident and the emergent radiation beams, the penetration length and absorption coefficient of the sample. However, the absorption coefficient

was usually obtained from the calibration of a solid sample with known density which might introduce error from the true absorption coefficient of the melt as a function of temperature.

On the other hand, the density can be determined by a simple pycnometric method which determines the density by measuring the volume of a melt with known mass. The volumes of the melts were determined from the measurements of the meniscus height of the melts inside a transparent furnace by *in situ* visual observation. The thermometer-shaped ampoules were made from fused silica [4]. The typical ampoule was made with a 7-8cm long, 15mm OD, 9mm ID "bulb" and a 6mm OD, 3mm ID stem that extended from the "bulb". The volume of the ampoule as a function of its height was measured by filling the ampoule with distilled water to various levels from reference marks which were thin slices of fused silica fused onto the stem area. The schematic drawing of an empty ampoule is illustrated in Figure 4.1. The volume corresponding to each mark's height was calculated from the difference between the total weight (ampoule + water) and the weight of empty ampoule and water density at room temperature. The density of water in the vicinity of room temperature from Ref.[7] was used. The measured volumes were plotted against the corresponding heights (relative to the marks) and showed a linear dependency in the stem section. The linear and volume expansion coefficients of fused silica [8] were applied to correct for the measured melt volume at elevated temperatures after measuring the distance between the meniscus level of the melt and one of the reference marks. Using this method, the density of pure Te, $Hg_{1-x}Cd_xTe$ (x = 0, 0.10, 0.20) [9,10], $Hg_{1-x}Cd_xTe$ (x = 0, 0.05, 0.10, 0.20) [5] and $Hg_{1-x}Zn_xTe$ (x = 0.10, 0.16) [4] were measured.

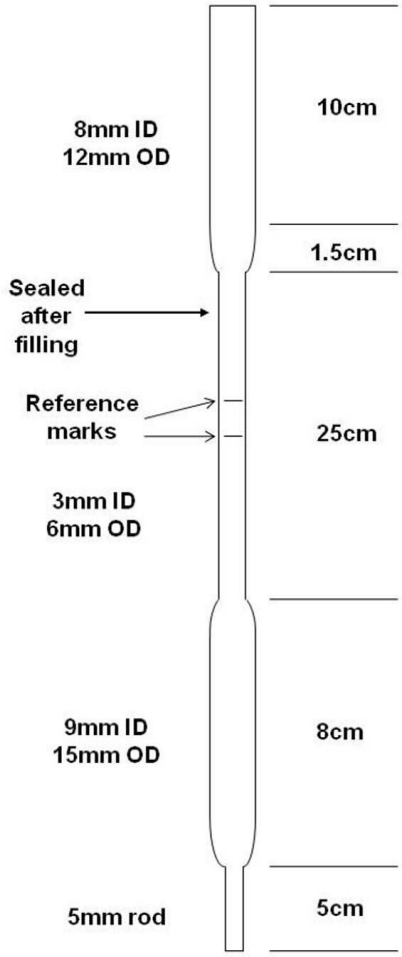

Figure 4.1 The schematic drawing of an empty ampoule for density measurements.

4.2 Sample Preparation

Although the following procedures were introduced as the preparation of density ampoules it can be used generally for the sample preparation of all other measurements described in this book. The ampoules were made from fused silica tubing supplied by Heraeus Amersil, Inc. The empty ampoule was first etched with HF for 20 – 30 seconds before cleaned with distilled H_2O, methanol, acetone and distilled H_2O again. After being air-dried, the ampoule was baked inside a furnace at 1283K overnight – about 16hrs. The starting materials were seven nines grade Hg from Bethlehem Apparatus and six nines grade Cd, Zn and Te from Johnson Matthey Co. After the weighing by a Mettler AT201 electronic balance with a resolution of 10^{-5}gram, the elements were loaded into the prepared ampoule which was then sealed under a vacuum of approximately 10^{-5}Torr. A small amount of extra Hg (0.003 to 0.018g) was added to compensate for the loss to the vapor phase during the experiment at elevated temperatures. The total masses and compositions of the samples are listed in Table 4.1.

The samples in the ampoules were synthesized to a complete homogenization in a rocking furnace following the procedure developed previously [11] to minimize the "wetting" of the ampoule wall. The essence of the process is the long period of solid-state diffusion to react Hg, Cd, Zn with Te before heating the samples above its melting point. The ampoule was first heated to a temperature about 10-20K below its solidus temperature and held there for 20 hrs before the temperature was raised to about 100K above its liquidus temperature. After the furnace rocking at the temperature for 20 hrs the temperature was raised to approximately 20K above the maximum temperature planned for the measurements. Then, the samples were solidified vertically by turning off the power to the rocking furnace.

Table 4.1. Masses and compositions for the density samples

Sample	Mass (g)
Te	14.0809
HgTe	53.5062
$Hg_{0.9}Cd_{0.1}Te$	43.2028
$Hg_{0.8}Cd_{0.2}Te$	39.2008
$Hg_{0.9}Zn_{0.1}Te$	43.4822
$Hg_{0.84}Zn_{0.16}Te$	43.7654

4.3 Experimental

The density ampoule was then placed vertically and coaxially in the center of a two-zone, 15cm and 35cm long for upper and lower zone, respectively, gold-plated transparent tubular furnace provided by Thermcraft, Inc with 3-4 calibrated K-type thermocouples positioned along the ampoule wall. The temperatures of the two zones were set with a positive temperature difference of 3K (hot on top) to avoid bubbles formation inside the melt during the measurement. A powerful lamp was placed at the back of the furnace to help delineating the positions of the meniscus and the reference mark. The liquid level was visible inside the gold-plated transparent furnace and the separation between the meniscus and the reference mark was measured by a cathetometer with 0.05mm resolution (corresponding to about 0.15% error in density) which was also monitored and recorded with a digital camera and a VCR. The volume of the melts was determined by measuring the distance from the meniscus of the melt to one of the reference marks with the reference to the volume calibration data.

4.4 Results and Discussions

4.4.1 Te liquid. The measured density of Te melt [12] are plotted in Figure 4.2 together with previous published data determined by the ɣ-ray attenuation method [13,14]. The data show good agreement with Thurn [13] except at temperatures just above the melting point where the data agree better with those from Tsuchiya [14]. The Te liquid showed the normal thermal expansion, i.e., its density decreases as temperature increases except at temperatures just above the melting point where it went through a maximum. The density increased from the melting

point of 723K to a maximum at 752K, then followed the normal thermal expansion. During the normal thermal expansion, the inter-atomic/molecular distance increases as temperature goes up. However, when there is a structural rearrangement in the melt, the normal expansion sometimes can be shadowed. Such a structural transition in liquid Te was also observed in the results of neutron scattering experiments [15]. The neutron spectrum showed that the average first coordination number of liquid Te atoms is 2.63 at its melting point which increased to approximately 3 at 873K and stayed at 3 as the temperature was raised to 1073K. It indicated that, at temperature just above 723K, the change of melt density is dominated by the increase in the average first coordination number which overshadows the normal thermal expansion. When the temperature increased above 873K, the first coordination number remained constant at 3 and the thermal expansion took over and the density of liquid Te decreased as the temperature increased.

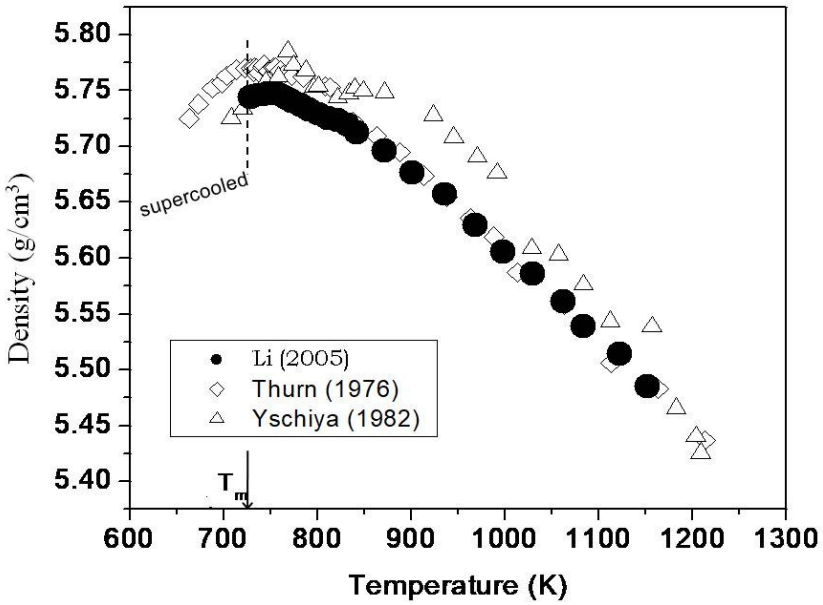

Figure 4.2 The measured density of Te liquid as a function of temperature by Li et al. [12] together with two results measured by gamma ray absorption method Ref.[13,14] (take from Figure 1 of Ref.[12]).

The neutron scattering results imply that from the Te melting point of 723K to 873K the structure of the liquid Te is a mixture of structural domains of two- and three-fold coordination and as temperature increases above 873K, the liquid Te mostly becomes three-fold coordination domains. Based on other neutron scattering result [16] and the Knight-shift data of the liquid Te by [17,18], Cabane and Friedel [19] included their nuclear magnetic resonance results and proposed that the two-fold coordination domain is semiconducting and the three-fold coordination domain is metallic in liquid Te. Adopting this inhomogeneous domain model, Cohen and Jortner [20-23] developed an effective-medium theory to quantitatively calculate the volume fraction of the metallic three-fold coordination region as a function of temperature as

shown in Figure 4.3. The volume fraction of this domain increases from 82% at the melting temperature to become saturated toward 100% at elevated temperature.

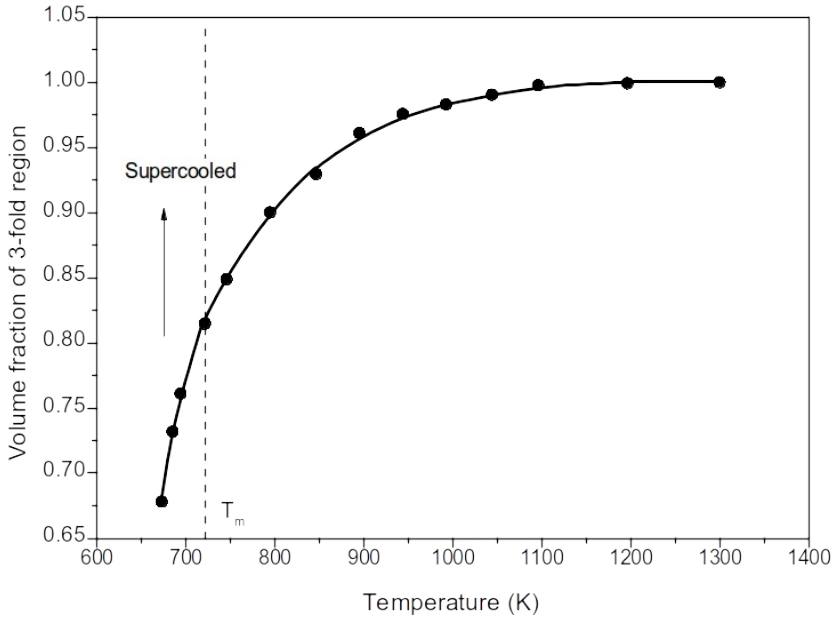

Figure 4.3 Calculated volume fraction of the metallic three-fold coordination domain in the liquid Te as a function of temperature (taken from Ref.[20]).

The structural fluctuation of liquid Te was investigated through the time relaxation of the measured density [24] after the liquid Te sample was maintaining at 1123K for 7 days, to ensure the equilibrium state, before rapidly cooled to 823K which took approximately 0.5 h in the transparent furnace. The density measurement started when the temperatures of the thermocouples outside of the ampoule wall reached 823K. Within the experimental error, the measured density stayed roughly at 5.72g/cm^3 over the next 7 hrs. Hence, it was concluded that no relaxation phenomenon was observed in the density of the liquid Te when the temperature was rapidly cooled from 1123K to 823K.

4.4.2 HgTe melt. The measured density of the HgTe melt as a function of temperature [10] is shown in Figure 4.4 together with previously published results by Glazov [1,2] using the gamma radiation attenuation method, as well as by Chandra [5], using the pycnometric method. In the figure, "Temp. up" and "Temp. down" indicates that the measurements were taken with increasing and decreasing temperature, respectively. There were over 200 data points reported in Ref. [1,2] in the temperature range from 943K to 1080K with the absolute error reported to be approximately $\pm$0.01g/cm^3. The fitting curve of these density data is shown as a solid line in the figure. The density of the HgTe melt increases with increasing temperature to a maximum value of 8.16g/cm^3 at about 1023K and then follows a slight downward trend. The measurements by the different processes of "Temp. up" and "Temp. down" seem to have no effects on the results. The previous works by Glazov [1,2] and Chandra [5] show a similar trend with their values

about 0.6% and 1.5-2.0% lower, respectively. As mentioned early, the absorption coefficient of the HgTe melt in the gamma ray radiation attenuation method was calibrated using a solid HgTe sample, which might have contributed to additional error in the density measurements. The underestimation in the densities of the HgTe melt by Chandra [5] was suspected by Glazov [1,2] to be due to the possible formations of tiny Hg bubbles in the HgTe melt because of the non-uniform temperature distribution in the melt during the density measurements.

Similar to the behavior of the Te melt, the density HgTe melt went through a maximum as a function of temperature, which implies a likely structural transition in the HgTe melt. A quantitative description of the density of the HgTe melt as a function of temperature was proposed by both Chandra [25] and Glazov [1,2] by applying an effective-medium theory developed by Cohen and Jornter [20-23]. In Chandra's assumption, the HgTe melt structure was considered to be a mixture of a low- and a high-coordination-number structures that have the same total number of Hg and Te atoms. The increase in density of the HgTe melt with increasing temperature was attributed to its continuous transformation from the low-coordination-number structure to the denser, high-coordination-number structure. The decrease in the density of the HgTe melt after reaching its maximum is caused by the thermal expansion of the two structures. In Glazov's assumption, which was based on an associated equilibrium solution theory, the structure of the HgTe melt consists of several kinds of structures namely, Hg, Te, HgTe, and Hg_2Te_3. The maximum in the HgTe melt density was attributed to the combined changes of the molar volumes and the volume fractions of the various structural species as functions of temperature.

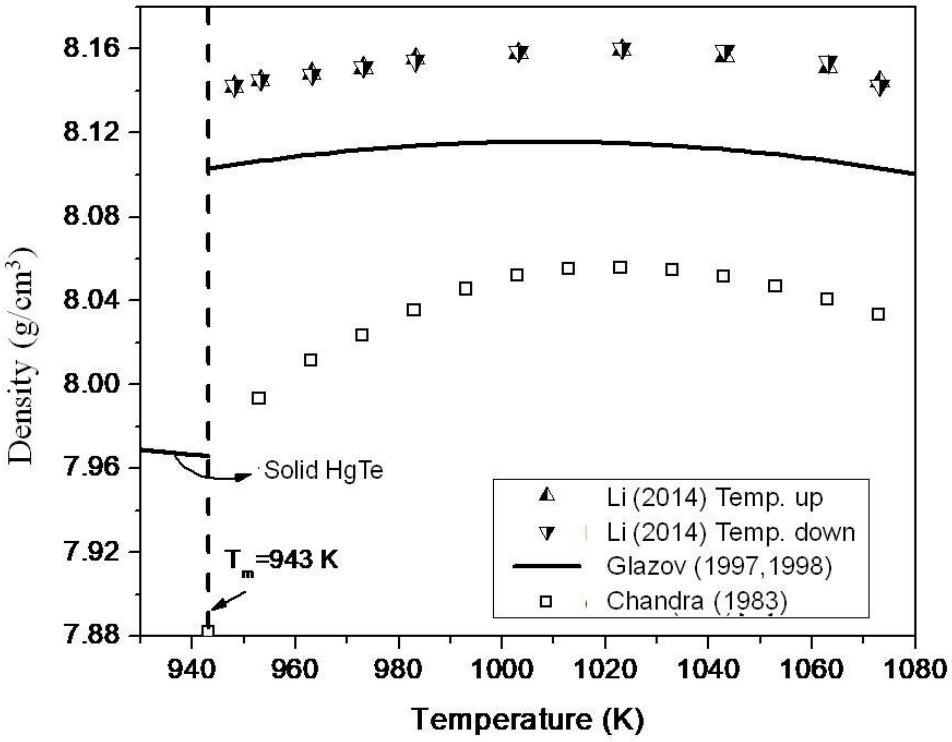

Figure 4.4 Density of HgTe melt as a function of temperature from Li [10], Glazov [1,2] and Chandra [5] (taken from Figure 1 of Ref.[10].

On the relaxation measurements [24], similar to the Te liquid, the measured density of the HgTe melt did not change as the meniscus of the melt in the ampoule remained at the same position, through the 8 hrs period after the temperature has been cooled from 1073K to 948K.

4.4.3 $Hg_{0.9}Cd_{0.1}Te$ melt. The measured densities of the $Hg_{0.9}Cd_{0.1}Te$ melts as a function of temperature [10] are shown in Figure 4.5. Previous results for the $Hg_{0.9}Cd_{0.1}Te$ melt measured by Glazov [1], shown as a curve from a 2nd-order polynomial fit, and by Chandra [5] are about 0.2% and 0.25% lower, respectively. The lower density values in those studies may be attributed to the same reasons/factors as described earlier for the HgTe melt. As shown in Figure 4.5, a maximum in our measured density of the $Hg_{0.9}Cd_{0.1}Te$ melt [10] was observed at a temperature of approximately 1020K, which agrees with Chandra's results [5] whereas the fitting curve of the density measured by Glazov [1] shows a maximum at 1029 K.

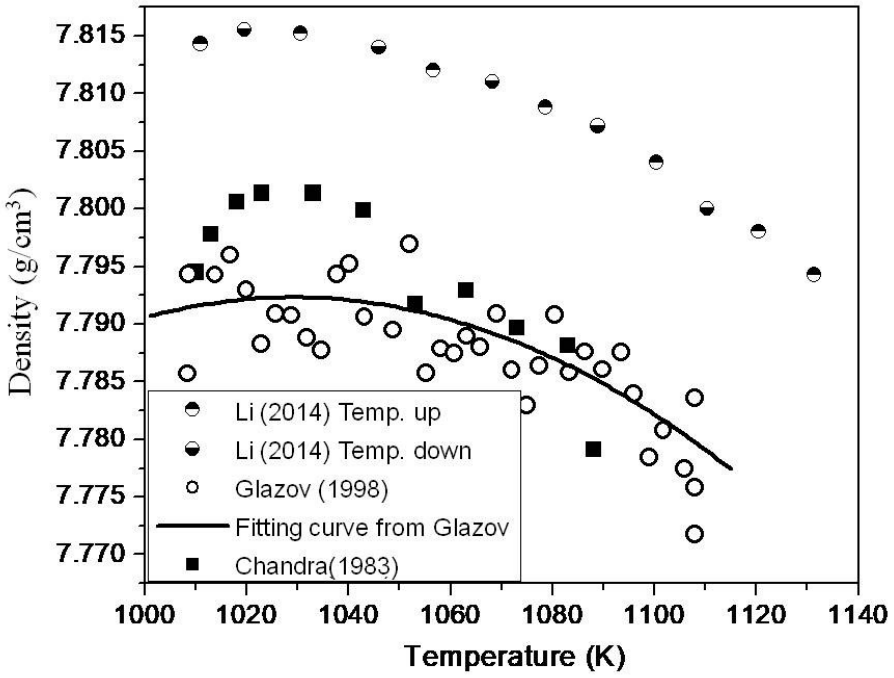

Figure 4.5 Temperature dependence of density for the $Hg_{0.9}Cd_{0.1}Te$ melt from Li [10], Glazov [1] and Chandra [5] (taken from Figure 2 of Ref.[10]).

The relaxation behavior on the density of the $Hg_{0.9}Cd_{0.1}Te$ melt was measured [24] after the melt was cooled from 1130K to 1010K, i.e., 15K above the liquidus temperature, with the cooling time of approximately 15 min. After the temperature of the thermocouples decreased to 1010K, the meniscus position of the $Hg_{0.9}Cd_{0.1}Te$ melt did not change as a function of time. It was also concluded that no relaxation phenomenon was observed in the density of the $Hg_{0.9}Cd_{0.1}Te$ melt.

4.4.4 $Hg_{0.8}Cd_{0.2}Te$ melt. Figure 4.6 shows the density of the $Hg_{0.8}Cd_{0.2}Te$ melt as a function of temperature [9] with the data from two other reports [2,5]. The data from Glazov [2] were about 1.3% higher than the other two sets of data. The measured density decreased with increasing temperature and no maximum was observed in all of these density measurements which imply that the change in the structural coordination number, if any, was overshadowed by the effect of thermal expansion.

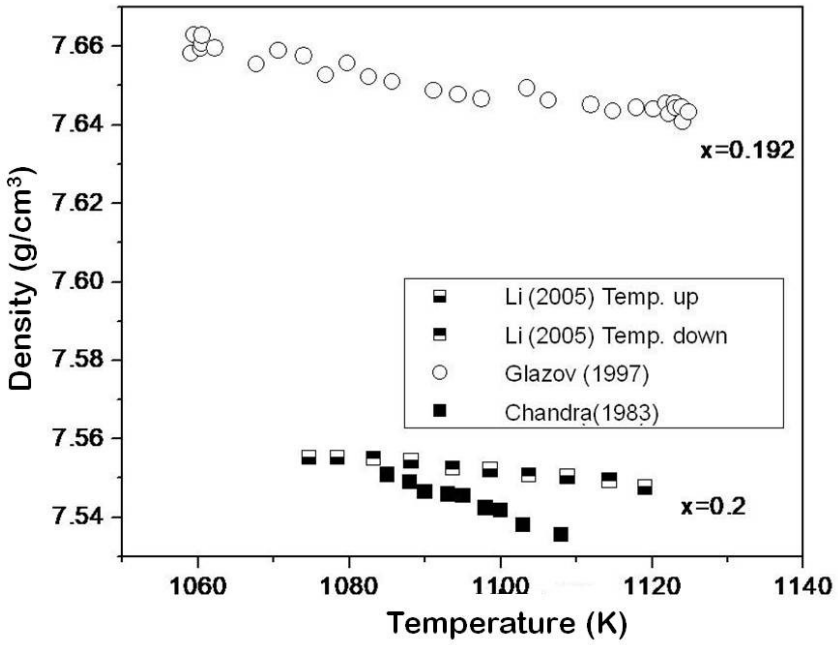

Figure 4.6 Temperature dependence of density for the $Hg_{0.8}Cd_{0.2}Te$ melt from Li [9], Glazov [2] and Chandra [5].

To have a better comparison, Figure 4.7 provides the density data of the $Hg_{1-x}Cd_xTe$ melts for x = 0, 0.1, and 0.2 measured by the same instrumental setup [9,10]. It shows that the density of the $Hg_{1-x}Cd_xTe$ melt decreases with an increase in x, the CdTe mole fraction in the melt, which is understandable as high-density Hg element being replaced by the low-density Cd atom. The approximately same temperature of the maximum density of the HgTe (1023K) and $Hg_{0.9}Cd_{0.1}Te$ (1020K) melts implies that the density change in the $Hg_{0.9}Cd_{0.1}Te$ melt is dominated by the density change of its HgTe component. For the $Hg_{0.8}Cd_{0.2}Te$ melt, with its liquidus temperature of 1160K [26], much higher than 1023K, no density maximum was observed.

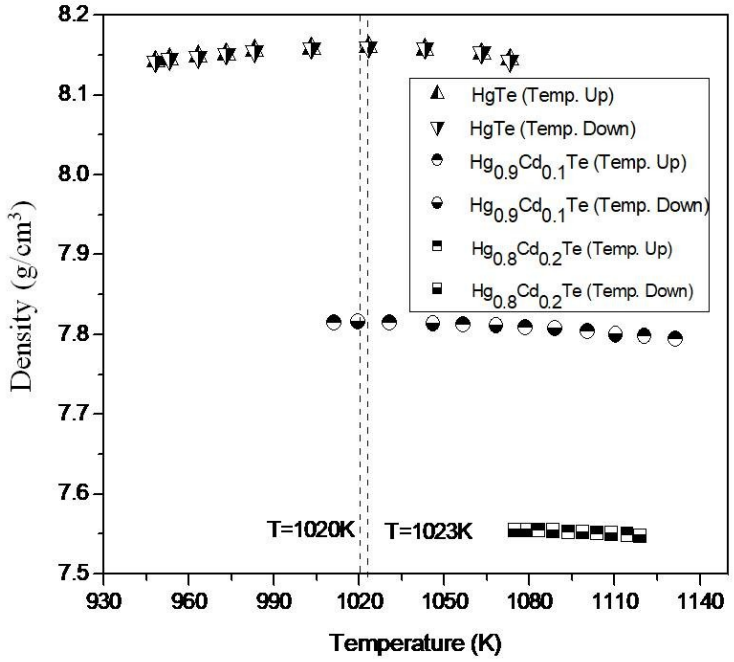

Figure 4.7 The measured density of the HgTe, $Hg_{0.9}Cd_{0.1}Te$, and $Hg_{0.8}Cd_{0.2}Te$ melts as functions of temperature from Ref.[9,10] (taken from Figure 3 of Ref.[10]).

.

The time dependence of the density of the $Hg_{0.8}Cd_{0.2}Te$ was measured [24] after the sample temperature was cooled from 1130K to 1073K, which is approximately 20K above the liquidus temperature. When the temperature of the thermocouples attached to the outside of the ampoule wall was cooled to 1073K, the density of the $Hg_{0.8}Cd_{0.2}Te$ melt did not change over a period of 7 hrs. Hence, no relaxation phenomenon was observed in the density of the $Hg_{0.8}Cd_{0.2}Te$ melt, same as the behavior of the HgTe and $Hg_{0.9}Cd_{0.1}Te$ melts.

4.4.5 $Hg_{0.9}Zn_{0.1}Te$ and $Hg_{0.84}Zn_{0.16}Te$ melts. The density of $Hg_{1-x}Zn_xTe$ melts have also been measured using the same pycnometric method [4]. For the $Hg_{0.90}Zn_{0.10}Te$ Te melts, the density measurements started from a temperature of 1009 to 1120K and then back to 1010K. The heating and cooling data showed a hysteresis behavior, as shown in Figure 4.8, with the largest discrepancy of $\pm$0.8% at 1068K and almost no difference at 1010K. The density results for the cooling measurements, shown in Figure 4.8, are believed to be more reliable because of the longer equilibration time at higher temperatures. The measured density of the $Hg_{0.90}Zn_{0.10}Te$ melt remained almost the same at 7.85g/cm^3 from 1010 to 1070K then started to decrease by 2.3%, to 7.67g/cm^3 at 1120K. The constant density in the lower temperature range may result from the thermal expansion cancelled by the increase in structural coordination number. Then, in the high temperature range, the thermal expansion dominated, and the density decreased with increasing temperature.

The densities of $Hg_{0.84}Zn_{0.16}Te$ melt were measured in the temperature range between 1070 and 1120K. The high liquidus temperature and the associated high Hg pressure limited the

measurements to a small temperature range of 50K. After four heating cycles between 1068 and 1123K, the sample was equilibrated at 1070K and the measurements were performed in an order of descending temperature. Figure 4.8 shows the measured density which displays a slight increase of 0.6% from 1070 to 1120K and, with the range of experimental error, can be treated as a constant of 7.48 g/cm^3. The measured density of the HgTe melt reported in [10] is also shown in Figure 4.8. Similar to the HgCdTe system, the increasing ZnTe content in the alloys results in a decrease in the density of the ternary melts. However, a maximum in the melt density was not observed here. The $Hg_{0.90}Zn_{0.10}Te$ Te melt displays the behavior of normal thermal expansion at higher temperature range and the data for the $Hg_{0.84}Zn_{0.16}Te$ Te melt are essentially constant in the small measuring temperature range.

As for the hysteresis seen in the measured densities of the $Hg_{0.90}Zn_{0.10}Te$ sample, similar behavior was also observed during viscosity measurements in the HgZnTe melt which will be presented later [27]. Possible mechanisms for this observed phenomenon might be attributed to the macroscopic or microscopic inhomogeneities. The macroscopic inhomogeneity can be present, for instance, due to (1) insufficient mixing during material preparation and (2) small size bubbles formation in the melt. More likely, the nature of the effect can be microscopic, such as subcritical clusters of the second phase [28] or the formation of associated molecular species [29,30] in the melt. Any changes in the temperature will induce microscopic reactions which cause the redistribution in the cluster size, or molecular species, and their composition. This process is diffusion controlled and can be rather slow.

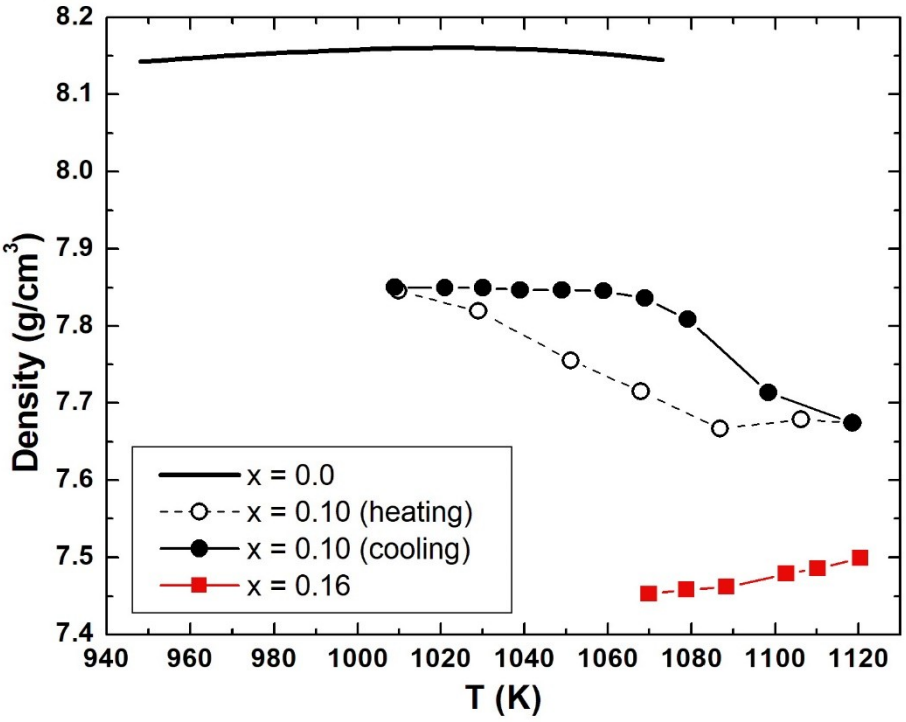

Figure 4.8. Measured density of $Hg_{1-x}Zn_xTe$ melts as functions of temperature.

The major error in the measured density of the melts came from the error in determining the liquid meniscus height. The shape of the meniscus was, most of the time, concave (toward the liquid) and an average level was measured. For the ampoules used here (with an approximated melt volume of 5.9cm^3) an error of 1mm in the measured meniscus height results in an error of 0.12% in the measured volume and the corresponding error in density. The contribution from thermal expansion of the fused silica crucibles to the measured melt volumes was found to be negligible.

References:

[1] V. M. Glazov and L. M. Pavlova, Thermochimica Acta 314 (1998) 265.
[2] V. M. Glazov and L. M. Pavlova, S. V. Stankus, J. Chim. Phys. 94 (1997) 1816.
[3] V. M. Glazov and L. M. Pavlova, J. Cryst. Growth 184/185 (1998) 1253.
[4] Ching-Hua Su, Yi-Gao Sha, K. Mazuruk and S. L. Lehoczky, J. Appl. Phys. 80 (1996) 137.
[5] D. Chandra and L. R. Holland, J. Vac. Sci. Technol. A 1 (1983) 1620.
[6] V. M. Glazov,S. N. Chizhevshaya and N. N. Glagoleva, *Liquid Semiconductors*, Plenum7ress, New York, (1969)
[7] H. A. Bowman, R. M. Schooner, and M. W. Jones, J. Res. Nat. Bur. Stand. (U.S.) 71C (1967) 179.
[8] R. Sosman, *The properties of silica*. The Chemical Catalog, Rutger State University (1965)
[9] C. Li, R. N. Scripa, H. Ban, B. Lin, Ching-Hua Su and S. L. Lehoczky, J. Non-Crystalline Solids 351 (2005) 1179.
[10] C. Li, Ching-Hua Su, S.L. Lehoczky, R. N. Scripa, H. Ban, and B. Lin, J. Non-Crystalline Solids 391 (2014) 54.
[11] Ching-Hua Su, S. L. Lehoczky, and F. R. Szofran, J. Appl. Phys., 60 (1986) 3777.
[12] C. Li, Ching-Hua Su, S. L. Lehoczky, R. N. Scripa, B. Lin and H. Ban, J. Appl. Phys. 97 (2005) 083513.
[13] H. Thurn and J. Ruska, J. Non-Cryst. Solids 22 (1976) 331.
[14] Y. Tsuchiya and E. F. W. Seymour, J. Phys. C 15 (1982) L687.
[15] A. Menelle, R. Bellissent, and A. M. Flank, Europhys. Kett. 4 (1987) 705.
[16] G. Tourand and M. Breuil C. R. Acad. Sci., Paris B270 (1970) 109.
[17] B. Cabane and C. Froidevaux, Phys. Lett. 29A (1969) 512.
[18] W. W. Warren Jr., Phys. Rev. B 6 (1972) 2522.
[19] B. Cabane and J. Friedel, J. Physique 32 (1971) 73.
[20] M. H. Cohen and J. Jortner, Phys. Rev. B 13 (1976) 5255.
[21] M. H. Cohen and J. Jortner, Phys. Rev. Lett. 30 (15) (1973) 699.
[22] M. H. Cohen and J. Jortner, Phys. Rev. Lett. 30 (15) (1973) 696.
[23] M. H. Cohen and J. Jortner, Phys. Rev. A 10 (1974) 978.
[24] C. Li, Ph.D. dissertation "*Thermophysical properties of Te, HgTe and $Hg_{1-X}Cd_XTe$ melts*" University of Alabama at Birmingham (2003).
[25] D. Chandra, Phys. Rev. Lett. B 31 (1985) 7206.
[26] F. R. Szofran and S.L Lehoczky, J. Electron. Mater. 10 (1981) 1131.
[27] K. Mazuruk, Ching-Hua Su, Yi-Gao Sha and S. L. Lehoczky, J. Appl. Phys. 79 (1996) 9080.

[28] V. I. Yukalov, Phys. Rep. 208, (1991) 395.
[29] R. F. Brebrick, Ching-Hua Su, and Pok-Kai Liao, in *Semiconductors and Semimetals,* edited by R. K. Willardson and A. C. Beer, Academic, New York (1983), Vol. 19, Chap. 3
[30] T.-C. Yu and R. F. Brebrick, J. Phase Equilib. 13 (1992) 476.

Chapter 5
Viscosity and Electrical Conductivity Measurements and Results

Abstract: The viscosities of Te, HgTe, $Hg_{0.9}Cd_{0.1}Te$, $Hg_{0.8}Cd_{0.2}Te$, and $Hg_{0.84}Zn_{0.16}Te$ melts were measured. Earlier in the research, the viscosities of HgTe, $Hg_{0.8}Cd_{0.2}Te$ and $Hg_{0.84}Zn_{0.16}Te$ melts have been measured by an oscillating-cup (OC) viscometer. However, the long duration for the measurements by OC, approximately an hour of continuous data collection, prevented the studies of systems with shorter relaxation time. Therefore, a novel transient torque viscometer (TTV) was developed to rapidly measure the viscosity by creating a rotating flow of the melt in the presence of a uniform rotating magnetic field (RMF). The measured transient rotation of the ampoule can be used to determine the viscosity of the melt. Because this transient process finishes in very short time, the required measurements can be completed within two minutes. More importantly, with the Lorentz force introduced by the RMF to the melt, the electrical conductivity can also be simultaneously measured as the torque that induced by the interaction between the RMF and the melt is a linear function of electrical conductivity of the melt. Then the viscosity of Te, HgTe, $Hg_{0.9}Cd_{0.1}Te$ and $Hg_{0.8}Cd_{0.2}Te$ melts and the electrical conductivity of the solids and melts of Te, HgTe, $Hg_{0.9}Cd_{0.1}Te$ and $Hg_{0.8}Cd_{0.2}Te$ were measured by TTV. The measured viscosity by TTV showed more consistency and less scattering comparing to the data obtained from the OC method. The theoretical analyses on the viscosity data of Te melt indicate a structural transition occurring in the liquid at 873K, about 150K above its melting point, which is consistent with the finding on the density of the liquid Te given in Chapter 4. The analyses of the measured viscosity on the melts of HgTe, $Hg_{0.9}Cd_{0.1}Te$ and $Hg_{0.8}Cd_{0.2}Te$ implies a structural transition approximately at 1078K and 1066K, respectively, for HgTe and $Hg_{0.9}Cd_{0.1}Te$ and no structural transition in the measured temperature range for the $Hg_{0.8}Cd_{0.2}Te$ melt. The measured electrical conductivity of the solids indicated a characteristic of metals or degenerate semiconductors. Above the melting point of HgTe and the solidus temperatures of $Hg_{0.9}Cd_{0.1}Te$ and $Hg_{0.8}Cd_{0.2}Te$, the measured electrical conductivity increases with increasing temperature, indicating a semiconductor-like behavior. As the temperature increasing, the measured electrical conductivity started to reach saturated values, implying a metallic behavior. The time relaxation behavior was studied by monitoring viscosity and electrical conductivity after rapidly lowering the sample temperature after long time soaking at elevated temperature. Two samples out of these melts, $Hg_{0.84}Zn_{0.16}Te$ and $Hg_{0.8}Cd_{0.2}Te$, showed relaxation behavior although their trends were different. During the relaxation, the viscosity of the $Hg_{0.84}Zn_{0.16}Te$ melt continuously increased by about 50% to reach its steady state value after 120 hrs whereas the viscosity for the $Hg_{0.8}Cd_{0.2}Te$ melt went through a maximum and then decreased 62% to its equilibrium value in about 60 hrs. At the same time, the measured electrical conductivity of $Hg_{0.8}Cd_{0.2}Te$ melts initially decreased and reached a minimum at approximately 3.4 hrs then it increased 5% to the equilibrium value after 50 hrs.

Keywords: Viscosity; Electrical conductivity; Oscillating cup viscometer; Transient torque viscometer; Tellurium (Te); Mercury-cadmium-tellurium (Hg-Cd-Te) system; Mercury-zinc-tellurium (Hg-Zn-Te) system

5.1 Introduction

Viscosity and electrical conductivity, besides being important thermophysical properties for semiconductor melts, are often used as indicators for structural transition and phase transformation of the melt because of their strong dependence on the molecular and electronic structure of the melt. For example, the viscosity of molten sulfur varies two orders of magnitude when the S_8 ring structure changes to the S_x chain structure as the temperature increases from 160 to 180°C [1]. Additionally, viscosity and electrical conductivity are the essential input parameters for the numerical simulations of crystal growth of a semiconductor from the melt as well as electromagnetic stirring of the melt. The reliable measurements of the temperature dependence of these thermophysical properties and the understanding of their effects on the melt during crystal growth will help to improve the quality of the semiconductor crystal.

There are two types of techniques commonly used to determine viscosity at elevated temperatures: the capillary and oscillatory methods. The capillary method is frequently used for materials with low vapor pressure [2-5]. For example, the viscosity of gallium was determined with temperatures up to 1100°C using a capillary method [2]. The oscillatory methods measure the viscous damping of a torsional oscillation of which either a solid, suspended by a long wire, is immersed in the liquid or a liquid contained in a vessel is suspended by a wire [6-15]. For the measurements of viscosity of material in elevated pressure condition there were various techniques available [9], but the techniques involved the exposure of the vapor phase above the melt to a cooler parts of the instrument. Hence, in the case of HgTe-based melts, mercury would sublime and condense on the cold section which causes the continuous shift of sample composition and weight as vapor transporting during the measurements. Therefore, a novel oscillating-cup method [16] was introduced in that the sample ampoule was hermetically sealed and maintained under the uniform high-temperature conditions. The instrument has successfully measured the viscosity as a function of temperature for the melts of HgTe, $Hg_{0.8}Cd_{0.2}Te$ and $Hg_{0.84}Zn_{0.16}Te$. However, the long period for the viscosity measurements by the oscillation cup, which typically requires approximately an hour of continuous data collection, prevents the studies of systems with shorter relaxation time. Therefore, a novel transient torque viscometer (TTV) was developed for (1) the rapid measurement of the viscosity and (2) the simultaneous measurements of electrical conductivity of a toxic, high vapor pressure melt at elevated temperatures [17,18].

The definition of viscosity can be extracted from Newton's equation which states that when applying a force to a Newtonian fluid in x-direction, the shear force (F/A) is proportional to the rate of shear deformation in y-direction (dv_y/dy), or the change of the flow velocity, v_y, along y-direction, with the constant being viscosity (μ):

$$\frac{F}{A} = \mu \frac{dv_y}{dy} \tag{5.1}$$

The left-hand side of Eq.(5.1), the shear stress is defined as the force applied to the plate divided by the area of the plate with the unit of N/m^2, or pascal [Pa].

Basically, viscosity is a measure of resistance of a fluid to flow, i.e., its rate of deformation. The SI unit of viscosity is pascal-second (Pa-s), and another common unit of viscosity is dyne second per square centimeter (dyne-s/cm^2), also known as poise with the conversion rate of 1Pa-s = 10poise. This viscosity is usually called absolute viscosity or dynamic viscosity and there is another measured quantity for viscosity, i.e., the kinematic viscosity, ν, which came from the frequently used instrument of capillary viscometer. It is a measure of resistance for a fluid to flow under the environment of gravity and can be converted from μ as:

$$\nu = \frac{\mu}{\rho} \tag{5.2}$$

where ρ is the density of the fluid. The SI unit of kinematic viscosity is m^2/s and sometimes in this book will be presented in the unit of cm^2/s, also known as Stokes, with the conversion ratio of $1m^2/s = 1x10^4 cm^2/s$.

5.2 Oscillating-cup Viscometer and Results

5.2.1 Experimental [16]. In this setup, as shown schematically in Figure 5.1, the sample was sealed under vacuum inside a fused silica ampoule with a flat bottom. A silica rod connects the ampoule to a flywheel, the moment of inertia of which can be adjusted with precision-machined brass rings (inertia rings) that fit on a central shaft. The flywheel is suspended with a hardened steel wire (0.24mm diameter) from a strain gauge assembly, which consists of four stainless steel foil springs (5.5x22x0.07mm) stretching between the top and bottom flange. Each foil spring has a strain gauge (Omega, model HBM 6/120 LY 11) glued to it. The torsional motion is recorded through the signal arising in a bridge arrangement with a strain gauge amplifier (Omega, model DMD 465) on the deformation of the strain gauges. With data collection in a PC, the torsional amplitudes of the flywheel/ampoule as small as fractions of degrees can be recorded. For the manual induction of torsional oscillations, a shaft on the top flange of the strain gauge assembly is fed through the enclosure. The lower half of the inconel tube, which contains the fused silica ampoule, is inserted inside a three-zone furnace. The temperature non-uniformity along the ampoule is within $\pm 2^oC$. The temperature of the metal tubing that houses the suspension wire and strain gage assembly is maintained at 22 ± 2^oC, thus the spring constant remained the same during the viscosity measurements. During the operation of the measurements, when the cup is released with an initial angular deflection, the torsional motion will oscillate along the axis of the ampoule. The viscous fluid inside the cup generates a damping force on the inner wall of the cup. This damping force increases the effective moment of the system, which results in an increase in the period and a decay of the amplitude of the oscillation. The fluid viscosity can be calculated from the logarithmic decrement of the amplitude of the angular displacement.

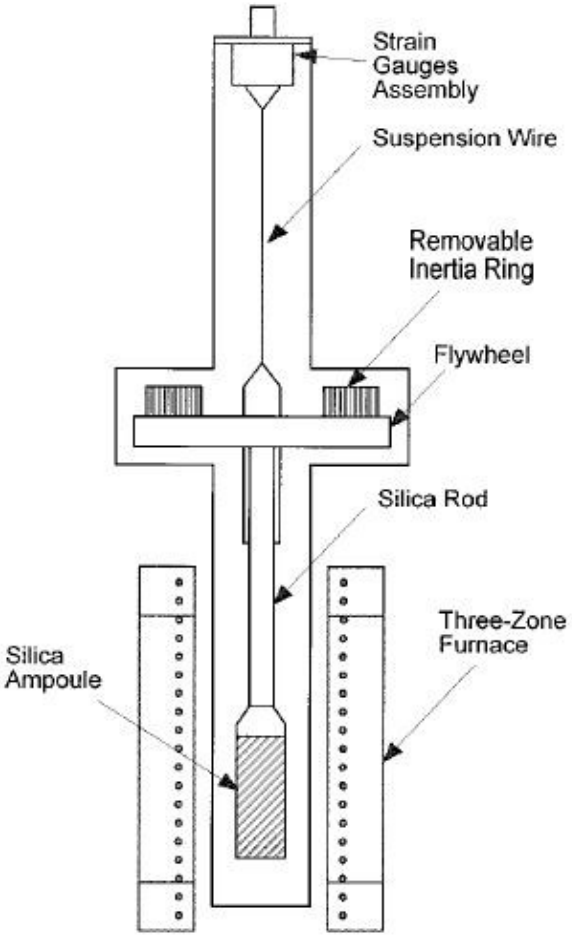

Figure 5.1 The schematics of the oscillating-cup viscometer.

With the oscillation periods of 5-10 seconds, data acquisition rate of ten readings per second was employed. The measured oscillation angles were fitted with four parameters to the function form of $a_0+a_1\sin(\omega t+\Phi)$. The logarithm of the determined amplitudes, a_1, was then plotted vs. time, which exhibited a strictly exponential decay as illustrated for one case in Figure 5.2. A well-defined logarithmic decrement Δ can be obtained from the slope p of the straight line as $\Delta = 2\pi p/\omega$. For the purpose of verification, the kinematic viscosity data were measured on Ga melt from 60 to 815°C using this novel oscillating-cup viscometer. By comparing the data with previous results [19] the estimated uncertainty of the measurements is <5%. The measurements were then applied to the HgTe melt from 700 to 790°C, the $Hg_{0.8}Cd_{0.2}Te$ melt above the liquidus from 790 to 850°C and $Hg_{0.84}Zn_{0.16}Te$ from 770 to 850°C [20].

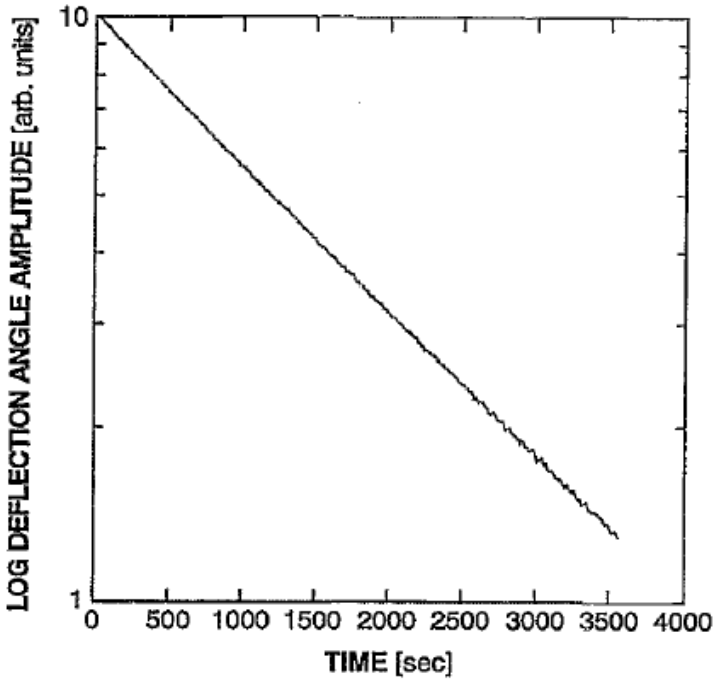

Figure 5.2. Plot of log oscillation amplitude vs. measurement time (taken from Figure 2 of Ref. [20]).

5.2.2 Results and discussions of HgTe melt. Stoichiometric amounts of Hg (74.138 g, Johnson Matthey, seven nines grade) and of Te (47.160 g, Johnson Matthey, six nines grade) were loaded into a cleaned and baked fused silica ampoule. The height of the liquid was estimated from the density reported in Chapter 4 to be 11.5cm. The sample was homogenized following the procedures described in Chapter 4.2. To minimize the time required for homogenization of the melt during the viscosity measurements, the temperature was initially held at 790°C for several hours. With the melting temperature of 670°C, the viscosity data were then taken during heating from 700 to 790°C then cooling back to 700°C. To ensure equilibrium with the vapor and minimize bubble retention, data were typically recorded after a new temperature had been attained for at least 2hrs. The measured kinematic viscosities are plotted in Figure 5.3 as a function of temperature. The data during heat-up and cool-down were reproduced within 3%.

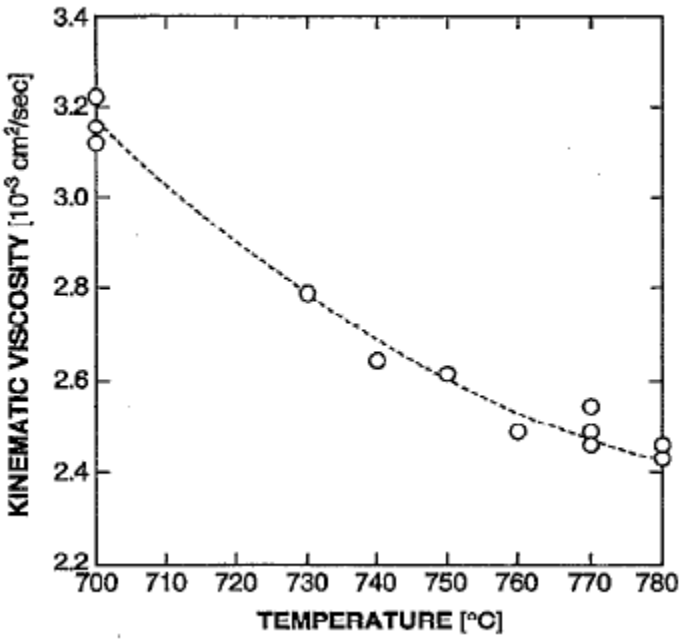

Figure 5.3 The measured kinematic viscosity of HgTe as a function of temperature (taken from Figure 5 of Ref.[20]).

5.2.3 Results and discussions of $Hg_{0.8}C_{0.2}Te$ melt. The $Hg_{0.8}C_{0.2}Te$ sample consisted of 20.810 g Hg, 3.169 g Cd, and 16.725 g Te and was estimated to be 7.1cm in height. From the Hg partial pressures data [21] and the free volume above the melt, an estimate of 0.172 g of Hg sublimed into the vapor phase at elevated temperatures which resulted in a composition of $Hg_{0.79}C_{0.21}Te$ for the melt. The sample was first held for several hours at 850°C, which is about 60°C above the liquidus point for this composition [21]. Then, data were taken during heating from 796 to 850°C then cooling back to 792°C. As shown by the plot in Figure 5.4, the scattering of the data, about 10%, is much higher than that in the HgTe run. This is understandable, since the total mass of the HgCdTe sample was only about one third of the HgTe sample, and the tendency for bubble formation might be more pronounced at these elevated temperatures.

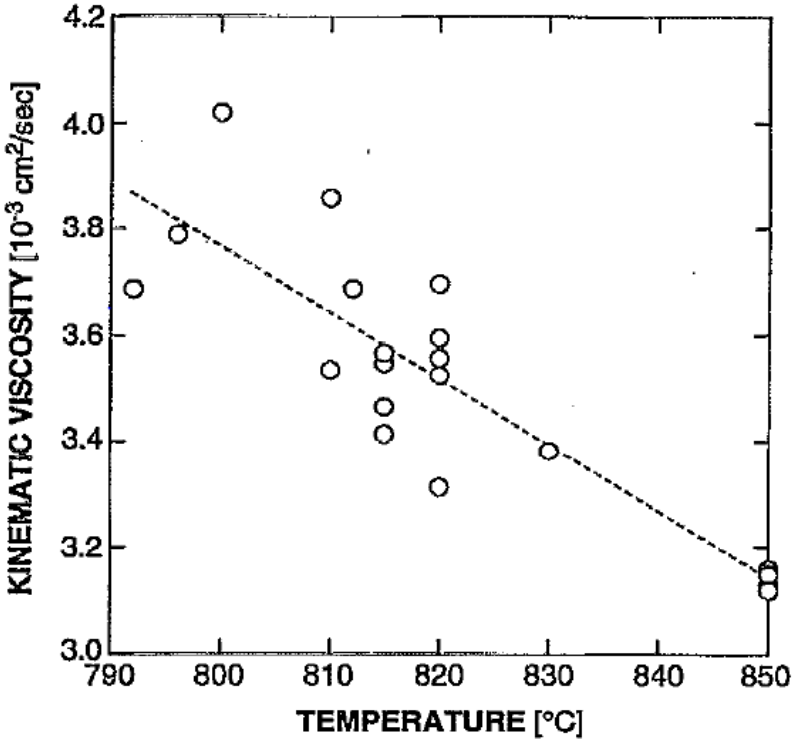

Figure 5.4 The measured kinematic viscosity of $Hg_{0.8}C_{0.2}Te$ as a function of temperature (taken from Figure 6 of Ref.[20]).

5.2.4 Results of $Hg_{0.84}Zn_{0.16}Te$ melt and its relaxation phenomenon. The kinematic viscosity of $Hg_{1-x}Zn_xTe$ pseudo-binary melts with x = 0.16 was also measured by the oscillating cup method. To test the consistency of the measurements, two samples were synthesized in the rocking furnace according to the procedure developed in Ref. [22]. The first sample was prepared by a two-step procedure. After the sample was synthesized, the ampoule was opened and a total of 118.64 g of $Hg_{0.84}Zn_{0.16}Te$ was loaded into the viscosity ampoule which was then sealed under vacuum. As for the second sample, material synthesis and viscosity measurements were conducted in the same ampoule. The following amounts of material were loaded into the second ampoule: 45.100 g of Hg, 34.076 g of Te and 2.793 g of Zn. Two different ampoule dimensions as well as two different operational parameters were employed for the measurements.

The sample temperature was gradually increased to 850°C and held for one day. Viscosity measurements were then taken as temperature decreasing at 5°C intervals, to the liquidus point. The results of early experiments revealed an unexpected time drift of the logarithmic decrement at temperatures near the liquidus point. Consequently, the measurements for the second sample were repeated after two weeks of soaking inside the rocking furnace at 820°C. This treatment did not change the observed behavior. A total of 150 measurements were performed for this study and the high temperature viscosity data were reproducible within 5% as shown in Figure 5.5. The measured viscosity values are about half of that for the HgCdTe

pseudo-binary melt but with different trend as the data go through a maximum around 815°C whereas the data for HgCdTe melts decrease almost linearly as temperatures increase.

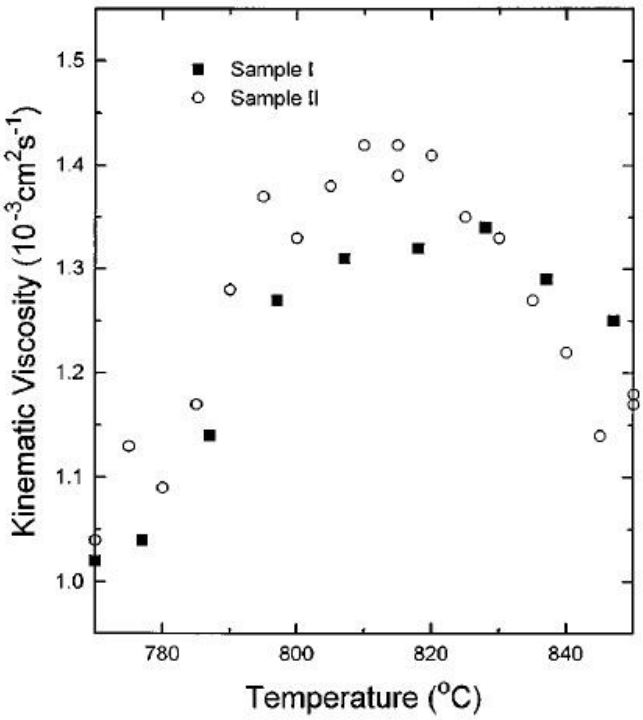

Figure 5.5 The measure kinematic viscosity of $Hg_{0.84}Zn_{0.16}Te$ pseudo-binary melt as a function of temperature (taken from Figure 3 of Ref.[20]).

During the relaxation studies on the viscosity of $Hg_{0.84}Zn_{0.16}Te$ melt, an interesting phenomenon was observed. As displayed in Figure 5.6, a slow relaxation of the measured data occurred when two sets of data were obtained as functions of time after the ampoules were cooled from 850°C and stabilizing at temperatures of 790 and 810°C. While it took one day for the equilibration at 810°C, more than 5 days was needed at 790°C to reach the steady state. As discussed earlier on the density hysteresis of the $Hg_{0.84}Zn_{0.16}Te$ melt, possible mechanisms for this observed relaxation of the measured viscosity during temperature cycling might be attributed to either macroscopic or microscopic inhomogeneities. Macroscopic inhomogeneities can be present, for instance, due to insufficient mixing during material preparation. Any local departure from stoichiometry will significantly change the viscosity, as it has a cusp-like sharp peak near the stoichiometric composition [23]. Also, bubble formation in the melt may cause significant effects. The nature of the effect can also be microscopic. Equilibrium density and composition fluctuations near the liquidus point can be qualitatively different from those at higher temperatures, i.e., different coordination number or subcritical clusters of a second phase can be present [24]. Noting that the group VI elements tend to polymerize when molten, it was also proposed that the enhancement of viscosity was the results of the slow formation of the Te atom chains, or the linear Te n-mers [25]. Any changes in the temperature will induce redistribution in the volume fractions of domains with different coordination numbers or the heterogeneous

cluster sizes and its composition. The time scale of the transition of coordination number or hetero-phase fluctuations can be quite long. On the other hand, recent x-ray studies of several binary metallic systems revealed a profound long lasting memory effect of the melt microstructure in relation to its thermal history [26]. The measured viscosity of some II–VI semiconductor compounds revealed a sharp increase in viscosity near the melting point also indicating the presence of some ordering [8].

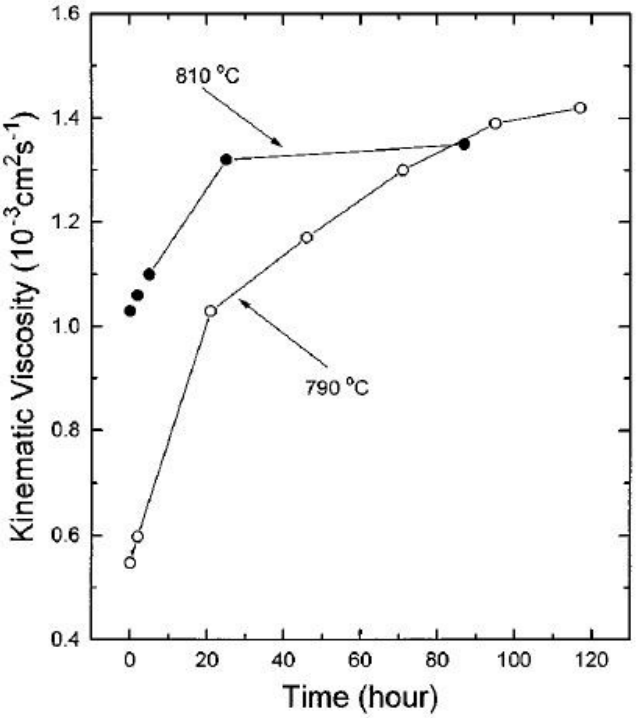

Figure 5.6 Relaxation phenomena of the kinematic viscosity after the $Hg_{0.84}Zn_{0.16}Te$ melts were cooled from 850°C to the prescribed temperatures, 810 and 790°C (taken from Figure 4 of Ref. [20]).

5.3. Transient torque viscometer (TTV)

5.3.1 Experimental setup. The long period for the viscosity measurements by the oscillation cup method, which typically requires approximately an hour of continuous data collection, prevents the studies of systems with shorter relaxation time. Therefore, a novel transient torque viscometer (TTV) was developed to rapidly measure the viscosity and, at the same time, to perform the electrical conductivity measurements of toxic, high vapor pressure melts at elevated temperatures [17,18]. The setup of TTV apparatus is similar to that of the oscillation cup viscometer, except the incorporation of a uniform rotating magnetic field (RMF) generated by electromagnets. The RMF creates a rotating flow of the melt from its motionless initial state and causes the ampoule to rotate around its axis with the torsional force to counter balance the viscous force from the fluid flow. The measured transient rotation of the ampoule can be used to determine the viscosity of the melt. Because this transient process finishes in truly short time, the required measurements can be completed in two minutes. This method

significantly reduces the measurement time as compared to other non-intrusive techniques such as the OC method. More importantly, with the Lorentz force introduced by the RMF to the melt in TTV, the electrical conductivity can also be simultaneously measured. According to Braunbeck [27], the torque that induced by the interaction between the RMF and the melt is a linear function of electrical conductivity of the melt if the proper magnetic field and sample dimensions were selected.

A schematic diagram of the TTV, without the data acquisition system, is shown in Figure 5.7. The viscometer consists of a set of electromagnets which provides a uniform RMF, a power supply which controls the strength and frequency of the RMF, a quartz fiber that suspends the ampoule containing the sample in the center of the RMF, a furnace capable of heating the sample up to 900°C, a MicroE rotary encoder system which measures the deflection angle of the ampoule with a resolution of approximately 2.7×10^{-7} degree, a data acquisition system which records the deflection angle, and a vacuum system which eliminates air flow disturbances and provides safety protection in case of ampoule failure. The RMF is generated by a set of electromagnets with each electromagnet consists of a series of coils placed in the stator core and connects to form 3 phase Y-connection windings. A Pacific 330-AMX series power supply is used to provide power for each phase. The power supply is capable of separately adjusting the voltages to each phase in order to obtain a uniform field at the center of the electromagnets. The furnace is made of a ceramic outer shell to allow magnetic field penetration and its heating elements are wound longitudinally to minimize the effect of the magnetic field generated by the heating element. The pictures of the TTV and a sample ampoule are shown in Figure 5.8.

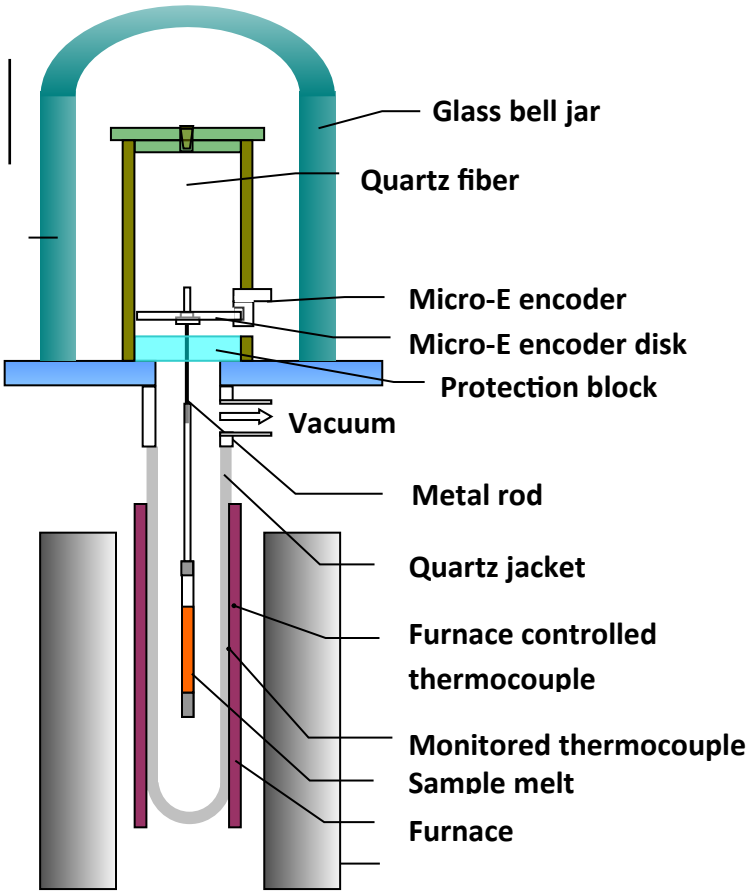

Electromagnets

Figure 5.7. Schematic diagram of the transient torque viscometer (TTV).

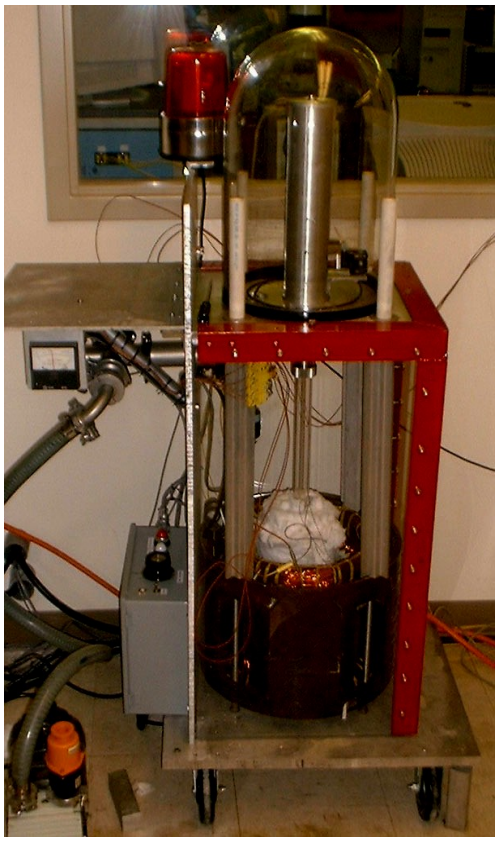

(a)

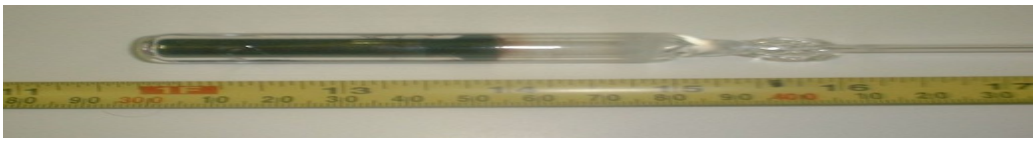

(b)

Figure 5.8 Pictures of (a) the transient torque viscometer and (b) the ampoule with sample.

Theoretically, there are two physically interacting systems involved in the TTV: a torsional oscillation system consisting of the ampoule assembly suspended by the fiber, and the liquid flow driven by the RMF. The interaction between the two systems is on their interface or boundary: the viscous shear of the liquid exerts a torque on the ampoule inner wall under the no-slip boundary condition for the liquid. These two systems can be described by their respective governing equations. Firstly, because the height of

the fluid column is much larger than its diameter, the liquid flow, created by the Lorenz body force, can be treated as a two-dimensional planar and axisymmetric flow with the Navier–Stokes equation for the laminar flow having only one component, the tangential fluid velocity. Secondly, the deflecting angle of the ampoule starts from zero, the initial motionless fluid, and follows the torsional oscillation equation when the torque exerted on the ampoule wall by the liquid flow inside the ampoule after the RMF is turned on. The detailed equations governed the interaction between the two systems are given in Ref. [17,18].

For the verification of viscosity measurement and the calibration of electrical conductivity measurement, an experimental run was performed on pure mercury at 28.2°C, or 301.3K, and the measured deflection angle as a function of time is shown in Figure 5.9. Initially, the sample and the ampoule were at rest at the equilibrium position of 0 degree angle. The RMF of 71 Gauss was turned on at about the time scale of 80 seconds and the ampoule immediately responded to the mercury flow caused by the Lorentz force. This transient process was superimposed with an oscillatory motion. The transient period lasted for about 30 seconds, after which the flow was no longer accelerated by the RMF and the ampoule oscillated around the new equilibrium position of – 1.03 degrees. At the time about 186 seconds, the RMF was turned off. After another 30 seconds of transient, the flow was diminished, and the ampoule oscillated around the original equilibrium position at 0 degree angle similar to the experiments in the case of oscillating-cup given in section 5.2. The two unknown variables, the viscosity and the nominal Lorentz force, were obtained by fitting the theoretical solution to the experimental data. Figure 5.9 shows the excellent agreement between the theory (solid line) and the dotted data points. In this specific case, the measured kinematic viscosity of 1.122×10^{-7} m^2/s is 0.09% higher than the published value [28]. Using the Lorenz force derived from this run and the reported value of electrical conductivity of 1.051×10^{6} ohm^{-1}-m^{-1}, measured using the four-probe method [29], this data was adopted as the calibration point. Using this calibration, the electrical conductivity measured on mercury at another temperature of 78.7°C, or 351.8K, showed a difference of 1.13% comparing to the published value [29].

For this transient torque measurement, the transient flow induced by the RMF reached the end of the transient process in about 40 sec, i.e., from the time scale of 80 seconds to 120 seconds, which shortened the measuring time to about 1% of that for the OC method. The data during the transient process were sufficient for the extraction of viscosity and electrical conductivity. The system then needed over an hour to return to its motionless state. A procedure was developed to apply the RMF opposite to the ampoule oscillation direction to rapidly damp the system oscillation and another transient torque measurement can be performed at 5 minute intervals. The TTV can also be used as an oscillation cup viscometer. The experimental data in Figure 5.9 from 186 seconds and on is actually oscillation damping by the fluid without RMF stirring. The logarithmic decrement can be obtained to calculate the viscosity of the fluid.

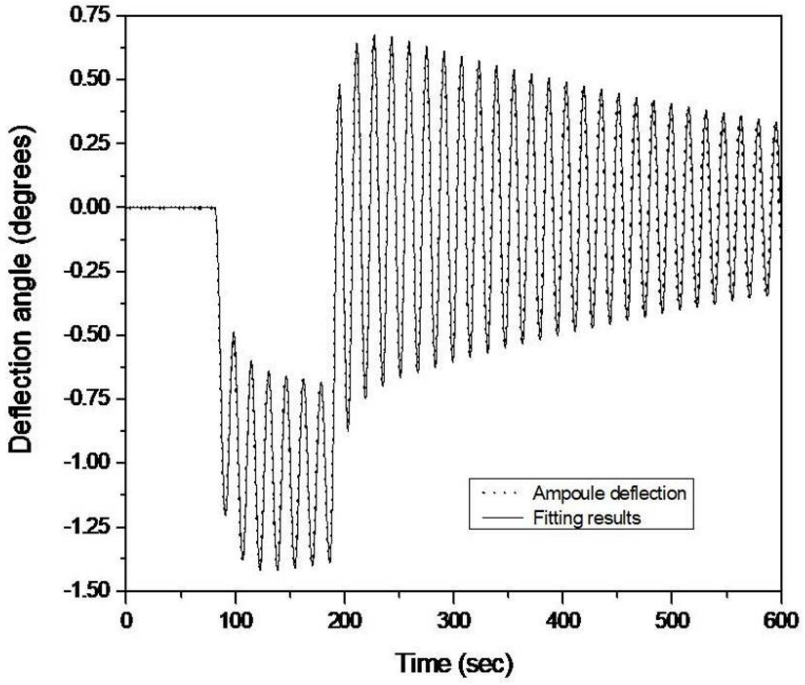

Figure 5.9. Measured deflection angle vs. time for a mercury sample at 28.2°C. The dots represent the experimental data, and the solid line is the best numerical fit to the governing equations (taken from Figure 3 of Ref.[17]).

With the verification of viscosity and the calibration of electrical conductivity by the Hg sample, two ampoules with pure Te sample, one ampoule each for HgTe, $Hg_{0.9}Cd_{0.1}Te$ and $Hg_{0.8}Cd_{0.2}Te$ were prepared for the TTV measurements. All of the HgCdTe samples for the TTV measurements were homogenized in a similar method as reported early in Chapter 4 for the density measurements with the masses of the elements in each of these ampoules listed in Table 5.1.

Table 5.1 Masses of the elements in the Te, HgTe, and $Hg_{1-x}Cd_xTe$ ampoules for the electrical conductivity and viscosity measurements.

Sample	Hg (g)	Te (g)	Cd (g)
Te (sample 1)	-	17.94673	-
Te (sample 2)	-	18.89443	-
HgTe	14.03774	8.92898	-
$Hg_{1-x}Cd_xTe$ (x = 0.1)	14.41327	10.19109	0.89760
$Hg_{1-x}Cd_xTe$ (x = 0.2)	13.41403	10.66649	1.87941

The overall experimental errors of the electrical conductivity and viscosity measurement were estimated using the uncertainties associated with each experimental parameter. The largest error of the measurement was the background noise of the ampoule oscillation. With a 0.55% uncertainty of the noise, the resulting error for the viscosity determination was approximately 3.6%. However, for the same noise, the error for the conductivity is estimated to be only 0.55%. The uncertainty in other parameters accumulated to approximately 1% error in the final result regarding viscosity and conductivity. The overall estimated errors for viscosity and electrical conductivity are approximately 4.6% and 1.6%, respectively.

5.3.2 Results and discussions on Te melt and solid

5.3.2.1 Viscosity. Figure 5.10 shows the kinematic viscosity of liquid Te as a function of temperature [30] together with the values measured by Glazov et al. using the OC method [8] for comparison. The kinematic viscosity of two liquid Te samples was measured from 10K above the melting point of 723K to 1170K. Each kinematic viscosity measurement was carried out after the Te sample was heated or cooled to the prescribed temperature and held there for at least 4 hrs to ensure that the liquid Te was in the equilibrium state. Both sets of data, i.e., measurements by TTV and OC, show similar trend with the data from the OC [8] slightly higher.

To have some perspectives of the value of the measured viscosity, during the verification of the TTV instrument, the viscosity of Hg measured at room temperature, 28.2°C, was $1.122\times10^{-7}m^2/s$ comparing to $3.56\times10^{-7}m^2/s$ for Te just above the melting point and about $1.2\times10^{-7}m^2/s$ at 1120K.

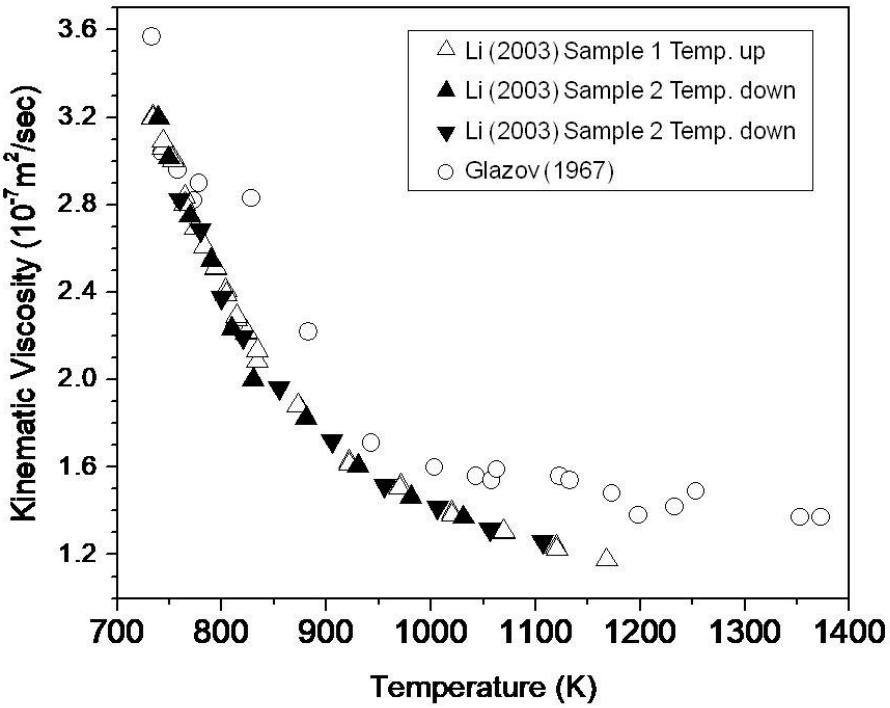

Figure 5.10 Temperature dependence of kinematic viscosity of liquid Te from Li [30] and Glazov et al. [8] (taken from Figure 4 of Ref.[30]).

According to the theory of rate process [31], the free activation energy of the viscous flow F_b can be expressed from the temperature dependence of the kinematic viscosity as:

$$F_b = RT \ln \frac{Mv}{Nh} = H_b - S_b T \quad , \tag{5.3}$$

where ν is the viscosity of the melt, M the molecular weight, N Avogadro's number, h Planck's constant, T the absolute temperature in K, and R the molar gas constant. The free energy F_b can then be expressed in terms of enthalpy H_b and entropy S_b. The equation resembles the expression for the chemical potential of an element in a multi-components system with (Mv/Nh) replacing the chemical activity of the element. Using Eq. (5.3), the calculated free activation energy of the viscous flow in Te liquid as a function of temperature is presented in Figure 5.11. The free activation energy increases slowly as a function of temperature just above the melting point of Te, 723K. At temperatures around 873K, the free activation energy increases more rapidly as a linear function of temperature. The product of the viscosity and molecular weight of the Te melt in the first 150K above its melting point has a rather flat activation energy and the viscosity decreases rapidly. As the temperature getting above 873K, the activation energy increases linearly with temperature and the decreasing rate in the measured viscosity becomes smaller. The difference in the slope of the activation energy, which might have been partially caused by a change in the average molecular weight, is another indication of a structural transition occurring in the liquid at 873K, which is consistent with the previous discussion on the density of the liquid Te given in Chapter 4. Assuming H_b and S_b are constants above 873K, the activation enthalpy and entropy of viscous flow for the Te liquid above 873K was determined to be 13.01kJ/mol, and –18.86J/mol-K, respectively.

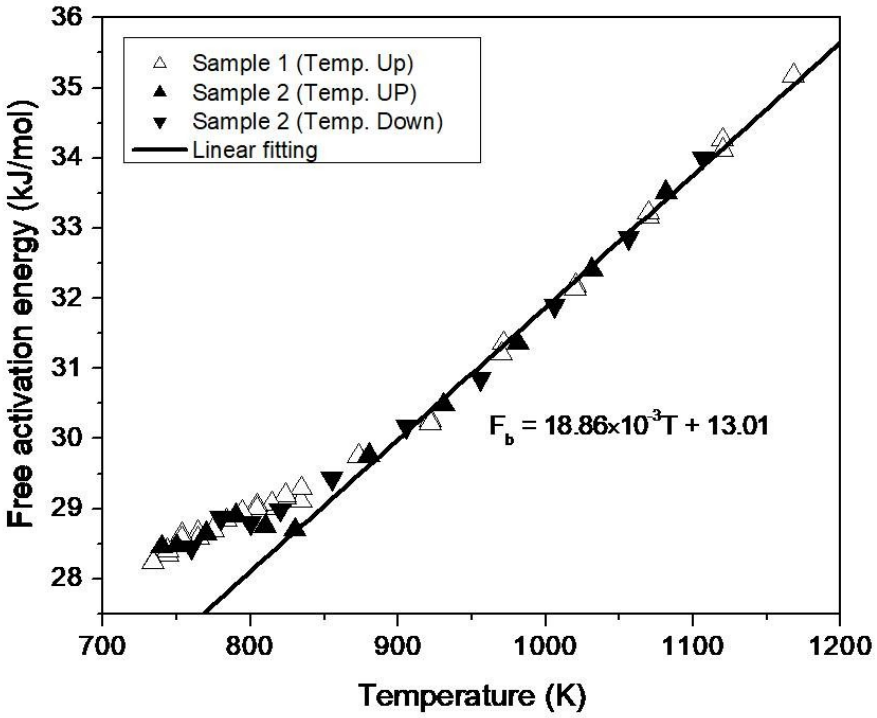

Figure 5.11 Temperature dependence of free activation energy of viscous flow for liquid Te (taken from Figure 5 of Ref.[30]).

In another study, Bachinskii [32] tried to correlate the viscosity to the structure and interaction of a liquid. Based on the assumption that the viscosity of a liquid is governed by the nature of the interaction between the atoms or molecules, Bachinskii's equation states that the reciprocal of the kinematic viscosity is a linear function of its density ρ if the melt structure is homogeneous:

$$\frac{1}{v} = \frac{1}{c} + \frac{b}{c}\rho \tag{5.4}$$

where c and b are constants. It is a simple physical concept that as the density of the melt increases, the resistance to the fluid flow increases which results in higher viscosity (with b negative).

Figure 5.12 shows the plot of the reciprocal of the kinematic viscosity vs. the measured density of liquid tellurium reported earlier in Chapter 4. It shows that the data above 880K can be fitted well by a straight line. As the temperatures getting below 880K, the data start to deviate from the linear line, which implies a structural transition in the liquid Te, i.e., the Te melt starts to maintain a homogeneous structure when the temperature reaches above 880K. The is consistent with the difference in the slope of the activation energy discussed above, indicating a structural transition occurring in the liquid at 873K. It is also consistent with the density results given in Chapter 4 that the measured density of Te melt shows a maximum at 752K. During the

normal thermal expansion, as temperature goes up the inter-atomic/molecular distance increases which causes the density to go down. However, the normal expansion sometimes can be shadowed, when there is a structural rearrangement in the melt, and created a maximum at a lower temperature. Such a structural transition in liquid Te was also observed in the results of neutron scattering experiments [15]. The neutron spectrum showed that the average first coordination number of liquid Te atoms is 2.63 at its melting point which increased to approximately 3 at 873K and stayed at 3 as the temperature was raised to 1073K.

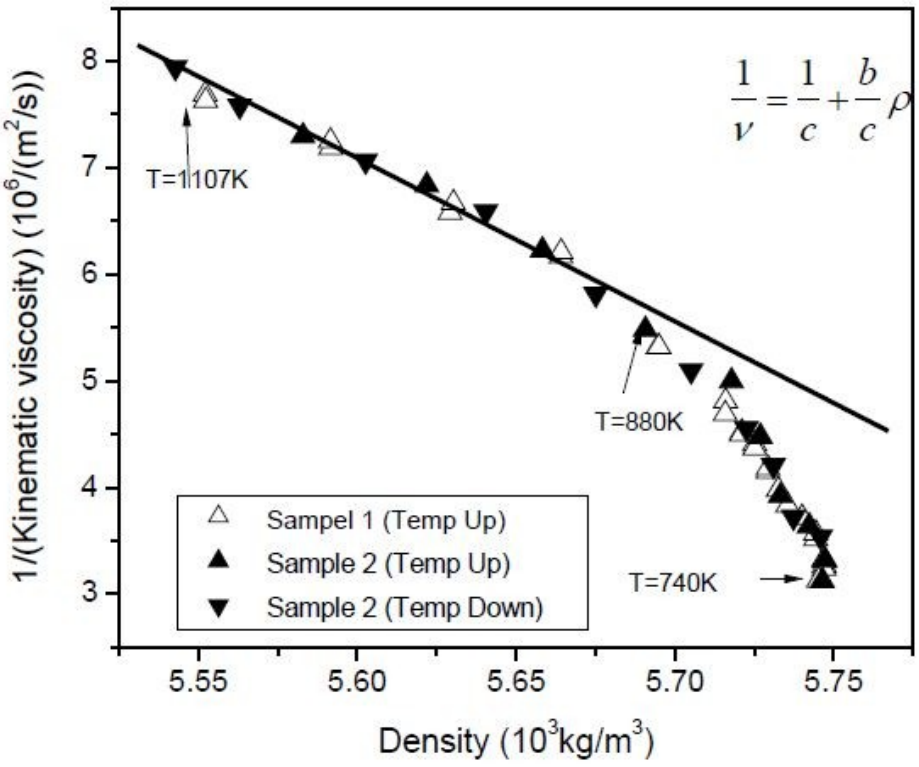

Figure 5.12 Dependence of the reciprocal of the kinematic viscosity on the density of liquid Te (taken from Figure 6 of Ref.[30]).

5.3.2.2 Electrical conductivity. Figure 5.13 shows the measured electrical conductivity of Te melt as a function of temperature between 723 and 1300K. The measured electrical conductivity of liquid Te was about $1.6\times10^5\Omega^{-1}m^{-1}$ just above the melting point and increased to a saturated value of $2.9\times10^5\Omega^{-1}m^{-1}$ at approximately 1000K. For comparison, previously published data for liquid Te by Perron [33,34] using the four-probe method, are also plotted in Figure 5.13 as a solid line which agreed fairly well with the present results below 850K and about 5% lower between 850 to 1180K .

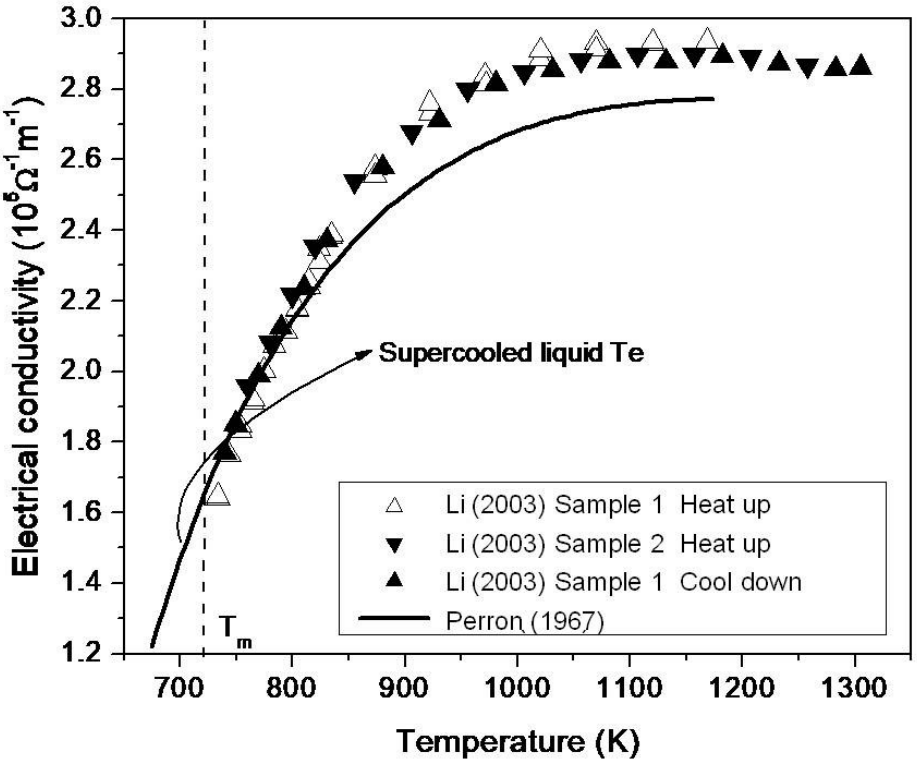

Figure 5.13 Temperature dependence of electrical conductivity of liquid Te from Li [30] and Perron [33] (taken from Figure 49 of Ref.[35])

To have a better understanding on the solid to liquid phase transition, the study has extended to the solid phase of Te by measuring its thermal and electrical conductivity. The sample of Te, 35.6g of 99.99999% purity from 5 N Plus Inc., was loaded into a previously cleaned and baked fused silica ampoule of 20mm O.D. and 16mm I.D. The sample was processed through directional solidification in a vertical tubular furnace with a thermal gradient of about 21°C/cm at the melting temperature of 450°C and a furnace translation rate of 1.0cm/hr. A rectangular prism in the shape of 2.5x2.5x14mm was cut in the middle section of the sample for the electrical conductivity and Seebeck coefficient measurements, which were conducted simultaneously from room temperature to 693K by a ZEM-3 instrument provided by ULVAC-RIKO Inc. The electrical conductivity was determined from ten measured I-V points and the Seebeck coefficient was derived from the values of Seebeck voltages measured over a 6mm distance along the sample length under three different applied thermal gradients.

The measured electrical conductivity of solid Te, σ, are plotted in Figure 5.14 as $\log(\sigma)$ vs. 1000/T(K). The measured values show a big jump at the melting points from $0.9\text{x}10^3$ of the solid to $1.6\text{x}10^5\Omega^{-1}\text{m}^{-1}$ of the liquid phase. As shown in the figure, the data of the solid phase can be fitted well by a straight line as: $\log_{10}\sigma$ (S/cm) = 5.025 – 0.7966(1000/T) which implies that the high purity Te sample shows characteristics of an intrinsic semiconductor. For a non-degenerate semiconductor, assuming that the mobilities of electron and hole are independent of temperature, the electrical conductivity can be expressed by:

$$\sigma = AT^{3/2}\exp(-E_g/2k_BT) \qquad (5.5)$$

where A is a constant, E_g the energy bandgap and k_B the Boltzmann constant ($8.617\text{x}10^{-5}$ eV/K). From the slope of the linear fit, the value of E_g can be derived to be 0.316eV which is a little lower than the reported value of 0.335eV [36] at room temperature. The difference could have been caused by the decrease in the energy bandgap when temperature increases as well as the factor of $T^{3/2}$ in Eq.(5.5).

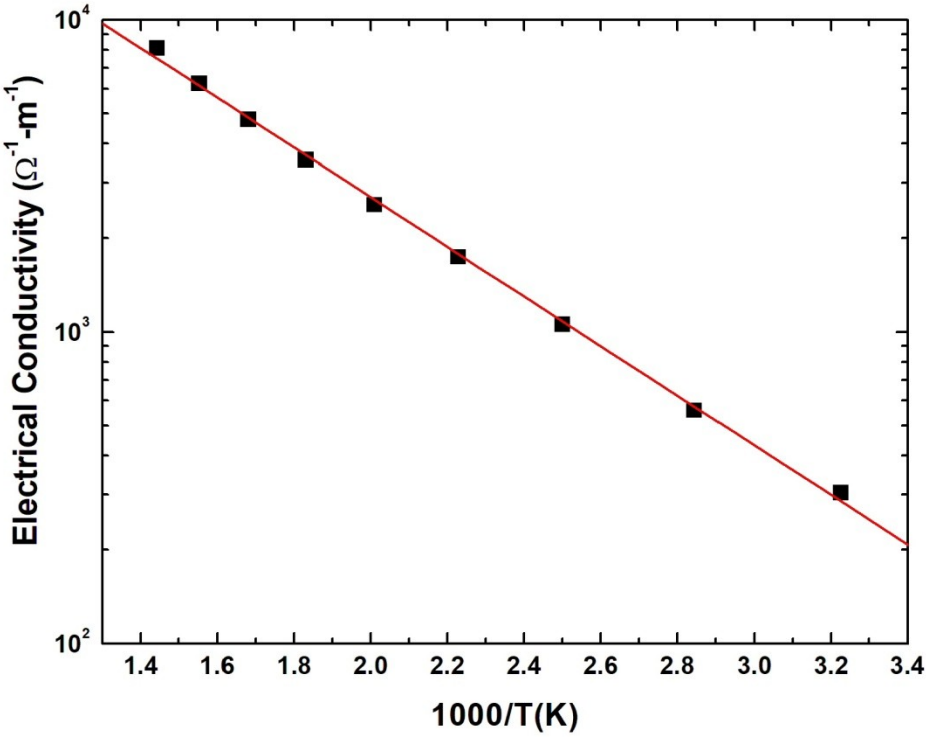

Figure 5.14 The measured electrical conductivity, σ, of Te solid plotted as log(σ) vs. 1000/T(K). The data of the solid phase can be fitted well by a straight line.

To examine the characteristics of the melt, the measured electrical conductivity of both the solid and liquid phase was plotted against 1000/T as shown in Figure 5.15. A red line segment with the same slope, i.e., the same energy bandgap as the solid, was also plotted from the melting point 723K to 833K. After melting, the measured value kept on increasing with the same slope as the solid Te until it reached about 790K when it started to flatten at higher temperatures. This implies that the Te liquid still preserves some of its solid structure after melting till about 65K above the melting temperature. This behavior is consistent with the semiconducting two-fold coordination to metallic three-fold coordination structural transition, observed in the density analysis discussed in Chapter 4 and from the neutron scattering spectra observed by Menelle [37] and Tourand [38], using the effective-medium theory.

Culter's bond orbital model [39,40] stated that the structure of the two-fold coordination regions in the liquid Te is the result from the break-up of the long helical chains upon the melting of solid Te. Based on the neutron results by Tourand [38], the formation of the third covalent bonds introduces large density of states in the valence band according to the bond orbital model. The electrical conductivity increases as a function of temperature resulting from the increase of electrons excited from the large density of states of valence band into the conduction band. When the transformation from a two-fold to a three-fold coordination domain in liquid Te is completed the energy band structure stops to change and the electrical conductivity of liquid Te reaches a saturated value.

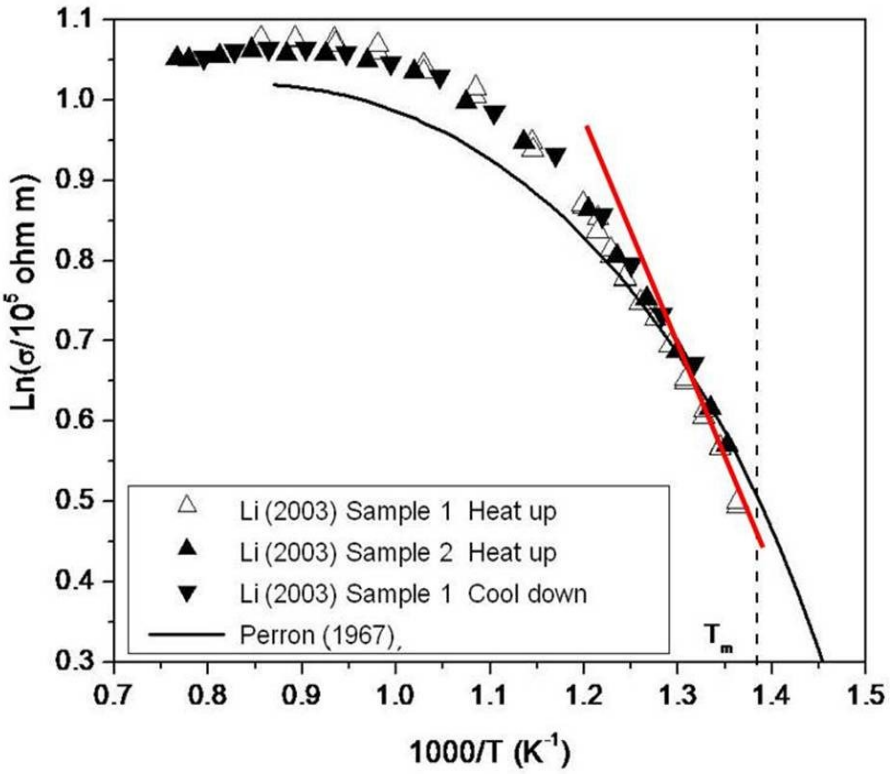

Figure 5.15 Logarithm of the electrical conductivity of liquid Te as a function of reciprocal temperature from Li [30] and Perron [33]. The red line segment has the same slope as that from Te solid shown in Figure 5.14 (data taken from Figure 3 of Ref.[30]).

The time relaxation measurement of the electrical conductivity and viscosity of the Te melt [30] was carried out in the TTV by monitoring the data after the sample was maintained at 1173K for 7 days before it was cooled rapidly to 830K. It took approximately another 0.5 h for the temperature inside the TTV furnace to reach the equilibrium temperature of 830K. The value of the first electrical conductivity measurements were $2.32\times10^5\Omega^{-1}m^{-1}$ as comparing to the equilibrium values of $2.29\times10^5\Omega^{-1}m^{-1}$ measured at 8.3 hrs, which agree well with the steady state values of $2.35\times10^5\Omega^{-1}m^{-1}$ shown in Figures 5.13. With the estimated experimental error, it was concluded that no relaxation behavior in the electrical conductivity was observed after the Te melt was rapidly cooled from 1173 to 830K. However, the measured viscosity of Te melt,

displayed in Figure 5.16 as a function of time, after the melt was quenched needed about 6 hrs for the measured values of viscosity to reach steady state value of $1.9 \times 10^{-7} m^2/s$ [25], agreeing with the data shown in Figure 5.10. Using a simple kinetic scheme for polymerization of tellurium atoms which assuming the rate of reaction for attaching and detaching one Te atom is the same for each step of polymerization, the change of Te viscosity as a function of time was calculated and agrees well with the experimental data as shown in Figure 5.16 [25].

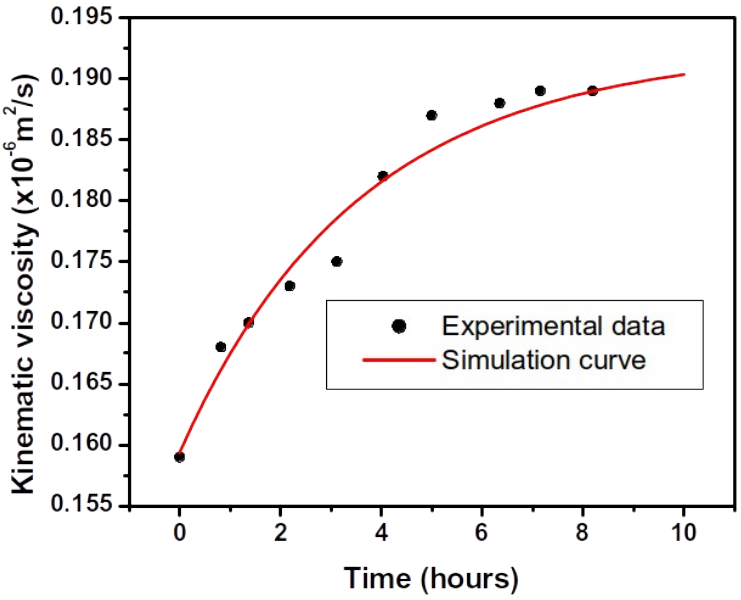

Figure 5.16 The measured viscosity of Te melt as a function of time after it was quenched from 1173 to 830K and the calculated solid line from Ref.[25].

5.3.3 Results and discussions of melts of HgTe, $Hg_{0.1}Cd_{0.9}Te$ and $Hg_{0.2}Cd_{0.8}Te$. The electrical conductivity and viscosity of HgTe, $Hg_{0.1}Cd_{0.9}Te$ [41] and $Hg_{0.2}Cd_{0.8}Te$ [42] were measured by the TTV method.

5.3.3.1. Viscosity. On the measurements of viscosity, the temperature dependence of the viscosity measured for the HgTe melt are shown in Figure 5.17 together with the results [20] from the oscillation cup method. Both viscosity data show similar trends in that the viscosity of the HgTe melt decreased rapidly as the temperature increased. The TTV results were approximately 20% lower than that measured by the OC method between 1040K and 1065K. The two possible reasons for the discrepancies are: (1) the possible Hg bubble formation in the melt during the OC measurements as suggested by Mazuruk et al. [20] and (2) the experimental error of the OC method caused by the airflow around the cup inside the hot furnace. The unstable airflow not only causes high background data noise but also changes the cup damping characteristics during the measurements. The TTV measures the viscosity with the ampoule under a vacuum environment of 10^{-4}Torr, which eliminates the air convection caused by the hot furnace. Also, comparing with the approximated one-hour measurement time needed in the OC method [20], the measurement time with the transient torque method is only about 100 sec,

which further reduced the possibility of additional measurement errors caused by the instability of the system.

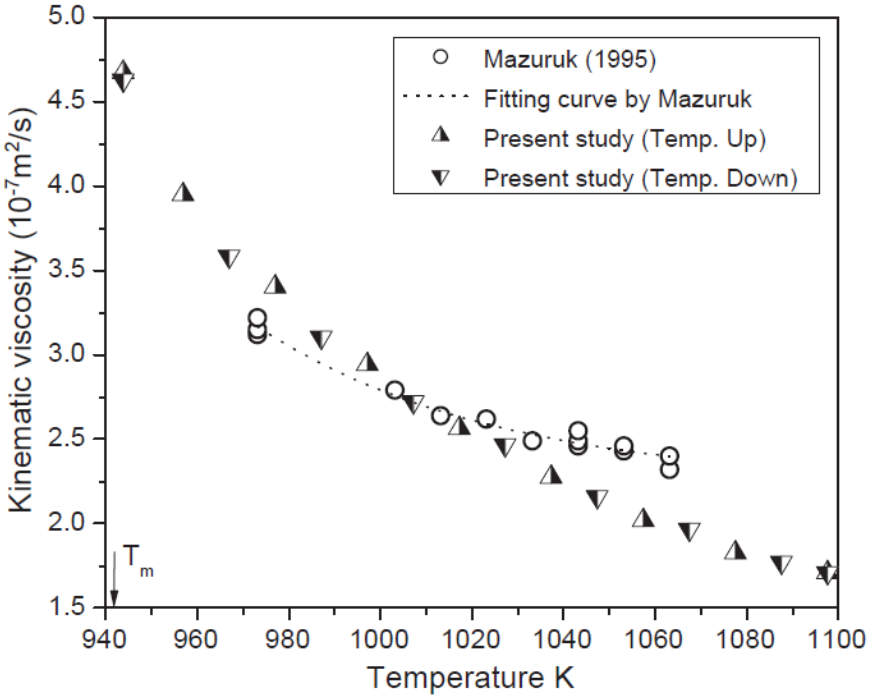

Figure 5.17. Kinematic viscosity of HgTe melt as a function of temperature from Ref.[41] and Mazuruk [20] (taken from Figure 8 of Ref.[41]).

The temperature dependent viscosity of $Hg_{0.8}Cd_{0.2}Te$ melt measured by TTV from Ref. [43], together with the previous results using the OC method [20], are plotted as functions of temperature in Figure 5.18. The viscosity data obtained by TTV showed more consistency and less scattering comparing to the data by the OC method which were approximately 30% higher than the former. The general trends are similar, i.e., the kinematic viscosity of $Hg_{0.8}Cd_{0.2}Te$ melt decreases as the temperature increases. The possible reasons for the discrepancies between these two sets of viscosity data are probably the same as the data for the HgTe melt discussed above.

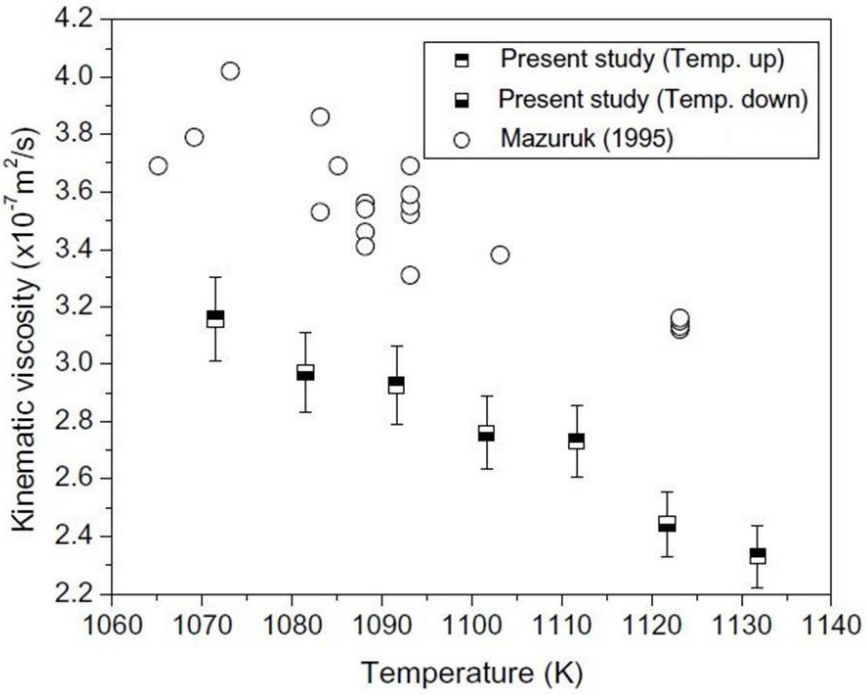

Figure 5.18. Kinematic viscosity of the $Hg_{0.8}Cd_{0.2}Te$ melt as a function of temperature Ref.[42] and Mazuruk et al. [20] (taken from Figure 3 of Ref.[42]).

For a comparison, all of the measured viscosity by the TTV, including the results from the HgTe, $Hg_{0.9}Cd_{0.1}Te$ [41] and $Hg_{0.8}Cd_{0.2}Te$ melts [42], are shown in Figure 5.19. The three sets of data show similar trend as functions of temperature. For a fixed temperature, the increase in the measured viscosity as a function of CdTe content, x, is likely the result from the higher viscosity of the CdTe melt than that of the HgTe melt. For instance, the viscosity reported by Glazov et al. [8] and displayed by Figure 3.1(a) in Chapter 3 shows a viscosity of 0.4 centi-stokes for CdTe at 1100°C, or 1373K, comparing to the value of $1.7x10^{-7}m^2/s$, or 0.17 centi-stokes, for HgTe at 1100K as shown in Figure 5.17 above.

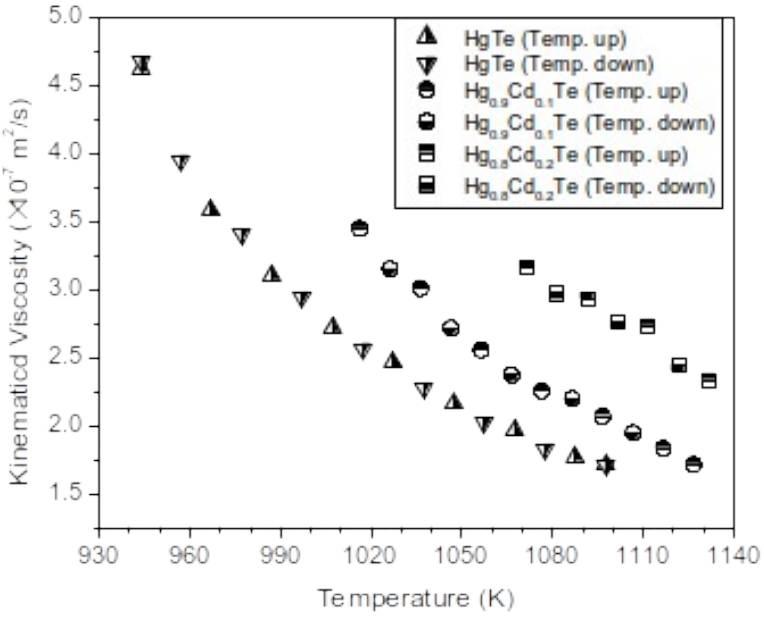

Figure 5.19 Kinematic viscosity of the HgTe, $Hg_{0.9}Cd_{0.1}Te$, and $Hg_{0.8}Cd_{0.2}Te$ melts as functions of temperature measured by TTV (taken from Figure 9 of Ref.[41]).

Using Eyring's theory, the values of F_b in Eq.(5.3) for the HgTe melt are shown in Figure 5.20 as a function of temperature. The deviation of F_b from a linear function just above the melting point, 943K, to 980K is considered to be caused by the transition in the liquid structure at 980K. From a linear fit, the activation enthalpy and entropy of viscous flow for the HgTe melt above 980K was determined to be 51.93kJ/mol and –6.435J/mol-K, respectively. For the $Hg_{1-x}Cd_xTe$ melt, the calculated F_b cannot be fitted by a linear function over the whole temperature range. According to the structural assumption made by Glazov [43] and Chandra [44], there existed at least three or more kinds of structures or species in the low temperature ranges, which eventually transform into a homogeneous structure at high temperature range.

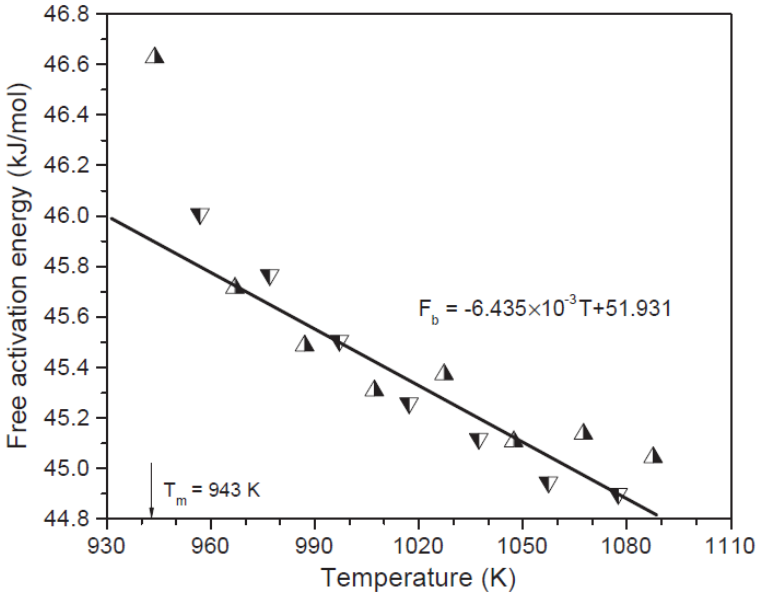

Figure 5.20 Temperature dependence of the free activation energy of viscous flow for the HgTe melt (taken from Figure 10 of Ref.[41]).

Using the Bachinskii theory given in Eq.(5.4), the dependences of the reciprocal of the kinematic viscosity on the density of the HgTe, $Hg_{0.9}Cd_{0.1}Te$ and $Hg_{0.8}Cd_{0.2}Te$ melts were assessed from the viscosity data and the measured density reported in Chapter 4. In Figure 5.21, a large deviation from a straight line of the $1/\nu$ vs. ρ plot for the HgTe melt is an indication of a structural transition in the melt. Similar plots for the $Hg_{0.9}Cd_{0.1}Te$ and $Hg_{0.8}Cd_{0.2}Te$ melts are shown in Figure 5.22 and 5.23, respectively. From the three plots for HgTe, $Hg_{0.9}Cd_{0.1}Te$ and $Hg_{0.8}Cd_{0.2}Te$, the temperatures where the deviations from linear line, or the structural transition, are approximately, 1078, 1066 and 1091K, respectively, although the scattering of the data for the $Hg_{0.8}Cd_{0.2}Te$ melt might suggest that there was no transition in the measured temperature range of the melt.

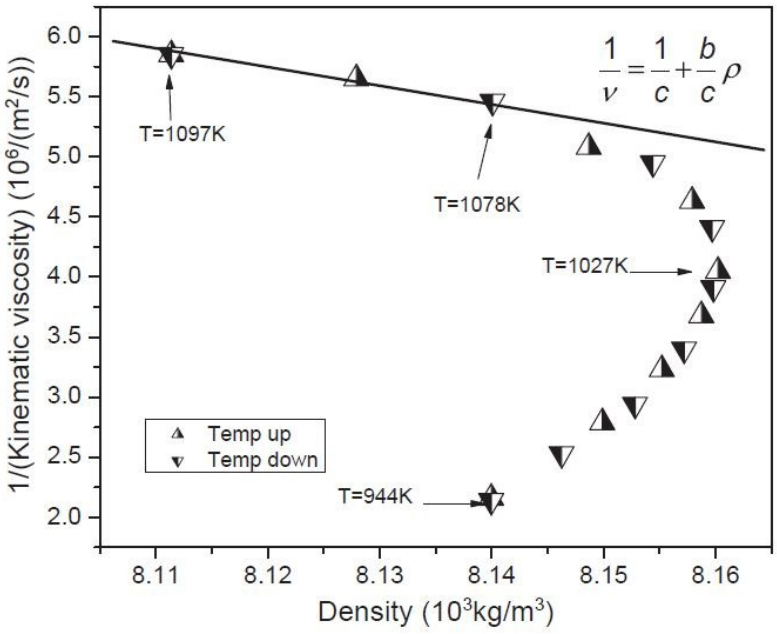

Figure 5.21. Dependence of the reciprocal of the kinematic viscosity on the density of the HgTe melt (taken from Figure 11 of Ref.[41]).

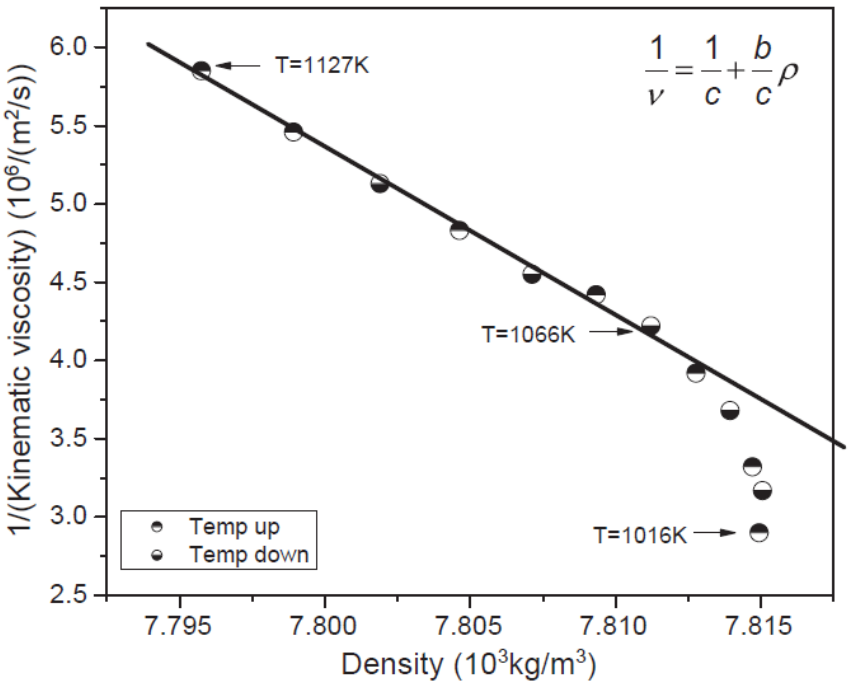

Figure 5.22 Dependence of the reciprocal of the kinematic viscosity on the density of the $Hg_{0.9}Cd_{0.1}Te$ melt (taken from Figure 12 of Ref.[41]).

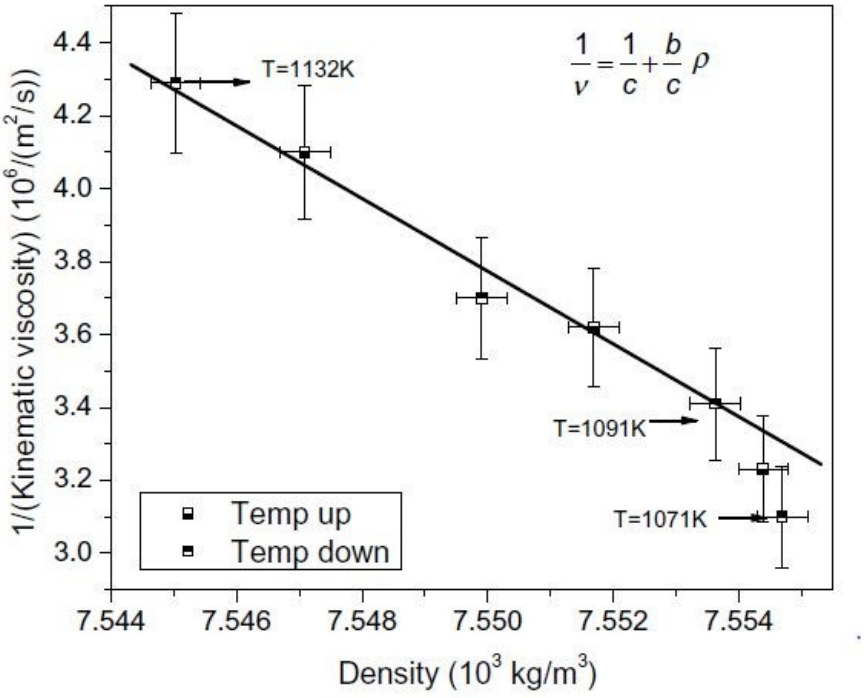

Figure 5.23 Dependence of the reciprocal of the kinematic viscosity on the density of the $Hg_{0.8}Cd_{0.2}Te$ melt (taken from Figure 5 of Ref.[42]).

5.3.3.2. Electrical conductivity. On the measurements of electrical conductivity, the measurements started at 750K, where the samples were in the state of solids. The measured electrical conductivities for the HgTe, $Hg_{0.9}Cd_{0.1}Te$ and $Hg_{0.8}Cd_{0.2}Te$ solids and melts as functions of temperature are shown in Figure 5.24, 5.25 and 5.26, respectively. As shown in all these figures, the trend of the measured electrical conductivity changes drastically at the melting temperatures. By monitoring the breaking temperatures of the electrical conductivity, the melting point of HgTe, $Hg_{0.9}Cd_{0.1}Te$ and $Hg_{0.8}Cd_{0.2}Te$ were determined to be within 1K of the previously reported results [45] measured by the precision differential thermal analysis (DTA).

As shown in the figures, the electrical conductivity in the solid temperature range was either decreasing (for HgTe) or flat as the temperature increasing, which indicated the characteristics of metal, degenerate or extrinsic semiconductors. Above the melting point of HgTe and the solidus temperatures of $Hg_{0.9}Cd_{0.1}Te$ and $Hg_{0.8}Cd_{0.2}Te$, the measured electrical conductivity increases with increasing temperature, indicating a semiconductor-like behavior. The logarithm of the electrical conductivity of the HgTe, $Hg_{0.9}Cd_{0.1}Te$ and $Hg_{0.8}Cd_{0.2}Te$ melts are plotted against 1/T in Figure 5.27 which shows similar trend as that of the Te melt with deviation from linear behavior in the high temperature range. The possible causes are that the energy gaps of the melts change as a function of temperature and/or there is a structural transition in the melts as temperature increasing. According to Gubanov's liquid model [46], the energy gap in liquid semiconductor is approximately constant as a function of temperature, assuming that no structural transition occurs in the melt. Hence, the trend of the electrical conductivity probably is caused by a structural transition in these melts.

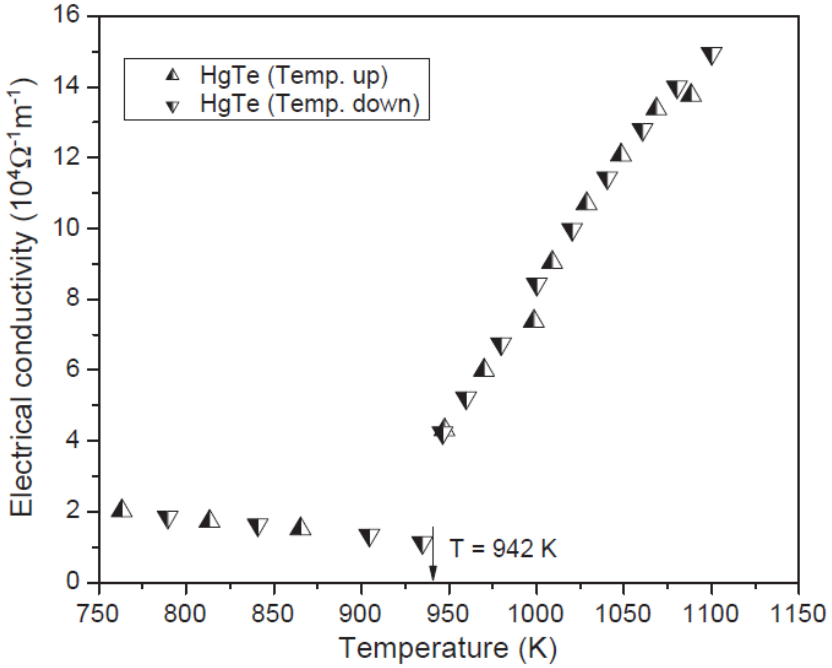

Figure 5.24 Electrical conductivity of HgTe as a function of temperature (taken from Figure 4 of Ref.[41]).

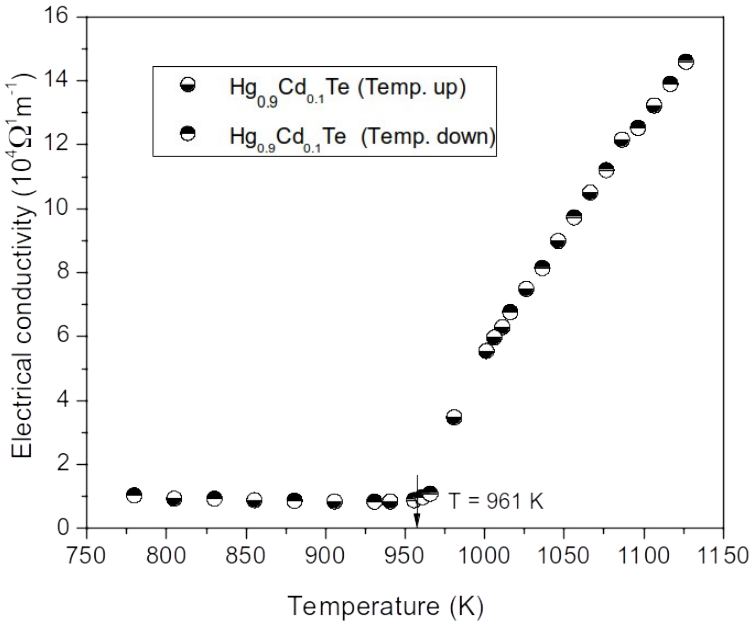

Figure 5.25 Electrical conductivity of $Hg_{0.9}Cd_{0.1}Te$ as a function of temperature (taken from Figure 5 of Ref.[41]).

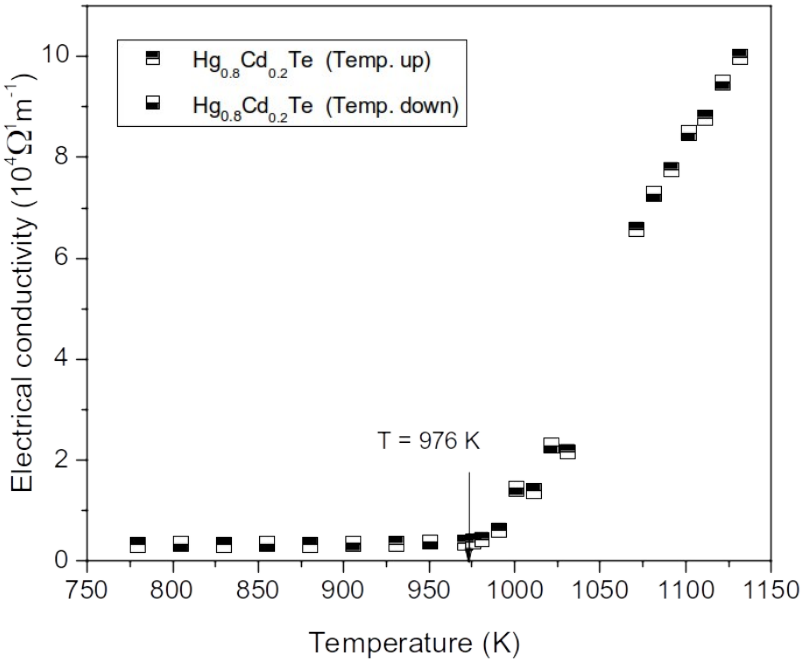

Figure 5.26 Electrical conductivity of $Hg_{0.8}Cd_{0.2}Te$ as a function of temperature (taken from Figure 2 of Ref.[42]).

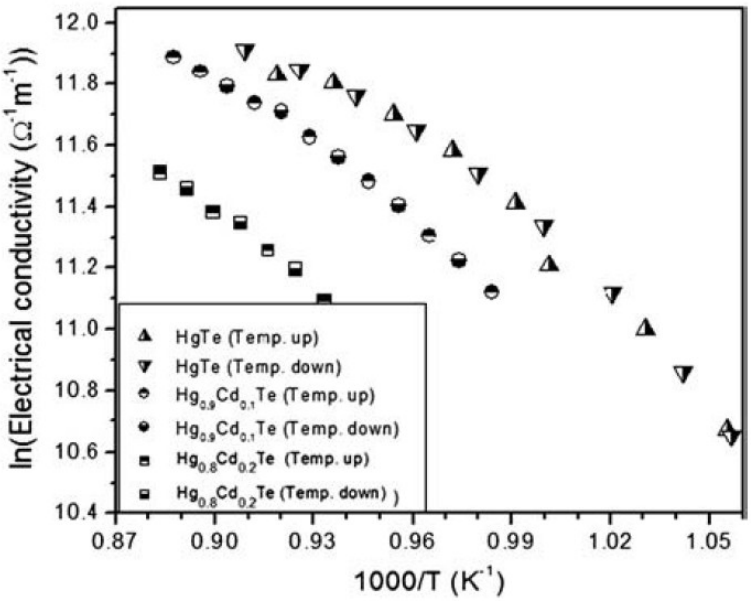

Figure 5.27 Electrical conductivity of the HgTe, $Hg_{0.9}Cd_{0.1}Te$ and $Hg_{0.8}Cd_{0.2}Te$ melts in the logarithm scale versus 1/T (taken from Figure 7 of Ref.[41]).

5.3.4 Relaxation phenomenon

5.3.4.1 HgTe melt. The time relaxation of the electrical conductivity and the kinematic viscosity of the HgTe melt were studied by cooling the melt rapidly from 1103K to 950K. The electrical conductivity and viscosity data taken at the initial 0.1 hrs were, respectively, higher and lower than their final equilibrium values measured after holding at 950K for approximately 7 hrs. The rest of the data scattered within the experimental error of 1.6% for the electrical conductivity and 4.6% for the viscosity measurement associated with the TTV. Thus, it is concluded that no relaxation behavior in the electrical conductivity and kinematic viscosity of the HgTe melt was observed.

5.3.4.2 $Hg_{0.9}Cd_{0.1}Te$ melt. The measured electrical conductivity and viscosity of the $Hg_{0.9}Cd_{0.1}Te$ melt as a function of time after the temperature was lowered from1130K to 1010K show the similar behavior as that for the HgTe melt. The electrical conductivity measured at the time of 0.25 hrs, $6.22x10^4\Omega^{-1}m^{-1}$, was about 0.6% higher than the equilibrium value of $6.18x10^4\Omega^{-1}m^{-1}$ measured at 24.5 hrs. The value of the first viscosity measurement at 0.25 hrs was about 2% lower than the equilibrium viscosity value measured at 24.5 hrs. It is therefore also concluded that, within the experimental error of the TTV, no relaxation behavior in the electrical conductivity and viscosity of the $Hg_{0.9}Cd_{0.1}Te$ melt was observed.

5.3.4.3 $Hg_{0.8}Cd_{0.2}Te$ melt. However, interesting phenomena were observed in the time dependence of the electrical conductivity and viscosity of the $Hg_{0.8}Cd_{0.2}Te$ melt after the temperature was lowered from 1130K to 1073K, which took the furnace approximately 20 min. The measured viscosity of the $Hg_{0.8}Cd_{0.2}Te$ melt as a function of time, given in Figure 5.28,

showed that the viscosity increased initially after the cooling. Then, at approximately 2 hrs, it went through a maximum of $5.15\times10^{-7}m^2/s$ and started to decline for approximately 50 hrs to reach its equilibrium value of $3.28\times10^{-7}m^2/s$, which agrees well with the steady value of $3.17\times10^{-7}m^2/s$ reported in Figure 5.18. During this relaxation time, the viscosity decreased approximately 62% from the maximum value to its equilibrium value.

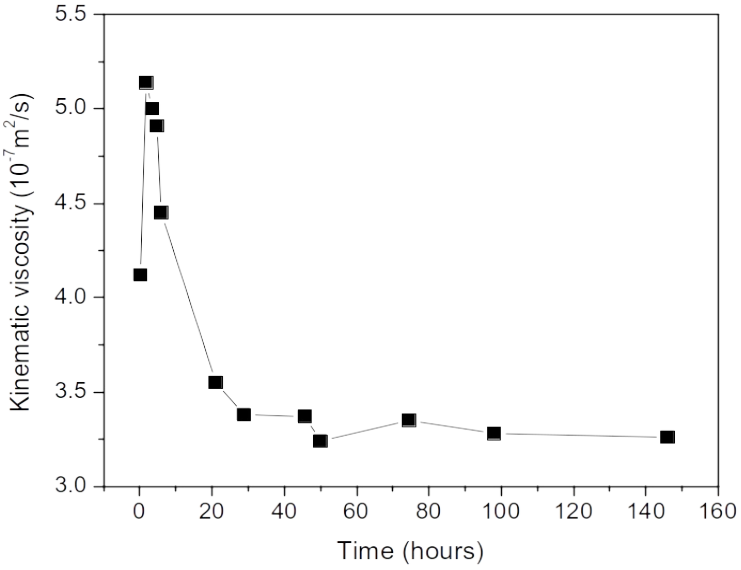

Figure 5.28 Time variation of the kinematic viscosity of the $Hg_{0.8}Cd_{0.2}Te$ melt after cooling from 1130K to 1073K (taken from Figure 81 of Ref.[35].

At the same time, as shown in Figure 5.29, after the rapid cooling, the measured electrical conductivity initially decreased as a function of time from $6.68\times10^{4}\Omega^{-1}m^{-1}$ to a minimum at approximately 3.4 hrs with a value of $6.53\times10^{4}\Omega^{-1}m^{-1}$. Then it increased to the equilibrium value of $6.79\times10^{4}\Omega^{-1}m^{-1}$ after nearly 46 hrs. This equilibrium value is 1.0% higher than the steady state electrical conductivity value, $6.86\times10^{4}\ \Omega^{-1}m^{-1}$ at 1073K, as shown in Figure 5.26.

The amount of fluctuation during relaxation in the measured electrical conductivity shows that the minimum of electrical conductivity was about 5% lower than its steady state value which was much smaller than the 62% on the relaxation behavior of kinematic viscosity. The possible reasons for this difference can be attributed to the structure of the melt as discussed in 5.2.4 for the HgZnTe system. The electrical conductivity essentially measures the sum of the products of the concentration of its n- and p-type carriers and their respective electrical mobilities. On the other hand, since viscosity is a measure of resistance to the shear force needed to create flow in the liquid, hence, it will depend significantly on the melt structure. As in the case of the $Hg_{0.84}Zn_{0.16}Te$ melt, this observed relaxation behavior might be attributed to either macroscopic or microscopic structural inhomogeneities in the melt. However, the trends were different for these two systems in that, during the relaxation, the viscosity of the $Hg_{0.84}Zn_{0.16}Te$ melt continuously increased by a factor of about 1.5 to reach its steady state value after 120 hrs

whereas the data for the $Hg_{0.8}Cd_{0.2}Te$ melt went through a maximum and then decreased 62% to its equilibrium value in about 60 hrs.

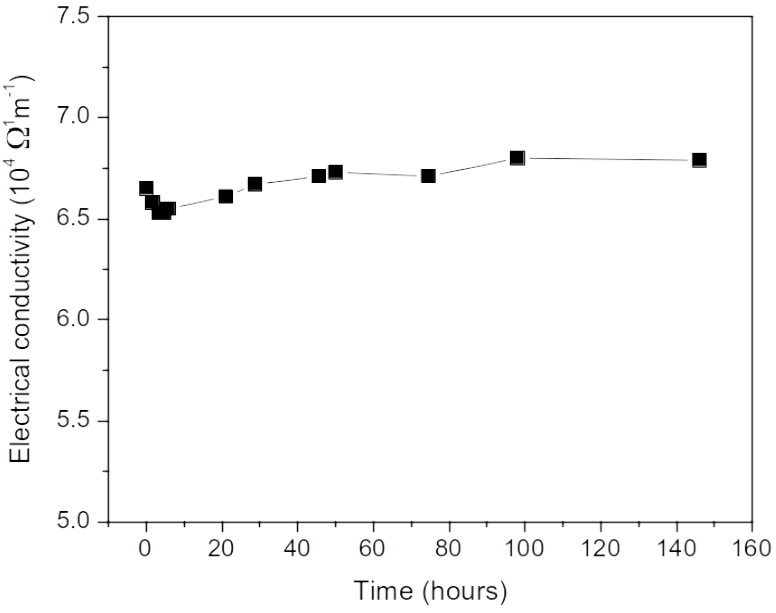

Figure 5.29 Time variation of the electrical conductivity of the $Hg_{0.8}Cd_{0.2}Te$ melt after cooling from 1130K to 1073K (taken from Figure 82 of Ref.[35].

References

[1] A. V. Tobolsky and W. J. MacKnight, *Polymeric Sulfur and Related Polymer*, Interscience Publishers (1965).
[2] R. Roscow and W. Bainbridge, Proc. Phys. Soc. London 72 (1958) 585.
[3] H. R. Thresh, AIME Trans. Metall. Soc. 23 (1965) 79.
[4] P. Banerjee and R. A. Overfelt, Int. J. Thermophys. 20 (1999) 1791.
[5] R. A. Overfelt, C. A. Matlock, and M. E. Wells, Metall. Mat. Trans. B 27 (1996) 698.
[6] R. Roscow, Proc. Phys. Soc. London 72 (1958) 576.
[7] X. Hong and K. Lu, Rev. Sci. Instr. 66 (1995) 4318.
[8] V. M. Glazov, S. N. Chizhevshaya, and N. N. Glagoleva, *Liquid Semiconductors*, Plenum Press, New York (1969).
[9] W. A. Wakeham, A. Nagashima, and J. V. Sengers, *Measurement of the transport properties of fluids*, Blackwell Scientific Publication, Oxford, London, Edinburgh, Carlton, (1991).
[10] T. Iida and R. I. L. Guthrie, *The Physical Properties of Liquid Metals,* Clarendon Press, Oxford (1988).
[11] P. Banerjee and R. A. Overfelt, Int. J. Thermophys. 20 (1999) 1791.

[12] D. Wang and R. A. Overfelt, Proceedings of Conference on Computational Modeling of Materials, Minerals and Metals Processing, Sep 23-26, 2001, San Diego, CA, United States, 2001 (Minerals, Metals and Materials Society), p. 523.
[13] D. Wang and R. A. Overfelt, Int. J. Thermophys. 23 (2002) 1063.
[14] M. Tomut and H. Chiriac, Mater. Sci. Eng. A 304-306 (2001) 272.
[15] Y. Sato, T. Nishizuka, T. Tahikawa, M. Hoshi, T. Yamamura, and Y. Waseda, High Temp. High Press. 32 (1999) 253.
[16] K. Mazuruk, Ching-Hua Su, S. L. Lehoczky, and F. Rosenberger, J. Appl. Phys. **77** (1995) 5098.
[17] C. Li, H. Ban, R. N. Scripa, Ching-Hua Su and S. L. Lehoczky, Review of Sci. Instr. 75 (2004) 2810.
[18] Heng Ban, Bochuan Lin, Chao Li, Rosalia Scripa, Ching-Hua Su and Sandor L. Lehoczky, Proceedings of 2004 Heat Transfer/Fluids Engineering Summer Conference, (HT/FED'04), HT-FED2004-56715 (2004).
[19] K. E. Spells, Proc. Phys. Soc. London 48 (1936) 299.
[20] K. Mazuruk, Ching-Hua Su, Yi-Gao Sha and S. L. Lehoczky, J. Appl. Phys. 79 (1996) 9080.
[21] R. F. Brebrick, Ching-Hua Su, and Pok-Kai Liao, in *Semiconductors and Semimetals,* Vol. 19, Chap. 3, edited by R. K. Willardson and A. C. Beer, Academic, New York (1983),
[22] Ching-Hua Su, S. L. Lehoczky, and F. R. Szofran, J. Crystal Growth 86 (1988) 87.
[23] S. Nakamura and T. Hibiya, Int. J. Thermophys. 13 (1992) 1061.
[24] V. I. Yukalov, Phys. Rep. 208 (1991) 395.
[25] James K. Baird, Yeong Woo Kim, Ching-Hua Su and S. L. Lehoczky, Phys. Chem. Liquids 40 (2002) 607.
[26] V. V. Bukhalenko, S. I. Slyusarenko, V. E. Laz'ko, L. A. Rostovskaya, and O. I. Slukhovskii, Phys. Metals 10 (1991) 1025.
[27] W. Braunbeck, Z. Phys. 73 (1932) 312.
[28] W. Menz, F. Sauerwald, and K. Fisher, Acta Metall. 14 (1966) 1617.
[29] G. T. Dyos and T. Farrell, *Electrical Resistivity Handbook*, Peter Peregrinus Ltd., London, United Kingdom (1992).
[30] C. Li, Ching-Hua Su, S. L. Lehoczky, R. N. Scripa, B. Lin and H. Ban, J. Appl. Phys. 97 (2005) 083513.
[31] S. Glasstone, K. J. Laidler and H. Eyring, *Theory of Rate Processes*, McGraw-Hill, New York (1941).
[32] A. I. Bachinskii, Izd. Akad. Nauk. SSSR, Moscow (1960).
[33] J. C. Perron, Adv. Phys. 16 (1967) 657.
[34] J. C. Perron, *Conduction in Low-Mobility Materials,* edited by N. Klein, D. S. Tannhauser and M. Pollak, Taylor and Francis LTD, London (1971).
[35] C. Li, Ph.D. dissertation "*Thermophysical properties of Te, HgTe and* $Hg_{1-X}Cd_XTe$ *melts*" University of Alabama at Birmingham (2003).
[36] H.-G. Junginger, Solid State Commun. 5 (1967) 509.
[37] A. Menelle, R. Bellissent, and A. M. Flank, Europhys. Kett. 4 (1987) 705.
[38] G. Tourand and M. Breuil, C. R. Acad. Sci., Paris B270 (1970) 109.
[39] M. Cutler, *Liquid Semiconductors*, Academic Press, New York (1977).
[40] M. Cutler, Phys. Rev. B 42 (1990) 7103.

[41] C. Li, Ching-Hua Su, S.L. Lehoczky, R. N. Scripa, H. Ban, and B. Lin, J. Non-Cryst. Solids 391 (2014) 54.
[42] C. Li, R. N. Scripa, H. Ban, B. Lin, Ching-Hua Su and S. L. Lehoczky, J. Non-Cryst. Solids 351 (2005) 1179.
[43] V. M. Glazov and L. M. Pavlova, J. Crystal Growth 184/185 (1998) 1253.
[44] D. Chandra, Phys. Rev. Lett. B 31 (1985) 7206.
[45] F. R. Szofran and S.L Lehoczky, J. Electron. Mater. 10 (1981) 1131.
[46] A. I. Gubanov, *Quantum Electron Theory of Amorphous Conductors*, Consultants Bureau, New York (1965).

Chapter 6
Thermal Conductivity Measurements and Results

Abstract: During the thermal conductivity measurements of the HgTe-based ternary melts, the samples need to be contained inside a sealed fused silica ampoule, therefore, the transient measurement by laser flash method was adopted. Most of the reported measurements were performed to obtain the thermal diffusivity and then, the thermal conductivity can be calculated from the data of density and heat capacity. The density of the HgTe-based melts has been reported in Chapter 4 and the diverse thermodynamic and phase diagram data, including the heat capacity, for the Hg-Cd-Te and Hg-Zn-Te ternary systems can be obtained by assuming an associated solution model for the liquid phase as given in Chapter 3. The detailed sample ampoule preparation, experimental setup and procedures for the measurements on the $Hg_{1-x}Zn_xTe$ pseudo-binary solids and melts by laser flash method are presented. Then the thermal diffusivity measurements on both solids and melts of the pseudo-binaries of $Hg_{1-x}Cd_xTe$, x=0, 0.05, 0.1, 0.2 and 0.3, and $Hg_{1-x}Zn_xTe$, for x = 0.10, 0.16, and 0.30, have been performed. The corresponding thermal conductivity were then calculated. The data show similar trends for both systems. The thermal conductivity of the solid decreased gradually as temperature increased and reach a minimum at solidus temperature and the data of the melt show an almost linear increase on the temperature after they were heated above the liquidus temperatures. At a fixed temperature, the measured values of thermal diffusivity and conductivity decreased monotonically with x, the content of CdTe. The other approach for the measurement of thermal conductivity basically used the same laser flash method but analyzed the data differently by including the heat transfer between the sample melt and the fused silica cell. Based on the assumption that the temperature response of the sample melt, including the rapid rise and the slow fall, was controlled by the thermal diffusivity and conductivity of sample and the fused silica cell, both thermal diffusivity and thermal conductivity of the sample can be obtained by a computational fitting process. An analytical solution, using parametric values and graphical results from the numerical simulation of the transient heat transfer, was developed.

Keywords: Thermal conductivity; Thermal diffusivity; Laser flash method; Heat capacity; II-VI compound semiconductors; Tellurium (Te); Mercury-cadmium-tellurium (Hg-Cd-Te) system; Mercury-zinc-tellurium (Hg-Zn-Te) system

6.1 Introduction

There are basically two different types of measurements on thermal conductivity of materials. One category is the steady state method that applies a known heat flux through a sample with known dimension, i.e., surface area and thickness, while measuring the temperature difference across the sample. When the steady state is achieved, thermal conductivity can be determined from the heat flux, sample dimension and the temperature difference by assuming one-dimensional heat flow using the Fourier's law. The other type is the transient method in that

a sensor measures the change of temperature over time, in the back side of a sample, in response to a heat impulse applied to the front side of the sample. The thermal conductivity can be determined from the shape of the data measured by the sensor through mathematical analysis. In general, the transient method can be performed more quickly since there is no need to wait for a steady state situation. But most importantly, the measurements of steady state method require the close contact between the thermal measuring devices, e.g., thermocouple, and the sample whereas an optical sensor can be adopted for the data collection in the transient method remotely. For the measurements of HgTe-based semiconducting melts, the samples need to be contained inside a sealed fused silica ampoule because of the high pressure and the extreme toxicity. Therefore, the transient measurement by laser flash method was adopted.

The temperature transient in a homogeneous material is given by the heat flow equation:

$$\rho C_p \frac{dT}{dt} = k \nabla^2 T \qquad (6.1)$$

where T is the sample temperature, t, k, ρ, and c_p are time, thermal conductivity, density, and heat capacity, respectively. Under the condition of one-dimensional heat flow, Eq.(6.1) can be expressed as a simple form of the differential equation:

$$\frac{dT}{dt} = D \frac{d^2 T}{d x^2} \qquad (6.2)$$

where D is thermal diffusivity, and the thermal conductivity k is related to D as:

$$k = \rho C_p D \qquad (6.3)$$

From the setup of these equations, there are two different approaches to utilize the laser flash method. Most of the measurements were performed to obtain the thermal diffusivity and, from Eq.(6.3), the thermal conductivity can be calculated from the known density and heat capacity. The laser flash method was first described by Parker et al. [1] and has been widely used to determine the thermal diffusivity of solid opaque materials. Eq.(6.2) shows that thermal diffusivity is the rate of heat transfer in a material from the hot side to the cold side along one direction which can be simulated with the laser flash method by using a sample in the shape of a thin disc/slab with its thickness much smaller than the cross-section area. In the laser flash method, after the sample cell was heated to reach a steady state at a preset temperature, the radiant energy of a high-intensity light/laser pulse was absorbed on the front surface of the cell and the resultant temperature rise on the rear face was recorded by an infrared (IR) detector. The characteristics of the temperature rising profile can be utilized to determine the thermal diffusivity of the sample.

On the analysis of the data of temperature rise, for a thin slab with uniform thickness, L, the heat flow equation can be described by a one-dimensional solution to Eq.(6.2). By assuming adiabatic sample conditions, the thermal diffusivity can be approximately by [1]:

$$D = \frac{0.1388\, L^2}{t_{1/2}} \tag{6.4}$$

where $t_{1/2}$ is the time when the temperature rises to ½ of ΔT_{Max}, i.e., the highest value of temperature rise. Because the actual value of the temperature rise is not required, this approach has been commonly adopted for the determination of thermal diffusivity on any laser flash system with the capability of measuring detailed signals of thermal history. The value of the constant, K_x, 0.1388 is specifically for the 50% rise and there are other constants for different % rise, given as K_x in Table 6.1 [2]. Once the thermal diffusivity is determined, the information of density and heat capacity as functions of temperature are required to derive the values of thermal conductivity through Eq.(6.3).

Table 6.1 Values of the constant, K_x, in Eq.(6.4) for different % rise of x.

x (%)	K_x	x (%)	K_x
10	0.0661	60	0.1622
20	0.0843	66.7 (2/3)	0.1811
25 (1/4)	0.0927	70	0.1919
30	0.1012	75 (3/4)	0.2105
33.3 (1/3)	0.1070	80	0.2332
40	0.1190	90	0.3035
50 (1/2)	0.1388		

The other approach basically used the same laser flash method but analyzed the data differently. Using a container for the sample, the heat transfer between the melt sample and the fused silica cell allows the thermal conductivity to be included in the analysis. Therefore, the temperature response of the sample melt, including the rapid rise and the slow fall, was controlled not only by the thermal diffusivity and conductivity of sample, but also by the thermal properties of the fused silica ampoule. Using a computational fitting process, both thermal diffusivity and thermal conductivity of the sample can be obtained [3,4] from the thermal response. More recently, the rear face temperature of the sample was described by an analytical solution and, with known properties of the fused silica cell, both thermal diffusivity and thermal conductivity of the sample can be obtained analytically by a parametric and graphic approach [5].

In this chapter, the reported values of thermal conductivity of the HgCdTe and HgZnTe solids and melts were determined by the first approach, i.e., from thermal diffusivity, density and heat capacity using Eq.(6.3). On the other hand, the thermal conductivity and diffusivity of the Te melt were determined by the second approach, i.e., using a computational fitting process on the transient temperature profile.

6.2 Heat capacity of HgCdTe and HgZnTe melts

Thermodynamic properties, such as heat capacity and enthalpy of mixing, of HgTe-based semiconductor melts cannot be easily determined experimentally because of the limitations imposed by the high Hg partial vapor pressures. However, as described in Chapter 3, an optimal fit of the diverse thermodynamic and phase diagram data for the Hg-Cd-Te ternary [6] and Hg-Cd-Zn-Te quaternary system [7] by assuming an associated solution model for the liquid phase can be used to obtain good estimates. The detailed description of the model was described in Chapter 3 and in Ref.[6]. A brief summary of the model and the calculated results for the heat capacity of the HgCdTe [8] and HgZnTe [9] pseudo-binary melts are described below.

It was assumed that the liquid phase of Hg-Cd-Te, Hg-Zn-Te systems consists of species of Hg, Cd/Zn, Te elements as well as HgTe, CdTe/ZnTe molecules, numbering consecutively as species 1-5, with species mole fractions y_i, i= 1.... 5. The thermodynamic components Hg, Zn, and Te are numbered consecutively 1-3 with atom fraction x_i , i = 1,2,3. The thermodynamic characterization will be completed by assuming an equation for the excess Gibbs energy of mixing, ΔG_m^x of forming the solution from the liquid elements:

$$\Delta G_M^x = \sum_{j=1}^{5}\sum_{i=1}^{5}(\alpha_{ij}+\beta_{ij}y_j¿¿)y_i y_j - y_4\Delta G_4^o - y_5\Delta G_5^o¿¿ \qquad (6.5)$$

where α_{ij} and β_{ij} are the interaction parameters and $\Delta G_4^o$and $\Delta G_5^o$are the Gibbs energy of dissociation for species 4 and species 5. The relative chemical potentials, μ_j, of each species can be derived from Eq.(6.5) and from which the relative partial molar enthalpies and entropies of each species can be obtained from the usual thermodynamic equations. The enthalpy and entropy of mixing per mole of the species can then be written as:

$$\acute{h}_j = \left(\frac{\partial \acute{\mu}_j/T}{\partial(1/T)}\right) \qquad (6.6)$$

and

$$\acute{S}_j = -\left(\frac{\partial \acute{\mu}_j}{\partial T}\right) \qquad (6.7)$$

The total quantity per more species is:

$$\Delta Z_M(mole\ species) = \sum_{i=1}^{5} y_i Z_i \qquad j \text{ from 1 to 5} \qquad (6.8)$$

where Z_M denotes either enthalpy H_M or entropy S_M. To convert the theoretical quantity per mole of species to the corresponding experimental quantities per gram-atomic weight of components, the following equation will be adopted:

$$\Delta Z_M(g-atom\ component) = (1+y_4+y_5)^{-1}\Delta Z_M(mole\ species) \qquad (6.9)$$

The constant pressure relative heat capacity can be expressed as:

$$\Delta C_P = \left(\partial \Delta H_M / \partial T\right)_{x_1, x_2, P} \tag{6.10}$$

and is the difference between the heat capacity of the melt and the sum of those of the unmixed liquid elements. So, the heat capacity per gram-atom of the melt can be obtained from the expression:

$$C_P = \Delta C_P + x_1 C_{P1}^l + x_2 C_{P2}^l + x_3 C_{P3}^l \tag{6.11}$$

where C_{P1}^l, C_{P2}^l and C_{P3}^l are the heat capacity of pure liquid elements, 1, 2 and 3, with composition x_1, x_2 and x_3, respectively.

6.2.1 $Hg_{1-x}Cd_xTe$ melts. The heat capacity for the $Hg_{1-x}Cd_xTe$ pseudo-binary melts were calculated between the liquidus temperature and 1100°C [8] using the interaction parameters from Ref.[6]. With the adopted constant heat capacity for pure liquid elements as 6.61, 7.10, and 9.0cal/g-atom for Hg, Cd and Te, respectively, the heat capacity of the $Hg_{1-x}Cd_xTe$ (l) is given by (6.61(1-x)+7.10x+9.0)/2 for an ideal solution, which means that C_P will be between 7.805cal/g-atom-K, for HgTe(l), and 8.05cal/g-atom-K, for CdTe(l). The results from the associated solution model, given in Figure 6.1, show that, for low CdTe content, x = 0 and 0.05, the calculated C_P lie between 7.2 and 8.3cal/g-atom-K with the highest C_P at the liquidus temperature and goes through a minimum. For higher values of x, the C_P values at the liquidus are higher, ranging from 8.8 to 11.2cal/g-atom-K, and keeps on decreasing as temperature increases. At a fixed temperature, such as 1100°C, the value of C_P goes up as x increasing from 0.2 to 0.7 and then comes down for x from 0.8 to 1.0. This behavior implies that the melts of the pseudo-binary are significantly different from the ideal solution when CdTe melt is added to the HgTe melt because (1) the value of C_P at the melting point are the highest, (2) the decreasing rate of C_p with T keeps on getting smaller with higher value of x and approaches zero at x = 1.0 and (3) at a fixed temperature, 1100°C for instance, the value of C_P doesn't go up monotonically with the values of x but reaches a maximum at x = 0.7. All of these phenomena indicate that the addition of CdTe(l) to the HgTe(l) causes structural and bonding changes because of the interactions between different atomic and molecular species.

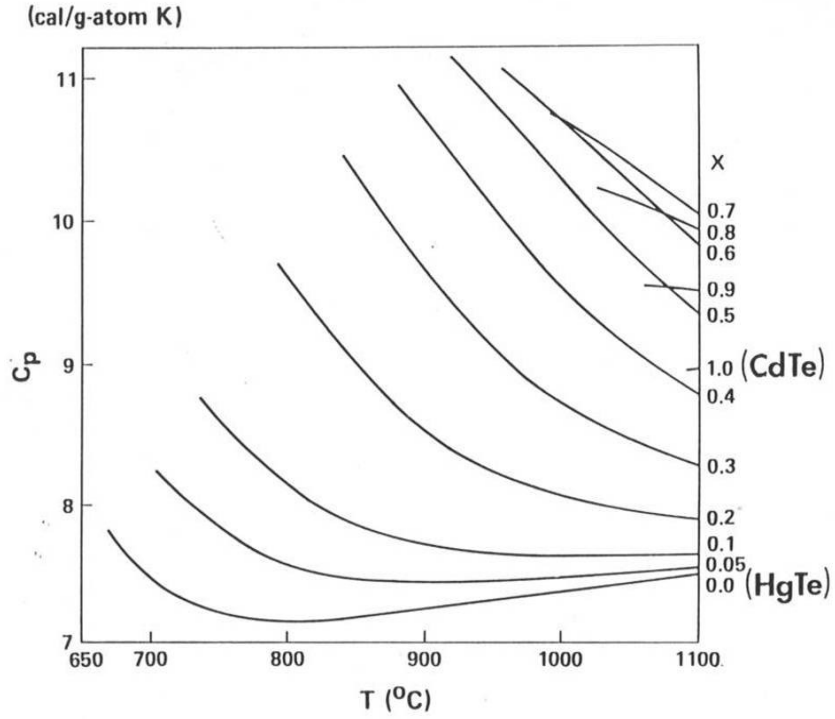

Figure 6.1 Calculated heat capacity in the $Hg_{1-x}Cd_xTe$ pseudo-binary melts for temperature between the liquidus temperatures and 1100°C (taken from Figure 1 of Ref.[8]).

6.2.2 $Hg_{1-x}Zn_xTe$ melts. The heat capacity for the $Hg_{1-x}Zn_xTe$ pseudo-binary melts were also calculated between the liquidus temperature and 1500°C [9] using the interaction parameters from Ref.[7] which has the parameters for the Hg-Te system slightly different from the ones in Ref.[6]. The constant heat capacity for pure Hg liquid elements, in Eq.(6.11) were also different from the constant value of 6.6cal/g-atom adopted for the calculation of HgCdTe(l). The temperature-dependent values of C_P adopted for Hg increases from 6.62cal/g-atom at 670°C, the melting temperature of HgTe(s), to 8.52cal/g-atom at 1290°C, the melting point of ZnTe(s), and 9.49cal/g-atom at 1500°C. The C_P for other two liquid elements was set at 7.5cal/g-atom for Zn and 7.87cal/g-atom for Te. The calculated C_P for various values of x in the $Hg_{1-x}Zn_xTe$(l) pseudo-binary are given in Figure 6.2 (a) and (b). The C_P at the melting points ranges from 6.8 to 10cal/g-atom and increases as the value of x getting larger. Comparing Figure 6.1 to 6.2 for the $Hg_{1-x}Cd_xTe$(l) and $Hg_{1-x}Zn_xTe$(l) melts, the C_P values for $x \leq 0.20$ are comparable to each other. However, for $x > 0.2$, the addition of ZnTe(l) to HgTe(l) behaves more normally, in thermodynamic sense, than the addition of CdTe(l) to HgTe(l) in that (1) right after the melting, the heat capacity increases with temperature and (2) the value of C_P does go up with increasing x monotonically.

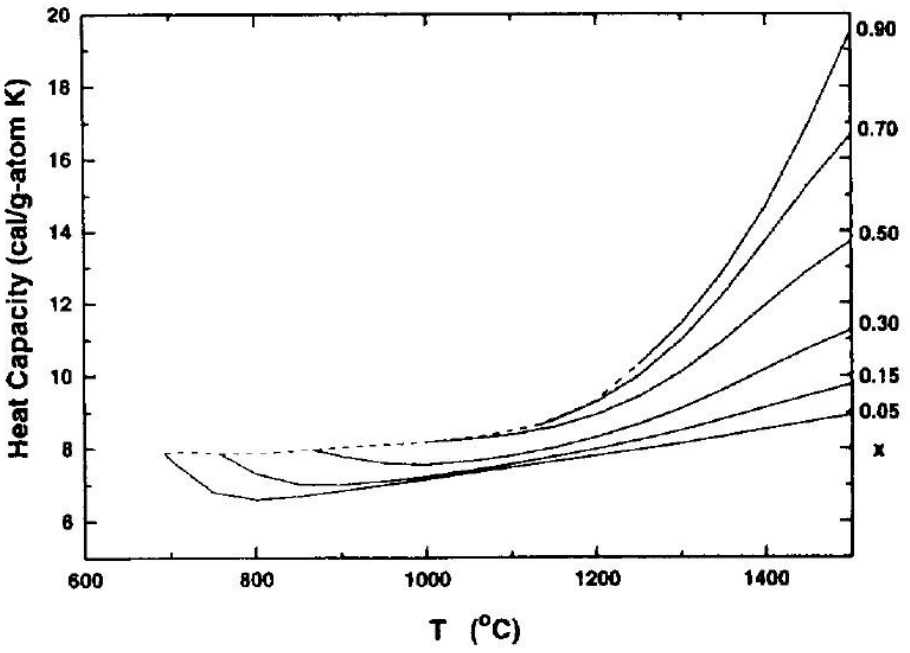

(a)

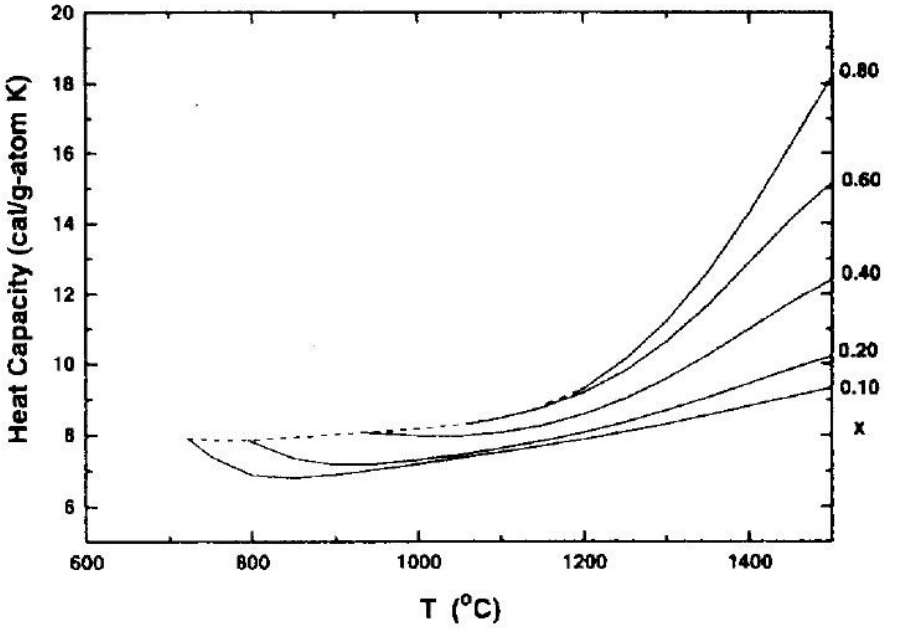

(b)

Figure 6.2 Calculated heat capacity in the $Hg_{1-x}Zn_xTe$ pseudo-binary melts between the liquidus temperatures and 1500°C for various values of x as labeled in (a) and (b). The dashed lines connect the different liquidus of $Hg_{1-x}Zn_xTe$(l) (taken from Figure 4 and 5 from Ref.[9]).

6.3 Thermal conductivity of HgCdTe and HgZnTe melts

6.3.1 Experimental measurements of thermal diffusivity by laser flash method. Because of the high Hg pressure associated with the HgCdTe and HgZnTe melts, the solution of Eq.(6.4) for the adiabatic condition was adopted to determine thermal diffusivity. The measurements of density reported in Chapter 4 and the heat capacity calculated above from the associated solution model on the HgTe-based ternary melts are employed in Eq.(6.3) to obtain thermal conductivity. The thermal diffusivities of $Hg_{1-x}Cd_xTe$ solids and melts [10] and those of pure Te and Te-rich HgCdTe and HgZnTe melts [11] as well as $Hg_{1-x}Zn_xTe$ solids and melts [12] were determined using the laser flash measurement system at Thermophysical Properties Research Laboratory (TPRL).

6.3.1.1 Optical cells. The optical cells for both ternary systems were similar in design. The detailed preparations for the HgZnTe pseudo-binary are given here [12]. The optical cells were made of fused silica tubing with two optical windows transparent to infrared wavelength shorter than about 4μm at both ends. The cell tubing was 16mm OD and 10mm ID with a sidearm attached to the cylindrical side, which allowed the sample to be loaded and sealed. The disk-shaped cavity for the sample was 9mm in diameter and 1–2 mm thick. The homogenization process of the HgZnTe cells [12] started with the loading of elemental Hg (79 grade), Zn (69 grade), and Te (69 grade, quadruple zone refined) from Johnson Matthey into the thoroughly cleaned and outgassed optical cell which was then sealed under vacuum of 10^{-5} Torr. The synthesis was carried out in a furnace by heating it from room temperature to 650°C over a period of several hours, held at this temperature for 3–5 days, and then cooled passively to room temperature. The cell was then placed with the sidearm vertically in the upward position in a vertical furnace. The sample was completely melted by raising the furnace temperature to about 900°C in 8 hrs and holding it for 16 hrs. After cooling of the sample, the sidearm of the cell was then shortened and resealed under vacuum and the cell reheated slowly to about 900°C to test its integrity. During this second heating procedure, several cells were observed to have developed or started to develop a crack near the flat surface of the sample optic disk. It was later concluded that the thermal expansion of the solid phase during heat-up was the cause. To avoid the cell failure, an alternative method of preparing the cells was adapted. The HgZnTe sample was first synthesized in another fused silica ampoule, collected afterwards by opening the ampoule, ground into powder, and reloaded and sealed into the optical cell. Enough material was prepared so that the optical cell cavity would be filled completely upon melting of the powder during the diffusivity measurements and all the material in the synthesis ampoule was collected to assure the accuracy in sample composition. Figure 6.3 shows photographs of the optical cells after the experimental runs.

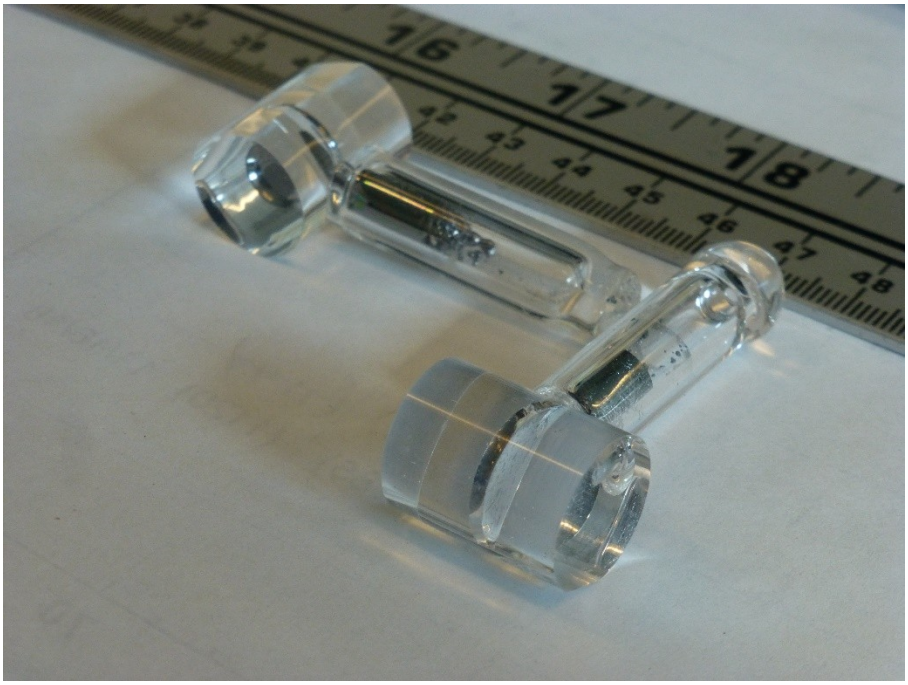

Figure 6.3 The photographs of two typical optic cells. Both were loaded with $Hg_{1-x}Cd_xTe$ samples: (left) x = 0.05 and (right) x = 0.30.

6.3.1.2 Thermal diffusivity measurements. The optical cells were held vertically by two stainless-steel plates bolted tightly against the cell. A split-heater furnace with independent temperature control for the top and bottom elements was used to heat the samples. A ceramic tube was placed inside the furnace coaxially to reduce the air convection caused by uneven heating. Such convection can cause fluctuation in the pyrometer signal, making it difficult to determine the base-line temperature. The laser used was a Korad K-2 pulsed neodymium glass laser with a wavelength of 1.06μm. A mercury cadmium telluride (MCT) IR photo pyrometer capable of detecting 0.05°C temperature resolution with a response time of milliseconds was employed to measure the temperature response of the rear face of the sample. The detector was coupled by an amplifier and an A/D converter to a computer-based data acquisition system. The computer collected the data, compared it with the corresponding theoretical curve, made the corrections for heat loss by the ratio method of Clark and Taylor [13] and by the thermal decay method of Cowan [14]. The results were then plotted to show the experimental and theoretical temperature rise curves. The thermal diffusivity can be calculated from the time needed for the rear face temperature rise to reach one half of its maximum value and the thickness of the sample as given by Eq.(6.4) [15,16].

6.3.2 Results of $Hg_{1-x}Zn_xTe$ pseudo-binary solids and melts. The measurements were conducted on five optical cells with sample composition, thickness, and total weight given in Table 6.2. Cell TZ20 contained pre-melted sample and the cell ruptured after the measurement at 534°C so that no data on melt were obtained. The other four cells contained powder samples and, therefore, were heated initially to the respective highest temperature of measurement to allow the samples to be completely melted and mixed. At these highest temperatures, the Hg partial

pressure inside the cell was 70, 75, 80, and 85atm for cell TZ10, TZ16, TZ30, and TZ40, respectively [7].

Table 6.2 Compositions, x, of $Hg_{1-x}Zn_xTe$ optical cells for thermal diffusivity measurement. L is the thickness of the sample disk.

Cell name	x	L(mm)	Total weight (g)	Remark
TZ10	0.10	1.558	1.1897	Powder
TZ16	0.16	1.404	1.1716	Powder
TZ20	0.20	1.577	1.2994	Melted
TZ30	0.30	1.278	1.2098	Powder
TZ40	0.40	1.772	1.3028	Powder

(Taken from Table 1 of Ref.[12])

Because of the wide separation between the solidus and liquidus curves in the HgZnTe phase diagram, rapid heating was used when the sample temperature was between its solidus and liquidus and a mixing procedure was devised after the sample was completely melted. The cell containing the melt was first brought to equilibrium in the furnace by holding the temperature for at least 20 min and then was pulsed with the laser at high power. The resulting Hg vapor pressure forces part of the cell content up into its stem which is directly above the cavity region. The cell was then observed to refill over the next few minutes. This procedure was repeated several times to ensure complete mixing of the sample. Inadvertent boiling was easily suppressed by applying a slight vertical temperature gradient. During cooling, a large vertical temperature gradient was applied to assure the sample was frozen from the bottom up. Rapid cooling was also essential to avoid the compositional segregation.

The measurements were made during the cooling for cells TZ10, TZ16, and TZ30. Cell TZ40 ruptured after the temperature had settled at 959°C for about 20 min, yielding only one data point for the melt. The combined data are plotted in Figure 6.4 which extended into much higher temperature range than the measurements on the $Hg_{1-x}Cd_xTe$ systems [10]. Each data point is the average of 2–7 measurements made at that temperature with a standard deviation ranging from 5% to 15%. As shown in the figure, the measured diffusivities for the solids of $0.10<x<0.30$ are about 60% of that of the HgTe solid, which will be presented later. The measured values for the melts rise rapidly with temperature but less so with increasing x. For $x = 0.30$, the diffusivity of the melt is about one third of that of the HgTe melt at 870°C.

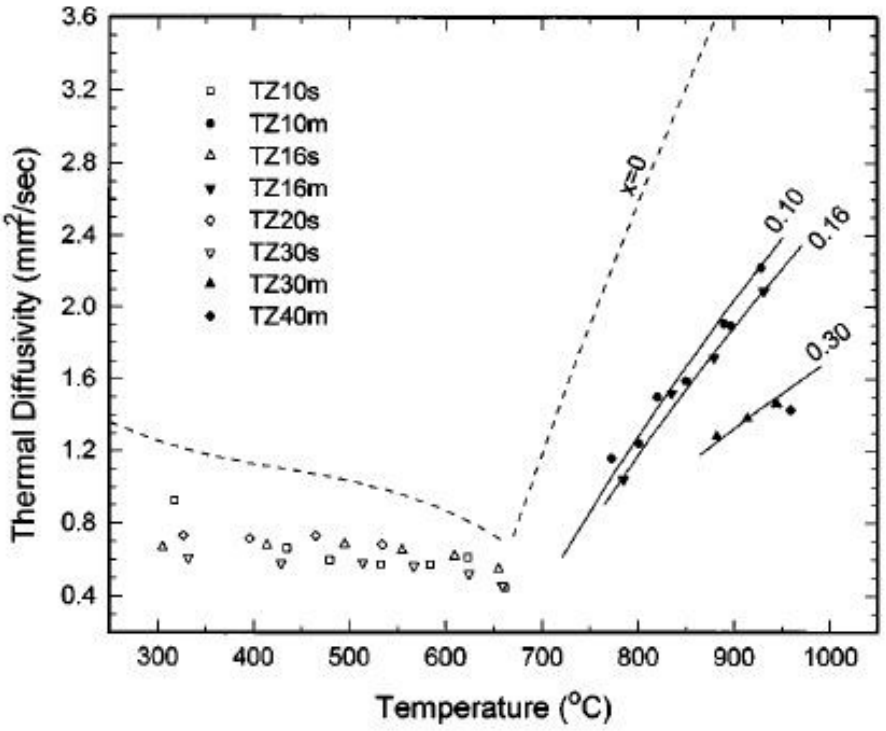

Figure 6.4. Thermal diffusivity of pseudo-binary $Hg_{1-x}Zn_xTe$ solid solutions and melts. Symbols are measured data and solid lines are the best-fit curves for the diffusivity of melts for x = 0.10, 0.16, and 0.30. The dashed lines are those of HgTe solid and melt taken from Ref. [10] (taken from Figure 1 of Ref.[12]).

Using the values of the calculated heat capacity from the associated solution model and the measured density reported in Chapter 4, the thermal conductivity for the pseudo-binary $Hg_{1-x}Zn_xTe$ solids of $0.10<x<0.30$ and for the melts of x = 0.10, 0.16, and 0.30 was derived as illustrated in Figure 6.5.

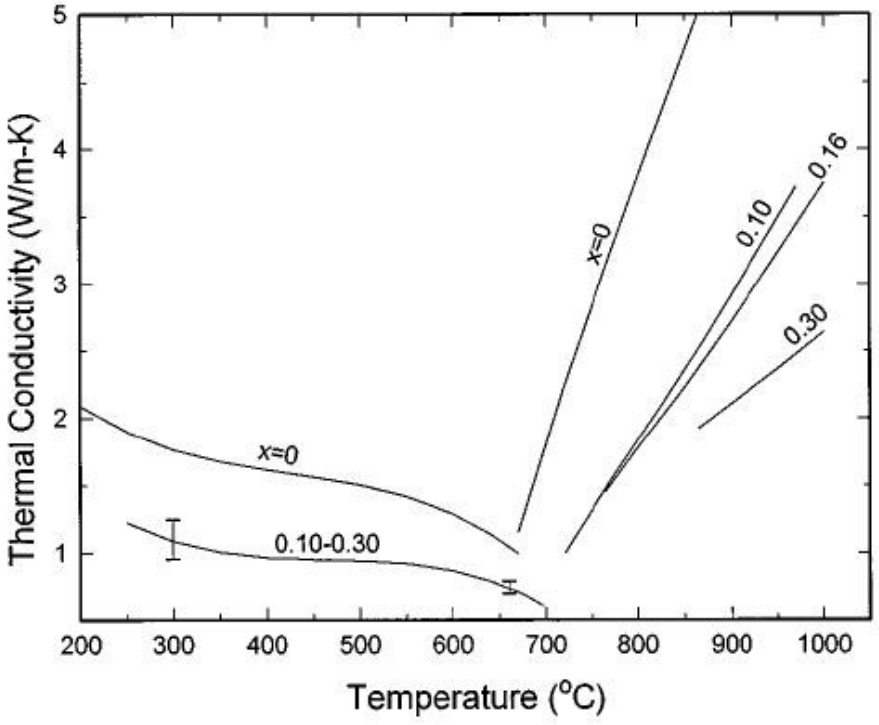

Figure 6.5. Calculated thermal conductivity of pseudo-binary $Hg_{1-x}Zn_xTe$ solids and melts (taken from Figure 2 of Ref.[12]).

6.3.3 Results of $Hg_{1-x}Cd_xTe$ pseudo-binary solids and melts. The thermal diffusivities of $Hg_{1-x}Cd_xTe$ solids and melts for values of x from 0 to 0.3 and over a temperature range from 100 to 900°C have been determined by the laser flash method at TPRL [10]. As shown in Figure 6.6, the curves represent the best-fit 3rd-order polynomial as functions of temperature to the experimental data. The diffusivity decreases from a maximum at $x = 0$ for both the solid and the melt, with the values observed at $x = 0.3$ being about 40% of those for $x = 0$. For the HgTe melt, the measured thermal diffusivity increases from 0.7mm^2/s at the melting point of 670°C to 3.5mm^2/s at 800°C.

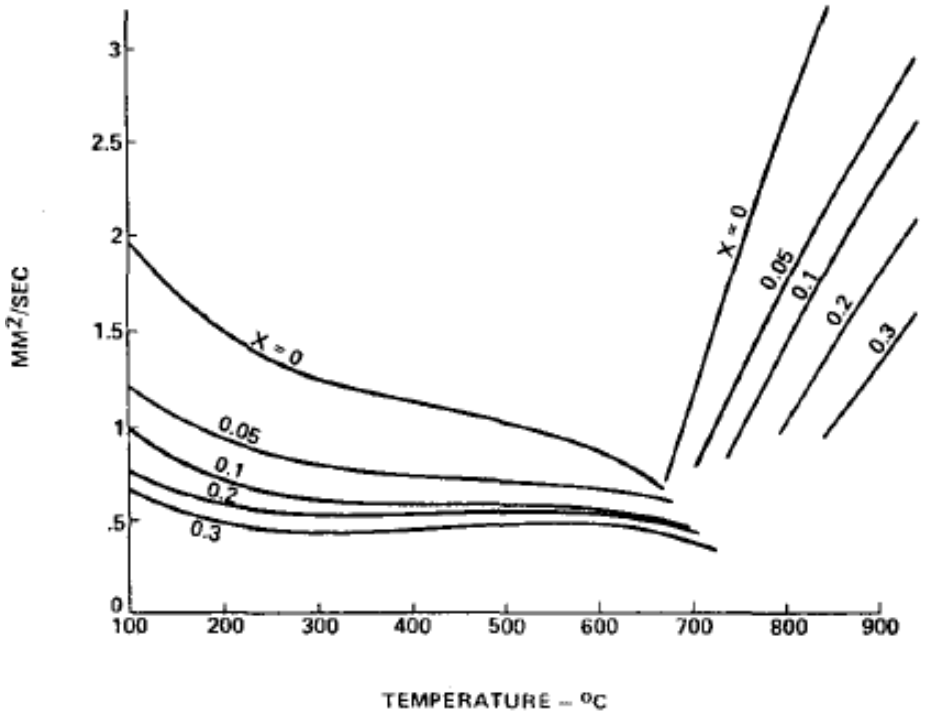

Figure 6.6 Thermal diffusivity of $Hg_{1-x}Cd_xTe$ solids and melts as functions of temperature (taken from Figure 4 of Ref.[10].

The thermal conductivity of $Hg_{1-x}Cd_xTe$ solids and melts as functions of temperature were then derived from these thermal diffusivity data, the heat capacity values calculated from the associated solution model in Chapter 3 [8], and the measured density data in Chapter 4 [17]. As shown in Figure 6.7, the data show almost linear dependence on the temperature for all the four compositions of the $Hg_{1-x}Cd_xTe$ melts. The thermal conductivity of $Hg_{1-x}Cd_xTe$ solids and melts are comparable to that of the of $Hg_{1-x}Zn_xTe$ system, given in Figure 6.5, after the unit conversion of 1cal/s cm K = 4.184W/cm-K.

.

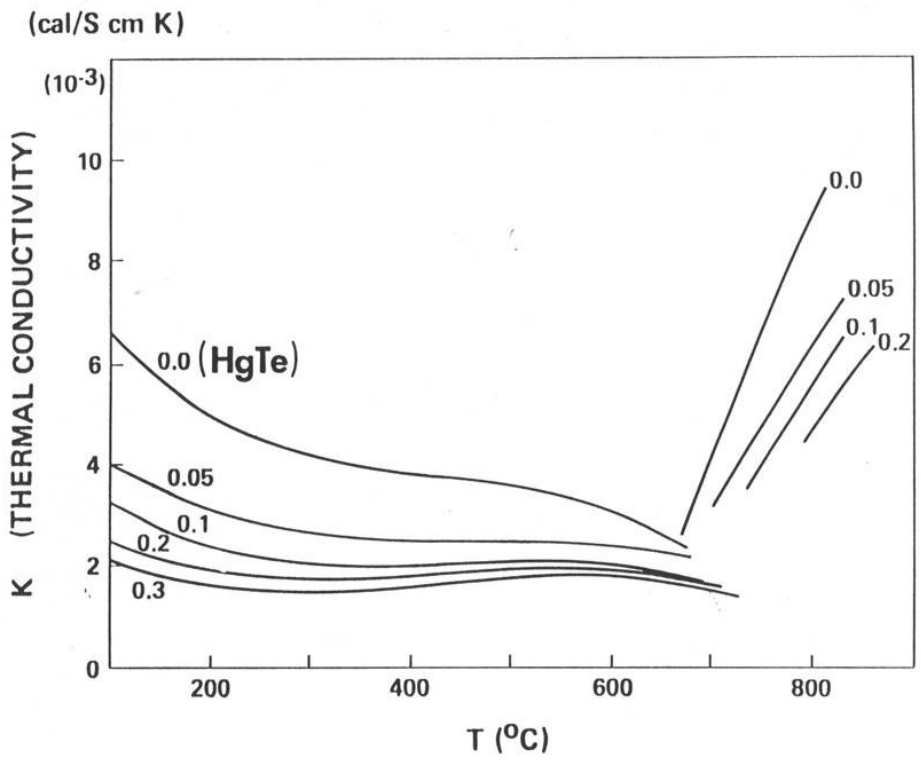

Figure 6.7. Thermal conductivity of $Hg_{1-x}Cd_xTe$ solids and melts as functions of temperature. Note: 1cal/s cm K = 4.184W/cm-K (taken from Figure 4 of Ref.[8]).

6.3.4 Results of Te-rich HgCdTe and HgZnTe melts. The thermal diffusivities of Te-rich $(Hg_{1-x}Cd_x)_{1-y}Te_y$ and $(Hg_{1-x}Zn_x)_{1-y}Te_y$, with $0.55 \leq y \leq 1.0$ and $0.0125 \leq x \leq 0.0547$, and of pure Te were measured from 350 to 850°C also by the laser flash technique [11]. The diffusivity of Te-rich $(Hg_{1-x}Cd_x)_{1-y}Te_y$ melt increased with increasing temperature. For instance, the measured thermal diffusivity of the melt with composition of x = 0.039 and y = 0.782 increases from 0.9mm^2/s at 485°C to 4.93mm^2/s at 851°C. For the Te-rich $(Hg_{1-x}Zn_x)_{1-y}Te_y$ melt with x = 0.0125 and y = 0.7944, a minimum diffusivity of about 2.6mm^2/s near 690°C was observed.

6.4 Thermal conductivity of Te liquid by modified laser flash measurements

6.4.1 Experimental. The experimental approach of this laser flash method was the same as that for the HgTe-based melts described above. Because of the high Hg pressure, the values of thermal conductivity for HgTe-based solids and melts were determined differently during the analyses of the data. The apparatus for the measurements of Te liquid, similar to the system at Thermophysical Properties Research Laboratory (TPRL) on the measurements of HgCdTe melts [11], was assembled and set up at NASA/MSFC. A schematic of the setup for the thermal conductivity measurements of the Te liquid [4] is shown in Figure 6.8.

High purity Te powder was sealed under vacuum inside a specially designed cylindrical-shape optical fused silica cell with optical windows. The outer and inner diameters of optical cell

were 15 and 10mm, respectively. The total length of the cell was 22mm with the sample thickness of about 2mm positioning in the center. The optical cell used for measurements was cleaned and furnace dried in air. About 2.3g of 99.9999% purity Te powder was loaded into the cell immediately after the Te ingots were granulated. The cell was then evacuated to $5x10^{-6}$Torr and was sealed by a H_2-O_2 torch. Sample cell was fastened into a stainless-steel block in the center of a furnace containing a heat pipe. The uniform temperature zone was about 10cm long with the variation in temperature less than 0.5K for the entire temperature range of measurements. A pulsed laser beam with 1064nm wavelength was uniformly spread to 10mm diameter and illuminates one side of the Te melt with the duration of 1ms. A Germanium detector, with a diameter of 2mm circular area focusing on the other side of the sample, measured the temperature rise as a function of time.

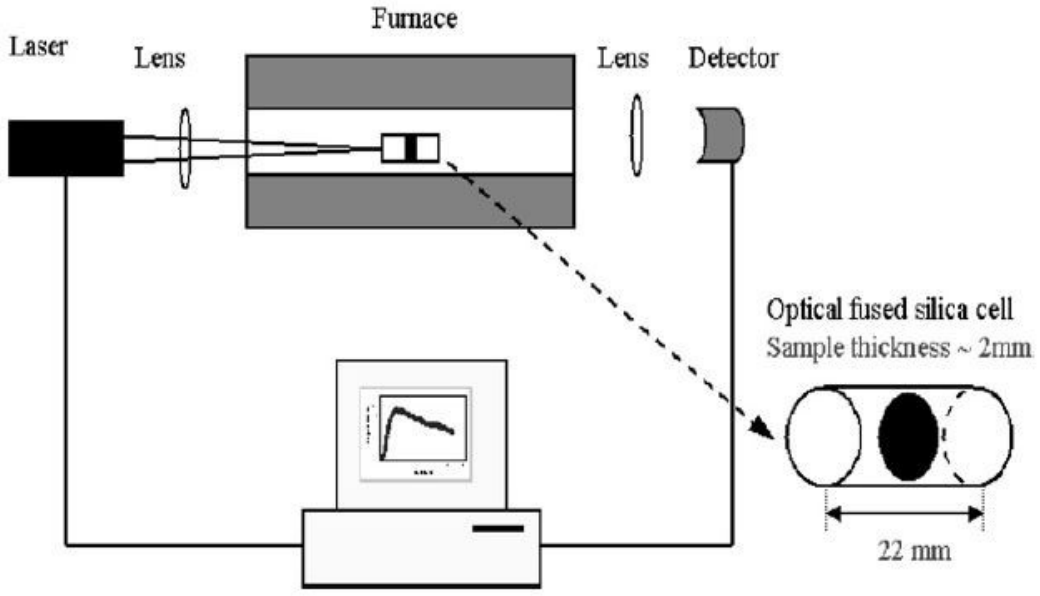

Figure 6.8 The schematic apparatus of laser flash measurement including an enlarged sample cell with the black plate being the 2mm thick Te sample (taken from Figure 1 of Ref.[4]).

The sealed cell containing Te powder was maintained at 1083K for 48 hrs to ensure a homogeneous liquid state. After reaching the steady state, five thermal diffusivity measurements were performed at each prescribed temperature. A 15 min waiting period was used between each measurement to allow melt temperature to reach the steady-state value. Measurements were made both during cooling and heating. The transient response was measured by the detector at a rate of 1KHz and converted into temperature. A typical measurement started about 1 sec before the laser illumination and lasted for 10 sec. Figure 6.9 shows the first 2 sec segment of the temperature transient for the liquid Te sample at 873K. It shows that the temperature at the back side of Te melt responded to the energy pulse by an increase in temperature with time and reached a ΔT_{Max} of about 2.4K at 0.5 sec and then slowly cooled down.

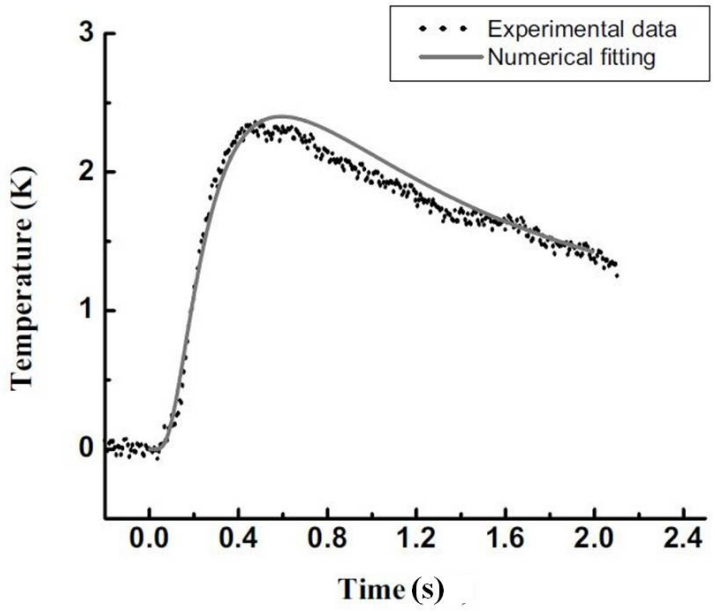

Figure 6.9 Temperature transient curves of liquid Te at 873K with the experimental measurement (dots) and the numerical fitting (solid line) (taken from Figure 2 of Ref.[4]).

6.4.2 Numerical solution. The data shown in Figure 6.9 for the Te melt indicate a significant heat loss through the fused silica optical cell during the measured time duration. Therefore, adiabatic boundary condition to obtain solutions to Eq.(6.4) cannot be applied. A numerical method was adopted to treat the overall heat flow problem. Since the sample length was about 2mm, the cell window thickness was 10mm on each side, and the heat travel time through the window was much shorter than the transient measurement time, the cell was treated as a semi-infinite cylinder. Eq.(6.1) was then discretized into 1200 finite control volumes and a central difference method was used with the time step of 0.1 ms. The fused silica properties were adopted from the supplier [18] and the Te melt density values were obtained from Ref.[19]. Using the temperature transient data and these inputs, the heat capacities and thermal conductivities of the sample were obtained from the best fits of the calculated temperature transients to the experimental data shown as the solid curve in Figure 6.9. The heat capacity of Te liquid resulted from the numerical fit for the measurement temperature range is shown in Figure 6.10. Previously published data [20-22] are also plotted in the figure for comparison.

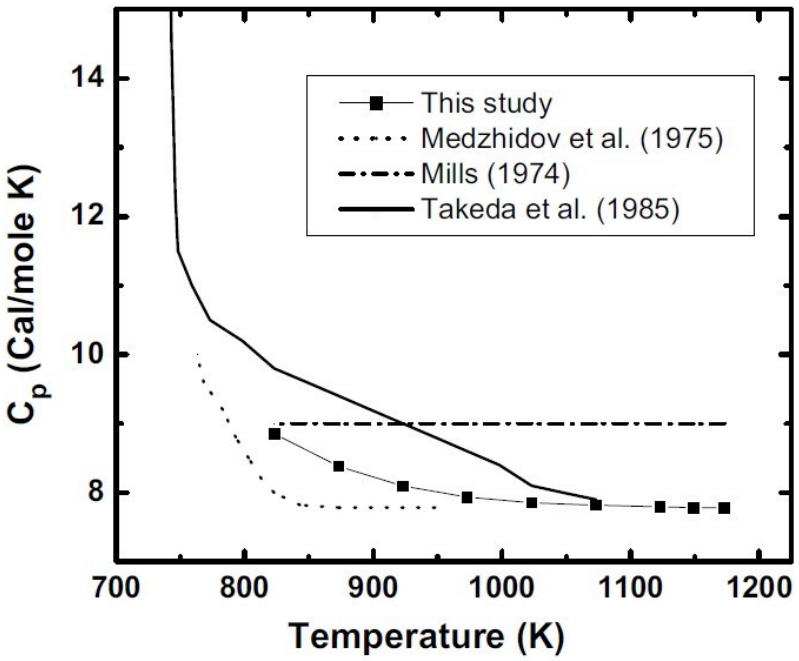

Figure 6.10 Measured heat capacity of Te liquid as a function of temperature from different reports (taken from Figure 3 of Ref.[4]).

The measured thermal conductivities for Te are shown in Figure 6.11 as a function of temperature with the data labeled “Temp. Up” and “Temp. Down” indicating the measurements taken during the heat-up and cool-down, respectively. The thermal conductivities reported by Yurchak et al. [23] show similar trends but are about 70% higher around 1073K (800ºC). They used a narrow-bridge method to simultaneously record the thermal conductivity and electrical resistivity, which may cause additional heating by electrical wiring. Our data agree much better with an early result [24]. The monotonic increase of the data as a function of temperature is consistent with the structural change in the melt reported by the neutron scattering spectra [25,26]. Particularly, at temperature higher than 850ºC, the thermal conductivity starts to saturate into a constant value. Neutron scattering experiments [26] showed the structure with a strong temperature dependence below 1073K (800ºC) with the initial coordination number of 2.63 which gradually increased to 3 at high temperatures that is similar to the trend of thermal conductivity data shown in Figure 6.11.

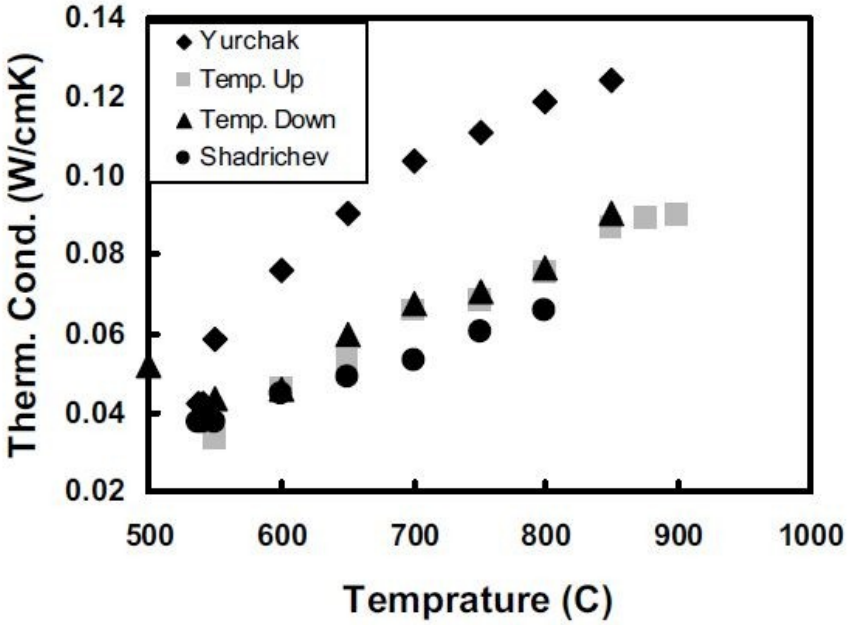

Figure 6.11 Measured thermal conductivity of Te liquid as a function of temperature: "Temp. Up" and "Temp. Down" from Zhu [4], Yurchak [23], and Shadrichev [24] (taken from Figure 4 of Ref.[4]).

The thermal diffusivities of Te liquid, calculated from the density, heat capacity and the thermal conductivity determined from the numerical solution, is given in Figure 6.12. The data agree reasonably well with the low temperature results from Maleki et a. [11]. Their thermal diffusivity data were measured at temperatures up to 923K, which can be extrapolated linearly to high temperatures. The linear diffusivity temperature trend agrees well with the neutron scattering measurements [25,26] before reaching the atomic Te structure state. If the liquid Te structure remains atomic structure at high temperatures as indicated by the neutron scattering measurements, the thermal diffusivity could be unchanged because it is proportional to thermal conductivity. The experimental data show a similar linear temperature dependence of thermal diffusivity extended to 1023K. After this temperature, the thermal diffusivity remains at a nearly constant value.

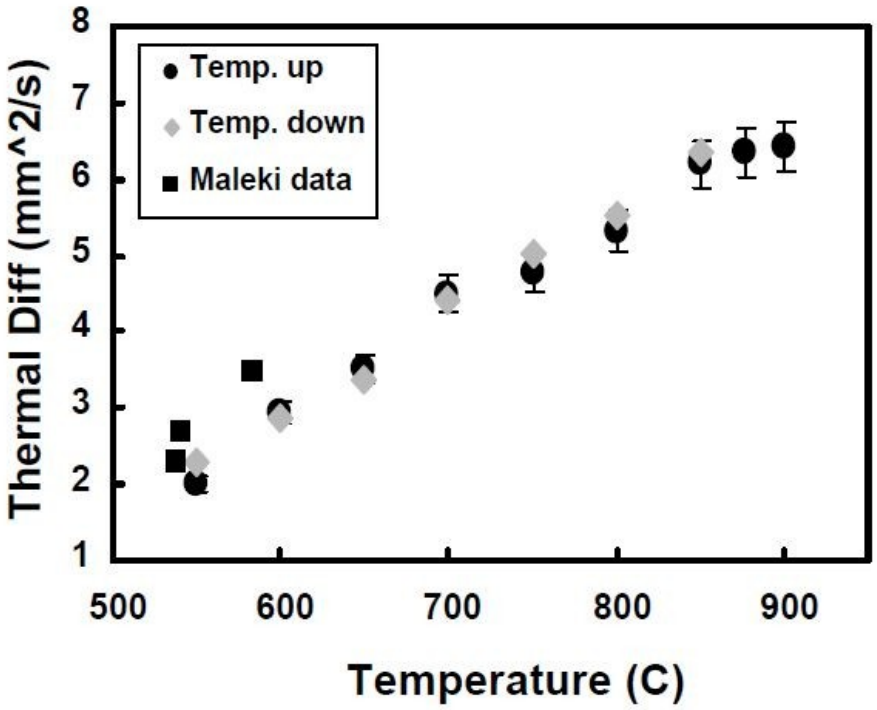

Figure 6.12 Thermal diffusivity of Te liquid as a function of temperature: "Temp. Up" and "Temp. Down" from Zhu [4] and Maleki [11] (taken from Figure 5 of Ref.[4]).

6.4.3 Graphical solution. Since the numerical solution described above cannot be easily adopted in the formulation of the software, an graphical solution, using parametric values for the transient heat transfer between the sample and fused silica cell, was developed to simultaneously determine the thermal conductivity and diffusivity [5]. The influence of fused silica cell was included and the heat transfer to the cell had a significant effect on the time-temperature response of the sample. The results indicated that this method was applicable for a wide range of sample and cell properties. The original solution assuming adiabatic environment for laser flash method became an extreme case in the current theory.

The determination of the thermal properties was presented with graphical relations between several parameters and is summarized below. The parameters include dimensionless temperature rise, ξ, time scale, τ, and parameter for thermophysical difference between the melt and the containing cell, γ.

$$\xi = \frac{\Delta T(t)}{\Delta T_{Max}} \tag{6.12}$$

where $\Delta T(t)$ is the temperature rise at time t and ΔT_{Max} is the maximum temperature rise. Then for different values of γ, the ξ vs. τ plot generated by the numerical simulation is given in Figure

6.13 below. The value of γ described the difference of thermal property between the measured sample and the known material of the cell. In the case of γ = 1, the curve represents that no cell, or, the cell is adiabatic, i.e., the thermal conductivity of the cell k_c = 0 and the time scale when ξ = 0.5 is $\tau_{1/2}$= 0.13879, the same as the value obtained by Parker [1]. There would be no heat loss, and the temperature would keep at constant after it reaches the maximum. When γ = 0, the cell has the same thermophysical properties as the sample. As shown in Figure 6.13, the decrease of the rear face temperature depends on the value of γ and, in the temperature increasing period, the time for half-temperature rise value (ξ = 0.5) changes slightly with $\tau_{1/2}$ = 0.13540 ~ 0.13879 for different values of γ.

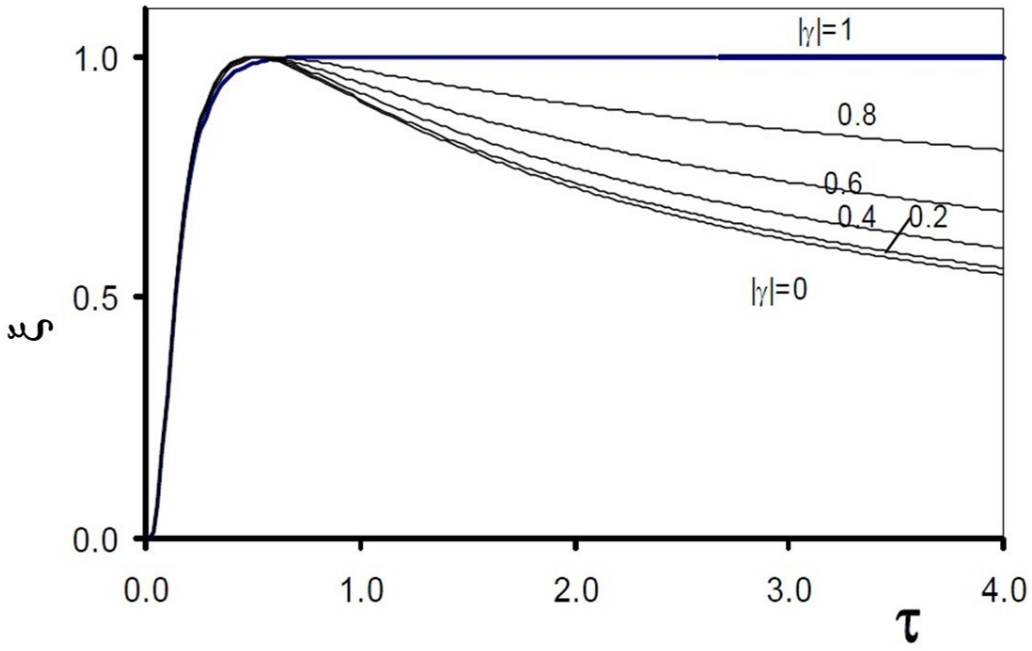

Figure 6.13 The temperature responses measured in the rear face of the cell for different values of the parameter γ (taken from Figure 4 of Ref.[5]).

To find out the value of the parameter γ from the temperature decreasing curve, two graphics have been generated from the numerical calculation. The plot of ξ vs. γ were calculated for four different values of $n\tau_{0.5}$ with n = 5, 10, 15 and 20 as given in Figure 6.14. This value of ξ at a specific time scale $n\tau_{0.5}$ can be determined from the temperature history of the experiments as shown in Figure 6.15. From this value of $\xi n\tau_{0.5,}$ the value of γ can be located in Figure 6.14 from the specific curve for each $n\tau_{0.5}$.

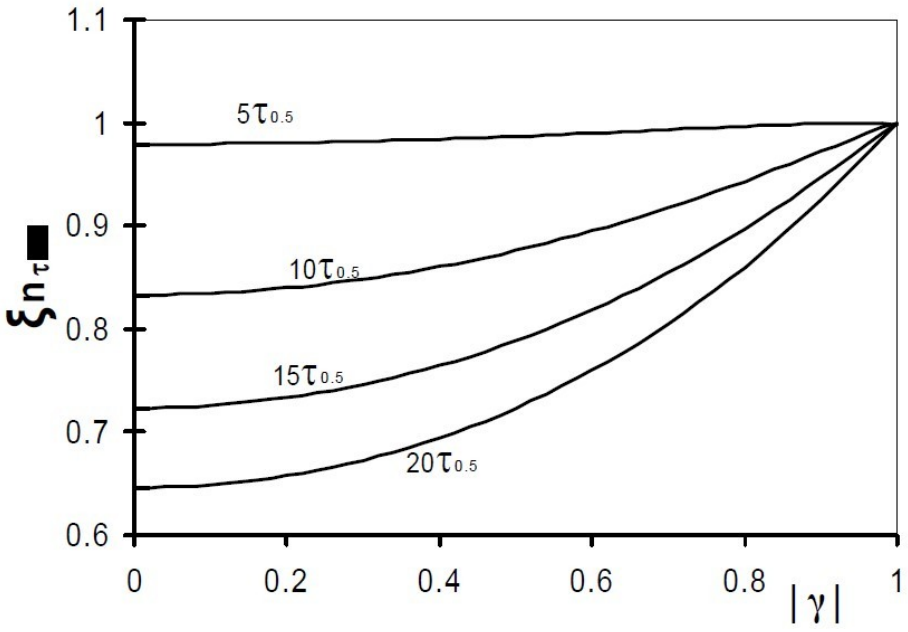

Figure 6.14 The influence of the parameter γ on the temperature at the rear face, ξ, at four different time multiples of $\tau_{0.5}$ (taken from Figure 7 of Ref.[5]).

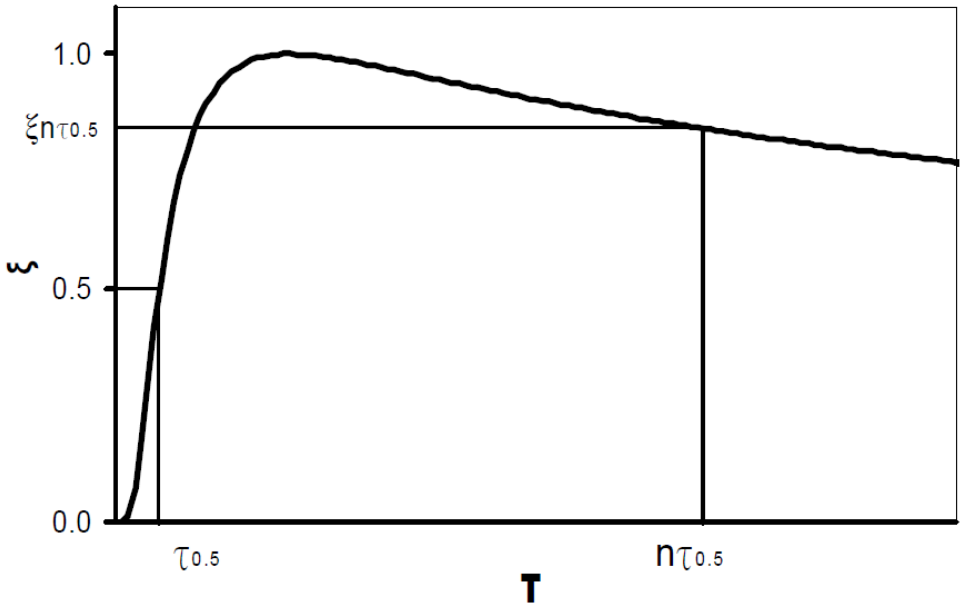

Figure 6.15 The determination of $\xi n\tau_{0.5}$ from the thermal history of the experiment (taken from Figure 6 of Ref.[5]).

The procedure to extract thermal properties of sample from experimental temperature history curve are the followings:

1. Normalize the temperature increase, $\xi(t)$, to dimensionless from 0 to 1 (Figure 6.13).
2. Determine the time to reach half of maximum temperature increase, $t_{0.5}$.
3. Find the dimensionless temperature of $\xi n\tau_{0.5}$ (in the temperature descending period) at certain appropriate time (such as $t = 10t_{0.5}$, etc.) as shown in Figure 6.15.
4. From this $\xi n\tau_{0.5}$, determine the value of γ from Figure 6.14.
5. With the value of γ , find the value of constant $\tau_{0.5}$ from Figure 6.13.
6. The value of thermal diffusivity of the melt could be obtained by:

$$D_m = \tau_{0.5} \frac{L^2}{t_{0.5}} \tag{6.13}$$

7. And the values of thermal conductivity k_m and specific heat capacity c_m of the melt can be obtained from D_m, γ, the thermal diffusivity of the cell material, D_c, and thickness and density of the sample, L and ρ_m, respectively:

$$k_m = \frac{1+\gamma}{1-\gamma} \sqrt{\frac{D_m}{D_c}} \frac{L^2}{t_{0.5}} \tag{6.14}$$

$$C_p = \frac{k_m}{\rho_m D_m} \tag{6.15}$$

This modified method is able to derive both thermal diffusivity and thermal conductivity of the melt as well as heat capacity with the knowledge of the sample density. The essence of this modified approach is that the value of 0.1388 in Eq.(6.4) adopted for the adiabatic condition needs to be modified when the rear face temperature is decreasing, as shown in Figure 6.9, because of the heat conduction between the sample and the containing cell and the adiabatic condition is no longer valid. The characteristic of the decreasing temperature results in a parametric value of γ which can be related to a constant $\tau_{0.5}$ different from 0.1388, usually smaller, to be applied in Eq.(6.13) to calculate the thermal diffusivity, D_m. Also, the thermal conductivity of the melt can be derived from the values of D_m, γ and D_c as given by Eq.(6.14).

The modified analysis described above shows that, by assuming the adiabatic condition, the usual adoption of the constant 0.1388 results in slight overestimation of the thermal diffusivity. In this heat transfer analysis only thermal conductivity (between sample and cell) was considered and, therefore, in the case of no cell container or the container is adiabatic or $\gamma = 1$ the sample temperature at the rear face remains constant after reaching its maximum. In the real thermal environment during experimenting, even in the case of no cell container, heat loss through radiation will occurs and the measured rear face temperature will decrease, maybe slightly, after its maximum. The magnitude of temperature decreasing depends on the temperatures of the sample and its surrounding environment.

References

[1] W. J. Parker, R. J. Jenkins, C. P. Butler and G. L. Abbot, J. Appl. Phys. 32 (1961) 1679.
[2] R. E. Taylor, J. Gembarovic and K. D. Maglic, *Characterization of Materials,* p.392 John Wiley & Sons, Inc. (2002).
[3] Bochuan Lin, Heng Ban, Chao Li, Rose Scripa, Ching-Hua Su and Sandor Lehoczky, Proceedings of 2003 ASME Summer Heat Transfer Conference, ISBN 0-7918-3679-7, Vol. 1, pp. 47448.1-7 (2003).
[4] Shen Zhu, C. Li, Ching-Hua Su, B. Lin, H. Ban, R.N. Scripa and S.L. Lehoczky, J. Crystal Growth, 250 (2003) 269.
[5] Bochuan Lin, Heng Ban, Chao Li, Rosalia Scripa, Ching-Hua Su and S. L. Lehoczky, proceedings of the International Mechanical Engineering Congress and Exposition (IMECE), IMECE2005-79932 p.725 (2005).
[6] R. F. Brebrick, Ching-Hua Su, and Pok-Kai Liao, in *Semiconductors and Semimetals,* Vol. 19, Chap. 3, edited by R. K. Willardson and A. C. Beer, Academic, New York (1983).
[7] T.-C. Yu and R. F. Brebrick, *J. Phase Equilib*. 13 (1992) 476.
[8] Ching-Hua Su, J. Crystal Growth 78 (1986) 51.
[9] Ching-Hua Su, Yi-Gao Sha, K. Mazuruk and S. L. Lehoczky, J. Appl. Phys. 80 (1996) 137.
[10] L. R. Holland and R. E. Taylor, J. Vac. Sci. Technol. A 1 (1983) 1615.
[11] H. Maleki and L. R. Holland, J. Appl. Phys. 76 (1994) 4022.
[12] Yi-Gao Sha, Ching-Hua Su, K. Mazuruk and S. L. Lehoczky, J. Appl. Phys. 80 (1996) 752.
[13] M. Clark and R. E. Taylor, J. Appl. Phys. 46 (1975) 714.
[14] R. D. Cowan, J. Appl. Phys. 34 (1963) 926.
[15] W. J. Parker, R. J. Jenkins, C. P. Butler, and G. L. Abbott, J. Appl. Phys. 32 (1961) 1679.
[16] J. A. Cape and G. W. Lehman, J. Appl. Phys. 34 (1963) 1909.
[17] D. Chandra and L. R. Holland, J. Vac. Sci. Technol. A 1 (1983) 1620.
[18] GE Company website, www.ge.com.
[19] H. Thurn and J. Ruska, J. Non-Cryst. Solids 22 (1976) 331.
[20] R. A. Medzhidovand S. M. Rasulov, Inorg. Mater. 11 (1975) 555.
[21] O. Kubaschewski and F. E. Witting, Elektrokhimiya 47 (1941) 433.
[22] S. Takeda, H. Okazaki, S. Tamaki, J. Phys. Soc. Jpn. 54 (1985) 1890.
[23] R. P. Yurchak, B. P. Smirnov and L. S. Kanevskaya, Sov. Phys. Semicond. 3 (1970) 923.
[24] E. V. Shadrichev and I. A. Smirnov, Sov. Phys. Semicond. 1 (1967) 416.
[25] A. Menelle, R. Bellissent, and A. M. Flank, Europhys. Kett. 4 (1987) 705.
[26] B. Cabane and J. Friedel, J. Phys. (Paris) 32 (1971) 331.

Chapter 7
Physics and Chemistry of Te and HgTe-based Ternary Melts

Abstract: With all of the experimental and theoretical results presented in the earlier chapters of this book, the review and analysis are focused on the physics and chemistry of the melts of Te and two HgTe-based ternaries, i.e., the Hg-Cd-Te and Hg-Zn-Te systems. Using the data of thermal and electrical conductivities of the solids and melts of Te, HgTe, $Hg_{0.9}Cd_{0.1}Te$ and $Hg_{0.8}Cd_{0.2}Te$, the derived Lorenz number indicates a transition from semiconductor to metal during melting. From the results and analyses of various thermophysical properties, the Te melt has consistently shown structural transformation. The implication of a two-fold coordination semiconducting domain transforms to the three-fold coordination metallic domain in the range of 500ºC to 600ºC was evident from the data of density measurements, neutron scattering, electrical conductivity, the free activation energy of the viscus flow and the viscosity-density correlation theory. From the Gibbs energy of dissociation for the molecular species, namely, HgTe, CdTe and ZnTe, in the binary systems, the structural transition of the liquid phase can be interpreted as, when the temperature increases, the atomic species gradually starts to dominant the liquid phase and eventually, at rather high temperatures for the cases of CdTe and ZnTe, approaches to become a normal homogeneous phase of atomic species. The neutron scattering measurements on the three binary systems show that, in the case of CdTe and ZnTe, the coordination number remains to be 4, same as the solid, but increases to about 6.3 for the HgTe melt. The heavier HgTe compound undergoes a major structural change from semiconducting to metallic during the melting that the bond distances and coordination numbers increase. An *Ab Initio* molecular dynamics simulation confirmed the cases of CdTe and ZnTe. In the HgCdTe system, the density for HgTe and $Hg_{0.9}Cd_{0.1}Te$ melts go through a maximum at temperatures just above the melting point, similar to the case of Te melt. From the viscosity-density correlation theory, the data of the HgTe and $Hg_{0.9}Cd_{0.1}Te$ melts imply a structural transition at approximately, 805ºC and 793ºC, respectively. On the studies of the relaxation behavior, after rapid cooling from 857ºC to 800ºC, the measured viscosity of the $Hg_{0.8}Cd_{0.2}Te$ melt went through a maximum after 2 hrs, then started to decline approximately 60% over a period of 50 hrs to reach its equilibrium value. On the HgZnTe system, a maximum in the melt density was not observed for the $Hg_{0.90}Zn_{0.10}Te$ and $Hg_{0.84}Zn_{0.16}Te$ melts and the density of $Hg_{0.90}Zn_{0.10}Te$ sample showed a hysteresis loop with a higher measured value during cooling than heating. The measured viscosity of the $Hg_{0.84}Zn_{0.16}Te$ melts start from $1.0x10^{-3}cm^2/s$ at 770ºC, just above the liquidus temperature, to a maximum of $1.4x10^{-3}cm^2/s$ at 810ºC and decreases to $1.2x10^{-3}cm^2/s$ at 850ºC. On the relaxation studies on the viscosity of $Hg_{0.84}Zn_{0.16}Te$ melt, two sets of data were obtained as functions of time after the ampoules were cooled from 850°C and stabilizing at temperatures of 810°C 790°C. It took one day and 5 days, respectively, for the 810°C and 790°C stabilization, to reach the steady state. Similar observation has been reported on the viscosity measurements in the Al-rich Al-Y melts and it was claimed to be the results of competition of two simultaneous effects. Lastly, the effects of these phenomena in the HgTe-based ternary melts on the process of crystal growth from melt are discussed.

Keywords: Relaxation; Tellurium (Te); Mercury-cadmium-tellurium (Hg-Cd-Te) system; Mercury-zinc-tellurium (Hg-Zn-Te) system

7.1 Lorenz numbers for the solids/melts of Te, HgTe, $Hg_{0.9}Cd_{0.1}Te$ and $Hg_{0.8}Cd_{0.2}Te$

7.1.1 Introduction. In the 1850's, Wiedemann and Franz reported that the ratio of thermal conductivity, κ, to electrical conductivity, σ, for different metals has the same value at room temperature [1]. In 1872, Lorenz further claimed [2] that this ratio increases linearly with absolute temperature T as:

$$\kappa / \sigma = LT \tag{7.1}$$

where L is the so-called Lorenz number. By assuming similar scattering models for the thermal and electrical conductions of free electron gas and applying Fermi-Dirac statistics for metals, Sommerfeld derived [3] the theoretical value for the Lorenz number, L_0, as:

$$L_0 = \frac{\pi^2}{3}\left(\frac{K_B}{e}\right)^2 = 2.44 \times 10^{-8} ¿) \tag{7.2}$$

where K_B is Boltzmann's constant, and e the electron charge.

Theoretically, with the assumption of equal electron mean-free-paths for the electrical and thermal conductions, this Lorenz number is only applicable to metals and degenerate semiconductors. In reality, the major electron scattering mechanisms in the electrical and thermal conductions of the solid consist of elastic scattering by the impurities and lattice defects in the low temperature range as well as the inelastic scattering by phonons in the high temperature range. Hence, depending on the band structure, the Fermi level and the carrier concentration, the measured Lorenz number can deviate from the value of L_0. The experimental Lorenz numbers have been reviewed for metals, semi-metals, alloys and degenerate semiconductors [4] and, in most cases, the values fall within the range between 1.8 and 5.4 x 10^{-8} (W/K^2). Recently, the subject of Lorenz number has been studied [5-8] on semiconductors for the thermoelectric applications which convert heat into electrical energy with an efficiency rated by Figure of Merit, $zT = \alpha^2(\sigma T/\kappa) = \alpha^2/L$ where α is Seebeck coefficient. These studies focused on the efforts to minimize Lorenz number (or thermal conductivity) while maintaining the level of electrical conductivity.

The thermophysical properties for the liquid metals have also been reported. However, in most of the cases, the value of L_0, give in Eq.(7.2), has been used to derive thermal conductivity from the measured electrical conductivity [9,10]. It has been reported [11] that for the pure liquid metals, such as Al, Sn, Pb and Cu, their thermal conductivities calculated from electrical conductivities, using the Wiedemann-Franz law given in Eq.(7.1) and (7.2), are close to the experimental results. In this section, using the measured thermal and electrical conductivity as functions of temperature, the Lorenz number for the solid/melt of Te, HgTe, $Hg_{0.9}Cd_{0.1}Te$ and

$Hg_{0.8}Cd_{0.2}Te$ will be examined to study the scattering nature of conduction in Te and $Hg_{1-x}Cd_xTe$ ternary.

7.1.2 Experimental measurements of Te solid. The present study has extended the knowledge of the published results, give in early sections, to the solid phase of Te by measuring its thermal and electrical conductivity [12]. The sample of Te, 99.99999% purity from 5 N Plus Inc., was loaded into a previously cleaned and baked fused silica ampoule of 20mm OD and 16mm ID. The sample was processed through directional solidification in a vertical tubular furnace.

The grown ingot was sliced into discs of 16mm diameter and 3mm thickness. The thermal diffusivity of the Te disc was measured by the Flashline 3050 System from Anter Corp. (now TA Instruments). In the flash technique, as described in Chapter 6, when the sample was heated to reach a steady state at a preset temperature, the radiant energy of a high-intensity light/laser pulse was absorbed on the front surface of the disc and the resultant temperature rise on the rear face was recorded by an IR detector. The diffusivity was calculated from the measured thermogram using the Clark et al. analysis [13]. The heat capacity of solid Te was adopted from Ref.[14] as:

$$C_p\ (J/mol\text{-}K) = 24.614 + 3.217 \times 10^{-3}T + 1.678 \times 10^{-6}T^2 \qquad \text{for } 198K < T < 723K \quad (7.3)$$

The crystal structure of Te has spiral chains of bonded atoms packed in hexagonal layers. The measured thermal expansion coefficients [15], in the $10^{-6}K^{-1}$ range, showed a negative value parallel to the c-axis and a positive value perpendicular to the c-axis. Hence, the density at room temperature, $6.24 g/cm^3$, was used for the temperature range between room temperature to the melting point of 450°C and the thermal conductivity was derived from the diffusivity, heat capacity and density given by Eq.(7.4).

$$\kappa = \rho C_p D \qquad (7.4)$$

After the thermal conductivity measurements, a rectangular prism in the shape of 2.5 x 2.5 x 14 mm was cut in the middle section of the sample disc for the electrical conductivity and Seebeck coefficient measurements, which were conducted simultaneously from room temperature to 420°C by a ZEM-3 instrument provided by ULVAC-RIKO Inc. The electrical conductivity was determined from ten measured I-V points and the Seebeck coefficient was derived from the values of Seebeck voltages measured over a 6mm distance along the sample length under three different applied thermal gradients.

congruent melting HgTe show an almost linear increase as a function of temperature. For the sample of $Hg_{0.9}Cd_{0.1}Te$, with the solidus and liquidus temperatures of 686°C and 739°C [17], respectively, the measured κ in the solid+liquid two-phase zone scattered by first decreasing from 0.0071W/cm-K at 687°C, 0.0069W/cm-K at 690°C, to 0.0067W/cm-K at 695°C and then increasing to 0.0126W/cm-K at 707°C and 0.0155W/cm-K at 736°C. After the complete melting of the sample, the measured thermal conductivity went up almost linear with temperature. Similar behavior can be described for the $Hg_{0.8}Cd_{0.2}Te$ sample. With the solidus and liquidus temperatures of 703°C and 799°C, respectively, the measured κ first decreased to 0.0063W/cm-K at 707 and 717°C and then increased to 0.0092W/cm-K and 0.0188W/cm-K at 752 and 797°C, respectively. The data in the complete melt region increased linear as a function of temperature. It is speculated that the data scattered in the two-phase zone because the optical pulsed heat could not be absorbed and transferred uniformly over the disc of the inhomogeneous (solid+liquid) samples. The data in the liquid phase were fitted by the expression:

$$\kappa \text{ (W/cm-K)} = A + BT \text{ (T: temperature in } ^oC) \tag{7.5}$$

The values of A and B, the correlation coefficient and the number of data for each sample are given in Table 7.1.

Table 7.1. The best fit parameters A and B in Eq.(7.5) for the thermal conductivity of each melt, the correlation coefficients (C.C.) and numbers of data points for the fit.

Sample	A	B	C.C.	Data number
Te	– 0.04142	1.4804×10^{-4}	0.997	10
HgTe	– 0.1242	2.0327×10^{-4}	0.997	13
$Hg_{0.9}Cd_{0.1}Te$	– 0.07232	1.2000×10^{-4}	0.998	13
$Hg_{0.8}Cd_{0.2}Te$	– 0.0572	0.9735×10^{-4}	0.998	6

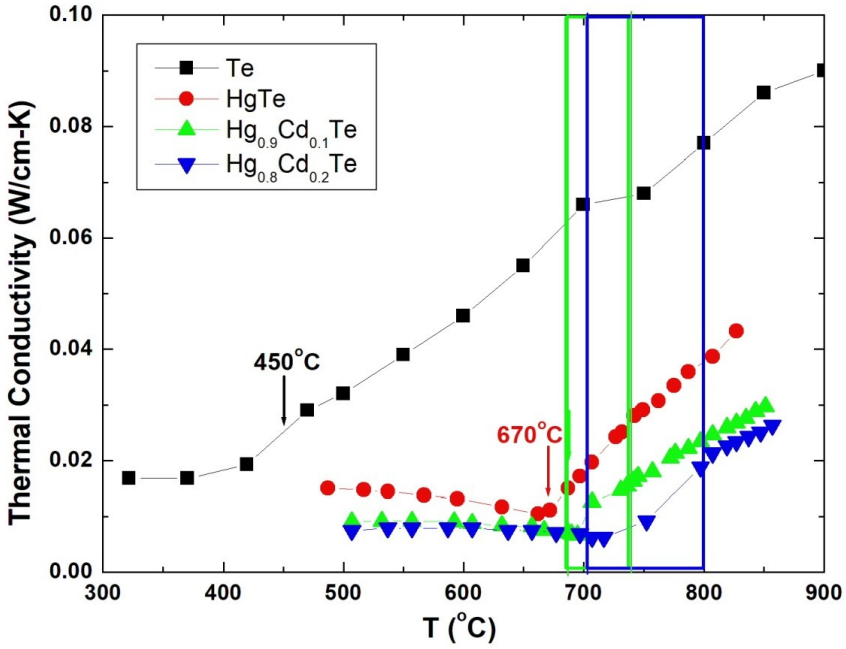

Figure 7.1. The measured thermal conductivities vs. temperature for the solid and liquid phases of Te, HgTe, $Hg_{0.9}Cd_{0.1}Te$ and $Hg_{0.8}Cd_{0.2}Te$ [16]. The melting temperatures for Te and HgTe were marked and the ranges between the solidus and liquidus temperatures for $Hg_{0.9}Cd_{0.1}Te$ and $Hg_{0.8}Cd_{0.2}Te$ are shown as bands in their respective colors.

7.1.4 Measured electrical conductivity of solids/melts of Te and $Hg_{1-x}Cd_xTe$. The measured electrical conductivity, σ, of solid Te and previous data for Te liquid [18] are plotted in Figure 7.2 as log(σ) vs. 1000/T(K). As shown in the figure, the data of the solid phase can be fitted well by a straight line as: $\log_{10}\sigma$ (S/cm) = 3.025 – 0.7966(1000/T) which implies that the high purity Te sample can be treated as intrinsic semiconductor. Assuming that the mobilities of electron and hole are independent of temperature, the electrical conductivity can be approximated by:

$$\sigma = AT^{3/2}\exp(-E_g/2K_BT) \qquad (7.6)$$

where A is a constant, E_g the energy bandgap and K_B the Boltzmann constant (8.617×10^{-5} eV/K). From the slope of the linear fit, the value of E_g can be derived to be 0.316eV which is a little lower than the reported value of 0.335eV [19] at room temperature. The difference could have been caused by the decrease in the energy bandgap when temperature increases as well as the factor of $T^{3/2}$ in Eq.(7.6). To examine the characteristics of the melt, a red line segment with the same slope, i.e., the same energy bandgap as the solid, was also plotted from the melting point 450°C to 560°C. After melting, the measured value kept on increasing with the same slope as the solid Te until it reached about 510°C where it started to flatten at higher temperatures. This implies that the Te liquid still preserves some of its solid structure after melting till about 60°C above its melting temperature.

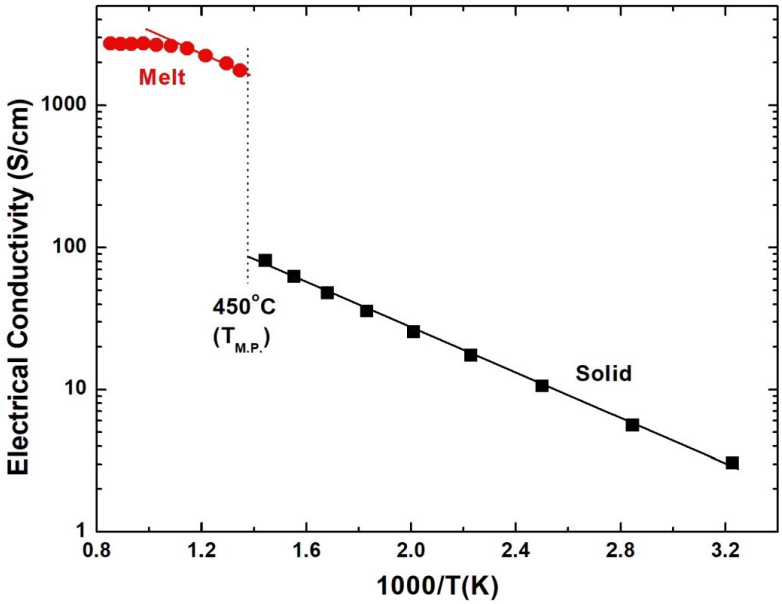

Figure 7.2. The measured electrical conductivity, σ, of high-purity Te solid and melt plotted as log(σ) vs. 1000/T(K). The data of the solid phase can be fitted well by a straight line and a red line with the same slope is plotted over the first few points of the melt.

The measured electrical conductivities for the HgTe, $Hg_{0.9}Cd_{0.1}Te$ and $Hg_{0.8}Cd_{0.2}Te$ solids and melts, shown in Figure 5.24, 5.25 and 5.26, respectively, together with the results of Te solid/melt are plotted as function of temperature in Figure 7.3. The measured σ for the solids are flat except a slight lowering trend with increasing temperature for HgTe, presumably caused by the presence of large amounts of Hg vacancies as acceptors [20]. The change in electrical conductivity from solid to liquid at the solidus temperature of HgCdTe samples is not as large as in the case for Te sample. In the temperature ranges of completely melted, the measured electrical conductivities increase with increasing temperature.

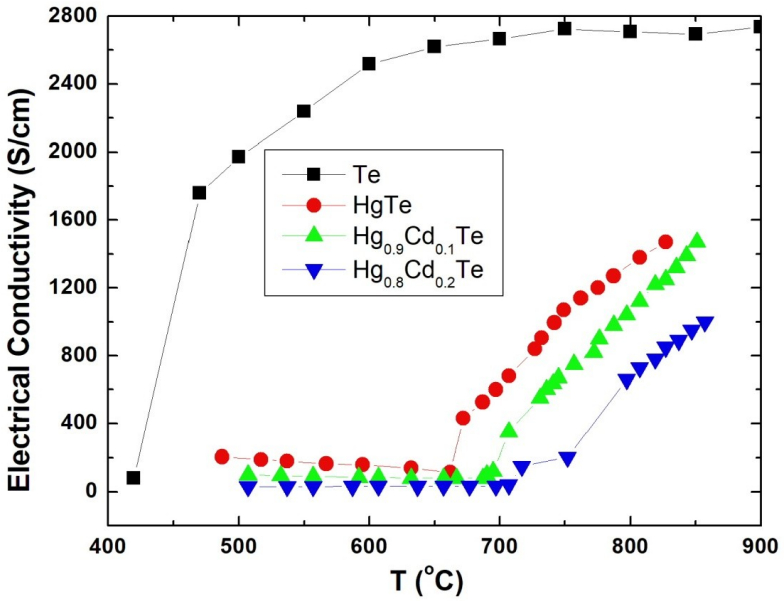

Figure. 7.3. The measured electrical conductivities of the solids and melts of three HgCdTe samples together with the data of pure Te element are plotted against temperature.

7.1.5 Lorenz number. The Lorenz numbers, L, for the solids and melts of Te, HgTe, $Hg_{0.9}Cd_{0.1}Te$ and $Hg_{0.8}Cd_{0.2}Te$ were calculated from the experimental results and are given in Figure 7.4. The L values for the Te solids in the low temperature range (not shown in the figure) start with a large number of $3.1x10^{-5}W/K^2$ at 37°C then gradually decrease to $2.5x10^{-6}W/K^2$ at 176°C, $8.7x10^{-7}W/K^2$ at 273°C and $4.4x10^{-7}W/K^2$ at 371°C. However, after the melting at 450°C, the Lorenz numbers were almost constant, close to L_0 of the free-electron gas, over the temperature range of 500 to 900°C. As the energy bandgap increasing with higher CdTe content, x, in the $Hg_{1-x}Cd_xTe$ materials, the measured L values showed a lower to higher deviation from L_0, following the order of x = 0, 0.1 and 0.2, i.e., from semi-metal to larger bandgap semiconductors. In the melt cases, just above the congruent melting temperature of 670°C, the Lorenz number of the HgTe melt at 672°C dropped rapidly from $9.7x10^{-8}$ to $2.7x10^{-8}W/K^2$ which is slightly higher than L_0. For the sample of $Hg_{0.9}Cd_{0.1}Te$, with the solidus and liquidus temperatures of 686°C and 739°C, respectively, the measured L values decreased from $9.3x10^{-8}$ at 687°C, $7.2x10^{-8}$ at 690°C, $5.8x10^{-8}$ at 695°C to $2.56x10^{-8}W/K^2$ at 736°C. For $Hg_{0.8}Cd_{0.2}Te$ sample, with the solidus and liquidus temperatures of 703°C and 799°C, respectively, the Lorenz number decreased slowly from $2.2x10^{-7}$ at 697°C, $1.6x10^{-7}$ at 707°C, $4.4x10^{-8}$ at 752°C to $2.7x10^{-8}W/K^2$ at 797°C. The Lorenz numbers for the solid of the ternary compositions were higher than the value of L_0, implying the characteristics of non-degenerate semiconductor. With the increasing value of x, or the larger the bandgap, the materials become more non-degenerate and the deviation from L_0 become larger. As the ternary solids started to melt, the measured values of L for all three samples start to decrease, as described above, and eventually reach values close to L_0 just above their respective liquidus and stay around L_0 at higher temperatures. The results suggest that, at temperatures high enough, the melts of Te, HgTe, $Hg_{0.9}Cd_{0.1}Te$ and $Hg_{0.8}Cd_{0.2}Te$ behavior similarly to metals or degenerate semiconductors, i.e., a body of free-electron gas with minimum contribution to thermal conductivity from the scattering of lattice defects or/and the inelastic scattering from the phonons.

As a comparison, for the wide bandgap semiconductor of CdTe solid, the thermal conductivity and electrical conductivity were measured over the temperature range between 346 and 772°C [21] and the corresponding Lorenz number deviate tremendously from L_0 – starting from 0.0076 at 346°C, decreasing to $7.7x10^{-4}$ at 494°C, to $1.1x10^{-4}$ at 693°C and to $3.9x10^{-5}W/K^2$ at 772°C.

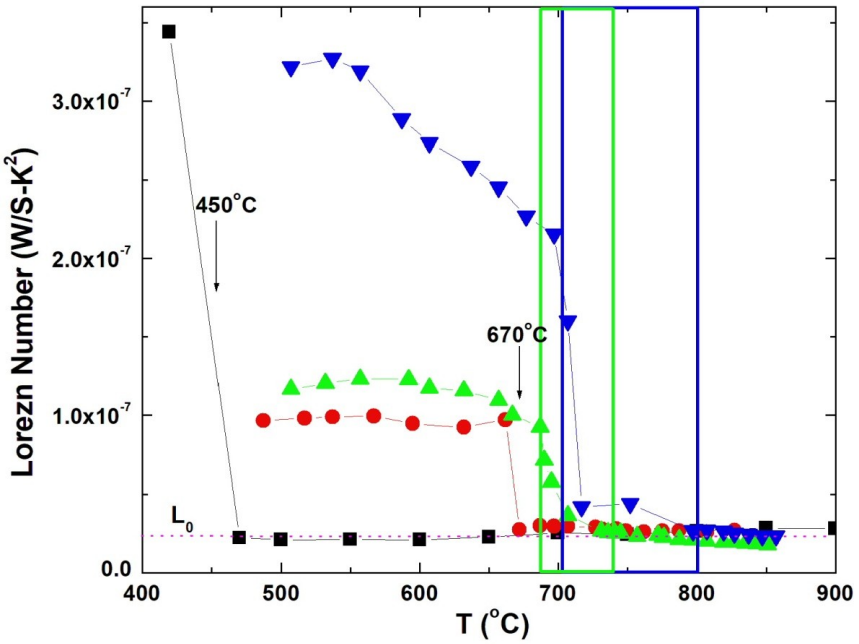

Figure 7.4. Calculated Lorenz numbers as functions of temperature for the solids and melts of Te, HgTe, $Hg_{0.9}Cd_{0.1}Te$ and $Hg_{0.8}Cd_{0.2}Te$ with the same symbols shown in Figure 7.3. The melting points for Te and HgTe are marked and the solidus temperatures of 686 and 703°C, and liquidus points of 739 and 799°C for x = 0.1 and 0.2, respectively. The two-phase regions are shown as two bands with their respective colors. The Lorenz number for free-electron gas, L_0 = 2.44×10^{-8} W/S-K^2, is also labeled as dotted line.

7.2 Physics and chemistry of Te melt

Usually, a liquid shows the normal thermal expansion when its density decreases as temperature increases because the inter-atomic/molecular distance increases as temperature goes up. However, when there is a structural rearrangement in the melt, the normal expansion sometimes can be shadowed. As shown in Figure 4.2, the density of Te increased from the melting point of 450°C to a maximum at 479°C before it followed the trend of normal thermal expansion. This structural transition was also observed in the neutron scattering experiments [22] that the average first coordination number of liquid Te atoms at its melting point was 2.63 which increased to approximately 3 at 600°C. It indicated that the increase of melt density is dominated by the increase in its average first coordination number which overshadows the normal thermal expansion. When the temperature increased above 600°C to 800°C, the first coordination number remained constant at 3 and the thermal expansion took over with the density of liquid Te decreasing as the temperature increased. A coordination number of 2.63 implies a mixture of structural domains of two- and three-fold coordination. Using other neutron scattering results [23] and the Knight-shift data [24,25], Cabane and Friedel [26] included their nuclear magnetic resonance (NMR) data and proposed that, upon melting, Te forms polymer-like chain segment and the two-fold coordination domain is semiconducting and the three-fold coordination domain is metallic with the transition occurs at about 477°C. This temperature agrees well with the temperature of density maximum 479°C where the normal thermal expansion starts to dominate.

Following the transition, the melt structure continuously changes with increasing temperature, until about 680ºC, the average number of nearest neighbor atoms is about three . Above this temperature, the melt structure is considered to be atomically homogenous with free-electron-like properties. Cohen and Jortner [27-30] proposed a model of continuous semiconductor to metal transition that the melt was considered inhomogeneous in the sub-macroscopical scale. Two separated domains coexist with one domain having a two-fold non-metallic characteristic and the other three-fold domain having a metallic one. The changes of the thermophyical properties as functions of temperature are induced by the relative change in the fractions of these two domains. Adopting this inhomogeneous domain model, they have developed an effective-medium theory and quantitatively calculate that the volume fraction of the metallic three-fold coordination region increases from 82% at the melting temperature to saturate toward 100% at elevated temperature as shown in Figure 4.3. As shown in Figure 7.2, above the melting point of 450ºC, the electrical conductivity, σ, jumps by more than ten times to about 2000S/cm and the value keeps on increasing with the same slope as the solid Te until it reaches about 520ºC when it starts to saturate at higher temperatures. This implies that the Te liquid still preserves some of the energy band structure of its solid after melting till about 70ºC above the melting point. Similar phenomena have been reported and interpreted with the inhomogeneous model in the systems of Se-Te, In_2Te_3 and Ga_2Te_3 on the molar volume, electrical conductivity, NMR and other thermophysical properties [31-34].

It was discussed in Chapter 5 that viscosity is a bulk property defined as a fluid's resistance to flow or to deform by shear or tensile stress. It can be viewed as a measurement of the average intermolecular forces between the species of atoms/molecules. For a regular liquid, as temperature increases, the average intermolecular distance increases and the average speed of species increases which results in the decrease of viscosity because of the lower resistance to move and flow. As shown in Section 5.3.2.1, the free activation energy of the viscous flow F_b can be calculated from the measured kinematic viscosity by Eq.(5.3) and can be expressed in terms of enthalpy H_b and entropy S_b [35]. The calculated free activation energy of the viscous flow in Te liquid, shown in Figure 5.11, increases slowly as a function of temperature just above the melting point of Te. Then, at the temperature around 600ºC (873K), the free activation energy increases more rapidly. Assuming H_b and S_b are constants, the activation enthalpy and entropy of viscous flow for the Te liquid were determined to be, respectively, 21.0 kJ/mole and –10.0J/mole-K below 600ºC and 13.01kJ/mole and –18.86J/mole-K above 600ºC. The difference in the slope means that the mechanism of resistance to viscus flow has changed which is another indication of a structural transition occurring in the liquid. The transition temperature of 600ºC is consistent with the temperature reported above where the coordination number reaches 3.

Based on another assumption that the viscosity of a liquid is governed by the nature of the interaction between the atoms or molecules, viscosity was correlated to the structure and interaction of a liquid by Eq.(5.4) [36] in Chapter 5, which states that the reciprocal of the kinematic viscosity is a linear function of its density if the melt structure is homogeneous. Figure 5.12 shows the plot of the reciprocal of the kinematic viscosity vs. the measured density of liquid tellurium that the data above 607ºC (880K) can be fitted well by a straight line. As the temperatures getting below 607ºC, the data start to deviate from the linear line, which implies a structural transition in the liquid, i.e., the Te melt starts to maintain a homogeneous structure when the temperature reaches above 600ºC. This is also consistent with the neutron scattering

results that the average first coordination number of liquid Te atoms is 2.63 at its melting point which increased to approximately 3 at 600°C and stayed at 3 as the temperature was raised to 800°C.

On the measurements of the relaxation behavior of Te melt reported in Chapter 4, 5 and 6, it was concluded that no relaxation behavior was observed both in the measured density when Te melt was rapidly cooled from 850°C to 550°C and in the electrical conductivity after cooled from 900°C to 550°C. However, the measured viscosity of Te melt, displayed in Figure 5.16 as functions of time after the melt was quenched from 900 to 557°C that about 6 hrs was needed for the measured values of viscosity to reach steady state value. The phenomenon was interpreted by the polymerization kinetics of the Te atom attaching and detaching reactions to the Te chain.

In summary, from the results and analyses of various thermophysical properties, the melt of Te has shown structural transformation consistently. Firstly, the density of Te melt increases from its melting point to a maximum at 479°C, which implies that a structural change is mostly completed, and normal thermal expansion starts to dominate at the temperature. Secondly, from the neutron scattering results, the Knight-shift data and NMR measurements, it was proposed that, upon melting, Te forms polymer-like chain segment with the two-fold coordination semiconducting domain transforms to the three-fold coordination metallic domain with the transition occurs at about 477°C. Thirdly, when the measured electrical conductivities, σ, were plotted as log(σ) vs. 1000/T(K), the measured values kept on increasing with the same slope as that of the solid Te after the melting until it reached about 515°C where it started to flatten out – implying a semiconductor to metal transition. Fourthly, the free activation energy of the viscous flow F_b derived from the measured kinematic viscosity as a function of temperature shows difference in its slope at about 600°C, indicating a structural transition occurring in the liquid. Fifthly, the correlation theory states that the reciprocal of the kinematic viscosity is a linear function of its density if the melt structure is homogeneous. The plot of the reciprocal of the kinematic viscosity vs. the measured density of liquid tellurium shows that the data above 607°C can be fitted well by a straight line, which implies a structural transition in the liquid.

7.3 Physics and chemistry Hg-Cd-Te system

7.3.1 Structural transformation in the melts

7.3.1.1 Dissociation of the molecular species. In the associated solution treatment of the liquid phase, given in Chapter 3, a three-element system such as the Hg-Cd-Te (or Hg-Zn-Te) system, the liquid is assumed to consist of five species: Hg, Cd and Te atomic species and HgTe and CdTe (or ZnTe) molecular species. From the calculated results of the model for the three binary systems [17], the mole fraction of the binary species in the liquid phase at the melting point with 50 atomic % Te and is 0.4894 for HgTe, 0.9465 for CdTe, and 0.9380 for ZnTe. It implies that, during melting of the binary compounds, about half of the HgTe lattice remains as species of HgTe molecules with the rest forming Hg and Te atomic species and more than 90% of the CdTe and ZnTe lattice stay as molecules of CdTe and ZnTe species. When the temperature of the melts going up, the dissociation reaction follows the Gibbs energy of dissociation, ΔG_D^o, for species 4, or AC, and species 5, or BC, respectively. As a term of Gibbs

energy, they have the usual form of $\Delta G_D^o = \Delta H_D - T\Delta S_D$. In the case of the Hg-Cd-Te melt, species 4 and 5 represents HgTe and CdTe whereas in the Hg-Zn-Te melt, species 4 and 5 represents HgTe and ZnTe. The values of ΔH_D and ΔS_D for the three binary species, listed in Table 3.1 and 3.2, are given in Table 7.2.

Table 7.2 Dissociation energy for the three molecular species in the liquid.

Molecular species	Species designation	Dissociation enthalpy and entropy
HgTe	Hg Te HgTe 1 3 4	$\Delta H_4^o = 42230$ cal $\Delta S_4^o = 26.877$ cal/K
CdTe	Cd Te CdTe 1 3 5	$\Delta H_5^o = 69288$ cal $\Delta S_5^o = -0.774$ cal/K
ZnTe	Zn Te HgTe 1 3 5	$\Delta H_5^o = 88499$ cal $\Delta S_5^o = 13.611$ cal/K

The chemical activity of each species, a_i, can be obtained from the product of its activity coefficient, γ_i, and mole fraction, y_i. From Eqs.(3.11) and (3.12), the ratio of the product of the activities of the atomic species to the activity of molecular species is related to the Gibbs energy of dissociation as:

$$\frac{a_1 a_3}{a_4} = \frac{\gamma_1 y_1 \gamma_3 y_3}{\gamma_4 y_4} = \exp\ ¿) \qquad (7.7)$$

$$\frac{a_1 a_3}{a_5} = \frac{\gamma_1 y_1 \gamma_3 y_3}{\gamma_5} = \exp\left(\frac{-\Delta G_5^o}{RT}\right) \qquad (7.8)$$

From the Gibbs energy of dissociate given in Table 7.2 and Eqs.(7.7) and (7.8), this ratio, defined by the left-hand side of Eqs.(7.7) and (7.8), is calculated as a function of temperature and plotted against 1000/T in Figure 7.5. The figure shows that, in the dissociation case of HgTe, this ratio is much higher than the cases of the CdTe and ZnTe species. This is consistent with the calculated mole fractions of the compound species at the melting temperature and 50 at.% Te discussed above. Although the CdTe molecule has the largest value of the associated species at the congruent melting point among the three systems, however, when they are compared with each other at one temperature, ZnTe still has the largest value for the mole fraction of the compound species at 50 atomic % Te. It should be noted that this activity ratio increases exponentially as a function of temperature for all three systems, with the highest rate for the ZnTe case, $\Delta H_5^o = 88{,}499$cal, and lowest for HgTe, $\Delta H_4^o = 42{,}230$cal. The structural transition of the liquid phase can be interpreted as, when the temperature increases, the atomic species

gradually starts to dominant the liquid phase and eventually, at rather high temperatures for the cases of CdTe and ZnTe, approaches to become a normal homogeneous phase of atomic species.

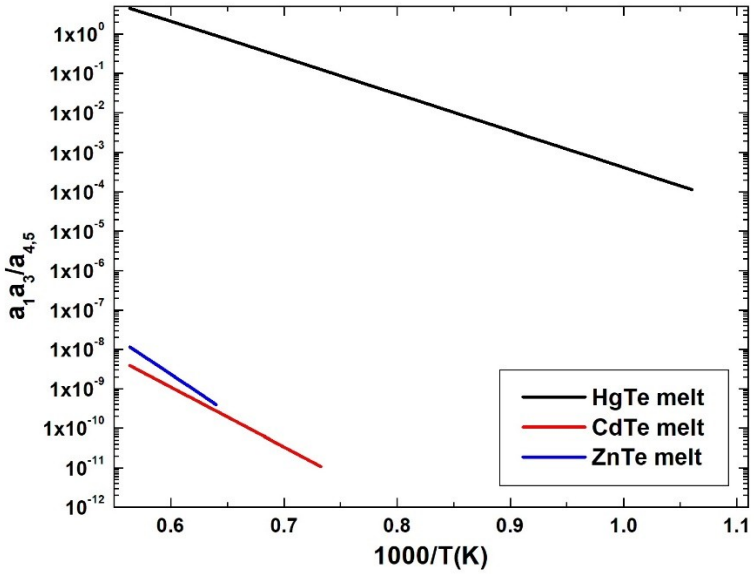

Figure 7.5 Ratios of chemical activity of atomic species 1 and 3 to that of molecular species 4 or 5 as functions of 1000/T(K) for the three melts at 50% at. % of Te.

The structures of HgTe, CdTe and ZnTe melts have been studied by neutron scattering at temperatures just above their respective melting points, i.e., 675, 1100 and 1300ºC [37]. The pair correlation function, g(r), for these II-VI melts, given in Figure 7.6, show the location of the nearest neighbors. For CdTe and ZnTe, the first and second neighbor distances remain almost the same as in the crystal. For instance, the distance of first neighbor for the liquid of ZnTe and CdTe is 2.69$\dot{A}$ and 2.83$\dot{A}$, respectively, comparing to 2.64$\dot{A}$ and 2.81$\dot{A}$ for the solid crystal. On the other hand, the nearest neighbor distance in liquid HgTe, 2.93$\dot{A}$, is significantly larger than that in the solid, 2.78$\dot{A}$. It is interesting that, from the area under the first peak of g(r), a coordination number close to 4 was obtained in the case of CdTe and ZnTe and about 6.3 for HgTe. The heavier HgTe compound undergoes a major structural change during the melting that bond distances and coordination numbers increase. The bond ionicity, calculated according to the Pauling rules, keeps on decreasing as the Group II element getting bigger and heavier. Similar to the cases of group IV elements and III-VI compounds [38,39], liquid HgTe becomes a sixfold coordinated metallic liquid phase which is consistent with the results from the Lorenz number analyses presented in Section 7.1.4. An *Ab Initio* molecular dynamics simulation has been performed on the CdTe and GaAs liquids [40]. It was found that, under high temperature, Group IV or III-VI melts favors a disordered and close-packed structure and, consequently, a transition occurs from a four-fold structure to a denser six-fold coordinated metallic structure. In the case of CdTe liquid, the higher ionicity of cation-anion bonds restricts the miscibility of different types of atoms and limits the delocalization of electrons which contributes to its semiconductor properties. Another *Ab Initio* calculation was performed on the ZnTe liquid [41] which shows similar results as the case of CdTe liquid. Both calculations found the formation of Te helical chains in which 40% of the Te atoms participate.

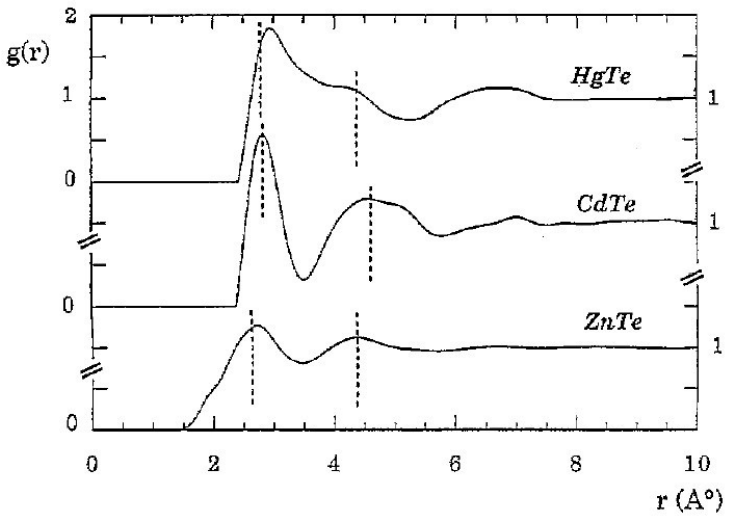

Figure 7.6 The pair correlation functions of liquid HgTe, CdTe and ZnTe. The dotted lines indicate the distances of the nearest neighbors in the melt (taken from Figure 2 of Ref.[37]).

During the diffraction experiments, the structure factor is a critical information in the interpretation of scattering patterns in neutron, X-ray and electron diffraction. Bhatia and co-workers [42-44] have expressed the partial scattering factor for binary and multi-component liquids in terms of wave-number-dependent fluctuation factors. At zero wave number, these factors are related to the thermodynamic properties of the liquid and thus a linkage between the thermodynamic properties and the structure as reflected by diffraction effects is provided. In particular, the composition fluctuation factor, $S_{CC}(0)$, defined as mean square fluctuation in the composition, for a binary system is given by:

$$S_{CC}(0)=¿ \qquad (7.9)$$

where ΔG_M is Gibbs energy of mixing. Note that in Eq.(3.14), the chemical potential of element with composition x is defined as the first derivative of $\Delta G_M$with respect to x, then the composition fluctuation factor is related to the reciprocal of the derivative of chemical potential. Using the interaction parameters given in Ref.[45], the composition fluctuation for the binary liquid of Hg-Te and Cd-Te at the melting temperatures of their solid compounds is illustrated in Figure 7.7. The curve with the strong minimum near 50 at.% of Te, for the Cd-Te binary, is due to the strong association of CdTe species. The maximum at 0.275 at 28 at.% of Te is higher than the value for ideal solution, which is x(1-x), and is indicative of clustering of like atoms and incipient phase separation which is evident by the flat shape of the Cd-rich liquidus line in Figure 3.2.

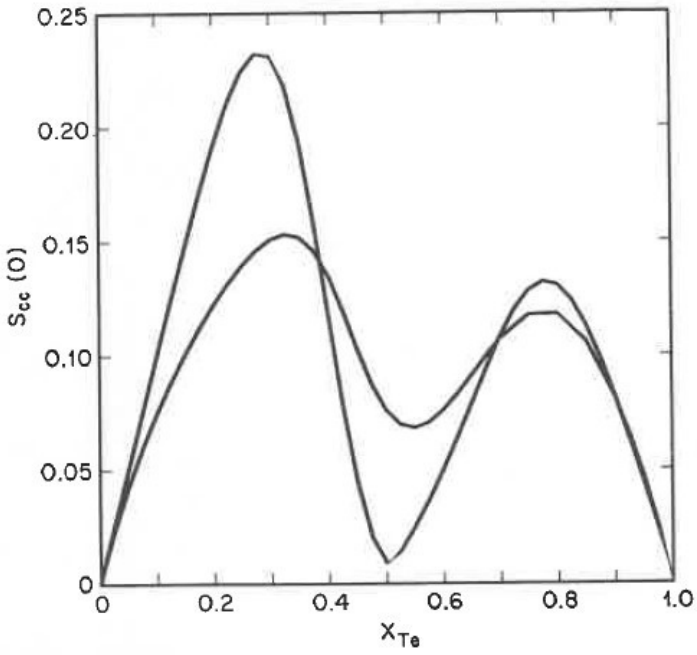

Figure 7.7 Calculated composition fluctuation factor at zero wave number in the liquid phase. The highest curve at $x_{Te} = 0.28$ is for Cd-Te at 1092°C. The other curve is for Hg-Te at 670°C (take from Figure 18 in Ref.[45]).

7.3.1.2 Heat capacity of the melts. The heat capacities, C_P, of the melts were calculated from the optimal interaction parameter of the associated solution model. Comparing Figure 6.1 to 6.2 for the $Hg_{1-x}Cd_xTe$ and $Hg_{1-x}Zn_xTe$ pseudo-binary melts, the C_P values are comparable to each other for $x \leq 0.20$. For $x > 0.2$, the addition of ZnTe to HgTe behaves normally, in the thermodynamic sense, in that (1) right above the liquidus temperature, the heat capacity increases with temperature and (2) the value of C_P does go up with increasing x monotonically. However, in the case of $Hg_{1-x}Cd_xTe$, for $x > 0.2$, the C_P values above the liquidus keeps on decreasing as temperature increases. At a fixed temperature, such as 1100°C, the value of C_P goes up with x increasing from 0.2 to 0.7 and then comes down for x from 0.8 to 1.0. This behavior implies that the melts of the pseudo-binary are significantly different from the ideal solution when CdTe is added to the HgTe melt in that (1) the value of C_P at the melting point are the highest, (2) the decreasing rate of C_p with T keeps on getting smaller with higher value of x and approaches zero at $x = 1.0$ and (3) at 1100°C, the value of C_P does not go up monotonically with the values of x but reaches a maximum at $x = 0.7$. These phenomena indicate that the addition of CdTe to the HgTe melt causes structural and bonding changes because of the interactions between different atomic and molecular species.

7.3.1.3 Density of the melts. The density of the HgTe, $Hg_{0.9}Cd_{0.1}Te$ $Hg_{0.8}Cd_{0.2}Te$ melts were reported in Refs.[46-50]. Similar to the density of Te melt, the data for HgTe and $Hg_{0.9}Cd_{0.1}Te$ melts from Refs.[46,47] showed the behavior of the normal thermal expansion except at temperatures just above the melting point where it goes through a maximum as shown in Figure 4.4 and 4.5. The density for HgTe melt started to increase from the melting point of

670°C, reached a maximum at about 750°C and started to decline. For the $Hg_{0.9}Cd_{0.1}Te$ melt, the density started to increase above the liquidus of 739°C and also went through a maximum at about 750°C. However, the density measured on the melts of $Hg_{0.8}Cd_{0.2}Te$, shown in Figure 4.6 did not follow this trend of maximum. The structural transformation in the liquid phase causing the density maximum at around 750°C probably have completed in the two-phase region (solid+liquid) for the case of $Hg_{0.8}Cd_{0.2}Te$ before it reached the liquidus temperature of 799°C.

As discussed in Chapter 4, the data from Refs.[48-50] by Glazov and Chandra showed more pronounced bumps and were a little lower than those data from Ref.[46,47] which were possibly due to the formations of tiny Hg bubbles. A quantitative description of the density of the HgCdTe melt as a function of temperature was proposed by both Glazov [48,49] and Chandra [50] by applying an effective-medium theory developed by Cohen and Jornter [27-30]. In Glazov's assumption the structure of the HgTe melt consists of several kinds of structures namely, Hg, Te, HgTe, and Hg_2Te_3. The maximum in the HgTe melt density was attributed to the combined changes of the molar volumes and the volume fractions of various structural species as functions of temperature. In Chandra's assumption, the HgTe, $Hg_{0.9}Cd_{0.1}Te$ $Hg_{0.8}Cd_{0.2}Te$ melt structure was considered to be a mixture of a low- and a high-coordination-number structures that have the same total number of Hg and Te atoms. Similar to the case of Te melt, the increase in density of the HgCdTe melt with increasing temperature was attributed to its continuous transformation from the low-coordination-number structure to the denser, high-coordination-number structure. When the temperature increases to the point of density maximum, most of the structural changes has been completed and the density starts to decrease as the temperature increases.

On the relaxation measurements, the density of HgTe, $Hg_{0.9}Cd_{0.1}Te$ $Hg_{0.8}Cd_{0.2}Te$ melts were measured after the melts were rapidly cooled to a temperature just above their liquidus temperatures [18]. In all of the three cases, the measured density of the melt did not change as the meniscus of the melt in the ampoule remained at the same position after a period of 7 to 8 hrs. Therefore, similar to the Te melt, it is concluded that no relaxation phenomenon was observed in the measured density of these three melts.

7.3.2 Viscosity of the melts. All the measured viscosities [46,47], including the results from the HgTe, $Hg_{0.9}Cd_{0.1}Te$ and $Hg_{0.8}Cd_{0.2}Te$ melts, were shown in Figure 5.19. The three sets of data as functions of temperature show the behavior of regular liquids in that, at temperatures just above the melting points, the high viscosity values start to show the characteristics of an exponential decay. At a fixed temperature, the measured viscosity increases when more CdTe content, x, is added to the melt which is likely the result from the higher viscosity of the CdTe melt than the HgTe melt. The viscosity reported for the CdTe melt at 1100°C, or 1373K, by Glazov et al. [51], given in Figure 3.1(a), shows a viscosity of 0.4 centi-stokes, comparing to the value of $1.75x10^{-7}m^2/s$, or 0.175 centi-stokes, for HgTe at 827°C, or 1100K.

The Bachinskii theory, given in Eq.(5.4), postulated the relationship between the reciprocal of kinematic viscosity and density. The measured viscosity, ν, and density, ρ, of the HgTe, $Hg_{0.9}Cd_{0.1}Te$ and $Hg_{0.8}Cd_{0.2}Te$ melts were assessed and presented in Figure 5.21, 5.22 and 5.23, respectively. A large deviation from a straight line of the $1/\nu$ vs. ρ plot is an indication of a structural transition in the melt. From the two plots for HgTe and $Hg_{0.9}Cd_{0.1}Te$, the temperatures

where the deviations from linear line, or the structural transition, are approximately, 805ºC (1078K) and 793ºC (1066K), respectively. The large scattering of the data for the $Hg_{0.8}Cd_{0.2}Te$ melt suggests that there was no transition in the measured temperature range of the melt.

7.3.3 Thermal conductivity and electrical conductivity. The measured thermal conductivity and electrical conductivity for HgTe, $Hg_{0.9}Cd_{0.1}Te$ and $Hg_{0.8}Cd_{0.2}Te$ melts, displayed in Figure 6.7 and 7.3, respectively, increase almost linearly with increasing temperature above their liquidus temperatures. From these two properties, the corresponding Lorenz number, shown in Figure 7.4, suggest that, at temperature high enough, the melts of Te, HgTe, $Hg_{0.9}Cd_{0.1}Te$ and $Hg_{0.8}Cd_{0.2}Te$ behave similarly to metals or degenerate semiconductors, i.e., a body of free-electron gas with minimum contribution to thermal conductivity from the scattering of lattice defects or/and from the phonons.

7.3.4 Relaxation phenomena. On the studies of the relaxation behavior, after rapid cooling from 857ºC to 800ºC, the measured viscosity of the $Hg_{0.8}Cd_{0.2}Te$ melt increased and went through a maximum after 2 hrs, then started to decline for 50 hrs to reach its equilibrium value. During this relaxation, the viscosity decreased approximately 60% from the maximum value to its equilibrium value.

7.4 Physics and chemistry Hg-Zn-Te system

7.4.1 Structural transformation in the melts. The increasing ZnTe content in the HgTe melt results in a decrease in the density of the HgZnTe pseudo-binary melts. However, a maximum in the melt density was not observed, as shown in Figure 4.8. The $Hg_{0.90}Zn_{0.10}Te$ melt behaves with normal thermal expansion and the density for the $Hg_{0.84}Zn_{0.16}Te$ melt are essentially constant. On the measurements of the $Hg_{0.90}Zn_{0.10}Te$ sample, the density showed a hysteresis loop in that, at a fixed temperature, the measured values during cooling were higher than heating. Similar behavior was also observed during viscosity measurements in the HgZnTe melt which will be presented in more detail below.

The structures of $Hg_{1-x}Zn_xTe$ melts, for x = 0, 0.2, 0.4, 0.6, 0.9 and 1.0, have been studied by neutron scattering at temperatures just above their respective melting points from 670 to 1300ºC [52]. The pair correlation function g(r), given in Figure 7.8, shows that the addition of ZnTe to the HgTe melt causes the decrease in the distance of first neighbor and, for x = 0.6 and 0.9, their g(r) show three pronounced peaks before the increase of the first neighbor distance to that of ZnTe. The coordination number, given by the area under the first peak of $4\pi r^2 g(r)$, are different for the cases of x = 0.6 and 0.9 in that it decreases to 1.7 and 2.1, respectively, while the area under the second peak is close to 4 in both cases. These features are fully compatible with a "deformed cinnabar" structure for the case of HgS melt Ref.[52] which shows a chainlike structure just above its melting point and tends to become tetrahedral at higher temperature. It can be summarized that the addition of HgTe to ZnTe melt first changes its tetrahedral (zinc blend) structure to the intermediate cinnabar structure when $x_{ZnTe} = 0.9$ and 0.6 and then evolves to the six fold NaCl structure of HgTe melt.

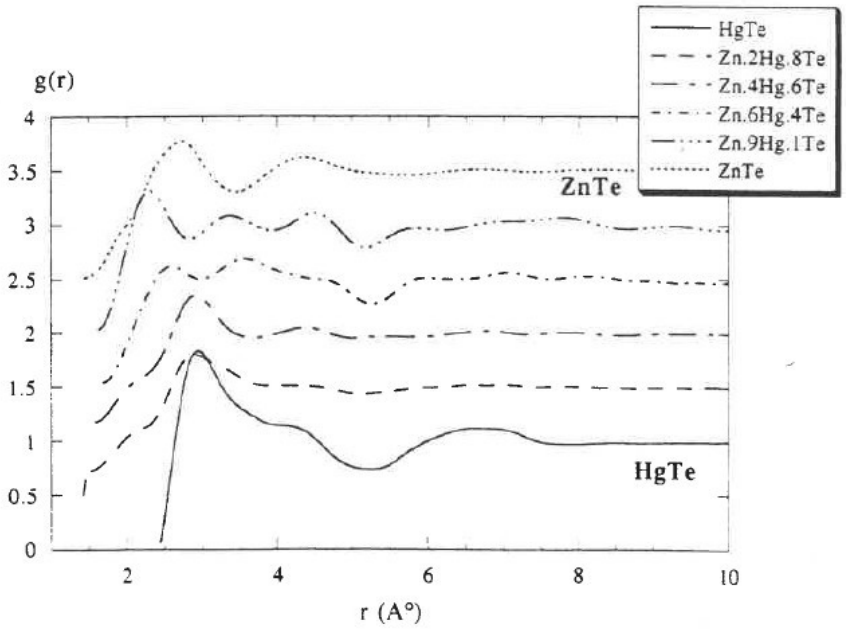

Figure 7.8 The pair correlation functions g(r) for $Hg_{1-x}Zn_xTe$ melts of x = 0, 0.2, 0.4, 0.6, 0.9 and 1.0 at temperatures just above their respective melting points from 670 to 1300°C [52].

7.4.2 Viscosity of $Hg_{0.84}Zn_{0.16}Te$ melt. The viscosity of $Hg_{0.84}Zn_{0.16}Te$ were measured by the oscillating cup (OC) method [53] as described in Chapter 5. The measured viscosity values are smaller than that for the $Hg_{0.8}Cd_{0.2}Te$ pseudo-binary melt but with a different trend. As shown in Figure 5.5 and displayed below in Figure 7.9, instead of the exponential decay, the data start from $1.0x10^{-3}cm^2/s$ at 770°C, just above the liquidus temperature, to a maximum of $1.4x10^{-3}cm^2/s$ at 810°C and decreases to $1.2x10^{-3}cm^2/s$ at 850°C. However, it should be noted that this different trend was resulted mainly because the measured value at the liquidus point was much lower than the data of the $Hg_{0.8}Cd_{0.2}Te$ melt which started from $3.2x10^{-3}cm^2/s$ at 800°C and decreased exponentially to $2.3x10^{-3}cm^2/s$ at 860°C. To test the consistency of the measurements, two samples with different ampoule dimension and sample mass (118.6g vs. 82.0g) were synthesized with different procedure. A total of 150 measurements were performed for this study and the viscosity data were reproducible within 5%.

Since there was no density maximum observed in this temperature range, the cause for higher resistance to flow in the melt at the maximum of viscosity was not well understood. It might be caused by different domain/phase or structural cluster with similar density to the host matrix. Possible mechanisms for this phenomenon can be attributed to the microscopic inhomogeneities such as subcritical clusters of the second phase [54] or the formation of associated molecular species [17,45] in the melt. Different terms are used for the definitions of these fragments: conglomerates, grains, domains, clusters, complexes, associations and so on. Such a variety reflects some uncertainty of the species sizes. Any changes in the temperature will induce microscopic reactions which cause the redistribution in the cluster size and their composition. This process is diffusion controlled and can be rather slow.

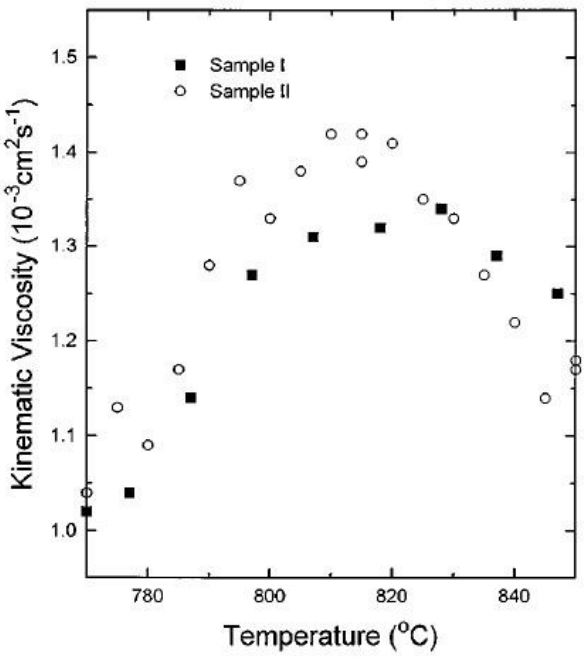

Figure 7.9 The measure kinematic viscosity of $Hg_{0.84}Zn_{0.16}Te$ pseudo-binary melt as a function of temperature (taken from Figure 3 of Ref.[53]).

7.4.3 Relaxation phenomenon. During the relaxation studies on the viscosity of $Hg_{0.84}Zn_{0.16}Te$ melt, another interesting phenomenon was observed. As displayed in Figure 5.6 and given below in Figure 7.10, two sets of data were obtained as functions of time after the ampoules were cooled from 850°C and stabilizing at temperatures of 790 and 810°C and it took five days and 1 day, respectively, for the measurements to reach steady state.

Possible mechanisms for the observed relaxation of the measured viscosity during temperature cycling, as well as the phenomena discussed earlier on the density hysteresis and abnormal behavior of viscosity of the $Hg_{0.84}Zn_{0.16}Te$ melt, might be attributed to microscopic inhomogeneities. Equilibrium density and composition fluctuations near the liquidus point can be qualitatively different from those at higher temperatures, i.e., different coordination number or subcritical clusters of the small second phase can be present [54]. Noting that the group VI elements tend to polymerize when molten, it was also proposed that the enhancement of viscosity was the results of the slow formation of the Te atom chains, or the linear Te n-mers [55,56]. Any changes in the temperature will induce redistribution in the volume fractions of domains with different coordination numbers or the heterogeneous cluster sizes and its composition. The time scale of the transition of coordination number or hetero fluctuations can be quite long.

It has also been reported that, during an isothermal holding for several hours at temperatures more than 100ºC above its liquidus, the viscosity in the Al-rich Al-Y melts increased significantly before a subsequent exponential decay [57]. It was claimed [58] that this

abnormality in viscosity was the result of the temporal competition of two simultaneous effects: (1) the growth of the initial and large Y-rich heterogeneity in the melt through the Ostwald ripening effect and (2) a slow dissolution of the heterogeneities resulting in the homogenization of the melt. On the other hand, recent X-ray studies of several binary metallic systems revealed a profound long lasting memory effect of the melt microstructure in relation to its thermal history [59]. In the studies of neutron diffraction on the molten NiP alloy of eutectic composition, Ni particles were found to exist at temperatures 150°C above the liquidus as well as after more than 30 hrs at different temperatures in the molten state [60]. It was also claimed [61] that there exists several types of micro-inhomogeneity and micro-heterogeneity in some liquid metallic solutions with their structure depending on their composition and pre-history. Using various environments of temperature, pressure and/or other physical effects, one can modify the structure. These changes retain in the melt down to the liquidus and affect the structure and properties of the solidified alloy.

In the case of the $Hg_{0.8}Cd_{0.2}Te$ melt, the amount of fluctuation during relaxation measurements shows a 62% variation on the relaxation behavior of kinematic viscosity. However, the trends were different for these two systems in that, during the relaxation, the viscosity of the $Hg_{0.84}Zn_{0.16}Te$ melt continuously increased by a factor of about 1.5 as a function of time to reach its steady state value after 120 hrs whereas the data for the $Hg_{0.8}Cd_{0.2}Te$ melt went through a maximum and then decreased 62% to its equilibrium value in about 60 hrs.

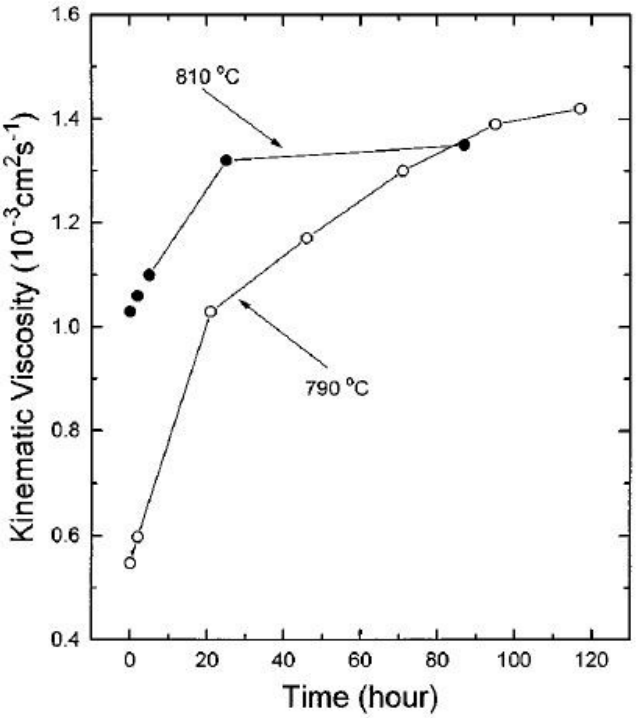

Figure 7.10 Relaxation phenomena of the kinematic viscosity after the $Hg_{0.84}Zn_{0.16}Te$ melts were cooled from 850°C to the prescribed temperatures, 810 and 790°C (taken from Figure 4 of Ref. [53]).

7.5 Effects on crystal growth process

In the cases of unseeded melt growth of II-VI compounds, namely, CdTe, CdZnTe and ZnSe, there were a large number of experimental facts showing the correlation between melt state and crystal quality [62-72]. It has been reported that the structure of the melt depends on the degree of superheating – the melts of CdTe and PbTe need to be superheated in excess of a critical value and duration to destruct the associated complex in the melt [62]. When the CdTe melt is superheated 110ºC above the melting point for 24 hours prior to the crystal growth process, an effective reduction of the Te particle concentration has been observed in the as-grown crystals [73]. The results are correlated to the highly associated melt structure which dissociates after a superheating of 110ºC. It is also believed that the crystalline quality can be improved, i.e., with reduced number of large angle grains and twins, if the melt was markedly superheated. The melts of II-VI elements are known to consist of high concentrations of associated species, such as CdTe and ZnTe, and the level of the association decreases as temperature increases. It is speculated that after high superheating the associated complex dissociate, and the spontaneous multi-nucleation is retarded. Similar behavior has been reported on the differential thermal analysis (DTA) near the melting point of CdTe [72] that some additional endothermic peaks above the melting point were observed. It was claimed that when the melt was heated to T_m + (9-10)K, where T_m is the liquidus, because the existing clusters serve as nuclei so that and no supercooling will be observed during cooling. But when the melt of CdTe was superheated above T_m + 10K, supercooling occurred. During the dynamic viscosity measurements of $Cd_{1-x}Zn_xTe$ ($0 \leq x \leq 0.1$) [71,74], the melt needed to be soaked for at least 48 hrs at T_m + 50K in order to completely dissolve any local clusters of Te-rich chains in the forms of branched chains of Cd_nTe_{3n+1} or Te atoms.

On the other hand, during melt growth by directional solidification, a large supercooling of the melt results in a large section of ingot solidifying uncontrollably under spontaneous nucleation [75] with poor-quality multi-crystalline crystal in the first-grown section, which cause the low yield of the commercial growth process. In the DTA measurements on a high-purity CdTe sample [76], during the cooling of the furnace, the sample temperature stayed at 1092ºC and eventually started to decrease when the furnace reached 1040ºC, i.e., a supercooling of 50ºC. To prevent the undesired formation of a large multi-grained spontaneous nucleation, i.e., to promote nucleation under the condition of small supercooling, a short-time mechanical perturbation was applied to the growth ampoule [77] at a critical time during growth when the melt at the ampoule tip just reached below the liquidus temperature. The technique was implemented to the directional solidification process of $Cd_{0.80}Zn_{0.20}Te$ crystals [76] to promote the nucleation in the melt and, consequently, a small section of solid, usually single or double grain, was formed at the growth tip which grew continuously throughout most of the ingot length. The effects of acoustic wave from the pulsed vibrations have been studied analytically through the classical nucleation theory [78].

References

[1] G. Wiedemann and R. Franz, Ann. Phys. Chem., 89 (1853) 497.
[2] L. Lorenz, Ann. Phys. 147 (1872) 429.
[3] A. Sommerfeld, Naturwissenschaften, 15 (1927) 825.
[4] G. S. Kumar, G. Prasad and R. O. Pohl, J. Mater. Sci. 28 (1993) 4261.
[5] E. Flage-Larsen and Ø. Prytz, Appl. Phys. Lett. 99 (2011) 202108.
[6] K. C. Lukas, W. S. Liu, G. Joshi, M. Zebarjadi, M. S. Dresselhaus, Z.F. Ren, G. Chen and C.P. Opeil, Phys. Rev. B 85 (2012) 205410.
[7] Hyun-Sik Kim, Zachary M. Gibbs, Yinglu Tang, Heng Wang, and G. Jeffrey Snyder, APL Mater. 3 (2015) 041506.
[8] C.-H. Su, Materials Today Physics 5 (2018) 58.
[9] G. Busch, H.-J. Güntherodt, W. Haller and P. Wyssmann, J. Physique Colloques, 35 (1974) C4-313.
[10] Matthias Leitner, Thomas Leitner, Alexander Schmon, Kirmanj Aziz and Gernot Pottlacher, Metall. & Mater. Trans. A 48A (2017) 3036.
[11] B. Giordanengo, N. Benazzi, J. Vinckel, J. G. Gasser and L. Roubi, J. Non-Cryst. Solids, 250-252 (1999) 377.
[12] Ching-Hua Su, submitted to J. Appl. Phys. Jan. 2021.
[13] W. J. Parker, R. J. Jenkins, C. P. Butler and G. L. Abbot, J. Appl. Phys. 32-9 (1961) 1679.
[14] R. A. Medzhidov and S. M. Rasulov, Inorg. Mater. 11 (1975) 555.
[15] H. Ibach and E. Ruim, Phys. Status Solidi (b) 41 (1970) 719.
[16] Ching-Hua Su, J. Crystal Growth 78 (1986) 51.
[17] T.-C. Yu and R. F. Brebrick, J. Phase equilibrium 13, (1992) 476.
[18] C. Li, Ph.D. dissertation "*Thermophysical properties of Te, HgTe and* $Hg_{1-X}Cd_XTe$ *melts*" University of Alabama at Birmingham (2003).
[19] H.-G. Junginger, Solid State Commun. 5 (1967) 509.
[20] Ching-Hua Su, Pok-Kai Liao, and R. F. Brebrick, J. Electron. Mater. 12 (1983) 771.
[21] Ching-Hua Su, AIP Advances 5 (2015) 051778.
[22] A. Menelle, R. Bellissent, and A. M. Flank, Europhys. Kett. 4 (1987) 705.
[23] G. Tourand and M. Breuil C. R. Acad. Sci., Paris B270 (1970) 109.
[24] B. Cabane and C. Froidevaux, Phys. Lett. 29A (1969) 512.
[25] W. W. Warren Jr., Phys. Rev. B 6 (1972) 2522.
[26] B. Cabane and J. Friedel, J. Physique 32 (1971) 73.
[27] M. H. Cohen and J. Jortner, Phys. Rev. B 13 (1976) 5255.
[28] M. H. Cohen and J. Jortner, Phys. Rev. Lett. 30 (15) (1973) 699.
[29] M. H. Cohen and J. Jortner, Phys. Rev. Lett. 30 (15) (1973) 696.
[30] M. H. Cohen and J. Jortner, Phys. Rev. A 10 (1974) 978.
[31] Y. Tsuchiya, S. Takeda, S. Tamaki, Y. Waseda and E. Seymour, J. Phys. C 15 (1982) 2561.
[32] Y. Tsuchiya and E. Seymour, J. Phys. C 15 (1982) L687.
[33] Y. Tsuchiya, S. Takeda, S. Tamaki and E. Seymour, J. Phys. C 15 (1982) 6497
[34] Y. Tsuchiya, J. Phys. C 20 (1987) 1209.
[35] S. Glasstone, K. J. Laidler and H. Eyring, *Theory of Rate Processes*, McGraw-Hill, New York (1941).
[36] A. I. Bachinskii, Izd. Akad. Nauk. SSSR, Moscow (1960).
[37] J.-P. Gaspard, J.-Y. Raty, R. Céolin and R. Bellissent, J. Non-Cryst. Solids 205–207 (1996) 75.

[38] Y. Waseda, *The Structures of Non-Crystalline Materials. Liquid and Amorphous Solids*, McGraw-Hill, New York (1981).
[39] C. Bergman, C. Bichara, P. Chieux and J. P. Gaspard, J. Phys. (Paris) C8 (46) (1985) 97.
[40] V. V. Godlevsky, J. J. Derby and J. R. Chelikowsky, Phys. Rev. Lett. 81 (1998) 4959.
[41] M. Jain, V. V. Godlevsky, J. J. Derby and J. R. Chelikowsky, Phys. Rev. B 65 (2001) 035212.
[42] A. B. Bhatia and D. E. Thornton, Phys. Rev. B8 (1970) 3004.
[43] A. B. Bhatia and W. H. Hargrove, Phys. Rev. B10 (1974) 3186.
[44] A. B. Bhatia and V. K. Ratti, Phys. Chem. Liq. 6 (1977) 201.
[45] R. F. Brebrick, Ching-Hua Su, and Pok-Kai Liao, in *Semiconductors and Semimetals,* Vol. 19, Chap. 3, edited by R. K. Willardson and A. C. Beer, Academic, New York (1983).
[46] C. Li, R. N. Scripa, H. Ban, B. Lin, Ching-Hua Su and S. L. Lehoczky, J. Non-Cryst. Solids 351 (2005) 1179.
[47] C. Li, Ching-Hua Su, S. L. Lehoczky, R. N. Scripa, H. Ban, and B. Lin, J. Non-Cryst. Solids 391 (2014) 54.
[48] V. M. Glazov and L. M. Pavlova, Thermochimica Acta 314 (1998) 265.
[49] V. M. Glazov and L. M. Pavlova, S. V. Stankus, J. Chim. Phys. 94 (1997) 1816.
[50] D. Chandra and L. R. Holland, J. Vac. Sci. Technol. A 1 (1983) 1620.
[51] V. M. Glazov, S. N. Chizhevskaya and N. N. Glagoleva, *Liquid Semiconductors*, Plenum, New York (1969).
[52] J. Y. Raty, J. P. Gaspard, R. Ceolin and R. Bellissent, Physica B 234-236 (1997) 364.

[53] K. Mazuruk, Ching-Hua Su, Yi-Gao Sha and S. L. Lehoczky, J. Appl. Phys. 79 (1996) 9080.
[54] V. I. Yukalov, Phys. Rep. 208, (1991) 395.
[55] C. Li, Ching-Hua Su, R.N. Scripa, B. Lin, H. Ban, and S. L. Lehoczky, presented at the Fourteenth American Conference on Crystal Growth and Epitaxy (ACCGE-14), Seattle, Washington August 5-9, 2002.
[56] James K. Baird, Yeong Woo Kim, Ching-Hua Su and S. L. Lehoczky, Phys. Chem. Liquids 40 (2002) 607.
[57] V. I. Lad'yanov, S. G. Men'shikova, A. L. Bel'tyukov and B. B. Maslov, Bull. Russ. Acad. Sci. Phys. 74 (2010) 1176.
[58] M. G. Vasin, S. G. Menshikova and M. D. Ivshin, Physica A 449 (2016) 64.
[59] V. V. Bukhalenko, S. I. Slyusarenko, V. E. Laz'ko, L. A. Rostovskaya, and O. I. Slukhovskii, Phys. Metals 10 (1991) 1025.
[60] U. Dahlborg, J.-G. Gasser, G. J. Cuello, S. Mehraban, N. Lavery and M. Calvo-Dahlborg, J. Non-Cryst. Solids 500 (2018) 359.
[61] V. Manov, P. S. Popel, E. Brook-Levinson, V. Molokanov, M. Calvo-Dahlborg, U. Dahlborg, V. Sidorov, L. Son and Yu. Tarakanov, Mater. Sci. Eng. A 304-306 (2001) 54.
[62] P. Rudolph and M. Muhlberg, Mater. Sci. Eng. B16 (1993) 8.
[63] P. Rudolph, Prog. Crystal Growth Charact. 29 (1995) 275.
[64] P. Rudolph, N. Schafer and T. Fukuda, Mater. Sci. Eng. R15 (1995) 85.
[65] M. Muhlberg, P. Rudolph, M. Laasch, and E. Treser, J. Crystal Growth 128 (1993) 571.
[66] B. W. Choi and H. N. G. Wadley, J. Crystal Growth 208 (2000) 219.
[67] I. Kikuma and M. Furukoshi, J. Crystal Growth 44 (1978) 467.

[68] I. Kikuma and M. Furukoshi, J. Crystal Growth 71 (1985)136.
[69] Y.-C. Lu, J.-J. Shiau, R. S. Feigelson an R. K. Route, J. Crystal Growth 102 (1990) 807.
[70] M. P. Kulakow, V. D. Kulakovskii and A. V. Fadeev, Inorg. Mater. 12 (1976) 1867.
[71] L. Shcherbak, P. Feichoul and O. Panchouk, J. Crystal Growth 161 (1996) 16.
[72] L. Shcherbak, J. Crystal Growth 197 (1999) 397.
[73] E. Saucedo, P. Rudolph and E. Diequez, J. Crystal Growth 310 (2008) 2067.
[74] L. Shcherbak, P. Feychuk, Yu. Plevachuk, Ch. Dong, O. Kopach, O. Panchuk and P. Siffert, J. Alloys and Compounds. 371 (2004) 186.
[75] Ching-Hua Su, S. L. Lehoczky, F. R. Szofran, J. Crystal Growth 86 (1988) 87.
[76] Ching-Hua Su, J. Crystal Growth. 410 (2015) 35.
[77] Ching-Hua Su, U. S. Patent # 8,535,440, September 2013.
[78] James K. Baird, Ching-Hua Su, J. Crystal Growth 487 (2018) 65.